SEVER INSTITUTE OF TECHNOLOGY

DOCTOR OF SCIENCE DEGREE

DISSERTATION ACCEPTANCE

(To be the first page of each copy of the dissertation)

DATE: October 2, 1996

STUDENT'S NAME: Donald G. Porter

This student's dissertation, entitled Fundamental Limits on the Storage Capacity of Magnetic Recording Media has been examined by the undersigned committee of five faculty members and has received full approval for acceptance in partial fulfillment of the requirements for the degree Doctor of Science.

APPROVAL: ______________________________ Chairman

____

____

____

____

Short Title: Storage Limits of Magnetic Media Porter, D.Sc. 1996

WASHINGTON UNIVERSITY
SEVER INSTITUTE OF TECHNOLOGY
DEPARTMENT OF ELECTRICAL ENGINEERING

FUNDAMENTAL LIMITS ON THE STORAGE CAPACITY OF MAGNETIC RECORDING MEDIA

by

Donald G. Porter

Prepared under the direction of Professors J. A. O'Sullivan and R. S. Indeck

A dissertation presented to the Sever Institute of
Washington University in partial fulfillment
of the requirements for the degree of

Doctor of Science

December, 1996

Saint Louis, Missouri

WASHINGTON UNIVERSITY
SEVER INSTITUTE OF TECHNOLOGY
DEPARTMENT OF ELECTRICAL ENGINEERING

ABSTRACT

FUNDAMENTAL LIMITS ON THE STORAGE CAPACITY OF MAGNETIC RECORDING MEDIA

by Donald G. Porter

ADVISOR: Professors J. A. O'Sullivan and R. S. Indeck

December, 1996
Saint Louis, Missouri

Rigid disk magnetic recording systems store information as patterns of magnetization on a thin-film recording medium. The capacity of a magnetic recording medium to store information is limited by its ability to sustain stable magnetic patterns. A micromagnetic model of recording media is developed and implemented to represent the magnetization patterns. The model is capable of representing a broad class of magnetic materials by selection of different values of model parameters. The model parameters are of two types. First, the intrinsic physical properties of a recording medium are represented by the values of five parameters: grain size, film thickness, saturation magnetization, anisotropy energy density, and exchange interaction strength. Second, the microstructural properties of the recording medium are represented by a single realization of a random manufacturing process. Simulations of a particular instance of the model calculate its bulk hysteresis properties, which may be used to identify that model instance with a particular physical recording medium. Simulations of recording and playback operations verify that properties of calculated medium noise waveforms are in agreement with those of experimental observations. Analysis of a simplified version of the model indicates that for media with small enough intergranular interactions, every model element is able to store one bit of information, and areal density is limited only by thermal constraints on the volume of elements which can sustain a magnetization, the superparamagnetic limit. For media with larger interactions, information storage density is limited below the superparamagnetic limit. The boundary between these two categories of media is calculated as a function of medium material properties over the class of non-oriented recording media. A simple analysis also predicts that when intergranular interactions are large enough to matter, attainment of information storage densities approaching the fundamental limit requires making use of information about the medium microstructure in the record and playback operations. Finally, a connection is made between certain instances of the medium model and the Hopfield model for associative memory neural networks, suggesting commonality among these systems which exhibit memory.

To my parents

Contents

List of Tables

List of Figures

Acknowledgments

The peril of offering a lengthy set of acknowledgments is that someone's worthy contribution will be inadvertently neglected. The reader can see by the length of this section that I've chosen to take the risk. I apologize to those persons who are not named here, yet without whom this work would not be what it is. I trust they know who they are.

I have been guided, advised, encouraged, and driven in this effort by three remarkable men who served as my research advisors in both official and unofficial capacity. Prof. Jody O'Sullivan has been my thesis advisor, research advisor, and academic advisor throughout my years as a graduate student. My work with Prof. O'Sullivan began as an undergraduate working on radar imaging algorithms, and both the work and the collaboration have only grown stronger as the years have passed. My deepest appreciation to him. I thank Prof. Ron Indeck for explaining the mysteries of recording systems to me again and again, not least of all the curious language and units of materials scientists and physicists, and for the regular weekly infusion of donuts and bagels. I thank Prof. Marcel Muller for sharing his keen understanding and great experience in the study of the physics of materials, as well as being the fine final rewrite man that he is. I will miss working regularly with these men, and leave hoping that although our collaboration will be far less frequent, it will nevertheless continue to enrich us all. My thanks also go out to the other two members of my doctoral examination committee for their service, Dean Christopher Byrnes and Prof. Donald Snyder. If any one man can be given credit for setting me on the path to research and graduate school, it is Prof. Snyder who first brought me into the Electronic Signals and Systems Research Laboratory to work on radar problems. I wrote my first research proposal for Prof. Snyder, and it must have been good practice, given the successful outcome of my most recent proposal, the NRC post-doc I now begin at the National Institute of Standards and Technology.

Working and studying alongside me in the Magnetics and Information Science Center and the Electronic Systems and Signals Research Laboratory have been several fellow graduate students. At times I have relied on each of them for data, insight, proofreading skills, contributions in technical discussions, patient repeated explanations of experimental procedures, and patience while I fooled around with the computers and the software, breaking them not quite as often as I fixed them. My thanks to Dakshi Agrawal, Mihir Sathe, Albrecht Jander, Elias Glavinas, Pallavi Dhagat, Horng-shiong Chen, Leslie He, Steve Jacobs, and Nick Cutaia. Also acknowledged are the contributions of several undergraduate students, both to the overall research project and to their specific assistance in my research work. My thanks to Sam Rosen, Eric Bjerkaas, Jeff Hutz, Monica Fisher, and Ch'ng Shi Baw. Special acknowledgement is due to Monica Fisher for her contributions in [27] which led to the probability density function calculations of Chapter 6.

Contributions to this research from colleagues outside Washington University include C. Bradford Barber and his colleagues at The Geometry Center at the University of Minnesota for their `qhull` program made freely available. Earlier versions of the software described in this thesis made use of the OATH C++ class library by Brian Kennedy of Texas Instruments. My thanks to them all.

The task of writing this thesis and editing it into an acceptable form has been greatly eased thanks to the LaTeXtemplates created by Kevin Ruland and maintained by Long Duan. My thanks to these volunteers and to the Association of Graduate Engineering Students which organizes their efforts.

Finally, I acknowledge my sources of financial support, the U.S. Department of Education Graduate Assistance in Areas of National Need Fellowship, the Washington University Department of Electrical Engineering, and the National Science Foundation Grant NCR-9406197.

Donald G. Porter

Washington University in Saint Louis
December 1996

Preface

This is a doctoral dissertation. Its intent is to demonstrate "an ability for critical and constructive thinking" and to represent "a definite contribution to knowledge in some field of engineering or applied science."[121] In this regard it is like any doctoral dissertation. Unlike many dissertations though, this one draws on material from two subfields of electrical engineering, information theory and physics of magnetic materials, which are often separated in both study and research. As a consequence, this thesis contains more background material than one might expect, in the author's hope of making its contents accessible to researchers in both fields. The reader is asked to forgive the inclusion of "obvious" or "well-known" material with the understanding that such evaluations are relative to one's familiarity with a field of study.

Notation and Conventions

Standard mathematical notation is used throughout this thesis. Where notation varies among standard sources, the following notational conventions are followed:

- The symbol j represents the imaginary unit, $\sqrt{-1}$.
- $\mathbf{N}$ denotes the set of all natural numbers. $\mathbf{R}$ denotes the set of all real numbers.
- Variables representing vector quantites are denoted using boldface ($\mathbf{h}$) or underlining ($\underline{\omega}$). Vectors occur in two contexts. First, vectors are used to represent the field quantities of electromagnetics (e.g., $\mathbf{H}$, $\mathbf{B}$). In this context, the standard electromagnetics notation as practiced in the United States is used. Second, vectors are used to represent finite, ordered collections of variables ($\mathbf{x} = (x_1, \cdots, x_N)^T$) arrayed in columns. In the second context, lowercase is used for vectors to distinguish them from matrices. The scalar product of two vectors is denoted by either the dot notation ($\mathbf{s} \cdot \mathbf{x}$) or matrix multiplication notation ($\mathbf{s}^T\mathbf{x}$).

- Variables representing matrix quantities are denoted using uppercase and boldface ($\mathbf{W}$).

- The unit vectors of a coordinate system are indicated using "hat" variables ($\hat{\mathbf{x}}$).

- The expression $\log(\cdot)$ denotes the base 2 logarithm. When logartihms of other bases are needed, the base is indicated by subscript ($\log_{10}$). The natural logartihm is denoted ln.

- The expression $\operatorname{sgn}(\cdot)$ denotes the sign function on the domain of the real numbers, $\mathbf{R}$, onto the range $\{\pm 1\}$, defined

$$\operatorname{sgn}(x) \triangleq \begin{cases} +1, & x \geq 0 \\ -1, & x < 0 \end{cases}$$

  The same notation is also used to denote the straightforward extension of this function to the domain $\mathbf{R}^N$ and the range $\{\pm 1\}^N$, for any $N \in \mathbf{N}$.

- The expression $\delta(\cdot)$ denotes the Dirac delta "function," which is properly not a function at all, but a distribution [130], defined by the sifting property,

$$\phi(0) = \int \delta(t)\phi(t)dt,$$

  for all complex-valued functions $\phi(\cdot)$ which have continuous derivatives of all orders and are zero-valued outside a finite interval of the real domain.

- For any set S, the expression $|S|$ denotes the cardinality of S. For finite sets, the cardinality of the set is the number of elements it contains.

- For any set S, the expression $I_S(\cdot)$ denotes the indicator function, defined

$$I_S(x) \triangleq \begin{cases} 1, & x \in S \\ 0, & x \notin S \end{cases}$$

- Given a probability space $(\mathcal{S}, \mathcal{F}, P)$, and a random variable $x : \mathcal{S} \to \mathbf{R}$, the expression

$$P_x(\lambda) \triangleq P\{\zeta \in \mathcal{S} : x(\zeta) \leq \lambda\}$$

denotes the probability distribution of x, and the expression

$$p_x(\lambda) \triangleq \frac{d}{d\lambda} P_x(\lambda)$$

denotes the probability density function of x, when it exists. The expression

$$E\{\cdot\}$$

denotes the expectation operation, the expression

$$\Phi_{\mathbf{x}}(\underline{\omega}) \triangleq E\{e^{j\underline{\omega}\cdot\mathbf{x}}\}$$

denotes the characteristic function of random vector $\mathbf{x}$.

- The expression $\mathrm{erf}_*(\cdot)$ denotes the probability distribution function of a standard normal real random variable,

$$\mathrm{erf}_*(x) \triangleq \frac{1}{\sqrt{2\pi}} \int_{-\infty}^{x} e^{-\frac{t^2}{2}} dt.$$

  This notation is in agreement with that of [115].

Units

Physical quantities are expressed in this thesis using SI units, unless otherwise indicated. Though nominally an international standard, in practice SI units are not commonly used in the literature on the physics of magnetic materials. Rather a traditional mixture of SI units, Gaussian units, and English units is used. For this reason, non-SI units will sometimes appear in this thesis, usually for the sake of comparison with values reported in the magnetics literature. A reference useful for sorting through the confusion is Chapter 23 of [120], a guide to understanding the many systems of units used in the magnetics literature, how they are related, and how quantities may be converted from one system to another.

Chapter 1

Background

With the dawn of the Information Age has arrived an ever-growing demand for information storage. This demand has been met by the research efforts of the magnetic recording industry, which continues to produce recording systems capable of greater and greater density of information storage. The growth of the areal density of rigid disk magnetic recording systems has followed a historical trend of an annual increase of about 27%, or a doubling of areal density every three years. Since 1990 this remarkable rate of growth has increased to an astounding annual increase of 60% [33]. Recent publications report that recording densities of 1.55 Mbit/mm^2 (1 Gbit/in^2) [127] and 3.10 Mbit/mm^2 (2 Gbit/in^2) [29] have been demonstrated as research prototypes. In March 1995, the IBM Advanced Magnetic Recording Laboratory announced that an areal density exceeding 4.65 Mbit/mm^2 (3 Gbit/in^2) had been achieved [114]. Continued evolutionary research, particularly the development of more sensitive read heads, is expected to continue the current trend into the near future, leading to magnetic recording technology with areal density of at least 7.75 Mbit/mm^2 (5 Gbit/in^2) in products by the year 2000 [33]. Beyond that, technology challenges have been identified that, when met, are expected to produce systems capable of recording densities of 15.5 Mbit/mm^2 (10 Gbit/in^2) [85].

These recording densities are approaching limits imposed by the laws of physics. One known limit to increasing recording density is the *superparamagnetic limit* [21, p. 314] [57, p. 25] [49, p. 130]. When the energy required to redirect the magnetization of a small magnetic particle is of the same order as the thermal energy available, the particle will not be able to sustain a magnetization in one direction. The smaller a particle, the less energy is required to redirect its magnetization. Thus, at a given absolute temperature T, there is a critical particle volume V_p below which a direction of magnetization cannot be sustained over a useful storage lifetime. Stability of the magnetization of a particle arises primarily from its anisotropy energy. The anisotropy energy density K_A of commonly used recording materials is roughly 100 kJ/m^3, and is expected to increase only up to about 400 kJ/m^3 in the forseeable future [55]. The accepted expression for the critical volume V_p for thermal stability over a period of t seconds is [49]

$$V_p = \ln(2 \times 10^9 t)\frac{k_B T}{K_A}. \tag{1.1}$$

Therefore, the critical particle volume for information storage at room temperature ($T = 300$ K) will remain greater than about 400 nm^3. Assuming spherical particles, this corresponds to a particle diameter of about 13 nm. For a rough estimate of the thermal limit on areal density, consider a limit of 10 nm square on the dimensions of a bit cell. The resulting thermal limit on areal density is 10 Gbit/mm^2 (6.45 Tbit/in^2). This limit is about four orders of magnitude beyond the density achieved by contemporary commercial products.

This estimation of the thermal limit assumes that each magnetic particle of the critical size is independently capable of storing a bit of information. In other words, a recording medium could be subdivided into *bit cells*, each capable of storing one bit of information, and each having area given by the superparamagnetic limit. This implies that each bit cell can be magnetized into one of two distinguishable magnetic states, independent of the magnetic states of the other bit cells. Such an assumption is not warranted. Because the bit cells are magnetized, they interact with one another through magnetic forces. As a result, the bit cells cannot sustain arbitrary magnetic states independent of one another. Instead, the overall magnetic state of an assembly of bit cells will naturally evolve to reduce the magnetic energy of the system. Only those magnetic states which persist over long periods of time are useful for information storage. Consequently the magnetic states of the bit cells are dependent on one another, and less than one bit of storage per bit cell can be achieved. The magnetic interactions reduce the limit on areal density below the simple thermal limit.

It is the subject of this thesis to investigate the nature of the limit on areal density imposed by the internal magnetic interactions of recording media. The investigation is based on the definition, simulation, and analysis of a mathematical model representing magnetic recording media at a microscopic scale. Micromagnetic models have been used to investigate many of the details of the recording and playback processes. The research described in this thesis adds to these prior investigations a consideration of the areal density limit implied by a micromagnetic medium model. Two features of the areal density limit should be emphasized. First, the micromagnetic model includes several parameters which represent intrinsic physical properties of the recording medium. The areal density limit is a function of the values of these parameters. The trends in parameter values which increase the areal density limit suggest that the corresponding trends in the intrinsic physical properties of recording media lead to media better suited to the task of information storage at high density. When viewed from this perspective, the areal density limit reported in this thesis serves as a guide to the design of recording media capable of greater areal density. Second, the areal density limit is derived wholly from the physical laws governing the recording medium itself. It represents the limitation of the capability of the material to store information. There is no consideration given as to whether a particular technology exists, or is even possible, to perform the recording and playback processes at the areal density limit. It is possible that a recording medium is ultimately capable of storing more information than the recording and playback processes are capable of carrying to and from it. It is certain, though, that the information storage capability of a whole magnetic recording system cannot exceed the areal density limits of the recording medium without violating the Data Processing inequality of information theory [23, p. 32]. The areal density limit of the recording medium is an upper bound on the storage capacity of the whole magnetic recording system. It is a technology-independent bound. That is, it holds for any magnetic recording system using that recording medium for storage. Improvements in the design of other system components and methodologies can then be aimed at the goal of approaching the areal density limit of the recording material.

The remaining sections of this chapter provide an introduction to relevant background material for this research. Section 1.1 is an introduction to basic terms and concepts regarding magnetic materials. Section 1.2 is an overview of conventional longitudinal digital magnetic recording systems. Section 1.3 reviews prior research work in which the storage capacity of magnetic recording systems has been estimated or bounded. Section 1.4 reviews prior research in the detailed measurement of medium noise. Section 1.5 reviews prior research work in the definition and simulation of micromagnetic models of recording media.

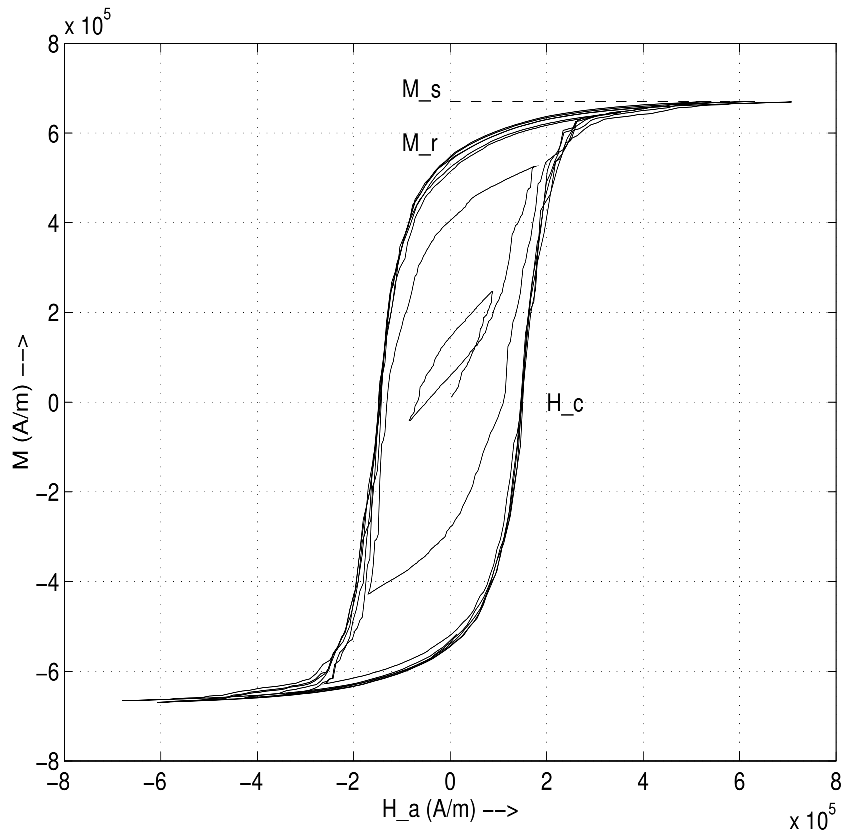

Figure 1.1: Hysteresis of magnetic materials

1.1 Basic Properties of Magnetic Materials

Applications of magnetic recording technology exhibit a wide variety of formats, including rigid disks, flexible disks, tape, and card stripes. Every example of a magnetic recording system includes a recording medium on which information is stored as patterns of magnetization. All recording media take the form of a magnetic layer deposited on a non-magnetic substrate. The magnetic layer must be able to sustain a spontaneous magnetization at the ambient temperature. Thus, it must include either ferrimagnetic or ferromagnetic materials with Curie temperatures above the ambient temperature. Throughout this thesis, such materials will be referred to simply as *magnetic materials*.

A magnetic material is characterized on a macroscopic scale by the response of its bulk magnetization to an applied field. As an illustration, Fig. 1.1 is a plot of the component of bulk magnetization in the direction of the applied field, M, versus the value of the applied field, H_a. The bulk magnetization does not vary as a single-valued function of the applied field. Instead the relationship exhibits *hysteresis* with changes in the bulk magnetization lagging behind changes in the applied field. As a result, M-H_a plots such as Fig. 1.1 take the form of *hysteresis loops* as the applied field H_a oscillates through positive and negative values. In Fig. 1.1, the magnitude of oscillation of the applied field is increased until the loop generated no longer changes with greater oscillation magnitude. The loop which is generated by sufficiently large oscillations of the applied field is called the *major loop* of the material. Loops generated by applied field oscillations of lesser magnitude are called *minor loops*.

It is common to characterize the macroscopic properties of a magnetic material by the features of its major hysteresis loop. The magnitude of bulk magnetization is bounded by the *saturation magnetization*, M_s, of the material. The bulk magnetization of a sample approaches the saturation magnetization under the influence of large applied fields. When the magnitude of the applied field is reduced to zero, the magnitude of the bulk magnetization does not fall from M_s to zero, but to a value M_r, the *remanent magnetization* of the material. The ratio of the remanent magnetization to the saturation magnetization is the *remanence squareness*, S,

$$S = \frac{M_r}{M_s}, \tag{1.2}$$

with a value between 0.0 and 1.0. In order to return the magnitude of bulk magnetization to zero, a magnetic field opposing the remanent magnetization must be applied. The magnitude of the opposing field required to accomplish this, H_c, is called the *coercive field*, or *coercivity* of the material. The slope of the major loop at $H_a = H_c$ is used to define another loop parameter, the *coercivity squareness*, S^*,

$$S^* = 1 - \frac{M_r}{H_c} \cdot \left.\frac{dH_a}{dM}\right|_{H_a=H_c}, \tag{1.3}$$

also with a value between 0.0 and 1.0.

The set of loop parameters, $\{M_s, M_r, H_c, S, S^*\}$ does not uniquely determine the major loop of a material. Furthermore, the major loop does not uniquely determine the M-H_a relationship over all values and histories for a material. Nevertheless, it is customary to characterize a material by these loop parameters, or even just a subset of them.

1.2 Conventional Recording Overview

The purpose of data storage systems is to reliably preserve information for long periods of time. Magnetic recording systems preserve information in patterns of magnetization on a recording medium. The great majority of magnetic recording systems in use today for data storage are digital recording systems which make use of longitudinal recording media.

As noted in the preceding section, the many available formats of magnetic recording media share the feature that the patterns of magnetization which store information are recorded in a magnetic layer. The magnetic layer is essentially planar from the perspective of recording and playback devices. A medium may be classified as *longitudinal* or *perpendicular* according to the relationship of its magnetization to the plane of the magnetic layer. Longitudinal magnetic recording media favor magnetization in the plane of the medium. Perpendicular media favor magnetization normal to the plane of the medium. This classification is more a statement of intent than a precise description, as magnetization in any direction in three dimensions may occur in either type of medium. The earliest magnetic recording systems used longitudinal recording, and longitudinal recording continues to dominate. Perpendicular recording has been the subject of strong research interest for many years but to date has not made a significant appearance in commercial recording systems.

Conventional digital magnetic recording on longitudinal media is best explained with reference to Fig. 1.2. At the top of Fig. 1.2 is a representation of a recorded magnetic pattern. Digital recording systems represent information using finite, discrete sets of symbols. The simplest example of a symbol set, and the symbol set in near universal use in information technology, is the set of *b*inary dig*its*, or *bits*, $\{0, 1\}$. Conventional recording systems map each bit of information to be stored to a region of the recording medium, a bit cell. A medium is subdivided into bit cells by recording data in tracks. Each track is a sequence of bit cells, and records a sequence of bits. A single recorded track is represented in Fig. 1.2.

Each bit cell is intended to store a bit of information. To accomplish this, the bit cell must be able to assume and retain either of two distinguishable magnetic states. For longitudinal recording media, the two magnetic states used are saturation magnetization in either of the two directions parallel to the recorded track. This convention is known as *saturation recording*. In Fig. 1.2, the colors represent the component of magnetization parallel to the recorded track according to a grey scale.

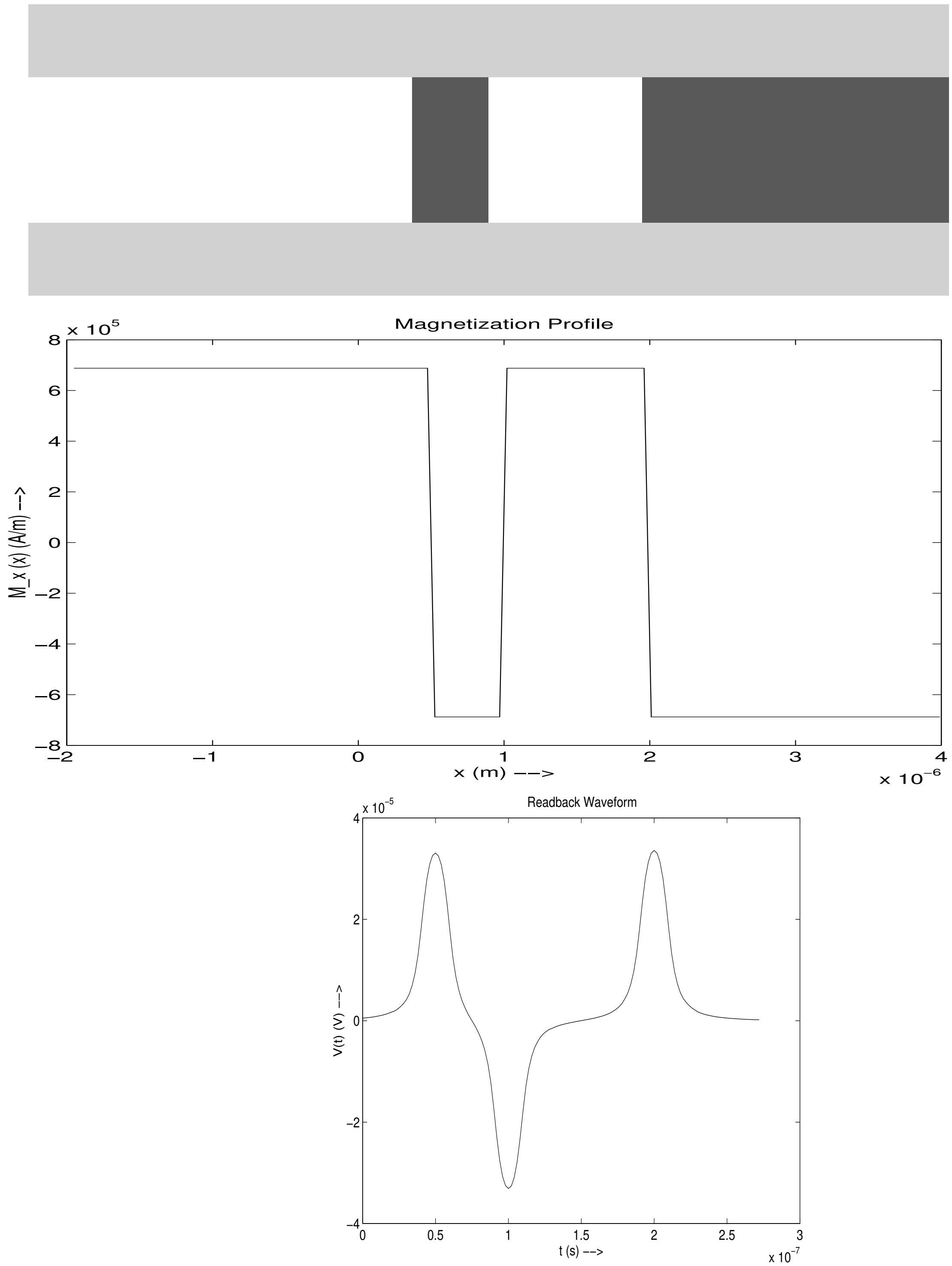

Figure 1.2: Idealized illustration of digital longitudinal magnetic recording

White represents magnetization fully saturated toward the right. Black represents magnetization fully saturated toward the left.

The remainder of Fig. 1.2 illustrates the recovery of the information stored in the bit cells of a longitudinal medium using an inductive read head. The middle of Fig. 1.2 is a plot of the component of magnetization parallel to the track M_x as a function of downtrack position x. Such a plot is called a *magnetization profile*, and represents an average across the track. In the idealized view of conventional recording presented in Fig. 1.2, this plot is a two-valued waveform. The magnetization profile alternates between two values, $+M_s$ and $-M_s$. The boundaries between bit cells of opposite magnetization are called *transitions*, and appear as discontinuities in the magnetization profile. The opposing magnetizations which meet at a transition are like two bar magnets with both north poles, or both south poles, brought together. Lines of magnetic flux emanate from the transition into nearby space so that the presence of a transition may be detected at a short distance. The principle of magnetic induction can be used to accomplish this detection. When a coil of wire links a time-varying magnetic flux, a voltage is induced in the wire proportional to the time rate of change of the flux linkage. By passing a coil of wire at a constant velocity over the spatially varying flux lines created by the recorded magnetic pattern, the magnetic pattern is read as a voltage waveform. An inductive read head is a practical device for achieving this simple detection idea. The bottom of Fig. 1.2 depicts the playback voltage waveform corresponding to the magnetic pattern recorded on the track. Each transition is detected as a voltage pulse. When the boundaries of bit cells are recorded at regular intervals, the pulses of the playback voltage signal occur at regular intervals. The presence or absence of a pulse in the playback voltage waveform at a bit interval may then be decoded as a sequence of bits with the same information content as the recorded pattern of magnetization. One common code is the assignment of a "1" to the presence of a pulse and a "0" to the absence of a pulse.

The strategy for increasing areal density within this idealized representation is trivial. A decrease in the area of a bit cell yields a corresponding increase in the areal density of information storage. Much of the history of increasing areal density of magnetic recording systems can be attributed to the development of technologies which allowed the recording and playback of narrower and narrower tracks, and the resolution of more and more closely spaced transitions. More recent and future developments require a more detailed understanding of the physics of recorded magnetic patterns.

Reality presents a picture more like Fig. 1.3. The magnetization of bit cells is not in fact fully saturated. The transitions between bit cells of opposite magnetization are not in fact ideally sharp. The analogy with two bar magnets with north poles brought together provides an explanation. Though such an arrangement generates the external flux needed for playback, it also represents an unstable configuration. Two north poles repel each other. Within the medium, the sharp transition spontaneously reshapes itself into a more stable zig-zag structure. This structure has non-zero width, and therefore limits how closely transitions may be placed together while still retaining recognizable bit cells. When zig-zag transitions are placed too close together they may overlap so that a band of reversed magnetization crosses a bit cell. This effect is called either *percolation* or *partial erasure*. The magnetization profile and playback voltage waveform for this more realistic representation of magnetic recording are also presented in Fig. 1.3. Because these waveforms do not look like their ideal counterparts in Fig. 1.2, it is said that they are corrupted by *medium noise*. Indeed, if one looks at the playback voltage waveform of Fig. 1.3 with the expectation that it look like that of Fig. 1.2, the natural conclusion is that the waveform observed has been corrupted by noise.

From this perspective, the attainment of greater areal density has been defined as a problem of understanding and defeating medium noise. The effect of medium noise on an isolated transition has been studied by assuming the magnetization profile of an isolated transition is well-represented by an arctangent function [82],

$$M_x(x) = \frac{2M_r}{\pi} \tan^{-1}\left(\frac{x - x_0}{a}\right), \tag{1.4}$$

selecting the values of x_0 and a as appropriate. It is in terms of these two parameters that the major effects of medium noise may be understood. The displacement of the transition center, x_0, from the intended spatial location of the transition is called *jitter*. The parameter a has units of length and can be taken as a measurement of the length of the zig-zag transition region. Because both of these effects of medium noise occur at a transition, they are sometimes called *transition noise*.

Under the arctangent magnetization profile assumption, the shortest length, a_d, of the transition region which can withstand the demagnetizing fields which arise from the transition is given by the expression [72, 18]

$$a_d = \frac{M_r \delta}{2\pi H_c}, \tag{1.5}$$

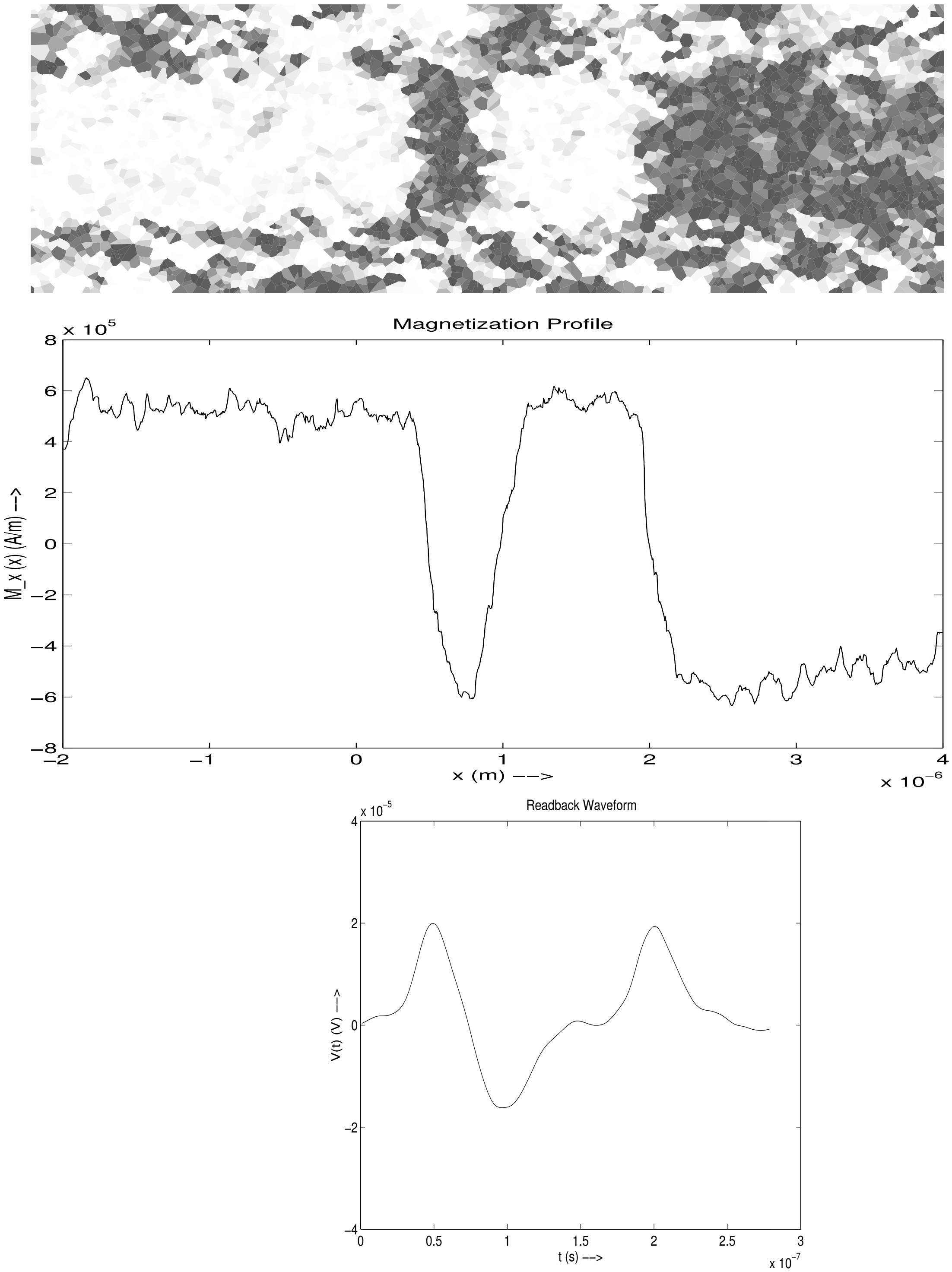

Figure 1.3: More realistic illustration of digital longitudinal magnetic recording

where δ is the thickness of the magnetic layer of the medium. In order to produce the sharpest transitions (i.e. transitions most like ideal recording), medium manufacturers aim to manufacture media with small remanent-magnetization-thickness product ($M_r\delta$) and large coercivity (H_c) consistent with other requirements of the recording system. In fact, it is common to report only these two values as a shorthand description of a magnetic layer material to claim its suitability for high-density magnetic recording. More complicated analyses [72, 123, 8] indicate that sharp transitions (small values of a) require small record-head to medium spacing, large coercivity squareness, and a large write-field gradient, in addition to small remanent-magnetization-thickness product and large coercivity.

Away from transitions, the ideal magnetization pattern is a uniform magnetization which induces no voltage in an inductive read head passing by. The voltage waveform which is in fact induced away from transitions arises from the spatial nonuniformity of the magnetization. This effect of medium noise is sometimes called *particulate noise* or *granularity noise*, as distinguished from transition noise.

Although classifications such as granularity noise or transition noise are useful descriptive terms, one should not be misled into believing they represent distinct physical phenomena. All medium noise arises from the spatial fluctuations of magnetization which are present in physical recorded patterns, but which are not a part of our idealized representations. Whether this is a failure of the physical medium or of our representations is a matter of perspective. The more common view seems to be the former. Medium noise is seen as a defect in the medium, something to be eliminated or suppressed by clever design of new materials. From this perspective, the path to better recording performance is to force nature to provide materials which behave as we wish them to behave. The latter perspective is less common, but is becoming more important as the limits of our ability to mold nature to our desires are reached. From this perspective, the path to better recording performance lies in deeper understanding of the nature of recorded magnetic patterns and the development of strategies for encoding information to be stored onto the set of magnetic patterns made available by nature. From either perspective, there will remain elements of recording systems which lie beyond our control. Fortunately, total control is not necessary for the reliable storage of information.

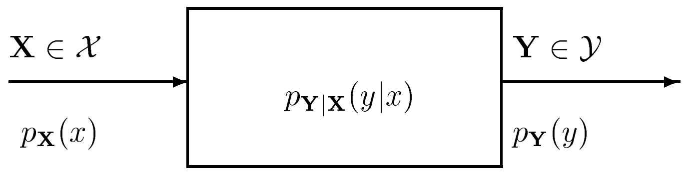

Figure 1.4: Channel model framework for information theory

1.3 Storage Capacity Studies

The reliable transmission of information in the presence of noise has been the subject of information theory since Shannon's seminal paper [108]. Shannon proved that it is possible to transmit information through a noisy channel with an arbitrarily small probability of error so long as the rate of transmission is less than a critical value associated with the channel, called its *capacity*. Conversely, transmission of information at any rate greater than capacity, by any method whatsoever, has vanishingly small probability of being error-free.

Within the Shannon framework, the starting point of analysis of a communication system is a representation of the system as a channel within a framework such as that illustrated in Fig. 1.4. The inputs and outputs of the channel are members of known sets, $\mathcal{X}$ and $\mathcal{Y}$ respectively. The "noisiness" of the system is modeled by representing its operation of generating output in response to inputs not as a deterministic function, but as a transition probability. That is, a particular input value x drawn from the input set $\mathcal{X}$ does not determine a unique output value y, but instead determines a probability density function $p_{y|x}(y|x)$ which describes the distribution of output values observed in response to that input value. The total collection of transition probabilities may be considered a function over the domain $\mathcal{X} \times \mathcal{Y}$. A channel is completely characterized within this framework when input and output sets $\mathcal{X}$ and $\mathcal{Y}$ and the transition probability $p_{y|x}(\cdot|\cdot)$ are specified.

Many analyses of the storage capacity of magnetic recording systems available in the literature are based on extensions of the analysis of the Gaussian channel. Fig. 1.5 depicts a block diagram of this channel. When $n(t)$ is a white Gaussian random process with power spectral density $S_n(f) = N_0/2$ watts/Hz, $x(t)$ is constrained to have average power no greater than P watts, and $h(t)$ is an ideal (flat) low-pass filter strictly bandlimited to W Hz, it is well-known [23, p. 250] that the capacity of this channel is

$$C = W \log\left(1 + \frac{P}{N_0 W}\right), \tag{1.6}$$

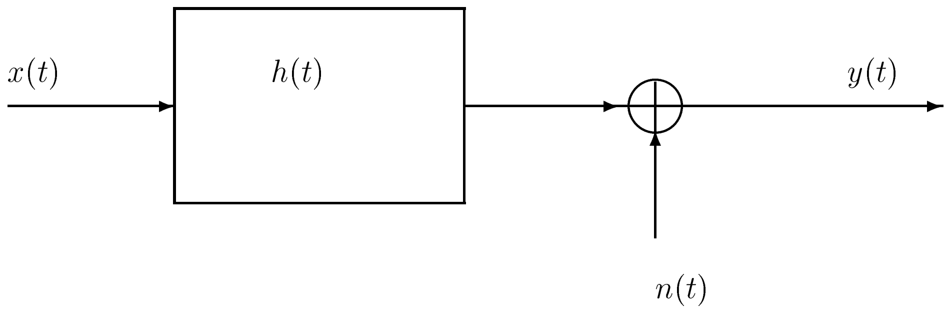

Figure 1.5: Block diagram of Gaussian channel

expressed in units of bits/s. This capacity is achieved by input signals made up of orthonormal basis functions matched to the channel transfer function whose coefficients are independent Gaussian random variables with zero mean and variance P.

When the transfer function, $H(f)$ (the Fourier transform of $h(t)$), is not flat, or the noise process, $n(t)$, is Gaussian, but not white, then the capacity may be computed using the "water-filling" approach for distributing power among the basis function coefficients, yielding [30, p. 388]:

$$C = \int_{F_L} \frac{1}{2} \log \left(\frac{|H(f)|^2 L}{S_n(f)} \right) df, \tag{1.7}$$

where L and F_L are determined by:

$$P = \int_{F_L} \left(L - \frac{S_n(f)}{|H(f)|^2} \right) df, \tag{1.8}$$

$$F_L = \left\{ f : L > \frac{S_n(f)}{|H(f)|^2} \right\}. \tag{1.9}$$

The expression (1.6) for capacity has proved very attractive to engineers developing a wide variety of applications, primarily because it presents capacity as a simple function of a signal-to-noise ratio (SNR), a quantity all engineers believe they understand. As a result, the expression for the capacity of a Gaussian channel has been adopted in many circumstances, sometimes with and sometimes without a careful identification of the input and output sets, a careful determination that the Gaussian channel is a good representation of the system, or a careful demonstration that the definition of SNR within the application is consistent with that of the Gaussian channel.

In 1974, Mallinson made use of frequency-domain expressions for signal power and noise power in magnetic tape systems to determine SNR. By a direct application of the Gaussian channel capacity expression, Mallinson concluded that areal densities of up to 1 Gbit/in^2 should be possible given the tape medium available at that time, though recording and playback at such densities were not then mechanically possible [56].

More recent applications of the Gaussian channel to magnetic recording systems have made a more careful identification of inputs and outputs. The input of the Gaussian channel, $x(t)$, is taken to be the magnetization profile of a written track. The filter, $h(t)$, represents the read head. The output of the channel, $y(t)$, is the playback voltage waveform, and the noise process, $n(t)$, represents medium noise. Constraints on the input waveforms have been added to represent the conventional digital recording strategy of saturation recording and to represent the limits on the amplitude and slope of magnetization profiles established by the medium [92, 106, 6]. The exact expressions for capacity depend on the particular transfer function assumed for the filter.

French and Wolf [28] further extended the Gaussian channel model, taking care to choose the transfer function of the filter so that it included the losses observed experimentally in recording systems, including thickness loss, spacing loss, and gap loss [119]. The parameters of this transfer function are given in terms of the parameters of the recording system, including parameters which characterize the medium, parameters which characterize the head, and parameters which characterize the way in which they are brought together. The noise process is defined to include a white Gaussian component, representing electronics noise, and a second component with power spectral density proportional to the square-magnitude of the transfer function, representing medium noise. Upper bounds are computed numerically from the water-filling bound, (1.7). Lower bounds are computed numerically using a modified version of the lower bound expressions from [92]. For the disk system studied, and for a write current of 20 mA and medium noise power at 75% of the total noise power, the information rate bounds computed are approximately

$$29 \leq C \leq 73 \tag{1.10}$$

in units of Mbit/s. Conversion to areal density bounds requires knowledge of the system's head-medium velocity and recorded track width. Adopting a head-medium velocity of 12.7 m/s from French and Wolf, and assuming a track width of 5 μm, the corresponding areal capacity is approximately

$$0.45 \leq C \leq 1.15 \tag{1.11}$$

in units of Mbit/mm^2 (0.29 to 0.74 Gbit/in^2).

McLaughlin and Neuhoff [68] report a similar study to that of French and Wolf. They use a simpler model for the transfer function, defining h(t) so that the step response is a Lorentz pulse,

$$L(t) = \frac{1}{1 + (\frac{2t}{\beta})^2}, \tag{1.12}$$

where β is the pulse width at half height. They also add a constraint that the input waveform (magnetization profile) be of the form

$$x(t) = \sum_k X_k \sqrt{P} p_T(t - kT) \tag{1.13}$$

with $X_k \in \{\pm 1\}$ and

$$p_T(t) = \begin{cases} 1, & -T \leq t \leq 0 \\ 0, & \text{otherwise} \end{cases} \tag{1.14}$$

Noise comprises two components as in the French-Wolf paper, with N_m scaling the medium noise component and N_e scaling the electronics noise component. The effect of two system parameters, the track density and the bit density, on capacity are examined. Under an assumption that signal power is proportional to the square of track width and noise power is proportional to track width, an upper bound on the capacity is derived. As track density and bit density are increased the bit cells have smaller area. However, the signal to noise ratio also decreases so that information storage reliability suffers. Not all of the decrease in bit cell area is translated into increased information storage density. The value of the bound for several values of track density and bit density is not calculated explicitly, but capacity gains over a nominal system are determined. The greatest increase in the upper bound is predicted for increases in bit density of about a factor of 4 and increases in track density of about a factor of 10, for which decreased signal to noise ratio requires redundancies for reliable storage which decrease storage density by a factor of 2, indicating an overall potential 20-fold increase in capacity just through modifying these system parameters.

Voois and Cioffi [118] report two approaches to the problem of determining recording system capacity. First they follow in the same vein as the other authors cited here, bounding capacity based on an extended Gaussian channel model. They enforce a mean square constraint on both power and slope of the input signal. In addition, they model the effect of crosstalk between nearby tracks on the medium. As the width of the reproduce head (and therefore the tracks) decreases, the effect of crosstalk increases while the area of the track decreases. Increasing crosstalk leads to decreasing areal capacity, while decreasing area leads to increasing areal capacity. Both medium noise and electronics noise are modeled. For a system with signal to medium noise ratio of 30 dB, and equal power for medium noise and electronics noise, they report a head width of 0.6 μm gives the maximum areal capacity value of about 5 Mbit/mm^2 (3.2 Gbit/in^2).

In their second approach, Voois and Cioffi take into account the two-dimensional nature of the magnetization patterns. The output of the channel is identified as a corrupted magnetization pattern rather than the playback voltage waveform. The corruption of the magnetization pattern is represented as the addition of *flux noise*, a two-dimensional white Gaussian process with power spectral density N_0. The same power and slope constraints are imposed on the two-dimensional magnetization pattern inputs as on the magnetization profiles. Though Voois and Cioffi report no proof of a channel capacity theorem for two-dimensional channels, they argue by analogy to the one-dimensional Gaussian channel that the appropriate expression for the capacity of their two-dimensional system, which they give the name *medium capacity*, is

$$C = \max_{S_m \in \mathcal{P}} \frac{1}{2} \int \int \log \left(1 + \frac{S_m(u,v)}{N_0} \right) dudv. \tag{1.15}$$

where $\mathcal{P}$ is the set of power spectral densities satisfying the power and slope constraints. The areal capacity predicted by this study is 92 Mbit/mm^2 (59 Gbit/in^2), indicating great potential for capacity gain by replacing the conventional single-head recording systems with another system which takes into account the two-dimensional nature of the input. One example is an array of heads so that signal processing may be used to defeat crosstalk.

The research to be described in this thesis shares the perspective of Voois and Cioffi's second approach. Investigation of the fundamental limits of recording densities on a magnetic recording medium requires that the output of the channel model be a corrupted magnetization pattern, not a playback voltage waveform. When the channel output is taken to be a waveform, an assumption must be made regarding the recording methodology and technology. Capacity limits determined under such assumptions reflect only the limits of systems which obey them. The fundamental limits of recording may be much less constraining. Voois and Cioffi's assumption of white Gaussian flux noise is open to question however, as medium noise measurements do not support it.

The references reviewed in this section serve as sufficient background to the research to be presented. Other references which report studies of the capacity of channels representing magnetic recording systems include [34, 37, 107, 35].

1.4 Medium Noise Measurements

Analyses of capacity limits are only as good as the channel models on which they are based. Several papers in the literature report experimental measurements of medium noise against which the predictions of these models may be compared. This section contains a review of a few of these papers, and the shortcomings of the models they reveal.

A common assumption in capacity studies is that medium noise may be represented as a white noise process in one or two dimensions. If medium noise is attributed to the microstructure of the medium, though, such an assumption is counterintuitive, as we expect there to be spatial correlation of the magnetization across the length of uniformly magnetized domains. Mian, Indeck, and Muller [70] report measurements of such a correlation length in the transverse (across the track) direction. For a variety of recording media, they report correlation lengths from 43 - 320 nm.

Another common assumption is that the medium noise is independent of the signal and that it may be well represented by a stationary process. However, it is well understood that the power and characteristics of medium noise vary with the magnetic state of the medium. It has already been pointed out that the effects of medium noise near a recorded transition have different qualitative descriptions from the effects away from a transition. For thin-film disks, transition noise has greater power than particulate noise. As bit densities are increased, the total noise power increases according to a linear relationship for low bit densities. At sufficiently high bit densities, the total noise power increases even faster than linearly with increasing bit density. An explanation for this behavior is that as bit density increases, at first the effect is just to increase the area of the medium within transition regions in comparison to the area of the medium far from a transition. Because transition noise has greater power, a linear increase in total noise power is observed. At sufficiently high densities, though, the transition noise itself becomes more powerful. This increase in transition noise power at high bit densities is usually attributed to the interaction of closely spaced bits through mechanisms such as percolation. Simple models which capture the dependence of medium noise power on the local magnetization magnitude have been developed [8, 59] and take the general form of predicting noise power at a downtrack position x according to

$$\sigma^2(x) \propto M_s^2 - M_x^2(x). \tag{1.16}$$

More detailed studies of transition noise have made use of the Karhunen-Loève (KL) decomposition of random processes. The noise waveform realizations are expressed as a linear combination of eigenfunctions of the noise process autocorrelation function. The autocorrelation function may be empirically estimated from a large collection of noise waveforms. The KL expansion identifies the eigenfunctions with largest eigenvalues as those component waveforms which best characterize the noise in the sense that they contain the largest fraction of noise power [129]. Empirical observations of transition noise for a single isolated transition reveal that the most significant noise components may be described qualitatively as causing jitter and pulse-spreading [53]. Measurements of transition noise for dibit [54, 136] and tribit [135] data patterns yield different transition noise properties, further bolstering the conclusion that medium noise is strongly dependent on the recorded signal.

Less widely appreciated is the fact that medium noise also exhibits a strong dependence on the particular position on the medium on which the signal is recorded. Hoinville made measurements of medium noise [38, 39] in which the spatial positioning of recording and playback were carefully controlled. He found that when the same signal is written at the same position, the medium noise waveforms measured are highly correlated. This correlation holds even when the medium is erased between the two measurements. Furthermore, the repeatable medium noise waveform for a state of positive saturation is highly negatively correlated with the repeatable medium noise waveform for a state of negative saturation, suggesting that the source of medium noise is to a great extent a permanent magnetic microstructure that is fixed for the lifetime of the recording medium. In fact, the repeatability of medium noise waveforms is so reliable that it has been proposed to make use of the medium noise to verify the identity of a recording medium [42]. This technique has acquired the informal name "magnetic media fingerprinting." Novel recording system architectures and recording precompensation techniques have been proposed to exploit the spatial repeatability of medium noise to improve recording system performance [89, 2, 88].

These differences between experimental measurements and channel models which have been studied indicate that better estimates of recording system capacities may be computed by analysis of models which more truly reflect the physical properties of recording media. The level of physical detail required to take such an approach leads us to the study of micromagnetic models of recording media.

1.5 Micromagnetic Modeling

An understanding of the properties of magnetic materials may be developed at several levels of detail. At a macroscopic level, a magnetic material may be described by its hysteresis loop, or by properties such as susceptibility which characterize its M-H relationship. At the other extreme, an understanding might be sought in terms of the principles of quantum mechanics operating on the sub-atomic particles which make up the material. In a middle range lies the level of micromagnetics. Micromagnetics concerns representing the behavior of magnetic materials at scales smaller than that of ordinary observations, yet at a large enough scale that the vector field quantities of Maxwell's equations may be taken to be continuous functions of space [16]. This level of study includes the domain theory of ferromagnetism.

Some of the earliest work which can be called micromagnetic dates to 1893 when Ewing attempted to explain ferromagnetism in terms of an assembly of a large number of magnets. Ewing's model was an actual assembly of magnets mounted on pivots [26]. Throughout the early decades of this century, micromagnetics was largely a field of mathematical analysis, developing models of domains, domain walls, and magnetization reversal mechanisms. Two models of particular interest to the research in this thesis are the Stoner-Wohlfarth model for magnetization reversal of a single uniaxial magnetic particle in response to an applied field [111], and the Gilbert form of the Landau-Lifshitz set of coupled differential equations representing the dynamics of an assembly of interacting magnetic domains [51, 32],

$$\frac{d\mathbf{M}}{dt} = \gamma_G(\mathbf{M} \times \mathbf{H}_{\text{eff}}) - \frac{\alpha_G}{|\mathbf{M}|}\left(\mathbf{M} \times \frac{d\mathbf{M}}{dt}\right), \tag{1.17}$$

where the effective magnetic field, $\mathbf{H}_{\text{eff}}$, arises in part due to the interactions of the domains, and in part due to an applied field. These models are well-known, having been included in textbooks on the physics of magnetism [21, 98].

The advent of computing devices of sufficient power to calculate nontrivial solutions of micromagnetic models triggered an interest in micromagnetic modeling of recording media, starting with the work of Hughes [41]. A number of micromagnetic models have been developed [131, 64, 75, 128] which represent magnetic recording medium materials as a collection of single-domain magnetic units, or *grains*, interacting through magnetic forces. The models vary a significant amount in their precise assumptions (e.g. two-dimensional vs. three-dimensional, choice of dynamics, exact mathematical expression for magnetic interactions) and in the implementation choices made to represent them (e.g. boundary conditions, calculation truncations, computation shortcuts, microstructure generation). The heart of the research described in this thesis is the development of a micromagnetic model for recording media. A comparison of the details of the published models is deferred until a definition of the model under study is presented. It should be emphasized that the intent is not to introduce complexity for its own sake. Micromagnetic representations of recorded magnetic patterns are necessary to represent the level of detail needed to explain repeatable features of medium noise measured on magnetic recording systems. Within the realm of micromagnetics, we prefer simpler modeling choices, so long as they are sufficient to represent well the features of experimental observation.

For the purposes of background it suffices to note that previous micromagnetic models have yielded a zig-zag transition structure [131, 77] in agreement with observations using many imaging techniques [43]. Also, micromagnetic models predict transition noise with statistical properties in agreement with empirical measurements [132, 133, 10, 129, 9, 136].

1.6 Summary

The chapter has presented a basic introduction to relevant background material to the research presented in this thesis. Although remarkable rates of increase in the areal density of magnetic recording systems have been sustained for many years, simple analyses indicate that the physical limits of storage density will stop this trend not too far into the future. The subject of the research presented here is a more detailed study of the physical limits of information storage on magnetic recording media. After an introduction to magnetic materials and conventional digital magnetic recording systems, a description of medium noise was presented. Medium noise is the most limiting factor in reliable information storage in contemporary recording systems. Efforts to defeat medium noise may be divided into two categories. First is the design of new system components, particularly recording media, which exhibit less medium noise. This effort is largely one of developing media with smaller remanent-magnetization-thickness product and larger coercivity. Second is the derivation of advanced signal processing and coding methods to overcome the effects of medium noise. The achievable gains from the second approach are limited by the fundamental theorems of information theory. Several information theoretic analyses of the magnetic recording channel as an extension of the Gaussian channel were reviewed. Experimental measurements indicate that these channel models do not reflect the true statistical nature of medium noise, however. Micromagnetic models do predict medium noise with statistical properties in good agreement with measurements, indicating that channel capacity analysis based on a micromagnetic medium model is more suitable to determining the storage capacity limits of a magnetic recording system.

Chapter 2

Model Definitions

2.1 Medium Model Definition

The starting point of information capacity analysis of magnetic recording media is the definition of a micromagnetic mathematical model of magnetic recording media. The model is intended to embody the physical laws which govern the behavior of physical media. As in all modeling, assumptions and approximations are made in the definition and analysis of the model. It is our aim to make conspicuous note of these assumptions and approximations. In pursuit of this aim, modeling assumptions are noted in this thesis with a bold declaration. The term *medium* is frequently used as shorthand to refer only to the magnetic layer of a magnetic recording medium, the subject of our modeling, omitting discussion of other layers required for the practical functioning of storage devices.

2.1.1 Model Geometric Structure

The media of interest are either thin-film media, common in rigid disk storage, or particulate media, common in tape storage. In either case, the magnetic layer in which magnetic patterns store information is thin. This observation leads to our first model assumption,

Assumption 2.1 : The model is planar. *That is, the field quantities which are properly functions of space are represented as functions of only two independent variables, spanning the plane of the medium. For example, the magnetization of the medium*

$$\mathbf{M} = \mathbf{M}(x, z). \tag{2.1}$$

Each point in the plane of the medium is associated with a Cartesian coordinate pair (x, z). The coordinate axes are defined with respect to the recording geometry of a conventional system. The positive x-axis is aligned with the recorded track, pointing in the direction of head motion. The z-axis is transverse to the recorded track. The y-axis is normal to the medium plane, oriented so that recording and playback heads move through the region of negative y values. The z-axis is oriented so that the coordinate axes are a right-handed system. The thickness of the medium is denoted δ, and is assumed constant throughout the medium plane, so that the magnetic layer lies in the space between the planes $y = 0$ and $y = \delta$. The value of δ (m) is a property of the medium. The vector field quantities of the model are assumed to have constant value through the thickness of the medium, with no variation in the y direction.

When the magnetic layer is very thin, demagnetizing fields suppress magnetization perpendicular to the medium plane. The small perpendicular components of the magnetization vector may be neglected. Media with this property are suitable for longitudinal recording. Perpendicular recording requires media specially manufactured to permit significant perpendicular components of magnetization. Such media are outside the scope of the research presented here.

Assumption 2.2 : The model represents longitudinal recording media. *Thus, vector quantities may be represented in terms of their x and z components, for example,*

$$\mathbf{M}(x, z) = M_x(x, z)\hat{\mathbf{x}} + M_z(x, z)\hat{\mathbf{z}}. \tag{2.2}$$

The magnitude of magnetization of a given medium is limited by the medium's saturation magnetization, M_s. The value of M_s (A/m) is a property of the medium. The model represents this physical limit by requiring the magnetization magnitude to be exactly M_s throughout the material, achieving macroscopic magnetization less than M_s by averaging $\mathbf{M}(x, z)$ over regions where the direction of magnetization varies.

Assumption 2.3 : Medium magnetization has constant magnitude M_s. *Thus, we may write*

$$\mathbf{M}(x, z) = M_s \cos\alpha(x, z)\hat{\mathbf{x}} + M_s \sin\alpha(x, z)\hat{\mathbf{z}}. \tag{2.3}$$

Here, α represents the angle between $\mathbf{M}$ and the positive x-axis.

Magnetic media are granular in nature. The granularity of media is represented in the model by a partition of the medium plane into disjoint connected regions. Each region is assumed to be uniformly magnetized. That is, the magnetization vector is a constant over each region in the partition.

Assumption 2.4 : Media comprise uniformly magnetized grains. *Let* $\{R_k, k \in \mathcal{I}\}$ *be a partition of the medium plane. The magnetization may be expressed*

$$\mathbf{M}(x,z) = M_s \sum_{k \in \mathcal{I}} (\cos\alpha_k \hat{\mathbf{x}} + \sin\alpha_k \hat{\mathbf{z}}) I_{R_k}(x,z). \tag{2.4}$$

Given the foregoing assumptions, the magnetization of the medium may be completely characterized from $\{R_k, k \in \mathcal{I}\}$ and $\{\mathbf{M}_k, k \in \mathcal{I}\}$, where

$$\mathbf{M}_k = M_s \begin{bmatrix} \cos\alpha_k \\ \sin\alpha_k \end{bmatrix} = M_s(\cos\alpha_k \hat{\mathbf{x}} + \sin\alpha_k \hat{\mathbf{z}}). \tag{2.5}$$

2.1.2 Model Magnetic Interactions

The magnetic energy of a magnetized body in the presence of a magnetic field $\mathbf{H}(x,y,z)$ is

$$W = -\mu_0 \int_V \mathbf{M}(x,y,z) \cdot \mathbf{H}(x,y,z) dxdydz, \tag{2.6}$$

where the integration is over the volume of the body. Following Assumption 2.1, assume $\mathbf{H}$ varies only with x and z within the magnetic layer. Then the magnetic energy of grain k is

$$W_k = -\mu_0 \delta \mathbf{M}_k \cdot \int_{R_k} \mathbf{H}(x,z) dxdz. \tag{2.7}$$

As a further simplifying assumption, we may replace the integration of the field over grain k by the product of the area of grain k,

$$\mathcal{A}_k = \int_{R_k} dxdz, \tag{2.8}$$

and the value of the field sampled at a point within grain k. This should be a good approximation so long as $\mathbf{H}$ varies only a small amount within the dimensions of a grain. A convenient point at which to sample the magnetic field is the centroid of grain k with coordinates (x_k, z_k). When grains are convex, the centroid lies within the grain. With this approximation, we may write

$$W_k = -\mu_0 \mathcal{A}_k \delta \mathbf{M}_k \cdot \mathbf{H}(x_k, z_k), \tag{2.9}$$

Then we may group the grain volume $(\mathcal{A}_k\delta)$ with the magnetization $\mathbf{M}_k$ to yield a magnetic moment which we consider to be located at the centroid of grain k.

Assumption 2.5 : Grain magnetizations may be represented as magnetic dipoles. *For purposes of computing magnetic interactions, represent the magnetization of each grain with a magnetic dipole of moment*

$$\mathbf{m}_k = \mathcal{A}_k \delta \mathbf{M}_k \tag{2.10}$$

at (x_k, z_k) .

Thus, the model represents the magnetic layer of a recording medium as an assembly of dipoles. The kth dipole moment will respond to the field at its location $\mathbf{H}_k \triangleq \mathbf{H}(x_k, z_k)$ by changing its value within the constraints of the model so as to minimize magnetic energy. Since magnetization magnitude is constant (Assumption 2.3) and the magnetization lies in the medium plane (Assumption 2.2), the magnetization will rotate within the plane to a local minimum of magnetic energy. When the magnetic energy is given by (2.9), the local minimum state is that in which the magnetization $\mathbf{M}_k$ is aligned parallel to the magnetic field $\mathbf{H}_k$. In order to represent the interaction of the dipole moments in the assembly, we can compute effective magnetic field components arising from the dipoles. In deriving the interaction equations, care must be taken that the energy expressions are correct.

Magnetostatic Interaction

Each magnetic dipole is the source of a magnetic field. Consider a magnetic dipole at the origin of a standard spherical coordinate system, (R, θ, ϕ), with moment

$$\mathbf{m} = m\hat{\mathbf{z}} \tag{2.11}$$

The magnetic field arising from the magnetic dipole is given by a well-known formula from elementary magnetostatics [20, p. 241],

$$\mathbf{H}(R, \theta) = \frac{m}{4\pi R^3}((2\cos\theta)\hat{\mathbf{R}} + (\sin\theta)\hat{\theta}). \tag{2.12}$$

It is straightforward to transform this formula into Cartesian coordinates and into a form which allows the source magnetic dipole moment $\mathbf{m}$ to have any value in the

x-z plane,

$$\mathbf{m} = m_x\hat{\mathbf{x}} + m_z\hat{\mathbf{z}}. \tag{2.13}$$

For details of this transformation, the reader is referred to Appendix A, which is an edited version of Appendix A of [94]. The result is the following formula for the magnetic field at (x, z) arising from a magnetic dipole of moment $\mathbf{m}$ at the origin,

$$\mathbf{H}_m(x, z) = \frac{1}{4\pi(x^2 + z^2)^{5/2}} \begin{bmatrix} 2x^2 - z^2 & 3xz \\ 3xz & 2z^2 - x^2 \end{bmatrix} \mathbf{m}, \tag{2.14}$$

where the vectors are represented in terms of their x and z components. The magnetic field $\mathbf{H}_m$ has no component perpendicular to the medium plane, consistent with Assumption 2.2.

Now consider the work done to bring a second magnetic dipole with moment $\mathbf{m}_k$ into the vicinity of the first with moment $\mathbf{m}_l$, starting from an infinite distance away and ending at coordinates (x_k, z_k). The field at (x_k, z_k) due to $\mathbf{m}_l$ at (x_l, z_l) is

$$\mathbf{H}_{m,kl} = \frac{1}{4\pi(x_{kl}^2 + z_{kl}^2)^{5/2}} \begin{bmatrix} 2x_{kl}^2 - z_{kl}^2 & 3x_{kl}z_{kl} \\ 3x_{kl}z_{kl} & 2z_{kl}^2 - x_{kl}^2 \end{bmatrix} \mathbf{m}_l, \tag{2.15}$$

with $x_{kl} \triangleq x_k - x_l$ and $z_{kl} \triangleq z_k - z_l$, and the field at infinite distance is zero. Thus the work done in assembling the dipole-dipole pair is

$$W_{m,kl} = -\mu_0 \mathbf{m}_k \cdot \mathbf{H}_{m,kl}, \tag{2.16}$$

which therefore must equal the magnetostatic interaction energy of the dipole-dipole pair.

Combining (2.15) with the notation of the foregoing assumptions, we express the magnetic field component at grain k due to the magnetostatic fields arising from the magnetization of all other grains,

$$\mathbf{H}_{m,k} = \sum_{\substack{l \in \mathcal{I} \\ l \neq k}} \frac{\mathcal{A}_l \delta}{4\pi(x_{kl}^2 + z_{kl}^2)^{5/2}} \begin{bmatrix} 2x_{kl}^2 - z_{kl}^2 & 3x_{kl}z_{kl} \\ 3x_{kl}z_{kl} & 2z_{kl}^2 - x_{kl}^2 \end{bmatrix} \mathbf{M}_l. \tag{2.17}$$

Appropriate definition of the magnetostatic interaction matrices, $\mathbf{A}_{m,kl}$, leads to a simplified notation,

$$\mathbf{H}_{m,k} = \sum_{\substack{l\in\mathcal{I}\\ l\neq k}} \mathbf{A}_{m,kl}\mathbf{M}_l. \tag{2.18}$$

It is not difficult to show that the magnetostatic interaction matrices, $\mathbf{A}_{m,kl}$, have the following properties,

$$\mathbf{A}_{m,kl} = \mathbf{A}_{m,kl}^T, \tag{2.19}$$

$$\mathcal{A}_k\mathbf{A}_{m,kl} = \mathcal{A}_l\mathbf{A}_{m,lk}. \tag{2.20}$$

A consequence of these properties is that

$$W_{m,kl} = W_{m,lk}, \tag{2.21}$$

which makes physical sense. The interaction energy of a pair of dipoles should not depend on how they were assembled. These properties will also be useful later in the analysis of the model's magnetic state evolution.

Finally, we consider the calculation of the total magnetostatic energy of the dipole assembly from the magnetization and field quantities. Following (2.9), we might write

$$W_m = -\sum_{k\in\mathcal{I}} \mu_0\mathcal{A}_k\delta\mathbf{M}_k\cdot\mathbf{H}_{m,k}. \tag{2.22}$$

However, further analysis shows that this summation is equivalent to

$$W_m = \sum_{k\in\mathcal{I}}\sum_{\substack{l\in\mathcal{I}\\ l\neq k}} W_{m,kl}, \tag{2.23}$$

in which it is clear that the magnetostatic interaction energy of each dipole pair is being counted twice in the summation. Therefore the correct expression for total magnetostatic energy of the entire medium, in J, is

$$W_m = -\frac{1}{2}\sum_{k\in\mathcal{I}} \mu_0\mathcal{A}_k\delta\mathbf{M}_k\cdot\mathbf{H}_{m,k}. \tag{2.24}$$

which may be written

$$W_m = -\frac{\mu_0\delta}{2}\sum_{k\in\mathcal{I}}\sum_{\substack{l\in\mathcal{I}\\ l\neq k}} \mathbf{M}_k^T(\mathcal{A}_k\mathbf{A}_{m,kl})\mathbf{M}_l. \tag{2.25}$$

At this point, another consequence of Assumption 2.5 should be noted. The magnetostatic fields are being computed assuming the sources are point dipoles, not extended magnetized grains. A correct calculation of the fields as arising from extended magnetized grains would require integration of the dipole source equation (2.15) over the area of the source grain, or a mathematically equivalent calculation of magnetic fields from a scalar magnetic potential function derived from magnetic "charges" on the boundaries of grains. A more detailed comparison of our approximation with the calculations of other researchers in micromagnetics is deferred until the next chapter.

Uniaxial Crystalline Anisotropy

The magnetization of a physical grain tends to prefer a few directions over others. This asymmetry is known as *anisotropy.* It arises from both the crystal structure and the shape of the grain. The simplest form of anisotropy is uniaxial, where only one axis of magnetization orientation is preferred over all others. The preferred axis of magnetization orientation is called the *easy axis.* The usual model for uniaxial anisotropy is to define an energy term as a function of the angle between the easy axis and the magnetization. Under an assumption that the easy axis of each grain lies in the plane of the medium, let θ_k represent the angle between the easy axis of grain k and the positive x-axis. Then the anisotropy energy of grain k is

$$W_{A,k} = \mathcal{A}_k \delta K_A \sin^2(\alpha_k - \theta_k), \tag{2.26}$$

where K_A is a quantity known as the anisotropy energy density. The magnetization of a magnetic material may also be affected by mechanical strain. The magnetoelastic energy can be included in the anisotropy term for purposes of this model.

Assumption 2.6 : Each grain exhibits uniaxial anisotropy with an easy axis in the plane of the medium. *All grains share a single value of K_A.*

The value of K_A (J/m^3) is a property of the medium. Then, the total anisotropy energy of the entire medium, in J, is

$$\begin{aligned} W_A &= \sum_{k \in \mathcal{I}} W_{A,k} \\ &= K_A \delta \sum_{k \in \mathcal{I}} \sin^2(\alpha_k - \theta_k) \mathcal{A}_k. \end{aligned} \tag{2.27}$$

Exchange Interaction

When two grains are in atomic contact, the constraints of quantum physics make a contribution to their magnetic energy. This effect is called the *exchange interaction.* A detailed understanding of the origins of the exchange interaction requires a study of quantum theory [65, 122], but a level of understanding sufficient for micromagnetic modeling is provided by a representation of the exchange interaction as an additional term in the expression of the magnetic energy of a body,

$$W_e = \frac{A_e}{M_s^2} \int_V \left[\left| \frac{\partial \mathbf{M}}{\partial x} \right|^2 + \left| \frac{\partial \mathbf{M}}{\partial y} \right|^2 + \left| \frac{\partial \mathbf{M}}{\partial z} \right|^2 \right] dxdydz \tag{2.28}$$

where the integration is over the volume of the body, and the quantity A_e (J/m) is a property of the medium material known as the exchange energy constant. The exchange energy constant A_e may be understood in terms of the quantities of quantum theory, or in terms of the Curie temperature and the lattice structure of the atoms of the solid. It can be measured experimentally in some materials by observation of spin wave resonance [98]. A typical value of A_e for ferromagnetic materials is 1×10^{-11} J/m. Equation (2.28) is a good approximation so long as the variation of magnetization over the distance between atomic spins is small.

The exchange energy is minimized when magnetization is uniform throughout the magnetized body. Therefore, in the absence of other forces, the exchange interaction favors the parallel alignment of the magnetization vectors of grains in atomic contact. To represent this effect simply and in agreement with our representation of magnetostatic interactions, an equivalent magnetic field component is used. The component of magnetic field at grain k due to its exchange interaction with neighboring grain l is

$$\mathbf{H}_{e,kl} = \frac{K_{x,kl}}{\mu_0} \mathbf{M}_l, \tag{2.29}$$

where $K_{x,kl}$ (H/m) is a scalar proportionality constant controlling the strength of the exchange interaction from grain l to grain k.

The value of $K_{x,kl}$ can be related to other properties of the medium following the argument of [84], which we generalize here. Consider two grains in atomic contact with different easy axes, and ignore any effect of magnetostatic interactions. The magnetization near the contact surface responds in conflicting ways to the anisotropy and exchange effects. Anisotropy favors a sharp transition from magnetization along one easy axis to magnetization along the other easy axis as the grain boundary is crossed. The exchange interaction favors a gradual transition from one magnetization direction to the other so that each atom has magnetic moment nearly parallel to that of its neighbors. Total energy is minimized in a compromise between these competing forces. That compromise configuration is a *domain wall*, through which the magnetization undergoes its change of orientation.

The theory of domain walls is well-established in the study of the physics of magnetic materials. One reference is [21, p. 186-204]. The domain wall configuration which minimizes the sum of exchange energy and anisotropy energy also has the property that the exchange energy and anisotropy energy are equal. When the anisotropy energy has the formulation assumed in our model, the total energy of the domain wall configuration per unit of contact area is [84]

$$\gamma_w = 2\frac{\sqrt{K_A A_e}}{M_s^2}(M_s^2 - \mathbf{M}_k \cdot \mathbf{M}_l). \tag{2.30}$$

Thus, the exchange energy of a domain wall per unit of contact area is

$$\gamma_e = \frac{\sqrt{K_A A_e}}{M_s^2}(M_s^2 - \mathbf{M}_k \cdot \mathbf{M}_l). \tag{2.31}$$

It is convenient to treat the exchange interaction in a manner analogous to the magnetostatic interactions. Therefore, let us express the energy at grain k due to the exchange field arising from grain l is of the form

$$W_{e,kl} = -\mu_0 \mathcal{A}_k \delta \mathbf{M}_k \cdot \mathbf{H}_{e,kl}, \tag{2.32}$$

and when the zero of energy is chosen to coincide with $\mathbf{M}_k = \mathbf{M}_l$ (when there is no wall), the expression becomes

$$W_{e,kl} = (M_s^2 - \mathbf{M}_k \cdot \mathbf{M}_l) K_{x,kl} \mathcal{A}_k \delta. \tag{2.33}$$

Then we set this energy equal to the exchange energy of the domain wall between grains k and l so that $W_{e,kl}$ is the exchange energy of the pair of grains.

$$\begin{aligned} W_{e,kl} &= \gamma_e a_{kl} && (2.34) \\ (M_s^2 - \mathbf{M}_k \cdot \mathbf{M}_l) K_{x,kl} \mathcal{A}_k \delta &= a_{kl}\frac{\sqrt{K_A A_e}}{M_s^2}(M_s^2 - \mathbf{M}_k \cdot \mathbf{M}_l), && (2.35) \end{aligned}$$

where a_{kl} is the area of atomic contact between grains k and l. Solving for $K_{x,kl}$ yields

$$K_{x,kl} = \frac{\sqrt{K_A A_e}}{M_s^2} \cdot \frac{a_{kl}}{\mathcal{A}_k \delta}. \tag{2.36}$$

Recall Assumption 2.1 that the medium model is planar. The contact area, a_{kl} between the two grains may be expressed as the product of the medium thickness, δ, and the length of the boundary between grains k and l in the medium plane, ℓ_{kl}. Also consider that the grains may be in atomic contact over only some fraction f of the grain boundary. Then the expression for $K_{x,kl}$ becomes

$$K_{x,kl} \triangleq \frac{\ell_{kl}}{\mathcal{A}_k} \cdot \frac{\sqrt{K_A}}{M_s^2} \cdot f\sqrt{A_e}. \tag{2.37}$$

The first factor depends only on the geometric relationship between grains k and l. The second factor comprises only quantities which have already been defined for other purposes. The third factor is one which may be varied freely in the model to examine different values of exchange interaction strength.

The exchange field at grain k, $\mathbf{H}_{e,k}$, is the sum of the component exchange fields arising from each of the other grains in atomic contact with grain k. Express this set of grains which are neighbors of grain k using the notation $N(k)$. Then,

$$\mathbf{H}_{e,k} = \sum_{l \in N(k)} \mathbf{H}_{e,kl} = \sum_{l \in N(k)} \frac{K_{x,kl}}{\mu_0} \mathbf{M}_l. \tag{2.38}$$

Assumption 2.7 : Exchange interactions are modeled by a magnetic field component. *The magnitude of the exchange field component is proportional to a quantity* $f\sqrt{A_e}$ *which is a constant for all grains in the medium.*

The value of quantity $f\sqrt{A_e}$ ($(\mathrm{J/m})^{1/2}$) is a property of the medium.

Appropriate definition of the (diagonal) exchange interaction matrices, $\mathbf{A}_{e,kl}$, leads to a simplified notation,

$$\mathbf{H}_{e,k} = \sum_{l \in N(k)} \mathbf{A}_{e,kl} \mathbf{M}_l. \tag{2.39}$$

It is not difficult to show that the exchange interaction matrices, $\mathbf{A}_{e,kl}$, have these properties in common with the magnetostatic interaction matrices,

$$\mathbf{A}_{e,kl} = \mathbf{A}_{e,kl}^T, \tag{2.40}$$

$$\mathcal{A}_k \mathbf{A}_{e,kl} = \mathcal{A}_l \mathbf{A}_{e,lk}. \tag{2.41}$$

As for the magnetostatic fields, a consequence of these properties is that

$$W_{e,kl} = W_{e,lk}, \tag{2.42}$$

which makes physical sense.

Finally, we consider the calculation of the total exchange energy of the medium from the magnetization and field quantities. As in the calculation of total magnetostatic energy, a simple summation of energy terms in the form of (2.9) has the consequence of counting each grain pair's exchange interaction energy twice in the summation. Therefore the correct expression for total exchange energy of the entire medium, in J, is

$$W_e = -\frac{1}{2} \sum_{k \in \mathcal{I}} \mu_0 \mathcal{A}_k \delta \mathbf{M}_k \cdot \mathbf{H}_{e,k}. \tag{2.43}$$

which may be written

$$W_e = -\frac{\mu_0 \delta}{2} \sum_{k \in \mathcal{I}} \sum_{\substack{l \in \mathcal{I} \\ l \neq k}} \mathbf{M}_k^T (\mathcal{A}_k \mathbf{A}_{e,kl}) \mathbf{M}_l. \tag{2.44}$$

A comparison of this representation of the exchange interaction with that of other researchers in micromagnetics is deferred to the next chapter. For an alternative formulation, see Appendix B.

Applied Field

In order to explore the hysteretic properties of a medium represented by our model, or to investigate the details of a recording process, the model must include a representation of an applied field. If the kth grain is in the presence of an applied field of $\mathbf{H}_{a,k}$ A/m, the resulting magnetic energy (sometimes called Zeeman energy) of grain k, in J, is

$$W_a = -\mu_0 \delta \sum_{k \in \mathcal{I}} \mathcal{A}_k \mathbf{M}_k^T \mathbf{H}_{a,k} \tag{2.45}$$

Our primary interest in defining a medium model is investigation of the medium's ability to store information. The storage task is achieved by the long-term stability of a magnetic state between the recording and read processes. During this period of storage, the applied field is zero-valued.

2.1.3 Model Magnetic State Evolution

The model is incomplete without a representation of how the magnetic interactions drive changes in the magnetic state. The history of the magnetic state of the model over an interval of time may be considered as a trajectory through the state space of the model. In the definition of algorithms for describing the evolving magnetic state of the model, several objectives are sought. First, the evolving state should plausibly represent nature. The laws of physics should not be flagrantly disobeyed by the model. Second, the state evolution algorithm should permit an efficient implementation. The model will be of limited interest if we can't perform simulations in reasonable time with available computing resources. Third, there should be enough freedom in the algorithm to permit both success and failure in duplicating experimental results. A model which cannot generate results in agreement with experiment is clearly inaccurate, while one which cannot fail to agree with experimental results cannot be validated on the basis of that agreement.

Minimal Properties of Relaxation

To address the first objective, physical plausibility of the representation of magnetic state evolution, two constraints on the algorithm are offered as a minimal requirement:

1. The trajectory of magnetic state through state space must be continuous.
2. The total magnetic energy of the magnetic states of the trajectory must decrease monotonically.

Any evolution of the model's magnetic state which obeys these constraints we call a *relaxation*. Clearly, if the model is in a magnetic state from which all continuous changes lead to an increase in total magnetic energy, then no relaxation can change the magnetic state. Therefore, magnetic states which are local minima of total magnetic energy will be *stable states* of any relaxation. Depending on what other constraints are assumed by a particular relaxation method, there may be other stable states of the relaxation algorithm as well.

Magnetic Torque Calculation

The total magnetic energy of the medium, in J, is the sum of all the magnetic energies so far described,

$$W = W_A + W_m + W_e + W_a. \tag{2.46}$$

The total magnetic energy of the medium is a function of the magnetic state of the medium. According to the model, the magnetic state is specified by the set of magnetization vectors $\{\mathbf{M}_k, k \in \mathcal{I}\}$. Because of Assumption 2.3, these vectors are completely determined by the set of angles $\{\alpha_k, k \in \mathcal{I}\}$. Therefore, changes in the magnetic state may be represented by changes in the values of the angles $\{\alpha_k, k \in \mathcal{I}\}$. Let us consider how the total magnetic energy varies with continuous changes in the angle of the magnetization of the νth grain, α_ν. The anisotropy energy variation,

$$\frac{\partial}{\partial \alpha_\nu} W_A = (\mathcal{A}_\nu \delta) \frac{\partial}{\partial \alpha_\nu} \left[K_A \sin^2(\alpha_\nu - \theta_\nu) \right], \tag{2.47}$$

and the applied field energy variation,

$$\frac{\partial}{\partial \alpha_\nu} W_a = (\mathcal{A}_\nu \delta) \left[-\mu_0 \mathbf{H}_{a,\nu} \cdot \left(\frac{\partial}{\partial \alpha_\nu} \mathbf{M}_\nu \right) \right]. \tag{2.48}$$

are both straightforward. Further simplification is possible for both of these expressions, but not helpful at this point. What is important is that the derivative still to be taken is the derivative of an expression which is a function of α_ν only, and not a function of any α_k for $k \neq \nu$. This means that the variation of the total magnetic energy of the entire medium may be expressed as a function of the variation of functions of only α_ν. A global energy variation may be expressed in terms of the variation of purely local quantities.

Expressions with the same property must be found for the variation of magnetostatic and exchange energies with α_ν. The magnetostatic and exchange energies share a common form. Therefore the analysis below of the magnetostatic energy variation also applies to the exchange energy variation. The magnetostatic energy variation is

$$\begin{aligned}
\frac{\partial}{\partial \alpha_\nu} W_m &= -\frac{\mu_0 \delta}{2} \sum_{k \in \mathcal{I}} \sum_{l \in \mathcal{I}} \frac{\partial}{\partial \alpha_\nu} \mathbf{M}_k^T (\mathcal{A}_k \mathbf{A}_{m,kl}) \mathbf{M}_l \\
&= -\frac{\mu_0 \delta}{2} \left\{ \sum_{k \in \mathcal{I}} \mathbf{M}_k^T (\mathcal{A}_k \mathbf{A}_{m,k\nu}) \left(\frac{\partial}{\partial \alpha_\nu} \mathbf{M}_\nu \right) + \sum_{l \in \mathcal{I}} \left(\frac{\partial}{\partial \alpha_\nu} \mathbf{M}_\nu \right)^T (\mathcal{A}_\nu \mathbf{A}_{m,\nu l}) \mathbf{M}_l \right\} \\
&= -\frac{\mu_0 \delta}{2} \sum_{l \in \mathcal{I}} \left(\frac{\partial}{\partial \alpha_\nu} \mathbf{M}_\nu \right)^T (\mathcal{A}_l \mathbf{A}_{m,l\nu}^T + \mathcal{A}_\nu \mathbf{A}_{m,\nu l}) \mathbf{M}_l \\
&\overset{(a)}{=} -\frac{\mu_0 \delta 2}{2} \mathcal{A}_\nu \left(\frac{\partial}{\partial \alpha_\nu} \mathbf{M}_\nu \right)^T \sum_{l \in \mathcal{I}} \mathbf{A}_{m,\nu l} \mathbf{M}_l
\end{aligned}$$

$$= \quad (\mathcal{A}_\nu \delta) \left[-\mu_0 \left(\frac{\partial}{\partial \alpha_\nu} \mathbf{M}_\nu \right)^T (\mathbf{H}_{m,\nu}) \right]$$

$$= \quad (\mathcal{A}_\nu \delta) \left[-\mu_0 \left(\mathbf{H}_{m,\nu} \right) \cdot \left(\frac{\partial}{\partial \alpha_\nu} \mathbf{M}_\nu \right) \right]. \tag{2.49}$$

where equality (a) follows from properties (2.19) and (2.20) of the magnetostatic interaction matrices. The final expression has precisely the property we desire.

Bringing all the pieces together, the variation of the total magnetic energy W with α_ν is

$$\frac{\partial}{\partial \alpha_\nu} W = (\mathcal{A}_\nu \delta) \left\{ \frac{\partial}{\partial \alpha_\nu} \left[K_A \sin^2(\alpha_\nu - \theta_\nu) \right] - \mu_0 \left(\mathbf{H}_{m,\nu} + \mathbf{H}_{e,\nu} + \mathbf{H}_{a,\nu} \right) \cdot \frac{\partial}{\partial \alpha_\nu} \mathbf{M}_\nu \right\} \tag{2.50}$$

This expression represents the torque on the magnetization of the νth grain, $\mathcal{T}_\nu$ due to the effect of all the magnetic interactions of the model. (Strictly speaking, the torque is a vector quantity with direction normal to the medium plane. Since the direction is understood due to the restriction of grain moments to the medium plane, only the scalar value representing the magnitude and direction of torque is noted in this discussion.) Let us define a total effective magnetic field at grain ν,

$$\mathbf{H}_\nu \triangleq \mathbf{H}_{m,\nu} + \mathbf{H}_{e,\nu} + \mathbf{H}_{a,\nu}. \tag{2.51}$$

Then $\mathbf{H}_\nu$ is not a function of α_ν, but is a function of $\{\alpha_k : \forall k \neq \nu\}$. The torque $\mathcal{T}_\nu$ may be expressed

$$\mathcal{T}_\nu = \frac{\partial}{\partial \alpha_\nu} W = (\mathcal{A}_\nu \delta) \left\{ 2K_A \sin(\alpha_\nu - \theta_\nu) \cos(\alpha_\nu - \theta_\nu) - \mu_0 \mathbf{H}_\nu \cdot \frac{\partial}{\partial \alpha_\nu} \mathbf{M}_\nu \right\} \tag{2.52}$$

This expression makes clear that the torque on the magnetization of the νth grain, $\mathcal{T}_\nu$, is a function of the magnetic state of the medium through two quantities: α_ν (which completely determines $\mathbf{M}_\nu$) and the effective field $\mathbf{H}_\nu$. The dependence of $\mathcal{T}_\nu$ on the magnetization of grains other than the νth grain is only through the effective field $\mathbf{H}_\nu$. This is the *local field concept*. If the local field value $\mathbf{H}_\nu$ is known (i.e. has been computed), then the local torque $\mathcal{T}_\nu$ may be computed without other reference to the values of $\{\alpha_k, k \neq \nu\}$.

The local field concept suggests a way to address the second objective of a state evolution algorithm, computational efficiency. If changes in the magnetic state permitted by the evolution algorithm are limited to those in which only one grain magnetization changes value, then only one torque need be computed to determine the direction of change. Furthermore, updates of the values of the effective fields take the form of a linear adjustment to one variable's changing value rather than a complete recomputation of a function of the entire magnetic state. Such efficiencies are quite attractive. The effect of this constraint on the results must be considered, however. This effect is discussed in Section 3.4.1.

In any magnetic state, if there is a grain k with $\mathcal{T}_k$ not equal to zero, then the sign of $\mathcal{T}_k$ determines a direction of continuous change in α_k which decreases total magnetic energy. Therefore, so long as that change in α_k is not disallowed by some other constraint on the relaxation procedure, it may be considered a candidate for the next step in the evolution of the magnetic state of the model.

Because the sign of the torque, $\mathcal{T}_k$, is of interest, it is convenient to work with normalized quantities. First, let us write $\mathbf{H}_k$ in the form

$$\mathbf{H}_k = H_k \cos\beta_k \hat{\mathbf{x}} + H_k \sin\beta_k \hat{\mathbf{z}}, \tag{2.53}$$

where both H_k and β_k are functions of $\{\alpha_l : \forall l \neq k\}$. Then make a customary definition of the *anisotropy field*,

$$H_K \triangleq \frac{2K_A}{\mu_0 M_s}, \tag{2.54}$$

and normalize the effective magnetic field to a scale where the anisotropy field is the unit,

$$\mathbf{h}_k \triangleq \frac{\mathbf{H}_k}{H_K} = h_k \cos\beta_k \hat{\mathbf{x}} + h_k \sin\beta_k \hat{\mathbf{z}}. \tag{2.55}$$

Also introduce normalized quantities for the grain magnetizations

$$\mathbf{m}_k \triangleq \frac{\mathbf{M}_k}{M_s} = \cos\alpha_k \hat{\mathbf{x}} + \sin\alpha_k \hat{\mathbf{z}}. \tag{2.56}$$

Then the torque $\mathcal{T}_k$ may be expressed

$$\begin{aligned}
\mathcal{T}_k &= 2K_A \mathcal{A}_k \delta \left\{ \sin(\alpha_k - \theta_k)\cos(\alpha_k - \theta_k) - \mathbf{h}_k \cdot \frac{\partial}{\partial \alpha_k}\mathbf{m}_k \right\} && (2.57)\\
&= 2K_A \mathcal{A}_k \delta \left\{ \sin(\alpha_k - \theta_k)\cos(\alpha_k - \theta_k) + h_k \sin(\alpha_k - \beta_k) \right\} && (2.58)\\
&= 2K_A \mathcal{A}_k \delta \frac{\partial}{\partial \alpha_k} \mathcal{F}_k(\alpha_k). && (2.59)
\end{aligned}$$

where

$$\mathcal{F}_k(\alpha_k) = \frac{1}{2}\sin^2(\alpha_k - \theta_k) - h_k \cos(\alpha_k - \beta_k). \tag{2.60}$$

With all the other grain magnetizations held fixed, the variation of total magnetic energy, W, with the angle of the magnetization of the kth grain, α_k is completely described by the objective function $\mathcal{F}_k(\alpha_k)$. Changes in α_k which decrease $\mathcal{F}_k(\alpha_k)$ will decrease W. Values of α_k which are local minima of $\mathcal{F}_k(\alpha_k)$ are local minima of W subject to the constraint that all other α are held fixed. Consider, then, a sequence of repeatedly selecting a grain index k from $\mathcal{I}$ and minimizing the objective function $\mathcal{F}_k(\alpha_k)$ in such a way that total magnetic energy monotonically decreases. A stable state of this process is reached when the magnetization angle α_k of every grain k is a local minimum of the corresponding objective function $\mathcal{F}_k(\alpha_k)$. In such a stable state, any continuous change in the magnetization of a single grain will lead to an increase in total magnetic energy. Included among these stable states are the local minima of total magnetic energy.

The vector quantities may be resolved into components parallel and perpendicular to the easy axis,

$$h_{\|,k} \triangleq h_k \cos(\beta_k - \theta_k), \tag{2.61}$$

$$h_{\perp,k} \triangleq h_k \sin(\beta_k - \theta_k), \tag{2.62}$$

$$m_{\|,k} \triangleq \cos(\alpha_k - \theta_k), \tag{2.63}$$

$$m_{\perp.k} \triangleq \sin(\alpha_k - \theta_k). \tag{2.64}$$

Then the kth objective function may be written

$$\mathcal{F}_k(\alpha_k) = \frac{1}{2}m_{\perp,k}^2 - h_{\|,k}m_{\|,k} - h_{\perp,k}m_{\perp,k}, \tag{2.65}$$

and the corresponding torque may be written

$$\mathcal{T}_k = 2K_A\mathcal{A}_k\delta(m_{\|,k}m_{\perp,k} + h_{\|,k}m_{\perp,k} - h_{\perp,k}m_{\|,k}). \tag{2.66}$$

These expressions are important because they allow the evaluation of the objective function and the torque without the need to compute trigonometric functions. Simple multiplication and addition operations are computable much faster than trigonometric functions.

Stoner-Wohlfarth Analysis

Since local minima of the total magnetic energy must be stable states of any relaxation process, let us investigate the necessary conditions for a local minimum. If a magnetic state represented by a set of angle values $\{\alpha_l\}$ is a local minimum of total magnetic energy, then each individual angle value, say α_k, must be a local minimum of the corresponding objective function $\mathcal{F}_k(\alpha_k)$. Since the objective function $\mathcal{F}_k(\alpha_k)$ is a continuous function on a compact set (the unit circle), it must have at least one local minimum (as well as one local maximum). Also, because $\mathcal{F}_k(\alpha_k)$ is periodic, local minima and maxima must be interleaved as α_k varies through a whole revolution on the unit circle. The objective function has continuous derivatives of all orders, so the values of α_k which are local minima must also yield a zero-valued first derivative. The first derivative is

$$\frac{d\mathcal{F}_k}{d\alpha_k}(\alpha_k) = \frac{1}{2}\sin[2(\alpha_k - \theta_k)] + h_k \sin(\alpha_k - \beta_k). \tag{2.67}$$

The first derivative has isolated zeros, and when it is zero-valued, so is the corresponding torque. Furthermore, because of limited frequency content of the first derivative, it can have at most four zeros within each period. This constraint combined with the interleaving of minima and maxima yields the conclusion that there are at most two values of α_k which are local minima. Also, when there are two minima, they are separated by the values $\theta_k \pm \pi/2$. In other words, one of the energy-minimizing magnetization vectors has a positive projection on the easy-axis; the other has a negative projection on the easy-axis.

Given a fixed value of $\mathbf{h}_k$, then, there are either one or two values for α_k which are local minima of the objective function. Therefore each grain has at most two magnetizations which are stable, no matter what the state of the other grains in the assembly, unless additional constraints are imposed on the relaxation process. To distinguish the circumstances which lead to two local minima from those which lead to a single local minimum, we further analyze the derivatives of the objective function. The first derivative must have two zeros to account for at least one minimum and one maximum of the objective function. When grain k has two stable magnetizations, the first derivative must have four zeros, the maximum possible number of zeros it can have, to account for the required interleaving of minima and maxima. The boundary between these two possibilities is the case when the first derivative has three zeros. Due to the necessary interleaving of minima and maxima, the only way the first

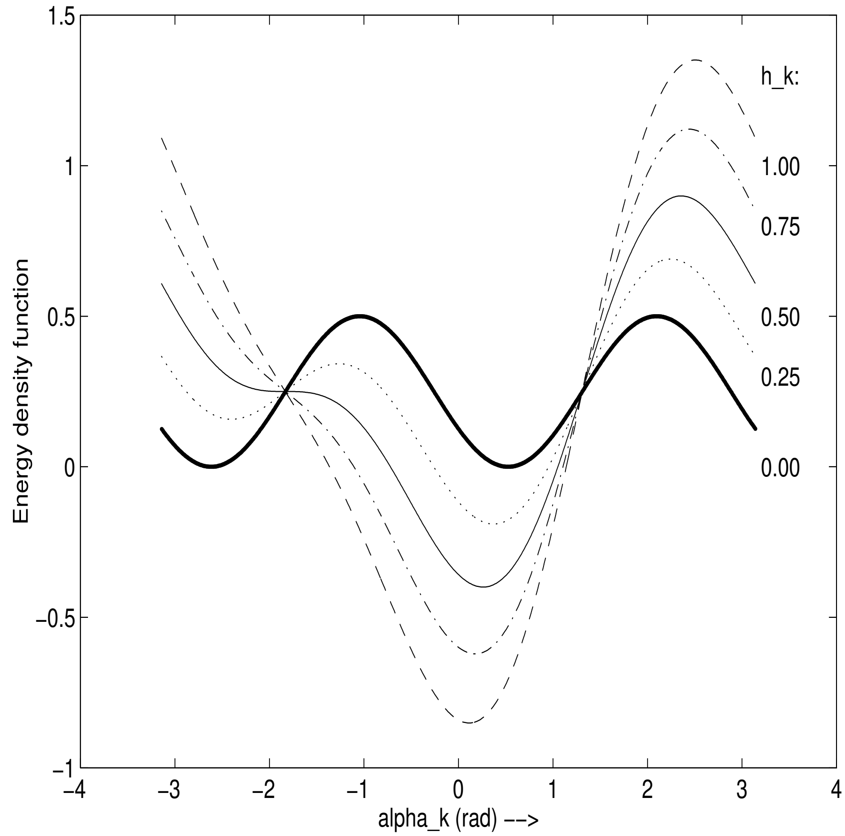

Figure 2.1: Illustration of one- and two-minima energy functions

derivative can have an odd number of zeros is for one of the zeros to not correspond to an extremum of the objective function. A zero of the first derivative is a local minimum of the objective function if it yields a positive second derivative. A zero of the first derivative is a local maximum of the energy density if it yields a negative second derivative. The only wasy a zero of the first derivative can exist which is not also an extremum of the objective function is if it is also a zero of the second derivative. Thus, for there to be three zeros of the first derivative, one of them must be an inflection point of the objective function.

As an illustration, consider Fig. 2.1, which depicts plots of the objective function with $\theta_k = \pi/6$, $\beta_k = -\pi/12$, and five selected values of h_k: $0, 0.25, 0.5, 0.75, 1.0$. All three possibilities are illustrated. Each distinct value of $\mathbf{h}_k$ (h_k and β_k), determines whether there are one or two local minima. In the plane of possible values for $\mathbf{h}_k$, the one-minimum and two-minima cases are separated by the boundary cases where an inflection point is present. We now solve for that boundary.

The second derivative of the objective function is

$$\frac{d^2\mathcal{F}_k}{d\alpha_k^2}(\alpha_k) = \cos[2(\alpha_k - \theta_k)] + h_k \cos(\alpha_k - \beta_k). \tag{2.68}$$

For an inflection point to exist, both the first and second derivatives must have a common zero $\hat{\alpha}_k$.

$$\frac{1}{2}\sin[2(\hat{\alpha}_k - \theta_k)] + h_k \sin(\hat{\alpha}_k - \beta_k) \quad = \quad 0 \tag{2.69}$$

$$\cos[2(\hat{\alpha}_k - \theta_k)] + h_k \cos(\hat{\alpha}_k - \beta_k) \quad = \quad 0 \tag{2.70}$$

In terms of components of the normalized magnetic field parallel and perpendicular to the easy axis of anisotropy, the system to be solved is

$$h_{\|,k} \sin(\hat{\alpha}_k - \theta_k) - h_{\perp,k} \cos(\hat{\alpha}_k - \theta_k) \quad = \quad -\frac{1}{2}\sin[2(\hat{\alpha}_k - \theta_k)] \tag{2.71}$$

$$h_{\|,k} \cos(\hat{\alpha}_k - \theta_k) + h_{\perp,k} \sin(\hat{\alpha}_k - \theta_k) \quad = \quad -\cos[2(\hat{\alpha}_k - \theta_k)] \tag{2.72}$$

Solutions of this system of equations must satisfy

$$h_{\|,k} \quad = \quad [-\cos(\hat{\alpha}_k - \theta_k)]^3 \tag{2.73}$$

$$h_{\perp,k} \quad = \quad [\sin(\hat{\alpha}_k - \theta_k)]^3. \tag{2.74}$$

These equations give a parametric form of the boundary between the one-minimum and two-minima regions of the plane of $\mathbf{h}_k$ values. The value of the inflection point $\hat{\alpha}_k$ may be any angular value on the unit circle. Varying $\hat{\alpha}_k$ through its set of possible values, traces out the desired boundary in the $\mathbf{h}_k$ plane. Fig. 2.2 depicts the boundary, still assuming $\theta_k = \pi/6$. The geometric figure displayed is known as the Stoner-Wohlfarth astroid, after the original authors of this analysis [111].

Two cusps of the Stoner-Wohlfarth astroid lie on the easy axis of anisotropy. The other two lie on an axis perpendicular to the easy axis, the so-called *hard axis*. It is easiest to express the Stoner-Wohlfarth astroid in terms of the components of $\mathbf{h}_k$ parallel and perpendicular to the easy axis. An equation for the Stoner-Wohlfarth astroid is

$$\left|h_{\|,k}\right|^{2/3} + \left|h_{\perp,k}\right|^{2/3} = 1. \tag{2.75}$$

Let us consider how the local minima of $\mathcal{F}_k$ will vary with changing local field $\mathbf{h}_k$. For values of $\mathbf{h}_k$ within the Stoner-Wohlfarth astroid, as the value of $\mathbf{h}_k$ varies

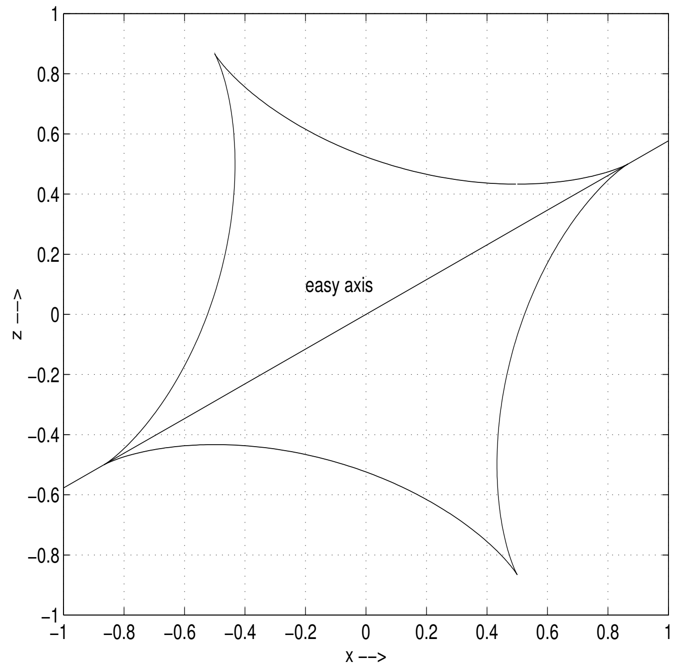

Figure 2.2: The Stoner-Wohlfarth astroid ($\theta = \pi/6$)

continuously, the locations of the two local minima $\hat{\alpha}_k$ also vary continuously. In physical terms, the magnetization of the grain rotates continuously and reversibly in response to a continuously varying local field. When the value of $\mathbf{h}_k$ crosses from the interior of Stoner-Wohlfarth astroid to the exterior, one of the energy minima disappears into the inflection point while the other continues to vary continuously with $\mathbf{h}_k$. A grain with magnetization corresponding to the disappearing minimum will experience a discontinuous and irreversible change in its magnetization to settle in the remaining energy minimum. The energy minimum which persists is the one whose magnetization projection on the easy-axis has the same sign as $h_{\|,k}$.

Rotation-relaxation

All the preceding discussion motivates a constrained relaxation algorithm. In addition to the constraints required of any relaxation, we impose only the constraint that only one grain's magnetization change at one time. At each step of the algorithm, one grain, say grain k, is selected. A local minimum of the corresponding objective function is computed (that is, a new value of α_k) so that the rotation of the grain's magnetization from its old value to its new value is a trajectory of monotonically decreasing total magnetic energy. The algorithm continues until all grains have magnetization angles α_k which are local minima of the corresponding objective functions. $\mathcal{F}_k(\alpha_k)$. A discussion of the implementation details of this algorithm is deferred until Section 3.4. We shall call any algorithm which conforms to this general description a *rotation-relaxation* algorithm.

Flip-relaxation

When considering the storage capacity of recording media, the exact properties of the stable magnetic states are not so important as being able to determine their number. With this in mind, we may impose additional constraints on the relaxation algorithm which sacrifice accuracy for simplicity. When $\mathbf{h}_k$ has zero value, the two stable magnetizations of grain k are aligned with the grain's easy axis. As $\mathbf{h}_k$ varies within the Stoner-Wohlfarth astroid, the two stable magnetizations of grain k rotate continuously and reversibly, one in each of the half-planes separated by the grain's hard axis. When $\mathbf{h}_k$ exceeds the Stoner-Wohlfarth astroid, the magnetization in the half-plane opposite of $\mathbf{h}_k$ loses stability, and the only remaining stable state is in the same half-plane as $\mathbf{h}_k$. These essential features are preserved in a model which ignores the continuous and reversible rotation of magnetization, and retains only the irreversible reversals of magnetization forced by values of $\mathbf{h}_k$ which exceed the Stoner-Wohlfarth astroid. This simplified model evolution assumes that the magnetization of grain k is aligned with its easy axis. That is,

$$\mathbf{m}_k = s_k(\cos\theta_k\hat{\mathbf{x}} + \sin\theta_k\hat{\mathbf{z}}), \tag{2.76}$$

where $s_k \in \{\pm 1\}$. With this assumption in force, the total magnetic state of a medium is completely characterized by $\{R_k, k \in \mathcal{I}\}$, $\{s_k, k \in \mathcal{I}\}$, and $\{\theta_k, k \in \mathcal{I}\}$. Both the geometric features of the granular regions, ($\{R_k, k \in \mathcal{I}\}$), and the orientation of the grains' easy axes, ($\{\theta_k, k \in \mathcal{I}\}$) are properties of the medium which are established in the manufacture of the medium, and are assumed to remain constant throughout the lifetime of the medium. Given their constant values, the medium's magnetic state is completely determined by the set of values $\{s_k, k \in \mathcal{I}\}$. The allowed change in grain magnetization $\mathbf{m}_k$, a total reversal of direction, is represented by an inversion of the sign value s_k. The constraints of relaxation require that magnetization reversal occur only when there is a continuous trajectory through state space from the initial magnetization to the new magnetization for which total magnetic energy monotonically decreases. The update rule which implements the relaxation constraints is

$$s_k^{\text{new}} = U(s_k, \mathbf{h}_k) \triangleq \begin{cases} \operatorname{sgn}(h_{\|,k}), & |h_{\|,k}|^{2/3} + |h_{\perp,k}|^{2/3} \geq 1 \\ s_k, & |h_{\|,k}|^{2/3} + |h_{\perp,k}|^{2/3} < 1 \end{cases} \tag{2.77}$$

Selection of grains and application of the update rule is continued until a magnetic state is reached in which no further reversals will occur. Such a magnetic state is a *fixed point* of the algorithm. The term *fixed point* is used rather than *stable state* to call attention to the extra constraint of this algorithm. The magnetic state changes which occur under this constrained evolution rule are sudden reversals, or *flips*, of the magnetization of a grain. For this reason, we call an algorithm which obeys this constraint a *flip-relaxation* algorithm. The constraints of a flip-relaxation algorithm are quite limiting. The only remaining freedom in describing a flip-relaxation algorithm is the choice of an algorithm to select the sequence in which the grains are selected. Grain selection algorithms may be either deterministic or pseudo-random. No matter which type of grain selection algorithm is chosen, the set of magnetic states which are fixed points of the flip-relaxation algorithm

$$\Omega = \{\mathbf{s} \in \{\pm 1\}^N : \forall_{k \in \mathcal{I}} : s_k = U(s_k, \mathbf{h}_k(\mathbf{s}))\} \tag{2.78}$$

is the same.

The reader might properly object that the additional constraint on a flip-relaxation algorithm violates our first stated objective of a state evolution algorithm, physical plausibility. It leaves every grain's magnetization aligned with its easy axis even when the physics plainly demands a rotation off the easy axis. For this reason, a flip-relaxation algorithm most certainly does not predict precisely the same magnetization states as a rotation-relaxation algorithm. Essentially, this objection states that the minimal requirements on a relaxation algorithm are not stringent enough in their representation of physical plausibility since they permit stable states which are not local minima of total magnetic energy. A rotation-relaxation model is a better choice when seeking to predict the physical behavior of a recording medium. The added constraints built into the flip-relaxation model generate unphysical behavior.

The reader might reasonably object, therefore, that replacing a rotation-relaxation model with a flip-relaxation model in order to analyze capacity limits is illegitimate. After all, the rotation-relaxation model permits a continuum of magnetic states, while the constraints of the flip-relaxation model permit only 2^N distinct magnetic states in an assembly of N grains. There are grounds for suspicion that the number of fixed points of the flip-relaxation model significantly underestimates the number of stable states of the rotation-relaxation model.

This is, in fact, not the case. As already noted, for a magnetic state to be a stable state of a rotation-relaxation algorithm, it is a necessary condition that each magnetization angle α_k be a local minimum of the corresponding objective function $\mathcal{F}_k(\alpha_k)$. Thus, the first derivatives of all N objective functions must be zero-valued,

$$\frac{d\mathcal{F}_k}{d\alpha_k} = m_{||,k}m_{\perp,k} + h_{||,k}m_{\perp,k} - h_{\perp,k}m_{||,k} = 0. \tag{2.79}$$

The normalized local fields $\{\mathbf{h}_k\}$ are each linear functions of the normalized magnetizations $\{\mathbf{m}_k\}$. Therefore (2.79) represents N equations of degree two in the components of normalized magnetizations. The model constraints also imply the equations

$$m_{||,k}^2 + m_{\perp,k}^2 = 1. \tag{2.80}$$

Taken together, there are $2N$ equations of degree 2 that must be solved simultaneously. Bezout's theorem [117] states that there can be at most 2^{2N} solutions to such a system. The solutions of this system of equations represent a set of critical points. It is *necessary* that a magnetic state belong to this set of solutions in order to be a stable point of any rotation-relaxation algorithm. Furthermore, only those solutions for which the second derivatives of all the objective functions are positive are in fact local minima of all the objective functions. There are N second derivatives to consider and each of them may be positive of negative. Thus, only one out of every 2^N critical points can be expected to be a stable state. (It is assumed that zero-valued second derivatives have zero probability, and can be ignored). The conclusion is that there are at most 2^N magnetic states which meet the necessary conditions to be stable states of a rotation relaxation algorithm. Thus, the flip-relaxation model does not rule out by its constraint large numbers of stable states that might otherwise be possible.

2.2 Inductive Read Head Model Definition

In order to compare the predictions of the model with laboratory measurements, it is necessary to simulate the processes used in taking measurements. The most common

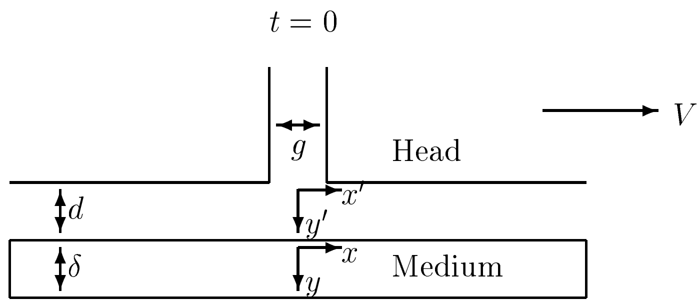

Figure 2.3: Head-medium interface geometry ($t = 0$)

measurement performed in the laboratory is to measure the voltage signal induced when an inductive read head is used to read the magnetic pattern written on the medium.

2.2.1 Reciprocity Principle

Inductive read heads operate on the principle that a voltage is induced in a coil of wire proportional to the time rate of change of magnetic flux through the coil. A head is designed so that the changes in flux are related to the magnetization pattern in the recording medium in a simple and predictable way. This relationship may be derived using the principle of reciprocity. This section presents the reciprocity principle, following the discussion in [72].

Consider two coils linked by a mutual inductance L_m. The flux ϕ through each coil due to the current I through the other is related by the equation:

$$L_m = \frac{\phi_1}{I_2} = \frac{\phi_2}{I_1} \tag{2.81}$$

Let coil 1 be the coil of an inductive head. The magnetic flux through coil 1 changes with time due to a relative motion of the head with respect to the medium at constant velocity V and the spatial variation of the magnetic field. Consider two sets of Cartesian coordinate axes, one anchored to the head, (x', y', z'), and the other anchored to the medium, (x, y, z). The two coordinate systems are related according to (see Fig. 2.3 and Fig. 2.4).

$$x' = x - Vt \tag{2.82}$$

$$y' = y + d \tag{2.83}$$

$$z' = z. \tag{2.84}$$

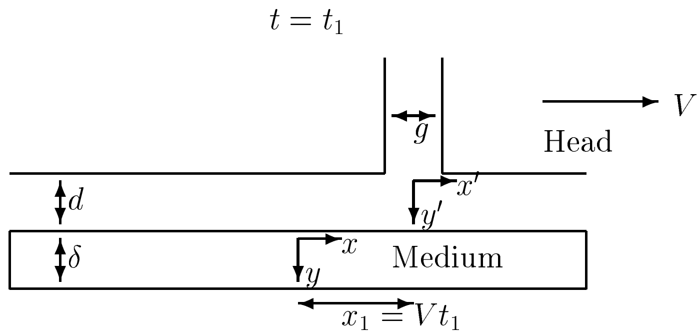

Figure 2.4: Head-medium interface geometry ($t = t_1$)

Let coil 2 be the magnetic current associated with a differential magnetized element of the recording medium located at head-coordinates (x_2', y_2', z_2'). Represent coil 2 as a rectangular current loop with dimensions dy by dz, and carrying a current I_2. When the head is energized by a current I_1 through its coil (coil 1), a magnetic field, $\mathbf{H}(x', y', z')$ is generated. The resulting differential flux through the differential coil 2 may be expressed

$$d\phi_2 = \mu_0 H_x(x_2', y_2', z_2') dy\, dz \tag{2.85}$$

The current through coil 2, I_2, is not a flow of free electric charge. It serves only to represent the magnetization of a differential element of the recording medium. The differential moment of the differential coil 2 is

$$d\mathbf{m} = I_2\, dy\, dz\, \hat{\mathbf{x}} \tag{2.86}$$

Magnetization is density of magnetic dipole moment,

$$\mathbf{M} \triangleq \frac{d\mathbf{m}}{dV} = \frac{d\mathbf{m}}{dx\, dy\, dz} = \frac{I_2}{dx}\hat{\mathbf{x}} = M_x \hat{\mathbf{x}} \tag{2.87}$$

Therefore,

$$I_2 = M_x(x_2, y_2, z_2) dx \tag{2.88}$$

where we have expressed the x-component of magnetization as a function of medium coordinates.

Recalling (2.81), we now write

$$d\phi_1 = d\phi_2 \frac{I_2}{I_1} = \mu_0 H_x(x_2', y_2', z_2') \frac{M_x(x_2, y_2, z_2)}{I_1} dx\, dy\, dz \tag{2.89}$$

Therefore, the total flux in the coil of the head due to the x-component of the magnetization pattern on the recording medium is

$$\phi_1 = \mu_0 \int\int\int \frac{H_x(x', y', z')}{I_1} M_x(x, y, z) dx\, dy\, dz \tag{2.90}$$

where the integral is over the total volume of the recording medium.

This argument may be repeated for the other components of the medium magnetization and the head field, to yield the result

$$\phi_1 = \mu_0 \int\int\int \frac{\mathbf{H}(x', y', z')}{I_1} \cdot \mathbf{M}(x, y, z) dx\, dy\, dz \tag{2.91}$$

which, by defining a head sensitivity function,

$$\mathbf{h}(x', y', z') \triangleq \frac{\mathbf{H}(x', y', z')}{I_1} \tag{2.92}$$

may be written

$$\phi_1 = \mu_0 \int\int\int \mathbf{h}(x', y', z') \cdot \mathbf{M}(x, y, z) dx\, dy\, dz \tag{2.93}$$

Finally substitution of the equations which related head-coordinates to medium coordinates yields either

$$v(t) = -\frac{d\phi_1}{dt} = -\mu_0 \frac{d}{dt} \int_{-\infty}^{\infty} \int_0^{\delta} \int_{-\infty}^{\infty} \mathbf{h}(x - Vt, y + d, z) \cdot \mathbf{M}(x, y, z) dx\, dy\, dz \tag{2.94}$$

or, in the other coordinates,

$$v(t) = -\mu_0 \frac{d}{dt} \int_{-\infty}^{\infty} \int_d^{d+\delta} \int_{-\infty}^{\infty} \mathbf{h}(x', y', z') \cdot \mathbf{M}(x' + Vt, y' - d, z') dx'\, dy'\, dz' \tag{2.95}$$

as expressions for the voltage signal read by an inductive head.

At this point, recall that by the assumptions of the medium model,

$$\mathbf{M}(x, y, z) = M_x(x, z)\hat{\mathbf{x}} + M_z(x, z)\hat{\mathbf{z}}. \tag{2.96}$$

Therefore, we may write

$$v(t) = -\mu_0 \frac{d}{dt} \int_{-\infty}^{\infty} \int_d^{d+\delta} \int_{-\infty}^{\infty} h_x(x', y', z') \cdot M_x(x' + Vt, z')\, dx'\, dy'\, dz' \tag{2.97}$$

$$- \quad \mu_0 \frac{d}{dt} \int_{-\infty}^{\infty} \int_{d}^{d+\delta} \int_{-\infty}^{\infty} h_z(x', y', z') \cdot M_z(x' + Vt, z')\, dx'\, dy'\, dz'$$

Further simplifications require an expression for the head sensitivity function, based on a particular model choice for the read head.

2.2.2 Karlqvist Head Model

A common simple model for inductive read heads is the Karlqvist head model [44]. It is based on the magnetostatic solution for the head field, assuming a head that is infinitely long (x direction), is infinitely wide (z direction), has an infinitely deep gap, and is uniformly magnetized when energized. For a head with gap length g and gain (gap field) H_g, and the head-medium interface geometry already specified, the components of the Karlqvist head model's head sensitivity function are

$$h_x(x', y', z') = \frac{H_g}{\pi} \left(\tan^{-1} \frac{g/2 + x'}{y'} + \tan^{-1} \frac{g/2 - x'}{y'} \right) \tag{2.98}$$

$$h_z(x', y', z') = 0 \tag{2.99}$$

Although physical recording heads have finite width, we shall not modify these expressions. The effect is that this model neglects the track edge effects of reading.

Substituting the Karlqvist model head sensitivity function in (2.97) and simplifying yields a scalar integral,

$$\begin{aligned} v(t) \quad = \quad & -\frac{\mu_0 V H_g}{\pi} \int_{-\infty}^{\infty} dx' \cdot \\ & \left(\int_{d}^{d+\delta} \left(\tan^{-1} \frac{g/2 + x'}{y'} + \tan^{-1} \frac{g/2 - x'}{y'} \right) dy' \right) \cdot \\ & \left(\int_{-\infty}^{\infty} \frac{\partial}{\partial x} M_x(x' + Vt, z')\, dz' \right) \end{aligned} \tag{2.100}$$

The y'-integral can be solved by use of the anti-derivative formula:

$$\int \tan^{-1} \frac{K}{y} dy \triangleq y \tan^{-1} \frac{K}{y} + \frac{K}{2} \ln(y^2 + K^2) + C, \tag{2.101}$$

to yield

$$\left[y' \tan^{-1} \frac{g/2 + x'}{y'} + \frac{g/2 + x'}{2} \ln(y'^2 + (g/2 + x')^2) \right]_{y'=d}^{y'=d+\delta}$$

$$+\left[y' \tan^{-1}\frac{g/2-x'}{y'} + \frac{g/2-x'}{2}\ln(y'^2+(g/2-x')^2)\right]_{y'=d}^{y'=d+\delta} \qquad (2.102)$$

This expression is formidable enough, and when fully expanded comprises eight terms, each of fairly high computational cost. For this reason, the y' integral is usually approximated instead by the expression,

$$\int_d^{d+\delta} h_x(x,y,z)dy \approx \delta h_x(x, d+\delta/2, z) \qquad (2.103)$$

The error introduced by this approximation is about one part in one thousand for typical values of g, d, and δ. Incorporating this approximation, (2.100) may be further simplified to

$$\begin{aligned} v(t) &= -\frac{\mu_0 V H_g \delta}{\pi}\int_{-\infty}^{\infty}\left(\tan^{-1}\frac{g/2+x'}{d+\delta/2} + \tan^{-1}\frac{g/2-x'}{d+\delta/2}\right)\cdot \\ &\quad \left(\int_{-\infty}^{\infty}\frac{\partial}{\partial x}M_x(x'+Vt, z')dz'\right)dx' \end{aligned} \qquad (2.104)$$

At this point, introduce the medium model assumption of granularity,

$$M_x(x,z) = M_s \sum_{k\in\mathcal{I}} \cos(\alpha_k) I_{R_k}(x,z). \qquad (2.105)$$

Although the indicator function is not formally differentiable, that is not necessary in this context. The theory of distributions (generalized functions) [130] lets us rewrite (2.104) as

$$\begin{aligned} v(t) &= \frac{\mu_0 V H_g \delta M_s}{\pi}\sum_{k\in\mathcal{I}}\cos\alpha_k \cdot \\ &\quad \int_{(x,z)\in R_k}\frac{\partial}{\partial x'}\left[\tan^{-1}\frac{g/2+x'}{d+\delta/2} + \tan^{-1}\frac{g/2-x'}{d+\delta/2}\right]_{x'=x-Vt} dx dz \end{aligned} \qquad (2.106)$$

which simplifies to

$$\begin{aligned} v(t) &= -\frac{4\mu_0 V H_g \delta M_s C D}{\pi}\sum_{k\in\mathcal{I}}\cos\alpha_k \cdot \\ &\quad \int_{(x,z)\in R_k}\frac{(x-Vt)dxdz}{[C^2+(D+x-Vt)^2][C^2+(D-x+Vt)^2]} \end{aligned} \qquad (2.107)$$

with $C = d + \delta/2$ and $D = g/2$.

To continue, we must know $\{R_k, \forall k \in \mathcal{I}\}$. For that reason, we defer further simplifications to the next chapter after a discussion of the generation of the geometric microstructure of the medium model.

2.3 Summary

This chapter has set out the basic definitions of two models. First a micromagnetic model of the magnetic layer of a magnetic recording medium was defined. The model represents the magnetic layer as a planar collection of single-domain grains which interact through magnetostatic, exchange, and anisotropy effects. Two rules governing state evolution of the model were defined: a rotation-relaxation model suitable for representing the physical nature of the magnetic layer, and a flip-relaxation model suitable for investigating the storage capacity of the magnetic layer. Second a model was defined for the computation of a playback voltage waveform induced in an inductive read head by the magnetic state of the medium model. The playback voltage waveform calculation is based on the reciprocity principle and the Karlqvist model of inductive read heads.

Chapter 3

Model Implementation

The preceding chapter has laid out the fundamental principles, assumptions, and equations on which our models of magnetic recording media and inductive heads are constructed. This chapter details a few of the implementation issues which arise in the creation of computer programs which implement the model definitions.

3.1 Microstructure Generation

The medium model contains three distinct types of variables. First are those variables which represent medium properties, listed in Table 3.1. These variables are single values which represent global properties of a recording medium. Furthermore, these values are global in the sense that they apply to all media composed of the same material. If several rigid disks are manufactured from the same materials and by the same process, then the same values of these properties are assumed to apply to the entire lot of disks.

Second are those variables which are different from one disk to another, but remain constant throughout the lifetime of the disk. These include all the variables necessary to describe the grain regions, $\{R_k, \forall k \in \mathcal{I}\}$, and the easy axes of uniaxial

Table 3.1: Model variables representing medium properties

Symbol	*Property*	*Units*
δ	Film Thickness	m
M_s	Magnetization Magnitude	A/m
K_A	Anisotropy Energy Density	J/m^3
$f\sqrt{A_e}$	Exchange Strength	(J/m)$^{1/2}$

anisotropy, $\{\theta_k, \forall k \in \mathcal{I}\}$. Taken together, these model variables describe the *microstructure* of the recording medium. To describe the variability of microstructure from one disk to the next, we shall consider these variables to be random variables whose values are fixed, or *quenched* at the time of manufacture. Each disk may then be viewed as a single realization of a random manufacturing process. Although a single microstructure cannot be assumed to exist over a whole lot of disks, the common manufacturing process they share may be reflected in statistical properties of the microstructure of the entire lot, or *ensemble*, of disks. For example, the manufacturing process may be designed to favor some orientations of easy axes over others. Different manufacturing processes may be represented by different probability distributions on the random variables which describe medium microstructure.

Third are those variables which describe the magnetic state of the medium. It is by inducing stable patterns in the values of these variables that the task of information storage is achieved. Depending on what relaxation model is in use, the magnetic state variables are either $\{\alpha_k, \forall k \in \mathcal{I}\}$ or $\{s_k, \forall k \in \mathcal{I}\}$.

Implementation of the medium property variables is trivial. Simply store the values of the appropriate variables. The magnetic state variables are likewise straightforward. Their values must evolve according to the selected evolution algorithm. This section examines the details of the generation of random variable realizations to represent medium microstructure.

3.1.1 Grain Geometry

It was established in Chapter 2 that the medium model is composed of uniformly magnetized grains and that the grains form a partition of the medium plane. In this section we establish the remaining details of grain geometry as implemented.

As reviewed in Section 1.5, many researchers have developed and investigated micromagnetic models of magnetic recording media. Nearly all of these models make use of a regular grain structure. The two most common grain geometries are hexagonal tiling and rectangular tiling. Regular grain structures have a number of advantages. They are simple. They allow for computer implementations which are efficient in their use of memory and processing resources. They form a space-filling partition of the medium plane. The primary disadvantages of regular grain structure are its spatial periodicity and anisotropy.

Miles and Middleton have demonstrated that such microstructure regularity yields unphysical anisotropic properties [74]. They have proposed an alternative randomized grain geometry [73, 79]. In the alternative strategy, grains are placed at random in the medium plane with care taken not to allow grain overlap. This strategy generates isotropic microstructures, but it also tends to generate microstructures with an unacceptably low packing density of grains. A multistage process is necessary to achieve an acceptable packing density.

Randomized grain geometry may instead be generated as a generalization of regular microstructure models. The resulting grain geometry is irregular, but also forms a partition of the medium plane with no gaps between grains. This grain generation algorithm is built on the concept of a *Voronoi diagram* [4].

Let $S \subset \mathbf{R}^2$ be a set of N planar points, $\{P_1, \ldots, P_N\} \subset \mathbf{R}^2$. The Voronoi diagram of S, $\mathcal{V}(S)$ is the set of regions, $\{R_1, \ldots, R_N\}$, where

$$R_k = \{x \in \mathbf{R}^2 : \forall_{l \neq k} : \|x - P_k\| \leq \|x - P_l\|\} \tag{3.1}$$

That is, a point in the plane belongs to the region R_k corresponding to the point P_k which is the least distance away among the points in S. Ignoring the region boundaries (which have no area), the Voronoi regions form a partition of $\mathbf{R}^2$. Voronoi diagrams are a generalization of the regular geometry of rectangular and hexagonal tiling patterns because those regular tiling patterns are themselves Voronoi diagrams of points which form a lattice. For both the rectangular and the hexagonal cases, the lattice points are in fact the centroids of the resulting rectangular or hexagonal regions.

Fig. 3.1 depicts the set of initial points S which form a rectangular lattice and the resulting rectangular Voronoi regions. As Figure 3.1 indicates, when constructing a regular rectangular microstructure, we assume that the boundaries of the rectangular grains are parallel to the x- and z-axes. A regular rectangular grain geometry is completely specified by the values of the length X and width Z of a single grain. In Figure 3.1, X and Z are both 50 nm (500 Å), and each grain has an area of 2500 nm^2. The size of the recording medium patch depicted in Figure 3.1 is 2μm $\times 2\mu$m.

Fig. 3.2 depicts the set of initial points S which form a hexagonal lattice and the resulting hexagonal Voronoi regions. As Figure 3.2 indicates, when constructing a regular hexagonal microstructure, we assume that the hexagonal grains are oriented so that each grain has a pair of edges parallel to the z-axis. A regular hexagonal

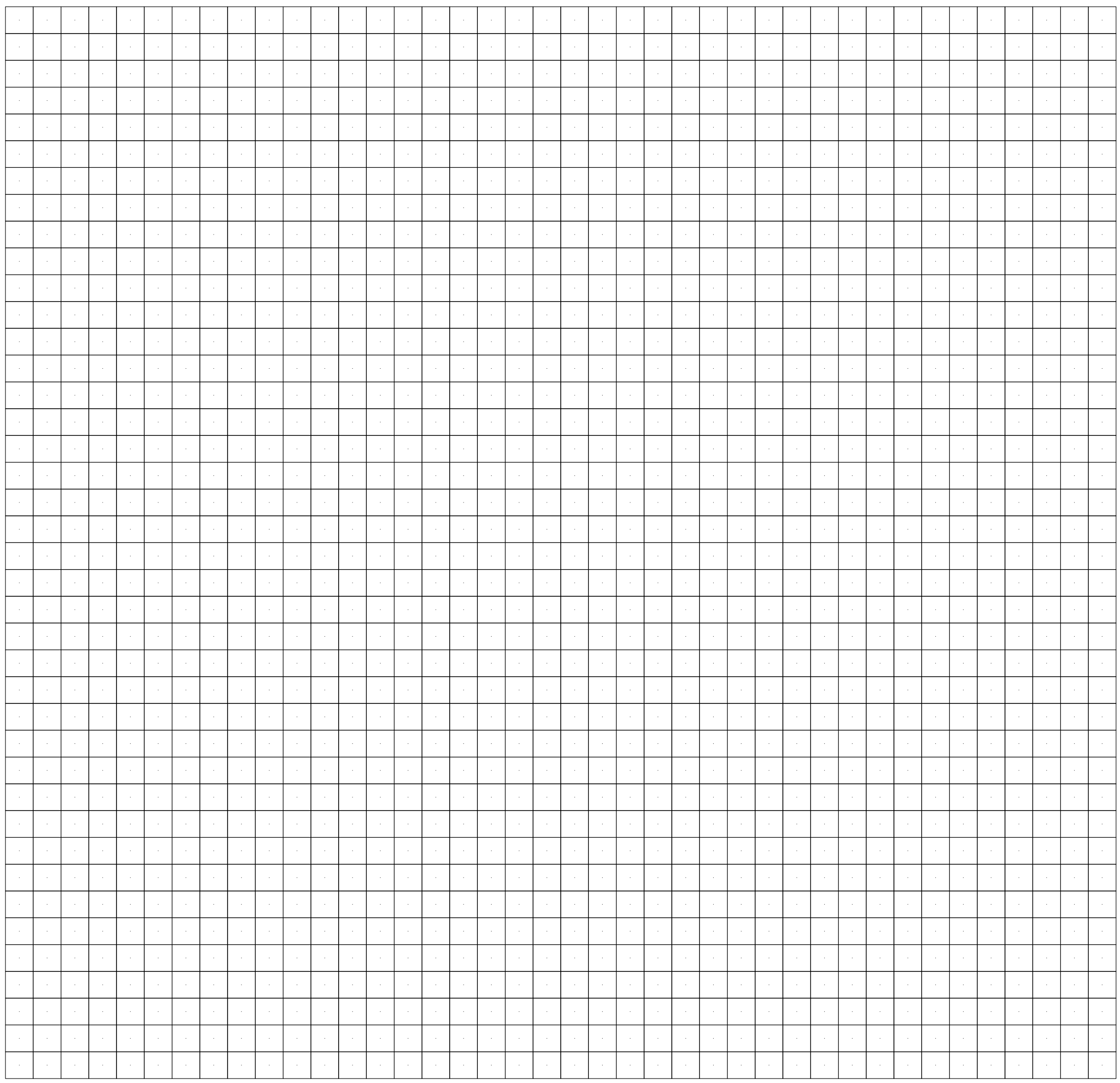

Figure 3.1: Rectangular grain structure

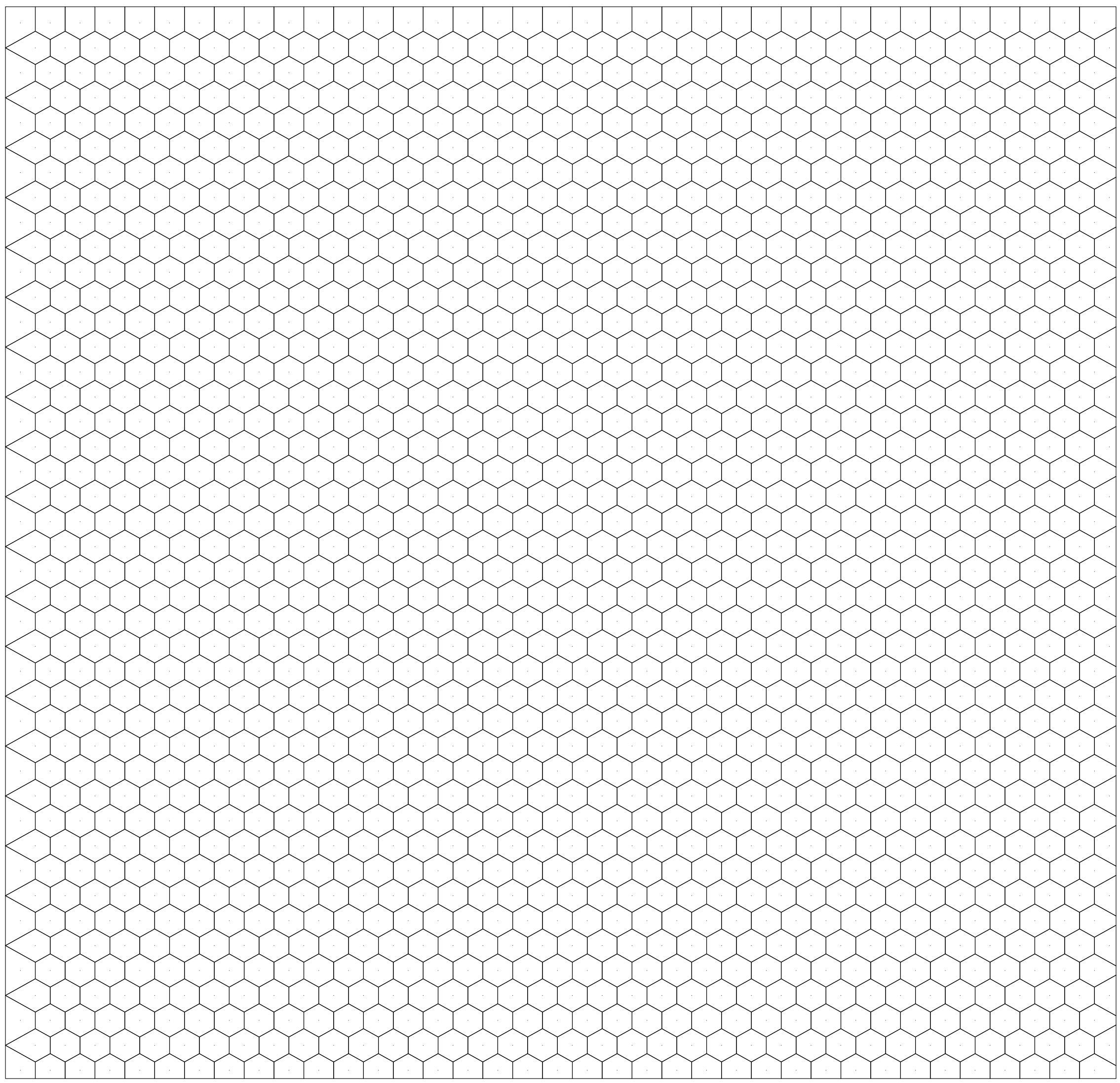

Figure 3.2: Hexagonal grain structure

grain geometry is completely specified by the value of the edge-to-edge diameter A of a single grain. In Figure 3.2, A is 53.7 nm and each grain (ignoring the irregularities at the edges) has an area of 2500 nm^2, same as the rectangular microstructure. The size of the recording medium patch depicted in Figure 3.2 is 2μm $\times$2μm.

A generalization to irregular structures is achieved by choosing a randomly dispersed set of initial points S. Thus a randomized microstructure may be generated, but because the Voronoi regions are computed, there is no issue of low packing density to resolve. In addition to irregular structure and high packing density, Voronoi regions are also an attractive grain model because they approximate the structure which results from crystal growth outward from nucleation sites represented by the points in S [31]. Fig. 3.3 depicts one set of randomized initial points and the resulting irregular Voronoi regions. By the definition of a Voronoi region, all the regions must be convex polygons. Therefore, the computation of the grain areas and the coordinates of the centroids can be achieved with standard algorithms of computational geometry [87]. It should be emphasized that for irregular grain structures the initial seed points do not correspond to the centroids of the Voronoi regions.

Implementation of the Voronoi region definition for grain geometry structures requires two stages of computation: generation of the initial set of points S and computation of the Voronoi diagram $\mathcal{V}(S)$ given S. An additional complication is that the medium represented in a computer program does not fill an entire plane; it is of limited extent. For simplicity, the portion of the medium plane actually represented in the computer implementation is a rectangular region with sides parallel to the x- and z- axes. This rectangular region, called a *bounding box*, is fully specified by the (x, z) coordinates of its lower left and upper right corners. The set of initial points S must be restricted to the bounding box, and the computed Voronoi diagram must be adjusted to coincide with the edges of the bounding box.

Generation of the points in S for rectangular or hexagonal grains is straightforward, given the values of X and Z, or A, as appropriate. For irregular grain structures, the points of S are generated by a Poisson point process with uniform density λ over the bounding box [109]. The value of λ is chosen to be the desired average density of grains in units of m^{-2}. The seed points depicted in Fig. 3.3 were generated with $\lambda = 4 \times 10^{14}$. The expected average grain area is 2500 nm^2. The whole medium patch depicted in Fig. 3.3 has dimensions 2μm $\times$2μm, and contains 1608 grains. After a set of seed points are generated according to a Poisson process with a uniform density, the set of points could be scaled in the x or z directions as

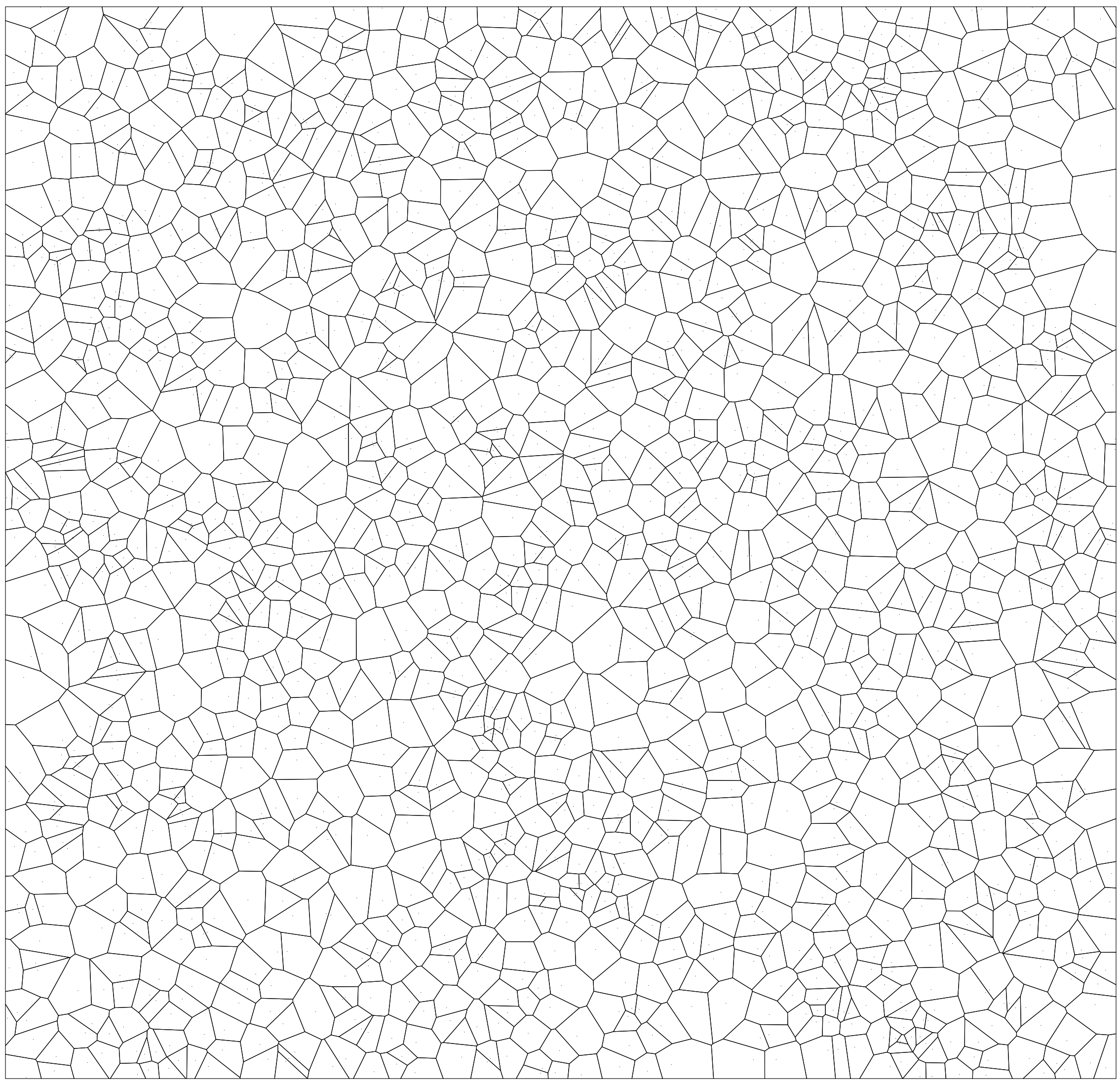

Figure 3.3: Irregular grain structure

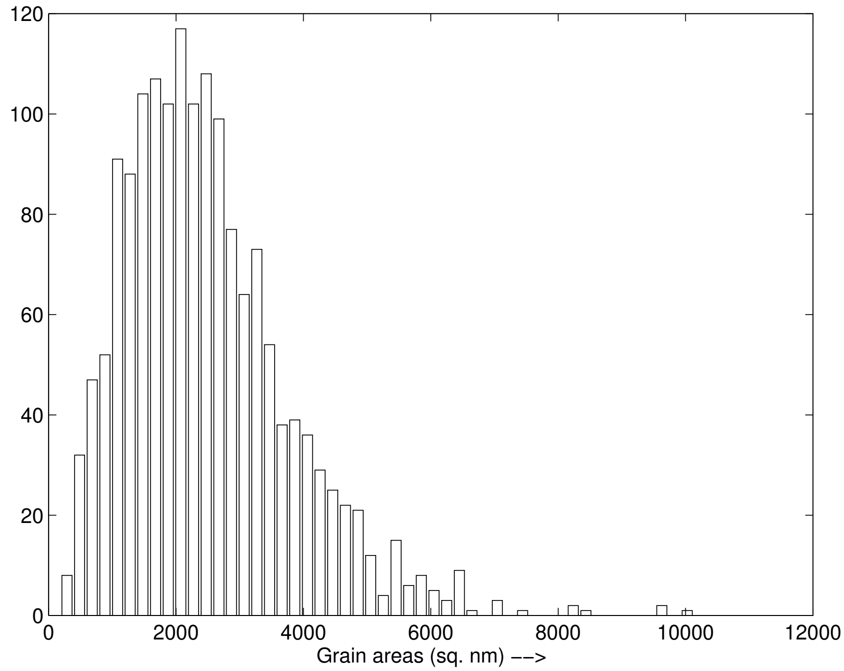

Figure 3.4: Irregular grain area histogram

desired to generate randomized grain structures which tend to be elongated in either of those two directions. Other adjustments to the seed points are also possible to yield desired properties such as limiting the aspect ratio of grains or constraining the number of nearest neighbors. In the absence of experimental evidence of such restrictions, or computational necessity to impose them, however, it is best not to make unwarranted assumptions.

Fig. 3.4 is a histogram of the areas of the irregular grains depicted in Fig. 3.3. The statistical properties of a Voronoi diagram computed from a Poisson set of initial points is an interesting and difficult problem in its own right. The means and variances of Voronoi diagram properties, including Voronoi region volume, have been derived [69, 31] for two and three dimensions. For our two-dimensional Voronoi diagram grain structure, the mean grain area is λ^{-1} and the variance of the grain area is $0.280 \times \lambda^{-2}$. The distribution of Voronoi region volume for a one-dimensional Voronoi diagram is an Erlang distribution. An expression for the form of the distribution in higher dimensions remains an open problem.

The computation of a planar Voronoi diagram from a set of initial points is a well-studied problem. One useful strategy transforms the initial planar set of seed points into three dimensions, computes the convex hull of the transformed set of points, and transforms the result back into the original plane. With the appropriate transformation, the result is the Delaunay triangulation of the original point set, the geometric dual of which is the Voronoi diagram [14]. Thus, if the three-dimensional convex hull problem has a solution, so does the planar Voronoi diagram problem. There is freely available software for computing convex hulls of points in spaces of arbitrary dimension, a common problem in the field of computational geometry. We make use of the `qhull` program from The Geometry Center at the University of Minnesota [7].

Finally, the problem of conforming the grain boundaries to the edges of the bounding box is solved by adding auxiliary points outside the bounding box which are "reflections" of initial points inside and near the bounding box boundary. This forces the Voronoi diagram to have boundaries which coincide with the bounding box. An iterative strategy guarantees that the final Voronoi diagram lies within the bounding box. The grain structures in Figures 3.1 through 3.3 have all been generated to fill a square bounding box with dimensions 2μm $\times 2\mu$m.

3.1.2 Orientation of Easy Axes

The orientation of the easy axis of the kth grain is completely determined by the value of θ_k, the angle the easy axis makes with the positive x-axis. A range of $-\frac{\pi}{2} < \theta_k \leq \frac{\pi}{2}$ is sufficient to account for all possible orientations of the easy axis in the plane of the medium. To represent the variability of easy axis orientation from one grain to the next and from one medium to the next, $\{\theta_k : k \in \mathcal{I}\}$ is taken to be a set of random variables with values fixed in the manufacture of the medium.

In order to represent statistical differences between manufacturing processes, each manufacturing process may be associated with a probability distribution from which the values of θ_k are drawn. One variation in manufacturing processes is the degree to which macroscopic orientation is induced. Previous micromagnetic simulations predict longitudinal recording performance is improved when easy axes are aligned more nearly parallel to the direction of a recorded track [128, 73]. Manufacturing processes which favor alignment of the easy axes with the track direction should be represented by a probability distribution on the θ_k which favors smaller values. Media manufactured in such a manner are known as *oriented* media.

A simple family of probability distributions for $\{\theta_k, k \in \mathcal{I}\}$ which permits the representation of varying degrees of oriented media is the following. Let each easy

Table 3.2: Microstructure generation parameters

		Parameter(s)	*Units*
Grain Geometry			
	Rectangular	X, Z	m
	Hexagonal	A	m
	Irregular	λ	m^{-2}
Orientation		ρ	-

axis orientation angle θ_k be drawn independently of all the others, and let all the orientation angles be drawn from a uniform distribution on the range,

$$-\frac{\rho\pi}{2} < \theta_k \leq \frac{\rho\pi}{2}, \tag{3.2}$$

where $0 \leq \rho \leq 1$ is a parameter which controls the degree of orientation of the medium. For $\rho = 0$, all easy axes are aligned parallel to the track direction. For $\rho = 1$, the easy axes are equally likely to point in any direction within the plane.

The microstructure generation methods described in this section determine the values of the model microstructure variables, $\{R_k, k \in \mathcal{I}\}$ and $\{\theta_k, k \in \mathcal{I}\}$. These variables take on different values, or *realizations*, for each medium represented by the model. However, several media created by the same manufacturing process do share the same values of the variables which govern the microstructure generation methods. These variables are summarized in Table 3.2 for the three different types of microstructure.

3.2 Karlqvist Head Response to Convex Polygonal Grains

Having established an implementation which generates grains which are guaranteed to be convex polygons, we may continue the derivation of the voltage signal generated by a Karlqvist read head in response to the magnetization pattern on the medium. Given a convex polygon and any point P in its interior, drawing the line segments from P to each vertex subdivides the polygon into triangles (see Fig. 3.5). Thus, if the Karlqvist head response to an arbitrary triangular grain can be derived, then the response to any convex polygon can also be determined.

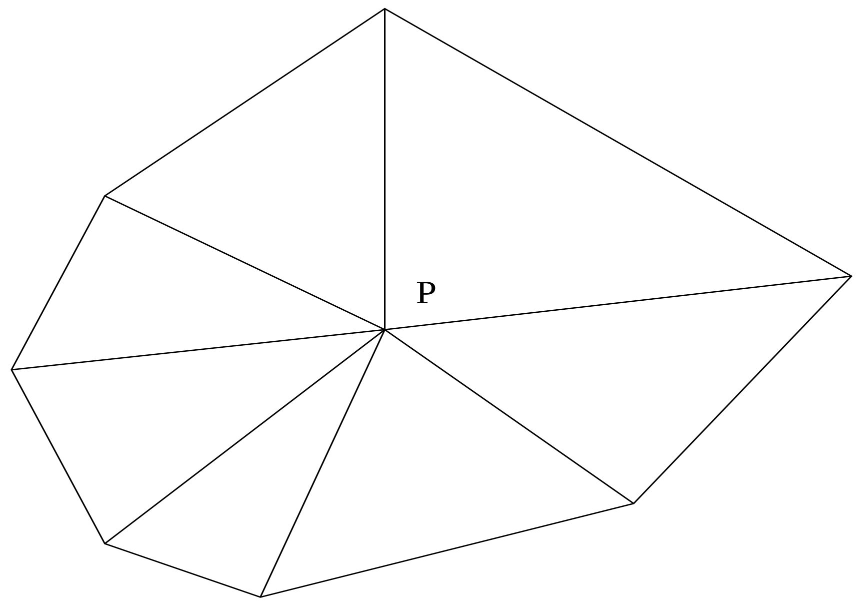

Figure 3.5: Subdivision of a convex polygonal grain into triangles

Let us reconsider the integral of (2.107), with the knowledge that the grain region R_k is a triangle. An arbitrary triangle is specified by the coordinates of its vertices (x_1, z_1), (x_2, z_2), and (x_3, z_3), with $x_1 < x_2 < x_3$. Fig. 3.6 depicts the two possible cases. As indicated by the vertical lines in Fig. 3.6, we may split the integral over the triangle into two integrals, one from x_1 to x_2, the other from x_2 to x_3. The first integral may be written, by the substitution $u = x - Vt$,

$$\int_{u_1}^{u_2} \int_{z_i(u)}^{z_f(u)} \frac{u\,du\,dz}{[C^2 + (D+u)^2][C^2 + (D-u)^2]}, \tag{3.3}$$

where $z_i(u)$ and $z_f(u)$ are the linear boundaries of the triangular region. For case (a) of Fig. 3.6,

$$z_i(u) = \frac{z_3 - z_1}{u_3 - u_1}(u - u_1) + z_1, \tag{3.4}$$

and

$$z_f(u) = \frac{z_2 - z_1}{u_2 - u_1}(u - u_1) + z_1. \tag{3.5}$$

For case (b), the expressions for $z_i(u)$ and $z_f(u)$ are reversed and the two cases differ only in sign. Simplification yields for the first integral

$$G \int_{u_1}^{u_2} \frac{u(u - u_1)du}{[C^2 + (D+u)^2][C^2 + (D-u)^2]}, \tag{3.6}$$

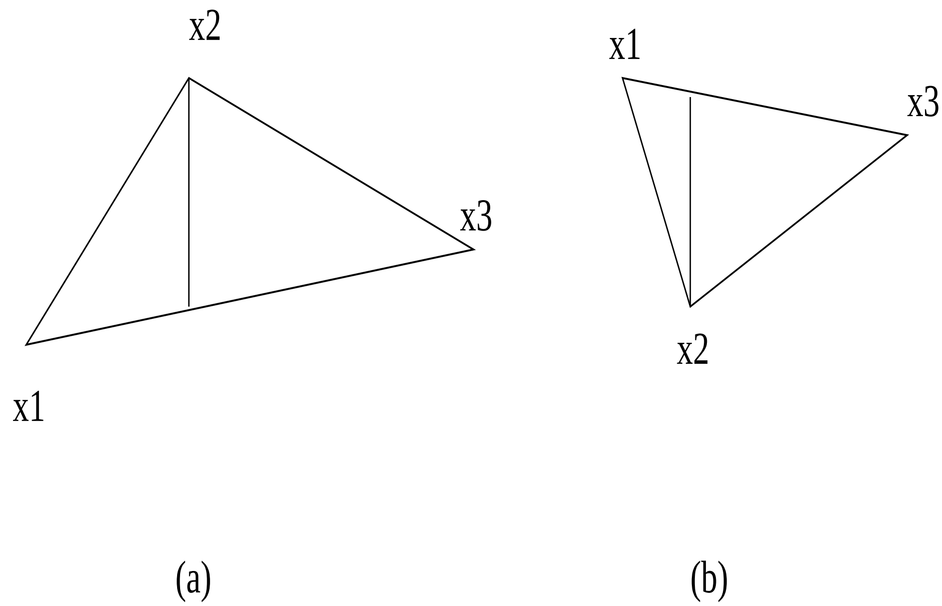

Figure 3.6: Two possible orientations of an arbitrary triangle

with

$$G = \pm \frac{x_1(z_3 - z_2) + x_2(z_1 - z_3) + x_3(z_2 - z_1)}{(x_3 - x_1)(x_2 - x_1)}, \tag{3.7}$$

where + applies in case (a) and − applies in case (b).

Similarly, the second integral equals

$$H \int_{u_3}^{u_2} \frac{u(u - u_3)du}{[C^2 + (D+u)^2][C^2 + (D-u)^2]}, \tag{3.8}$$

with

$$H = \mp \frac{x_3(z_1 - z_2) + x_2(z_3 - z_1) + x_1(z_2 - z_3)}{(x_1 - x_3)(x_2 - x_3)}, \tag{3.9}$$

where − applies in case (a) and + applies in case (b).

Both integrals have a common form,

$$\int \frac{u(u - \hat{u})du}{[C^2 + (D+u)^2][C^2 + (D-u)^2]}, \tag{3.10}$$

with anti-derivative

$$g(u : \hat{u}, C, D) = \frac{1}{4CD} \cdot \Big[(D - \hat{u}) \tan^{-1} \frac{u - D}{C} + (D + \hat{u}) \tan^{-1} \frac{u + D}{C}$$

$$+\frac{C}{2}\ln\left(C^2+(D-u)^2\right)-\frac{C}{2}\ln\left(C^2+(D+u)^2\right)\Big]. \quad (3.11)$$

The total integral is:

$$Gg(u_2:u_1,C,D)+Hg(u_2:u_3,C,D)-Gg(u_1:u_1,C,D)-Hg(u_3:u_3,C,D). \quad (3.12)$$

Close examination of (3.11) leads to a combination of the first two terms,

$$(G+H)g(u_2:\frac{Gu_1+Hu_3}{G+H},C,D)-Gg(u_1:u_1,C,D)-Hg(u_3:u_3,C,D) \quad (3.13)$$

and this may be further simplified to

$$(G+H)g(u_2:u_2,C,D)-Gg(u_1:u_1,C,D)-Hg(u_3:u_3,C,D). \quad (3.14)$$

In this expression, all three coefficients ($G+H$, $-G$, and $-H$) share a common form, and the expression may be rewritten:

$$\sum_{p=1}^{3}\kappa_p\hat{g}(x_p-Vt:C,D), \quad (3.15)$$

where

$$\kappa_p=\frac{x_p(z_{CCW(p)}-z_{CW(p)})+x_{CW(p)}(z_p-z_{CCW(p)})+x_{CCW(p)}(z_{CW(p)}-z_p)}{(x_{CCW(p)}-x_p)(x_p-x_{CW(p)})}, \quad (3.16)$$

and

$$\hat{g}(u:C,D)=4CDg(u:u,C,D). \quad (3.17)$$

In this formulation, the subscripts CW and CCW indicate the operations of moving one vertex clockwise and one vertex counter-clockwise respectively. In expressions below, the dependence of $\hat{g}$ on the parameters C and D is suppressed.

Substituting into (2.107) yields a formula for the voltage response of a Karlqvist head to a single triangular grain with magnetization direction given by the angle α,

$$v(t)=-\frac{\mu_0 VH_g\delta M_s}{\pi}\cos\alpha\sum_{p=1}^{3}\kappa_p\hat{g}(x_p-Vt). \quad (3.18)$$

Using the response of the Karlqvist head to a triangular grain as a building block, it is straightforward to sum the responses to all the triangles within one convex polygonal grain. The result has a satisfyingly simple form. Using the variable p to sum over *all* the vertices, V_k, of the kth polygonal grain, the voltage response of a Karlqvist head to a single polygonal grain with magnetization direction given by the angle α,

$$v(t) = -\frac{\mu_0 V H_g \delta M_s}{\pi} \cos\alpha \sum_{p \in V_k} \kappa_p \hat{g}(x_p - Vt). \tag{3.19}$$

Finally the total voltage response is computed by summing over all of the grains of the medium:

$$v(t) = -\frac{\mu_0 V H_g \delta M_s}{\pi} \sum_{k \in \mathcal{I}} \cos\alpha_k \sum_{p \in V_k} \kappa_p \hat{g}(x_p - Vt). \tag{3.20}$$

The foregoing analysis fails for those triangular grains where either $x_1 = x_2$ or $x_2 = x_3$, but handling these degenerate cases is straightforward with proper care. With this warning in mind, the appropriate formula for the regular rectangular or hexagonal grain structures may be derived. A medium made up of rectangular grains of length X and width Z generates a voltage signal response in a Karlqvist head according to

$$\begin{aligned} v(t) &= -\frac{\mu_0 V H_g \delta M_s Z}{\pi} \sum_{k \in \mathcal{I}} \cos\alpha_k \cdot \\ &\quad \left(f(x_k - \frac{X}{2} - Vt : C, D) - f(x_k + \frac{X}{2} - Vt : C, D) \right), \end{aligned} \tag{3.21}$$

where

$$f(u : C, D) = \tan^{-1}\frac{D - u}{C} + \tan^{-1}\frac{D + u}{C} \tag{3.22}$$

and the notation x_k refers to the x coordinate of the centroid of the kth rectangular grain. A medium made up of hexagonal grains of edge-to-edge diameter A with a pair of edges parallel to the z-axis generates a voltage signal response in a Karlqvist head according to

$$\begin{aligned} v(t) &= -\frac{2\mu_0 V H_g \delta M_s}{\pi\sqrt{3}} \sum_{k \in \mathcal{I}} \cos\alpha_k \cdot \\ &\quad \left(2\hat{g}(x_k - Vt) - \hat{g}(x_k - \frac{A}{2} - Vt) - \hat{g}(x_k + \frac{A}{2} - Vt) \right), \end{aligned} \tag{3.23}$$

where the notation x_k refers to the x coordinate of the centroid of the kth hexagonal grain.

3.3 Calculation Truncation

When a computer simulation is required to sum a large number of terms to compute a quantity of interest, great efficiency gains are possible by truncating the summations so as to only include those terms which have a significant effect on the total. Often a large number of terms, all having small magnitude, may be omitted, yielding a result with only a small approximation error at a great savings of computational resources. Two computations so far described may take advantage of this strategy: the summation of field components from all grains in the medium when computing a magnetostatic field, and the summation of voltage response components from all grains in the medium when computing the Karlqvist response.

3.3.1 Magnetostatic Field Calculation

Efficient computation of the magnetostatic field is one of the key problems of micromagnetic modeling. Efficiency is of great importance because this calculation is repeated frequently. Several strategies have been proposed in past modeling work, including spatial frequency domain methods [61, 62], hierarchical mean field approximations [75], and truncation of the calculation to sum only over those grains within a limited radius of the grain under study [131]. Our use of irregular grain geometry makes the last of these options the most practical. In this section, we derive a reasonable strategy for setting the value of the radius limit on the computation of the magnetostatic field.

The formula for the magnetostatic field component arising from a dipole, (2.12), shows that the magnitude of the field component contribution decreases with the cube of the distance. Furthermore, the magnitude of the field component contribution from the differential medium element $R\,dR\,d\theta$ is bounded,

$$|\mathbf{H}_m(R,\theta)| \leq \frac{M_s \delta R\,dR\,d\theta}{2\pi R^3}. \tag{3.24}$$

Therefore, even in the unlikely event that all source dipoles are oriented so as to maximize the magnetostatic field at the point under study, the magnitude is bounded

$$|\mathbf{H}_m| \leq \frac{M_s \delta}{2\pi} \int \frac{dR\,d\theta}{R^2}. \tag{3.25}$$

where the integral is over the region of source dipoles of interest.

Let us consider the maximum magnitude of magnetostatic field component that may arise from source dipoles at a distance from the point of interest greater than a limiting radius R_L. Solving the integral yields

$$|\mathbf{H}_m| \leq \frac{M_s \delta}{R_L}. \tag{3.26}$$

As the limiting radius increases, the bound on the approximation error becomes arbitrarily small. This analysis establishes that imposing a radial limit on the calculation of magnetostatic fields is a sensible strategy for a planar medium model.

The simulation programs which compute the magnetostatic field are coded so that the user may select the value of the calculation radius R_L. A good choice for the value of R_L should be large enough to keep the approximation error small, but small enough to keep the number of source dipoles for each computation small. One criterion for selecting R_L is to guarantee that the approximation error is kept smaller than a given fraction ϵ of the anisotropy field H_K [see (2.54)]. This criterion leads to the prescription

$$R_L > \frac{\mu_0 \delta M_s^2}{2\epsilon K_A}. \tag{3.27}$$

Because this analysis considers an unlikely worst case scenario, in practice a relatively modest value of $\epsilon = 0.1$ is sufficient for good approximation error control.

Because the medium magnetization is modeled by grains, the calculation radius limitation is implemented based on the location of the centroid of the grain. A grain is included in the field calculation if and only if its centroid is within the calculation radius. In order for the above analysis (which ignores granularity) to apply, the radius limit must include at least a few grain lengths. When no calculation radius is specified by the user, a default value for R_L is set to the be the larger of the value given in (3.27) with $\epsilon = 0.1$ and three times the square root of the average area of a grain.

In previous work [91, 95], the effect of truncating the calculation of magnetostatic fields was considered empirically. In a special case where the grains are all squares, truncation errors were found to be negligibly small when a 17×17 grid of grains was used to compute the magnetostatic field at the center grain of the grid. This roughly corresponds to a calculation radius of nine grain widths. Given the other model parameters of that study, the corresponding value of $\epsilon = 0.54$. The approach presented here is preferred for several reasons. It is a worst case analysis rather than a typical or average case analysis, so it is more conservative in its protection against errors. This explains why empirical typical case observations lead to acceptance of such a large value of ϵ. It is quantitative rather than depending on some vague judgment of "negligibly small" error. It includes whole ranges of values for model parameters rather than requiring more empirical observations for each new choice of parameter values. Finally, it includes a "tuning" parameter ϵ so that a variety of truncation options may be easily tried. One shortcoming of this approach is that it can in practice be too conservative, tending to err on the side of long computation times rather than admitting larger, yet perfectly acceptable, calculation errors. This is especially the case when the value of K_A is small. K_A does not enter directly into the calculation of the magnetostatic field. It only determines the relative size of the anisotropy field, and together with ϵ determines the quality standard which the truncated calculation must meet. For this reason, it may help in practice to raise the value of ϵ when performing simulations on media with small values of K_A.

Recalculation of the magnetostatic field values is most frequent in programs which simulate a relaxation process. As the medium progresses through a sequence of magnetic states, it is necessary to compute the corresponding sequence of magnetostatic field values. Additional efficiency is attained by controlling the nature of the evolution of magnetic states. In both relaxation models discussed in Section 2.1.3, the magnetic state of the medium is changed only one grain at a time. Furthermore, the magnetostatic field values are a linear function of the magnetic state. Thus, the change in the magnetostatic field values is a linear function of the change in the magnetic state. Because the magnetic state changes in only one state variable at a time, the change in the magnetostatic field values is a function of only the change of the magnetic state of a single grain. Updating the magnetostatic field values by this differential strategy is far more efficient than a full recalculation of the fields at each relaxation step.

3.3.2 Karlqvist Head Footprint

Each formula [(3.20),(3.21),(3.23)] derived for the voltage response of a Karlqvist head at time t includes a summation over all grains in the medium. The voltage calculation can be made more efficient by limiting the sum to only those grains which are nearest to the position of the head at time t. We call the region of the medium nearest the head which contributes to the voltage calculation the *footprint* of the head. For simplicity, we consider the head footprint to be the set of grains which have centroids within a rectangular window centered at the head location. The footprint is completely specified by the length and width of the rectangular window.

The width of the window is selected to represent the width of the head. Thus, the width of the corresponding footprint represents the width of the track read by the head. Because the footprint is composed of whole grains, its boundary may be irregular. In particular the edge of the track may be irregular. Because the Karlqvist model does not properly account for the track edge effects of reading, any irregularity of the track edge causes artifacts in the computed voltage signal. These artifacts may be avoided by selecting the footprint width to cover the entire bounding box of the medium patch under simulation.

The length of the window is selected to yield an acceptable approximation error. For the sake of analysis, we consider the case of rectangular grains, consistent with the implicit assumptions of the literature on the Karlqvist head model. Compare (3.22) to (2.98) to see that

$$f(u : d + \delta/2, g/2) = \frac{\pi}{H_g} h_x(u, d + \delta/2). \tag{3.28}$$

Therefore (3.21) may be written,

$$\begin{aligned} v(t) &= -\mu_0 V \delta M_s Z \sum_{k \in \mathcal{I}} \cos \alpha_k \cdot \\ &\quad \left(h_x(x_k - \frac{X}{2} - Vt, d + \delta/2) - h_x(x_k + \frac{X}{2} - Vt, d + \delta/2) \right). \end{aligned} \tag{3.29}$$

In this form, the structure is apparent. Each rectangular grain contributes two pulses h_x, one arising from its leading edge, the other from its trailing edge. The Karlqvist sensitivity function h_x is the step response of the head. An alternative form of the Karlqvist sensitivity function may be verified by a straightforward geometric analysis [60, p. 49],

$$h_x(x, y) = \begin{cases} \frac{H_g}{\pi} \tan^{-1} \left[\frac{yg}{x^2+y^2-(g/2)^2} \right], & x^2 + y^2 > (g/2)^2 \\ \frac{H_g}{2}, & x^2 + y^2 = (g/2)^2 \\ H_g + \frac{H_g}{\pi} \tan^{-1} \left[\frac{yg}{x^2+y^2-(g/2)^2} \right], & x^2 + y^2 < (g/2)^2 \end{cases} \tag{3.30}$$

From this expression, the half-angle formula for the tangent function may be used to determine the pulse width at half height [72],

$$PW_{50}^2 = g^2 + (2d+\delta)^2. \tag{3.31}$$

Likewise, the width of the pulse at any arbitrary fraction ϵ of the pulse amplitude may be calculated,

$$PW_{\epsilon}^2 = \frac{2g(2d+\delta)}{\tan\left[\epsilon \tan^{-1}\left(\frac{2g(2d+\delta)}{(2d+\delta)^2 - g^2}\right)\right]} + g^2 - (2d+\delta)^2. \tag{3.32}$$

In order to compute the voltage response of the Karlqvist head with approximation error controlled by ϵ, a footprint length of $PW_{\epsilon} + X$ should be used. For non-rectangular grains, X is replaced with the appropriate value to describe a typical grain length. A default value of $\epsilon = 0.01$ yields voltage responses without visible artifacts.

Finally, an alternative strategy for computing playback waveform responses in a Karlqvist head should be mentioned. From the reciprocity relationship expressed in medium coordinates (2.94), and the simplifications permitted by the Karlqvist head model, we may express the playback voltage as a correlation integral,

$$v(t) = -\mu_0 \delta \int_{-\infty}^{\infty} \left(\frac{d}{dt} h_x(x - Vt, d + \delta/2)\right) \cdot \left(\int_W M_x(x,z)dz\right) dx. \tag{3.33}$$

The z-integral integrates over the width of the recorded track. The result of the z-integral is a magnetization profile like those illustrated in Figures 1.2 and 1.3. Samples of the magnetization profile are easy to calculate accurately for a granular model, and can be calculated for any choice of track width. Proceeding in this manner, we can avoid the track edge artifacts mentioned earlier. However, the subsequent correlation integral must then be performed using only the samples of the magnetization profile. So long as the samples are spaced closely enough, the accuracy can be made arbitrarily good. Unless track edge artifacts are an issue, however, the direct calculation is preferred so as to avoid consideration of sampling issues. Programs have been implemented using both strategies so that either may be selected as appropriate.

3.4 Rotation Relaxation Implementation

Section 2.1.3 began a discussion of algorithms for computing the evolution of the model's magnetic state. In this section, we continue that discussion and include consideration of the implementation details. Three objectives of a magnetic state evolution algorithm were identified in Section 2.1.3:

1. Physical plausibility.
2. Computational efficiency.
3. Potential for either success or failure in matching experiments.

The first of these objectives was further defined by two conditions on the state trajectories generated by any state evolution algorithm called a *relaxation*:

1. The trajectories are continuous.
2. The trajectories have monotonically decreasing total magnetic energy.

3.4.1 Stable States vs. Local Energy Minima

As noted before, any local minimum of total magnetic energy must be a stable state of any relaxation algorithm. However, additional constraints of the relaxation algorithm may lead to additional stable states which are not local minima of total magnetic energy. For example, flip-relaxation algorithms constrain the magnetic state from one algorithm step to the next to have all grain magnetizations aligned with easy axes. In these magnetic states there may be non-zero torques, leading to a physical interpretation that the magnetizations should rotate off the easy axes. However, unless a complete reversal of magnetization is possible under the monotonic decrease of total magnetic energy constraint, these changes will not occur under a flip-relaxation algorithm. Thus, fixed points of the relaxation may not be local minima of total magnetic energy. More generally, any relaxation algorithm, including rotation-relaxation should be carefully examined to determine whether there are stable states of the algorithm which are not local minima of total magnetic energy.

This distinction between stable states of a relaxation algorithm and local minima of total magnetic energy is important in evaluating physical plausibility. The physics of a conservative field can be described in terms of potential energy minimization. Physical forces are described as negative gradients of energy surfaces, and they act to move a physical system through its state space until a local minimum of the energy surface is reached. This perspective views Mother Nature as a great Solver of optimization problems. From this perspective, a more stringent requirement for physical plausibility of a relaxation algorithm would include a requirement that any stable state would be (or be "sufficiently close to") a local minimum of total magnetic energy. Indeed it is on grounds similar to these that we judge flip-relaxation algorithms to be less physically plausible than rotation-relaxation algorithms. The former may leave the model in a state with non-zero torques, clearly not a local minimum. The latter minimize N objective functions, each of a single variable. It must still be considered whether this is sufficient to guarantee a local minimum of the total magnetic energy.

Under a rotation-relaxation algorithm, the magnetic state of the model is expressed with N variables $\{\alpha_k, k \in \mathcal{I}\}$ representing the angles of each grain's magnetization with respect to the x-axis. The total magnetic energy of our model, W, is a continuous function of those N variables with continuous derivatives of all orders. A local minimum, $\underline{\alpha}^*$, of a function, W, with these properties must meet two necessary conditions:

1. The gradient evaluated at $\underline{\alpha}^*$ must be zero.

2. The matrix of second derivatives, known as the *Hessian* matrix, evaluated at $\underline{\alpha}^*$ must be non-negative definite.

The components of the gradient in our model are the torques,

$$\mathcal{T}_k = \frac{dW}{d\alpha_k} = 2K_A\mathcal{A}_k\delta\left(m_{\|,k}m_{\perp,k} + h_{\|,k}m_{\perp,k} - h_{\perp,k}m_{\|,k}\right) \tag{3.34}$$

$$= 2K_A\mathcal{A}_k\delta\frac{\partial}{\partial\alpha_k}\mathcal{F}_k(\alpha_k). \tag{3.35}$$

Since the stable states of rotation-relaxation are those states which simultaneously minimize all the objective functions $\mathcal{F}_k(\alpha_k)$, each derivative $\frac{\partial}{\partial\alpha_k}\mathcal{F}_k(\alpha_k)$, must be zero-valued at a stable state. Therefore, the stable states of a rotation-relaxation algorithm meet the first necessary condition of a local energy minimum.

Let us now consider the Hessian matrix, $\mathcal{Q}$. First the diagonal entries,

$$\mathcal{Q}_{kk} = \frac{\partial}{\partial\alpha_k}\mathcal{T}_k = 2K_A\mathcal{A}_k\delta\left(m_{\|,k}^2 - m_{\perp,k}^2 + h_{\|,k}m_{\|,k} + h_{\perp,k}m_{\perp,k}\right) \tag{3.36}$$

$$= 2K_A\mathcal{A}_k\delta\frac{\partial^2}{\partial\alpha_k^2}\mathcal{F}_k(\alpha_k). \tag{3.37}$$

Then the off-diagonal entries,

$$\mathcal{Q}_{kl} = \frac{\partial}{\partial \alpha_l}\mathcal{T}_k = -\mu_0 M_s^2 \mathcal{A}_k \delta \begin{bmatrix} -m_\perp & m_{\|} \end{bmatrix}_k \mathbf{G}_{kl} \begin{bmatrix} -m_\perp \\ m_{\|} \end{bmatrix}_l, \tag{3.38}$$

where the matrix $\mathbf{G}_{kl}$ is

$$\mathbf{G}_{kl} = \begin{bmatrix} \cos\theta_k & \sin\theta_k \\ -\sin\theta_k & \cos\theta_k \end{bmatrix} (\mathbf{A}_{m,kl} + \mathbf{A}_{e,kl}) \begin{bmatrix} \cos\theta_l & -\sin\theta_l \\ \sin\theta_l & \cos\theta_l \end{bmatrix}, \tag{3.39}$$

so that the normalized local fields arise from the applied field and other normalized magnetizations according to

$$\begin{bmatrix} h_{\|} \\ h_\perp \end{bmatrix}_k = \begin{bmatrix} h_{\|} \\ h_\perp \end{bmatrix}_{a,k} + \frac{\mu_0 M_s^2}{2K_A}\sum_l \mathbf{G}_{kl}\mathbf{m}_l. \tag{3.40}$$

Since the stable states of rotation-relaxation simultaneously minimize all the objective functions $\mathcal{F}_k(\alpha_k)$, each second derivative $\frac{\partial^2}{\partial \alpha_k^2}\mathcal{F}_k(\alpha_k)$, must be non-negative at a stable state. This means the diagonal entries of the Hessian matrix at a stable state are non-negative. It is a necessary condition for a non-negative definite matrix that it have non-negative diagonal entries.

However, it is not sufficient. In general, a Hessian matrix may have all non-negative diagonal entries, yet not be non-negative definite. To visualize this possibility, consider an energy surface over two independent variables. The two variables represent two orthogonal directions on the surface. A zero-valued gradient and positive diagonal entries of the Hessian matrix mean that in each of these orthogonal directions, the energy surface is concave upward, indicating that the current state is a local minimum. However, in a direction other than those representing single variable variations, the function may be concave downward. Thus, there may be states in a neighborhood of the current state which have less energy. Stated another way, a stable state of rotation-relaxation, with zero-valued gradient and non-negative diagonal entries of the Hessian matrix, might not be a local minimum. Instead, it could be a saddle point with concave downward curvature in a direction corresponding to simultaneous change of more than one variable. This possibility of a stable state which is not a local energy minimum exists because of the algorithm constraint that only one magnetization change at a time. This objection to the local field approach is raised by Brown [15], who presents examples in which a stable state of a rotation-relaxation algorithm is not a local minimum of total magnetic energy. He cautions that because of this possibility, rotation-relaxation algorithms may tend to overestimate coercivity values. For greater physical plausibility, one should pay the price in computation to permit simultaneous changes of magnetization of several grains at once. However, this price should only be paid if it truly makes a difference. In the following chapter, we will investigate the degree to which physical plausibility of our rotation-relaxation algorithms is undermined by the possibility of stable states which are not local minima.

Heeding Brown's warning, Hughes has developed a micromagnetic model [41] which permits the simultaneous rotation of all grain magnetizations. At each state, (defined by $\{\alpha_k\}$ in the notation of our model), a local approximation to the energy function by a quadratic function is made. The quadratic approximation is based on a second-order Taylor series expansion, and includes the torque vector and the Hessian matrix. With this approximation, a method of conjugate directions is used to compute increments, $\{\delta\alpha_k\}$, so that the new state, $\{\alpha_k + \delta\alpha_k\}$, minimizes the quadratic energy function. In order to maintain the validity of the quadratic approximation, a penalty on large increments is imposed if a non-penalized computation yields an increment greater than 0.1 radians in any angle. The minimization procedure is stopped when all normalized torque values are near zero (absolute value less than 0.001).

3.4.2 Determinism of Trajectories

We have been representing the natural evolution of our micromagnetic model as a trajectory through its state space. The minimal conditions on a relaxation algorithm require that the trajectory exhibit monotonic decrease of total magnetic energy. In terms of our energy surface visualization, the trajectory must always proceed "downhill." It is common to place more stringent requirements on dynamic models of physical systems. The usual viewpoint is that natural evolution involves the simultaneous response of each grain's magnetization to its local field. Within the constraints of the model, this means the simultaneous rotation of each grain magnetization vector in response to the local torque. In other words, the trajectory follows the gradient of the energy surface.

Such an additional constraint would disallow the single-grain variation approach we have adopted in rotation-relaxation. The trajectory cannot follow the gradient if it is constrained to follow paths in which only one grain magnetization changes. Thus, if it is determined that physical plausibility demands the trajectory of magnetic state evolution follow the gradient, then we must abandon the computational efficiency of representing magnetic state evolution as a sequence of steps in each of which a single grain changes its magnetization.

Also, if the constraint that the trajectory follow the gradient is accepted, then at any state where the gradient is not zero, the next differential piece of the trajectory is well-defined and determined. So long as the trajectory does not pass through one of the non-minimum critical points of the magnetic energy function, the trajectory is uniquely determined by its initial state, and it terminates in a unique minimum. A state evolution algorithm which accepts this constraint is a deterministic function mapping initial states to local energy minima.

Is a deterministic algorithm a good choice to represent the evolution of magnetic state? A comparison with experimental measurements at first glance suggests that it is. As discussed in Section 1.4, when the same magnetic pattern (magnetic state) is written at the same position on a recording medium (same microstructure) a number of times, the measured medium noise waveforms are highly correlated. A simulation of these experiments with a deterministic state evolution algorithm would yield identical medium noise waveforms every time the simulation is run. Identical waveforms are indeed highly correlated; they are perfectly correlated! However, note that we can predict this result without ever running a simulation. Perfect repeatability is designed into the model by selection of a deterministic state evolution algorithm. It is not an emergent feature which could validate or invalidate the model. The fact of repeatability of medium noise waveforms is a given, and observation of that result alone reveals nothing about the magnetic energy function of the model under study. Therefore, a deterministic algorithm for state evolution fails to meet our third objective for a state evolution algorithm, potential for both success and failure.

For these reasons, we have chosen not to require relaxation algorithms to follow the energy gradient. Instead they are required only to obey the constraint of monotonic decrease of total magnetic energy. Within this constraint, a single initial state may evolve to any of a number of stable states which can be reached following a trajectory of monotonic decrease of total magnetic energy. If such a model nevertheless predicts a high degree of correlation among medium noise waveforms, that result is remarkable. It is evidence that such a model may be a reasonable representation of the physical recording system. Likewise, a model which did not exhibit such repeatability of medium noise could be rejected as unsuitable. Because the degree of repeatability of medium noise could range over a continuum of values given such a model, the actual degree of repeatability generated by simulation could be used in the identification of model parameters. Furthermore, depending on what constraints are placed on the energy-minimization algorithm, the set of final stable states reachable from a single initial state in a sequence of simulations can reveal information about the nature of the total magnetic energy function of the system.

The simplest way to introduce non-determinism into rotation-relaxation algorithms is to let the sequence in which the grain magnetizations are selected for updating be pseudo-random. Random selection of a number from a range of integers is a common task on computers, and is easily implemented. Variability from one simulation to another is provided by initializing the random number generator with a value taken from the microseconds field of the computer's system clock. Forced repeatability is also provided for by allowing the user to specify the random number generator seed. When started with the same seed, a random number generator will produce the same "random" sequence.

3.4.3 Verification of Monotonic Energy Decrease

The minimal requirements established for a relaxation algorithm require that it generate a continuous trajectory with monotonic decrease of total magnetic energy. A computer algorithm cannot literally generate a continuous path, however. Computers operate in discrete time and must represent trajectories as a sequence of discrete states. The additional constraint of rotation-relaxation is that only one grain magnetization may change at a time. Therefore, each state in the sequence of discrete states representing a trajectory generated by a rotation-relaxation algorithm must differ from its successor in only one variable. The trajectory from the discrete state $\underline{\alpha}(t)$ to discrete state $\underline{\alpha}(t+1)$ in the state sequence is one of continuous rotation of the single variable, say α_k, in which the two states differ. The constraint that the whole trajectory be one of monotonic decrease in total magnetic energy may then be restated as a constraint that every piece of the trajectory between two discrete states in the sequence must be one of monotonic decrease in total magnetic energy.

At time t, let the kth grain be selected for updating. The kth grain's magnetization makes an angle $\alpha_k(t)$ with the x-axis. To complete this step of the algorithm, a new magnetization angle $\alpha_k(t+1)$ must be found so that there is a continuous rotation from $\alpha_k(t)$ to $\alpha_k(t+1)$ which represents a trajectory of monotonically decreasing energy and $\alpha_k(t+1)$ is a local minimum of the objective function $\mathcal{F}_k(\alpha_k)$.

As discussed in Section 2.1.3, the objective function $\mathcal{F}_k(\alpha_k)$ has either one or two local minima, depending on whether the local field exceeds the Stoner-Wohlfarth astroid. With the local field outside the astroid, there is only one local minimum, so there is no issue to consider whether monotonic decrease of energy is obeyed. All rotations lead to the single local minimum. With the local field within the astroid, there are two minima, and the appropriate one must be selected to obey the monotonic energy decrease constraint. Before we consider the details of making that selection, let us consider a method for solving for the local minima of the objective function.

As noted in Section 2.1.3, the objective function may be expressed in terms of vector components of magnetization (2.65),

$$\mathcal{F}_k(\mathbf{m}_k) = \frac{1}{2}m_{\perp,k}^2 - h_{\|,k}m_{\|,k} - h_{\perp,k}m_{\perp,k}. \tag{3.41}$$

A value of $\mathbf{m}_k$ is sought to minimize $\mathcal{F}_k(\mathbf{m}_k)$ subject to the constraint,

$$m_{\|,k}^2 + m_{\perp,k}^2 = 1. \tag{3.42}$$

This problem may be solved using Lagrange multiplier techniques. The k subscripts will be suppressed, as they are arbitrary and understood. The Lagrangian is

$$L(m_\|, m_\perp, \lambda) = \frac{1}{2}m_\perp^2 - h_\| m_\| - h_\perp m_\perp + \lambda\left(m_\|^2 + m_\perp^2 - 1\right), \tag{3.43}$$

leading to a system of equations to be solved,

$$\begin{aligned} \frac{\partial L}{\partial m_\|} &= -h_\| + 2\lambda m_\| = 0 && (3.44)\\ \frac{\partial L}{\partial m_\perp} &= -h_\perp + h_\perp + 2\lambda m_\perp = 0 && (3.45)\\ \frac{\partial L}{\partial \lambda} &= m_{k,\|}^2 + m_{k,\perp}^2 - 1 = 0. && (3.46) \end{aligned}$$

An equivalent system is

$$m_\| = \frac{h_\|}{2\lambda} \tag{3.47}$$

$$m_\perp = \frac{h_\perp}{2\lambda + 1} \tag{3.48}$$

$$f(\lambda) = 16\lambda^4 + 16\lambda^3 + 4(1 - h_\|^2 - h_\perp^2)\lambda^2 - 4h_\|^2\lambda - h_\|^2 = 0. \tag{3.49}$$

It is readily apparent that all the work is in finding the real roots of a fourth order polynomial in λ, $f(\lambda)$. From our previous analysis of the objective function, we know that there will be four real roots when the local field is within the Stoner-Wohlfarth astroid, yielding four critical points including two local minima and two local maxima. Likewise, for local field values exceeding the Stoner-Wohlfarth astroid, there will be only two real roots. Unfortunately, the polynomial does not factor in general. It can be written in an alternative form, however,

$$f(\lambda) = (2\lambda - h_\|)(2\lambda + h_\|)[2\lambda + (h_\perp + 1)][2\lambda - (h_\perp - 1)] - h_\|^2 h_\perp^2 = 0, \tag{3.50}$$

which allows for direct solution if either $h_\| = 0$ or $h_\perp = 0$. In either case the four roots may be written,

$$\lambda_1^* = -\frac{1}{2} - \frac{|h_\perp|}{2} \tag{3.51}$$

$$\lambda_2^* = -\frac{1}{2} + \frac{|h_\perp|}{2} \tag{3.52}$$

$$\lambda_3^* = -\frac{|h_\||}{2} \tag{3.53}$$

$$\lambda_4^* = \frac{|h_\||}{2}. \tag{3.54}$$

So long as

$$|h_\|| + |h_\perp| < 1, \tag{3.55}$$

the roots are ordered,

$$\lambda_1^* \leq \lambda_2^* < \lambda_3^* \leq \lambda_4^*. \tag{3.56}$$

For all local fields within the Stoner-Wohlfarth astroid this ordering is valid.

When neither $h_\|$ nor $h_\perp$ is zero-valued, it is still true for any $1 \leq \nu \leq 4$ that

$$f(\lambda_\nu^*) = -h_\|^2 h_\perp^2 < 0. \tag{3.57}$$

Given these points as landmarks, and the "W" shape of a fourth order polynomial, we can determine ranges in which the actual roots, λ_1 through λ_4 must lie. When the local field exceeds the Stoner-Wohlfarth astroid, the inner peak of the "W" is negative, and only λ_1 and λ_4 are roots. When the field is within the Stoner-Wohlfarth astroid, the actual roots obey

$$\lambda_1 \leq \lambda_1^* \leq \lambda_2^* \leq \lambda_2 \leq \lambda_3 \leq \lambda_3^* \leq \lambda_4^* \leq \lambda_4. \tag{3.58}$$

Careful examination reveals that roots λ_1 and λ_2 correspond to local maxima and roots λ_3 and λ_4 correspond to local minima. The local minimum corresponding to λ_4 is the one which remains even for fields exceeding the Stoner-Wohlfarth astroid, so it must be the local minimum in the same half plane as the local field. Solving for the local minimum of the objective function means deciding which root, λ_3 or λ_4 is appropriate, solving for the appropriate root numerically and substituting into (3.47) and (3.48) to compute the local minimum values of $m_{||}$ and $m_{\perp}$. These could in turn yield a value for α, but for purposes of computer simulation, the vector components contain the same information and avoid expensive forward and inverse trigonometric computations.

Solving for either λ_3 or λ_4 is straightforward given the limits on the intervals in which they must lie. A simple strategy of dividing the interval in half and using evaluation of $f(\lambda)$ and its derivative to determine which half to keep converges to a solution quickly. The roots must be computed to a precision of 0.0001 so that the corresponding vector components $m_{||}$ and $m_{\perp}$ describe a vector with magnitude 1.00 ± 0.01. The effect of this precision may be investigated, as it has been implemented to be user-selectable.

Selecting between λ_3 and λ_4 is also straightforward, though the selection algorithm takes several lines to describe. First, if the local field is outside the Stoner-Wohlfarth astroid, only λ_4 is a root, and it corresponds to the sole local minimum. If the local field is within the Stoner-Wohlfarth astroid, we must select with care. The selection is best described with reference to Figure 3.7. The arrow out from center of the circle represents the local field. The axes are the easy (horizontal) and hard (vertical) axes. The circle represents the space of possible values of the magnetization. The dashed lines are

$$m_{\perp} = h_{\perp} \tag{3.59}$$

and

$$m_{||} = -h_{||}, \tag{3.60}$$

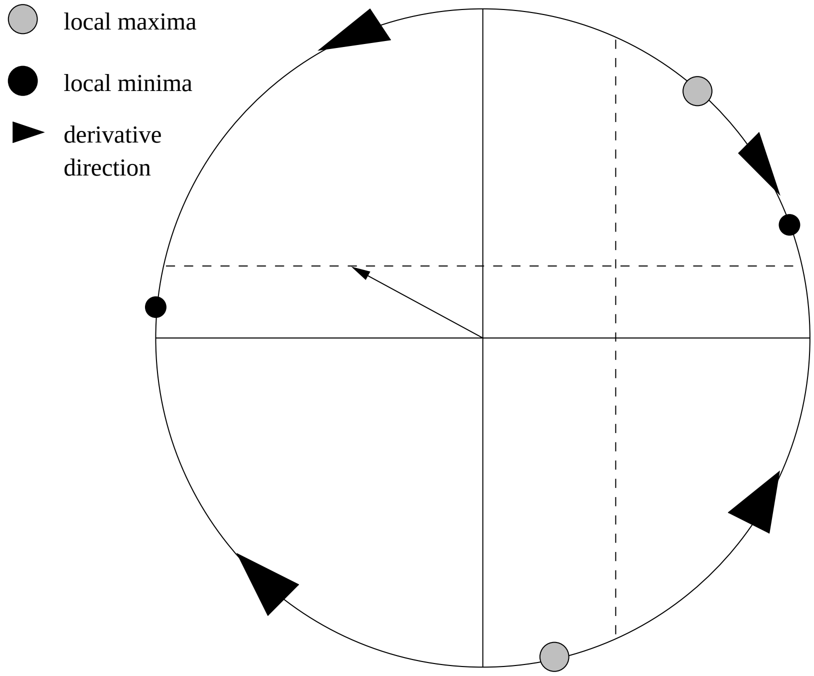

Figure 3.7: Diagram of objective function extrema

and intersect the circle at the magnetization values corresponding to λ_1^* through λ_4^*. Just as we know the direction of the displacements of the roots λ_1 through λ_4 from λ_1^* through λ_4^*, we know the direction of the displacements of the local extrema from the dashed lines. Using those directions of displacements, the local minima and maxima have been drawn on the diagram. From this diagram, we can complete the algorithm for selecting between λ_3 and λ_4. First, divide the plane of local field values into two half-planes by the hard axis. If the magnetization before update is already in the same half plane as the local field, it will remain there, so λ_4 is the appropriate root. For remaining field values, divide the plane of local field values into two half planes by the easy axis. If the magnetization before update is in the half plane opposite the local field, then the derivative (torque) is sufficient to determine whether λ_3 or λ_4 is appropriate. This leaves the upper right quadrant of the diagram to consider. From the derivative, we can determine whether the magnetization before update lies between the maximum and the minimum in that quadrant. If so, then the nearby minimum is correct, so the appropriate root is λ_3. For the other sign of the derivative, though, there remains an ambiguity. The two regions with that sign of the derivative must be distinguished. Clearly, if we can directly compute the value of some magnetization which lies between the maximum and the minimum in

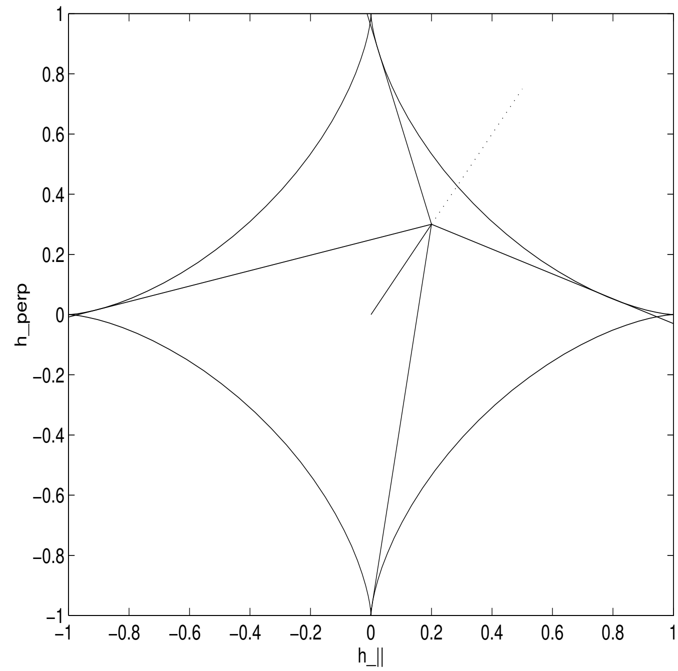

Figure 3.8: Geometric construction of Stoner-Wohlfarth local extrema

the quadrant, then that point can be used to separate the two ambiguous regions. Fortunately such a point can be computed.

The Stoner-Wohlfarth astroid has been presented as a boundary between those local field values which yield one local minimum and those which yield two local minima. It has another application as well. It can be used in a geometric construction to find the local minima, the very task for which we have used Lagrange multiplier techniques. The Lagrange multiplier techniques are more directly amenable to computer implementation, but the geometric construction yields additional insights.

Figure 3.8 depicts the Stoner-Wohlfarth astroid with a local field vector drawn within it. Tangent lines to the astroid from the tip of the field vector have been drawn. It can be shown [98] that the slopes of these tangent lines are the magnetization angles which are the local minima and local maxima of the objective function. The complete derivation is not important here. What is important is that this construction enables us to identify the computable separation point we need. Consider increasing the magnitude of the local field along the dotted line in Figure 3.8. Clearly the two points of tangency in the same quadrant as the local field will come together and finally meet at the point where the dotted line intersects the astroid as the local field value exceeds the Stoner-Wohlfarth boundary. Thus, it is clear that this point will separate those two points for all local field magnitudes within the astroid. Those two points correspond to the local minimum and local maximum we wish to separate. Therefore, we seek to compute the point of intersection of the astroid and the dotted line for use as the separation point we need.

Points on the dotted line may be expressed in terms of the local field value and a variable K: $(Kh_{||}, Kh_{\perp})$. Then substitution into the equation for the Stoner-Wohlfarth astroid allows solution for K. The result is

$$K = \left[\frac{1}{|h_{||}|^{\frac{2}{3}} + |h_{\perp}|^{\frac{2}{3}}}\right]^{\frac{3}{2}} \tag{3.61}$$

Using (2.73) and (2.74), we determine that the two remaining regions of Figure 3.7 may be distinguished based on a threshold test on the magnetization value before update,

$$m_{||}^2 \lesseqgtr \frac{|h_{||}|^{\frac{2}{3}}}{|h_{||}|^{\frac{2}{3}} + |h_{\perp}|^{\frac{2}{3}}} \tag{3.62}$$

A description of the algorithm to compute the appropriate local minimum of the objective function $\mathcal{F}_k(\alpha_k)$ is now complete. This procedure is performed sequentially on grains selected in a random sequence. All that remains is to specify a stopping criterion. First, there is no need for the minimization procedure to be performed on a selected grain if it is already in a local minimum. This possibility is tested for by computing the first and second derivatives of the objective function,

$$\frac{\partial}{\partial \alpha_k}\mathcal{F}_k(\alpha_k) = m_{||,k}m_{\perp,k} + h_{||,k}m_{\perp,k} - h_{\perp,k}m_{||,k}, \tag{3.63}$$

$$\frac{\partial^2}{\partial \alpha_k^2}\mathcal{F}_k(\alpha_k) = m_{||,k}^2 - m_{\perp,k}^2 + h_{||,k}m_{||,k} + h_{\perp,k}m_{\perp,k}. \tag{3.64}$$

The grain is already in a local minimum if the first derivative is zero-valued and the second derivative is non-negative. Testing for a zero-valued first-derivative is a matter of some complication in a computer implementation. There is always some quantization error in floating point numbers. Also, requiring an exact calculation of the local minimum is unnecessary. We need only be sure that the answer is within a desired precision. By default, the test in the implementation is that the first derivative have magnitude less than 0.001 and the second derivative be non-negative. The effect of different precisions may be investigated, as it has been implemented to be user-selectable.

A stable state of the relaxation-rotation algorithm has been reached if all grains when tested in this manner evaluate as being in a local minimum. This condition is not explicitly tested for in the algorithm as implemented. Instead the following strategy is followed. The random sequence of selecting grains is broken into blocks of N selections — the same number of selections as there are grains. After each block, the number of grains for which the minimization procedure was performed is evaluated. If the number is zero (that is, every grain selected in the most recent block reported evaluated to already be in a local minimum), then a counter is incremented. If the number is non-zero, the counter is reset to zero. The algorithm stops when the counter reaches a prescribed value. By default this value is three, but the effect of this value may be investigated, as it has been implemented to be user-selectable.

3.4.4 An Alternative Evolution Algorithm

The rotation-relaxation implementation detailed so far in this section meets all the requirements of a relaxation algorithm. Whether these requirements are sufficient to represent physical plausibility is subject to debate. As already discussed, there is the possibility, still to be investigated, that stable states of the algorithm exist which are not local minima of total magnetic energy. Also, traditional approaches of gradient-driven dynamics have not been followed. Another possible objection may also be considered. When the local minimum value of magnetization for a randomly selected objective function is computed, it may differ a great deal from the previous magnetization value. In physical terms, the magnetization of a single grain may be rotated through a large angle in a single step. As the grain magnetization rotates through a large angle, it passes through several intermediate states. For each of these intermediate states, there would be a corresponding set of field values representing the effect of these states on other grains in the model. These intermediate states and their consequences are skipped over by the rotation-relaxation algorithm. One might reasonably object that for this reason, the algorithm lacks physical plausibility.

To check the validity of this objection, an alternative state evolution algorithm has been implemented which imposes a limit on the magnitude of the angle through which a grain's magnetization may rotate in a single step. This limit is user-selectable, with a default value of 0.1 radian. Safeguards similar to those described for the rotation-relaxation implementation are applied to be sure that when there are two minima available, the rotation proceeds toward the correct one and does not overshoot to the wrong one by "leaping" over a local maximum. The constraint of monotonic decrease of total magnetic energy is not enforced however. It is permitted for this procedure to overshoot a local minimum, and therefore have the trajectory beyond the local minimum be of increasing total magnetic energy. For each rotation step, so long as the final state has lower energy than the initial state, there is no check that there has been no lower energy along the rotation to get to the final state. For small enough angle limits, this difference should be of no consequence. Also, for small enough angle limits, this algorithm should approximate a gradient-driven algorithm. In Chapter 4, a comparison of the results of this algorithm with those of the rotation-relaxation algorithm will determine whether the differences matter in terms of the quantities to be calculated and in terms of the computational resources required.

3.5 Comparison with Other Micromagnetic Models

Now that the micromagnetic model which is the subject of this research has been presented in detail, and the reader is familiar with some terminology, it is a good point to present an overview of how this model compares with other micromagnetic models of recording media for which simulation results have been published. It is hoped that by laying out this detailed comparison of available models, differences in the results they generate may be attributed to the different assumptions made. The comparisons in this section are made with the models of Hughes (H) [41], Zhu and Bertram (ZB) [131], Mansuripur (M) [64], and Miles and Middleton (MM) [76].

3.5.1 Model Geometry

The first basis for comparison of the several micromagnetic models under study is their geometric representation of model components, including dimension, grain structure, easy axis orientation distribution, boundary conditions, and texture.

Model dimension

Our model is both planar (Assumption 2.1) and two-dimensional in its representation of magnetization and magnetic fields (Assumption 2.2). The same assumptions apply to Hughes model. Other models (ZB, M, MM) consider magnetization and magnetic field values to be three-dimensional vector quantities.

Grain Structure

All the models under study represent a recording medium as a collection of uniformly magnetized grains. The grains of our model are the regions of a Voronoi diagram, allowing for either irregular or regular grain structures. Miles and Middleton also allow for randomized microstructure composed of randomly placed ellipsoids [73, 79], as well as hexagonal grain structure. Other models are limited to hexagonal (H, ZB) or rectangular (M) grain structure.

Easy Axis Orientation Distribution

The easy axes of our model have randomly distributed orientation in the medium plane. The range of the distribution is controlled to generate more or less oriented media. Randomly oriented easy axes have been a common feature, both in two and three dimensions. Zhu has considered specially designed easy axes to represent bicrystal film [126].

Boundary Conditions

The model represents a medium only within a bounding box of limited extent. Outside of that bounding box, the model assumes there is nothing. This is not a particularly good assumption for representing recording media. Medium patches a few microns in size are not representative of recording media, but only of a small piece of a recording medium. To take into account the surrounding magnetic material, all other models considered in this study make use of either periodic or anti-periodic boundary conditions. Future development should include this option for our model as well. There are difficulties involved because of the need to match neighbor grains across the bounding box boundaries in the presence of irregular grain structure. Also to be considered is the effect of long, straight grain boundaries imposed by the bounding box boundaries within a medium of irregular grain structure. These difficulties may be resolved by merging periodicity and randomized structure with the method outlined by Schrefl and Fidler [103].

Texture

Texture is not considered by our model. The medium is assumed to be of constant thickness δ. This is the usual assumption of the other models as well. There have been a few investigations of texture though. Random texture has been examined by Zhu [80], and the effect of circumferential polishing of rigid disks has been examined by Miles and Middleton [78].

3.5.2 Model Interactions

The next major category of model features is the manner in which the magnetic interactions are represented and computed, including exchange interactions, magnetostatic interactions, and other effects.

Exchange Interaction

Our model represents the exchange interaction between neighboring grains by means of an effective magnetic field. Each component of the exchange field is a scalar multiple of the magnetization of a neighboring grain (2.29). The scalar multiple (2.37) has been derived from domain wall principles, following [84]. Other micromagnetic models which include an exchange interaction (Hughes does not) make use of a simpler formulation. In the simpler formulation, an effective field is still used, and it is still the sum of field components which are each scalar multiples of a neighboring grain magnetization. The difference is in the scalar multiple and its relation to medium model parameters. In the notation of our model and in SI units, a component of the exchange field arising from the magnetization of a neighboring grain is given by

$$\mathbf{H}_{e,kl} = \frac{2A^*}{\mu_0 M_s^2 (x_{kl}^2 + z_{kl}^2)} \mathbf{M}_l, \tag{3.65}$$

where A^* (J/m) is a value less than A_e to indicate less than full exchange interaction across grain boundaries. A similar notion is represented by our fractional atomic contact parameter f. Thus, as a means of comparison we might consider an equivalence

$$A^* = f A_e. \tag{3.66}$$

The derivation of this simpler formulation of exchange energy [11] starts with the same expression for exchange energy (2.28), copied here for convenience,

$$W_e = \frac{A_e}{M_s^2} \int_V \left[\left| \frac{\partial \mathbf{M}}{\partial x} \right|^2 + \left| \frac{\partial \mathbf{M}}{\partial y} \right|^2 + \left| \frac{\partial \mathbf{M}}{\partial z} \right|^2 \right] dxdydz. \tag{3.67}$$

The coordinate system is aligned so that the line connecting the centers of grains k and l is parallel to the x-axis, and they are a distance $\sqrt{x_{kl}^2 + z_{kl}^2}$ apart. The derivative along this line is approximated by a finite difference,

$$\frac{\partial \mathbf{M}}{\partial x} \approx \frac{\mathbf{M}_l - \mathbf{M}_k}{\sqrt{x_{kl}^2 + z_{kl}^2}}. \tag{3.68}$$

From there, setting the two equations for exchange energy of a pair of grains equal and solving for the equivalent magnetic field component $\mathbf{H}_{e,kl}$ yields (3.65). The approximation is exact only if the variation of magnetization from grain center to grain center is linear. A linear variation of magnetization is troubling for two reasons. First, such a variation does not maintain a constant magnetization magnitude of M_s. Second, it ignores any role of anisotropy energy in the shaping of the domain wall. Including a consideration of anisotropy energy has the effect of reducing the thickness of the domain wall. This concentrates the change in magnetization in a smaller space, causing an increase in the exchange energy. Because the simpler formulation presented here ignores this effect, it tends to underestimate the exchange energy in a medium. It also predicts a different variation of exchange interactions as medium parameter values such as A_e and K_A are varied.

In Appendix B, an even more physically plausible formulation of the exchange interaction is presented. It has not been adopted in the model because it has disadvantageous computational properties.

Magnetostatic Interaction

The model represents the magnetostatic interaction based on a representation of each grain's magnetization by a point dipole at the centroid (Assumption 2.5). This simple representation is inaccurate in the short-range. For this reason, most other models have adopted a more sophisticated representation based on the assumption of uniform magnetization within a grain. Under that assumption, the magnetic poles (or surface "charges") may be computed for each surface of a grain. Application of standard formula for the fields arising from magnetic poles [83], yields expressions for the magnetostatic fields. The fundamental nature of the effective fields calculated by the more sophisticated representation is the same as for our simpler model. An effective field value is computed which is the sum of field components each of which is a linear function of the magnetization of another grain in the assembly. All that must be changed to adopt the more sophisticated model are the linear coefficients. In an implementation where these coefficients are precomputed and stored for use in calculations, the extra computational effort should be expended to yield greater accuracy. In our implementation, coefficients are calculated each time they are needed. Here we quantify the errors introduced by this approximation.

Consider the regular grain structure of an array of square grains with sides of length D m. Let source grain l be centered at the origin of a Cartesian coordinate system. Each grain boundary may be considered to be a line source of magnetic "charge" of magnitude given by the component of magnetization normal to the boundary. The magnetic field at $\mathbf{r}$ arising from a constant line magnetic charge density σ_m along curve C is

$$\mathbf{H}(\mathbf{r}) = \int_C \frac{\sigma_m}{4\pi} \frac{(\mathbf{r} - \mathbf{r}')}{|\mathbf{r} - \mathbf{r}'|^3} dl. \tag{3.69}$$

Applying this relationship to the boundaries of the source grain yields an expression for the magnetostatic field components at coordinates (x, z) as a linear function of the magnetization of source grain l,

$$\mathbf{H}(x, z) = \frac{1}{4\pi D} \begin{bmatrix} A(\frac{x}{D}, \frac{z}{D}) & B(\frac{x}{D}, \frac{z}{D}) \\ B(\frac{x}{D}, \frac{z}{D}) & C(\frac{x}{D}, \frac{z}{D}) \end{bmatrix} \mathbf{M}, \tag{3.70}$$

where

$$\begin{aligned} A(p, q) \quad = \quad & \left[\frac{q + 1/2}{(p - 1/2)\sqrt{(p - 1/2)^2 + (q + 1/2)^2}} \right. \\ - \quad & \frac{q - 1/2}{(p - 1/2)\sqrt{(p - 1/2)^2 + (q - 1/2)^2}} \\ - \quad & \frac{q + 1/2}{(p + 1/2)\sqrt{(p + 1/2)^2 + (q + 1/2)^2}} \\ + \quad & \left. \frac{q - 1/2}{(p + 1/2)\sqrt{(p + 1/2)^2 + (q - 1/2)^2}} \right], \end{aligned} \tag{3.71}$$

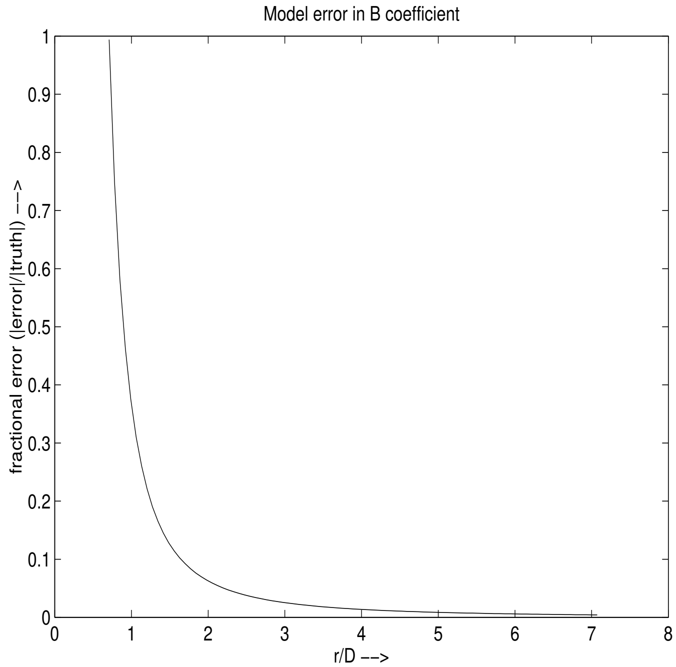

Figure 3.9: Dipole approximation error

$$
\begin{aligned}
B(p,q) &= \left[\frac{1}{\sqrt{(p-1/2)^2+(q-1/2)^2}}\right. \\
&- \frac{1}{\sqrt{(p+1/2)^2+(q-1/2)^2}} \\
&- \frac{1}{\sqrt{(p-1/2)^2+(q+1/2)^2}} \\
&+ \left.\frac{1}{\sqrt{(p+1/2)^2+(q+1/2)^2}}\right],
\end{aligned} \tag{3.72}
$$

and

$$C(p,q) = A(q,p). \tag{3.73}$$

Comparison of these coefficients with those of (2.17) permits a quantification of the error in our approximation. As an example, numerical analysis reveals that the errors in the coefficient $B(p,q)$ in our model are greatest along the line $p = q$. Figure 3.9 is a plot of the fractional error in the $B(p,q)$ coefficient as a function of the distance from the origin r normalized to the grain size D. In the regular square grain structure, there are centroids of other grains along this line. The dipole interaction coefficient at the diagonal neighbor grain exhibits an error of about 15% compared with the more sophisticated model. The model error two diagonal grains away falls to about 3% and the error continues to decrease with increasing distance. Similar errors may be computed for the other coefficients, leading to the conclusion that except for a neighborhood with radius of one to two grains, the dipole approximation is quite good.

Induced Clusters

The exchange interactions between grains of our model are determined according to neighborhood and geometric relationships. All exchange interactions share a fundamental constant $f\sqrt{A_e}$, though, which characterizes the strength of the exchange interaction. Both Miles and Middleton [79] and Zhu [126] have considered the effect of a spatial variation of the exchange interaction strength. With this additional model freedom, clustering behavior can be induced by increasing exchange within selected sets of grains and decreasing exchange between these sets.

3.5.3 Model Magnetic State Evolution

Evolution Algorithm

The magnetic state evolution algorithms of our model have been described in great detail in previous sections, including a discussion of alternative approaches. It is very much unlike other models under study, which have chosen to follow a more traditional gradient-driven minimization strategy.

In order to describe gradient-driven trajectories through state space, many micromagnetic models [131, 64, 76] make use of the phenomenological system of differential equations due to Landau and Lifshitz [51] in the form established by Gilbert [32],

$$\frac{d\mathbf{M}}{dt} = \gamma_G(\mathbf{M} \times \mathbf{H}_{\text{eff}}) - \frac{\alpha_G}{|\mathbf{M}|}\left(\mathbf{M} \times \frac{d\mathbf{M}}{dt}\right), \tag{3.74}$$

or an equivalent formulation [58],

$$\frac{d\mathbf{M}}{dt} = \frac{\gamma_G}{1+\alpha_G^2}(\mathbf{M} \times \mathbf{H}_{\text{eff}}) - \frac{\alpha_G\gamma_G}{|\mathbf{M}|(1+\alpha_G^2)}\left(\mathbf{M} \times (\mathbf{M} \times \mathbf{H}_{\text{eff}})\right), \tag{3.75}$$

where $\mathbf{H}_{\text{eff}}$ is an effective magnetic field representation of all magnetic energies under consideration, including anisotropy. Computer solutions of the Landau-Lifshitz-Gilbert (LLG) system of differential equations are computed by numerical integration techniques. With proper care the errors introduced in numerical simulation can be controlled so that an accurate computation of the trajectory may be achieved. Note that the LLG system of equations presumes a three-dimensional model; that is, a model where magnetization and field vectors are permitted to have directions out of the medium plane.

The LLG equation comprises two terms, known as the *precession term* and the *damping term*. By scaling the coefficients, each can be made dominant. Under "infinite damping" the damping term dominates, and the numerical integration of the LLG equations corresponds to a gradient-driven energy minimization. The important feature is that the stable states of this representation of micromagnetic dynamics are the local minima of magnetic energy, which must also be stable states of any rotation-relaxation algorithm. Thus, both methods compute the same stable states (modulo the two-dimensional vs. three-dimensional diffferences). The energy minimization methods we prefer for their computational properties tend to move more directly to stable states, which are the subject of our interest, at the expense of not being useful at all in investigating the micromagnetic dynamics of the modeled medium. If our interests change to include the micromagnetic dynamics of the medium, a more appropriate model state evolution algorithm should be adopted.

Thermal Effects

Among the micromagnetic models of recording media included in this comparison, none includes an investigation of thermal effects. Our only consideration of thermal effects has been to identify the superparamagnetic limit on the minimum volume of magnetic particle suitable for information storage. A more recent study [55] indicates that at recording densities of 15.5 Mbit/mm^2 (10 Gbit/in^2) thermal decay over a period of time as little as six months may seriously affect recording performance. Continuing development of micromagnetic models of recording media should include a consideration of thermal effects.

3.5.4 Computational Issues

The greatest variation among the models in the details of their computation strategies is in the variety of methods for computing magnetostatic fields. Because these fields are long-range, and must be updated continually throughout a simulation, an efficient method of their computation is essential to a good micromagnetic model. Another computational feature of the micromagnetic work under comparison is a listing of the computer architectures used in each case.

Magnetostatic Interaction Calculation

The computational burden of magnetostatic field calculation has been somewhat relieved in our model by allowing for the truncation of the long-range interaction beyond a user-selectable radius R_L. This same strategy was adopted by Hughes and in the early work of Zhu and Bertram. Mansuripur developed an efficient strategy based on the Fast Fourier Transform algorithm for computing the magnetostatic field. When a spatially periodic microstructure is adopted, the magnetization of the medium is known at regular spatial intervals and the magnetic field values are desired also at regular spatial intervals. The linear, spatially-invariant relationship between a source magnetization, and the magnetic field which arises from it can be represented as a convolution operation. In this framework, the use of FFTs to compute the magnetostatic fields is a straightforward application of two-dimensional signal processing techniques, and has been developed for both rectangular [63] and hexagonal [62] microstructures. This method has since been adopted in the later work of Zhu and Bertram. Miles and Middleton have chosen a hierarchical mean field strategy described in [75]. The contribution of nearby grains to a magnetostatic field are computed directly. More distant grains are grouped according to a hierarchical segmentation. Each group is then represented by its mean field in the computation.

Computer Architecture

Our model has been implemented on a Sun Microsystems workstation. Hughes did not report his computing platform. Other researchers have used one variety or another of “supercomputer,” a CRAY X-MP (ZB), a Connection Machine (M), or an Amdahl VP1200/VP1100 vector processor (MM).

3.6 Summary

Several implementation details of the micromagnetic model have been presented in this chapter. A microstructure generation algorithm has been developed which produces both the regular microstructures common in other micromagnetic models and irregular microstructures expected to yield more physically realistic results. The derivation of expressions for voltage waveforms induced in a read head was completed for magnetic patterns represented by the medium model. Calculation approximations which yield greater program efficiency were presented. The details of competing magnetic state evolution algorithms were discussed. Finally, the micromagnetic model as implemented was compared with a number of other micromagnetic models for which simulation results have been published.

Chapter 4

Medium Model Simulations

In this chapter we record the results of several computer simulations of the micromagnetic model defined and implemented as described in the preceding chapters. The results reported are not exhaustive. They serve primarily as a check on the model and its implementation through verification that these simulations correctly calculate known solutions of micromagnetic problems. Only a few simulations have been performed as investigations in their own right. Many more are possible, and may serve as the starting point for future work.

Two types of data are generated by the computer simulations of the model. First are M vs. H_a hysteresis loops characterizing the macroscopic magnetic properties of the simulated medium material. Hysteresis loops are useful for determining how the intrinsic material properties used in the model relate to the extrinsic magnetic properties of materials that may be empirically measured. Second are the recording and playback of information bearing signals with an inductive head as represented by the Karlqvist model. Examination of simulated playback voltage signals reveals how the intrinsic properties of the medium and head models are reflected in the features of the signal and noise in magnetic recording systems. By means of these two types of computer simulations, reasonable default values for the model parameters are determined to represent magnetic recording media, and the validity of our algorithms is supported.

4.1 Hysteresis Loop Simulations

The prediction of hysteresis loops by computer simulation is a straightforward application of our model. The applied field $\mathbf{H}_a$ is an element of our model which may be varied. Calculation of a hysteresis loop is simply a matter of varying the magnitude of $\mathbf{H}_a$ along a preselected axis, and simulating the response of the medium to the applied field by computing a magnetization state evolution algorithm. The component of medium bulk magnetization along the preselected axis may then be computed and recorded. For the sake of simulation on a computer, the varying applied field is represented as a sequence of applied field values, and upon the application of each applied field value, the magnetization state of the medium evolves until it reaches a stable state of the evolution algorithm. For good physical plausibility, the magnetization state evolution algorithm will be a rotation-relaxation unless otherwise noted. The hysteresis loops are then a sequence of value pairs of applied field magnitude and resulting bulk magnetization component. With a similar technique, model predictions of rotational hysteresis or transverse hysteresis loops may also be investigated, if they are of interest.

4.1.1 Single Stoner-Wohlfarth Particle

In Chapter 2, the Stoner-Wohlfarth astroid was derived to describe the response of the magnetization of a grain to an effective magnetic field when the magnetic energy derives from the effective field and a uniaxial anisotropy energy. A uniformly magnetized body which responds to an effective magnetic field in this manner is known as a Stoner-Wohlfarth particle. The simplest representation of a medium within the framework of the model is a single Stoner-Wohlfarth particle. When there is only a single particle, there are no interactions, and the effective field exactly equals the applied field. The hysteresis properties of a Stoner-Wohlfarth particle vary with the orientation θ of the particle's easy axis with respect to the direction of the applied field in a manner entirely predictable from the Stoner-Wohlfarth astroid. Our first check of our computer implementation is to verify that the predicted hysteresis properties of a Stoner-Wohlfarth particle are calculated by our computer programs. In plotting the results, we make use of the same normalizations used in the derivation of the Stoner-Wohlfarth astroid. Applied field values H_a are reported on a scale where the anisotropy field H_K is the unit. Magnetization values are reported on a scale where the saturation magnetization M_s is the unit.

Fig. 4.1 is a plot of the hysteresis loops for a single Stoner-Wohlfarth particle at orientations of $\pi/10$ and $2\pi/5$ radians. It should be noted that the loops displayed are not envelopes within which the M - H_a response of the particle is contained. They

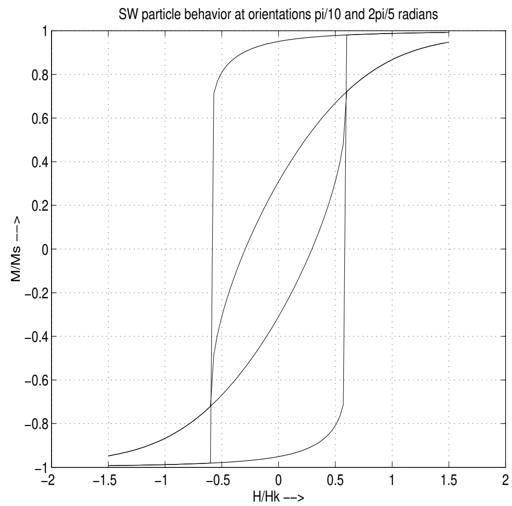

Figure 4.1: Stoner-Wohlfarth particle switching behavior

are in fact the complete characterization of the particle's M - H_a response. There are no minor loops. When there is zero applied field, the magnetization of the particle will align with the easy axis, so the value of remanent magnetization M_r of a particle at orientation θ in normalized units is

$$\frac{M_r}{M_s} = \cos\theta = S. \tag{4.1}$$

Note that this quantity is also the remanence squareness S of the loop.

Each loop may be divided into three intervals of applied field with the middle interval that for which two magnetization states of the particle are possible. The middle interval is symmetric about zero applied field and is bounded in absolute value by a quantity known as the *switching field*, denoted H_s. For a single Stoner-Wohlfarth particle, the switching field H_s is a more meaningful feature of the hysteresis loop than the coercivity. The switching field is exactly that magnitude of applied field required to exceed the Stoner-Wohlfarth astroid at the orientation of the particle, which can be predicted by the Stoner-Wohlfarth astroid to be

$$\frac{H_s}{H_K} = \left[(\cos\theta)^{2/3} + (\sin\theta)^{2/3}\right]^{3/2}. \tag{4.2}$$

This explains why the two loops of Fig. 4.1 have the same switching field. The orientations are symmetric about an orientation of $\pi/4$ radians, where the switching field is a minimum. Fig 4.2 is a plot of the predicted dependence of the switching

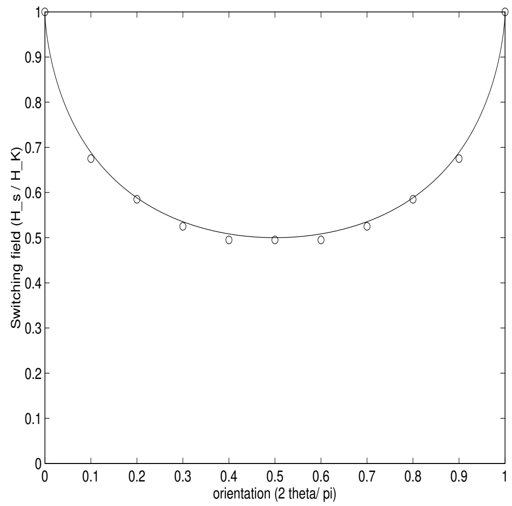

Figure 4.2: Switching field as function of orientation

field H_s on the particle orientation θ. Plotted on the same axes are open circles indicating the switching fields of a particle at a variety of orientations as determined from calculated hysteresis loops. The very small disagreement is due to the step size in the sequence of applied fields used to calculate the loop. Smaller steps in the applied field sequence could calculate the switching field correctly to greater precision. The agreement of our model calculations with predictions for switching field and remanent magnetization values indicates that the computer programs are correct in their most fundamental routines, those which implement objective function minimization.

4.1.2 Assembly of Non-interacting Particles

Now let's consider an assembly of non-interacting grains, each behaving as a Stoner-Wohlfarth particle. Each grain in the assembly may have its easy axis at a different orientation with respect to the applied field direction. Consider the direction of applied field to be fixed along the x-axis of the coordinate system used in the definition of the medium model. The easy axis orientation angles θ_k are assumed in the definition of the medium model to be independent random variables with values fixed once in the manufacture of the medium. For assemblies of a large number of non-interacting grains, the hysteresis behavior of the assembly will closely approximate the expected behavior of a single grain, where the expectation is taken over the probability distribution of the orientation angles. As an example, the normalized remanent

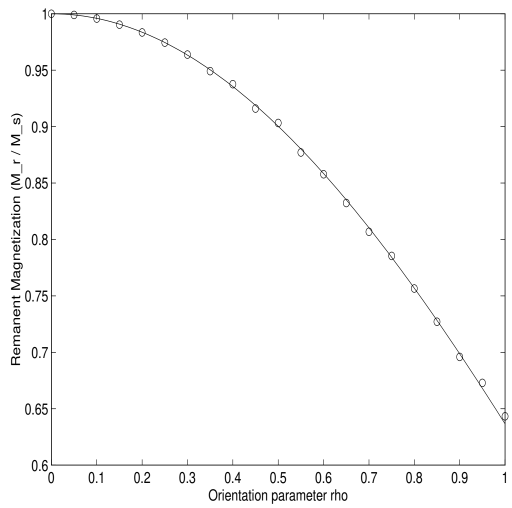

Figure 4.3: Remanent magnetization as a function of orientation parameter

magnetization of an assembly of N grains is given by

$$\frac{M_r}{M_s} = \frac{1}{N}\sum_{k=1}^{N} \cos\theta_k, \tag{4.3}$$

which for large N is well-approximated by

$$\frac{M_r}{M_s} \approx E_\theta\{\cos\theta\}. \tag{4.4}$$

The probability density function of the easy axis orientation angles is selected from a family of uniform probability densities by a parameter ρ, according to

$$p_\theta(\eta) = \begin{cases} \frac{1}{\rho\pi}, & |\eta| \leq \frac{\rho\pi}{2} \\ 0, & \text{otherwise} \end{cases}. \tag{4.5}$$

As introduced in Chapter 3, the parameter ρ is a means of controlling the degree to which the simulated medium is oriented. Under this representation, the normalized remanent magnetization of the assembly of non-interacting grains is found to be

$$\frac{M_r}{M_s} \approx \frac{\sin\frac{\rho\pi}{2}}{\frac{\rho\pi}{2}}. \tag{4.6}$$

Fig 4.3 is a plot of the predicted dependence of normalized remanent magnetization M_r/M_s on orientation parameter ρ. Plotted on the same axes are open circles indicating the normalized remanent magnetization calculated by the model for non-interacting assemblies of grains with easy axes drawn from the probability distribution specified by ρ. The model calculations were performed on an assembly of approximately 1600 grains. In order to represent non-interacting particles with the model, both exchange and magnetostatic interactions must be suppressed. Exchange interactions are eliminated simply by setting the exchange strength parameter $f\sqrt{A_e}$ to be zero. Magnetostatic interactions are eliminated by setting the calculation radius R_L which truncates the calculation of magnetostatic fields to a value so small that it contains no other grains in the assembly.

Prediction of the remanent magnetization as a function of ρ is straightforward because the magnetization state of each grain at remanence is known. With no interactions and no applied field, the magnetization of each grain is aligned with the easy axis. Analysis of the coercivity of an assembly of non-interacting particles is not so simple. In the coercive state, the magnetization of each grain will be rotated off the easy axis. Furthermore, the magnetization of some of the grains may have switched. The magnetization state at coercivity is therefore non-trivial to determine. Instead, we shall be satisfied by a consideration of other states which permit the prediction of bounds on the coercivity of the assembly.

In the coercive state, the component of total magnetization of the assembly along the applied field direction is zero-valued by definition. If the applied field is set to zero with the assembly in the coercive state, the magnetization of each grain will rotate to align with the local easy axis, with direction determined by whether or not the magnetization had switched in the coercive state. Because the orientation of magnetization of a grain always lies between its easy axis and the applied field, the rotation back to easy axes from the coercive state is larger for those grains which have not reversed. The effect is that the remanent state after the applied field is removed from the coercive state will have positive magnetization. If instead, we apply a reverse field of large enough magnitude so that the remanent state after the applied field is removed has zero magnetization, it follows that the magnitude of the reverse field we applied must be greater than the coercive field. Therefore, we have a means of computing an upper bound on the coercivity by consideration only of remanent states, exactly those states which are easy to analyze.

The division of grains into those which have switched and those which have not for a given magnitude of applied field is determined by the switching field dependence on grain orientation plotted in Fig. 4.2. It is clear that for a normalized applied field,

$$h_a \triangleq \frac{H_a}{H_K}, \tag{4.7}$$

between 0.5 and 1.0, the set of grains which switch are those with easy axis orientation angle θ in the range

$$\frac{\pi}{4} - \theta_c \leq \theta \leq \frac{\pi}{4} + \theta_c, \tag{4.8}$$

where θ_c is determined from Fig. 4.2 and the value of h_a. This formulation provides all we need to determine the upper bound on coercive field as a function of orientation parameter ρ. Because all functions in the analysis are even functions of grain easy axis orientation angle θ, it is sufficient to consider only positive values θ. Given ρ, the value of θ_c required so that the remanent state has zero magnetization is determined as the solution of

$$\int_0^{\frac{\pi}{4}-\theta_c} p_\theta(\eta : \rho) \cos\eta d\eta - \int_{\frac{\pi}{4}-\theta_c}^{\frac{\pi}{4}+\theta_c} p_\theta(\eta : \rho) \cos\eta d\eta + \int_{\frac{\pi}{4}+\theta_c}^{\frac{\pi}{2}} p_\theta(\eta : \rho) \cos\eta d\eta = 0. \tag{4.9}$$

Solution requires consideration of two cases. The first case is that $\frac{\rho\pi}{2} > \frac{\pi}{4} + \theta_c$. The equation to solve becomes

$$\int_0^{\frac{\rho\pi}{2}} \cos\eta d\eta = 2\int_{\frac{\pi}{4}-\theta_c}^{\frac{\pi}{4}+\theta_c} \cos\eta d\eta, \tag{4.10}$$

with solution

$$\theta_c = \sin^{-1}\left[\frac{1}{2\sqrt{2}} \sin\left(\frac{\rho\pi}{2}\right)\right]. \tag{4.11}$$

The other case is that $\frac{\rho\pi}{2} < \frac{\pi}{4} + \theta_c$. The equation to solve becomes

$$\int_0^{\frac{\pi}{4}-\theta_c} \cos\eta d\eta = \int_{\frac{\pi}{4}-\theta_c}^{\frac{\rho\pi}{2}} \cos\eta d\eta, \tag{4.12}$$

with solution

$$\theta_c = \frac{\pi}{4} - \sin^{-1}\left[\frac{1}{2} \sin\left(\frac{\rho\pi}{2}\right)\right]. \tag{4.13}$$

The dividing line between the two cases is

$$\rho = \frac{2}{\pi}\tan^{-1} 2 \approx 0.704. \tag{4.14}$$

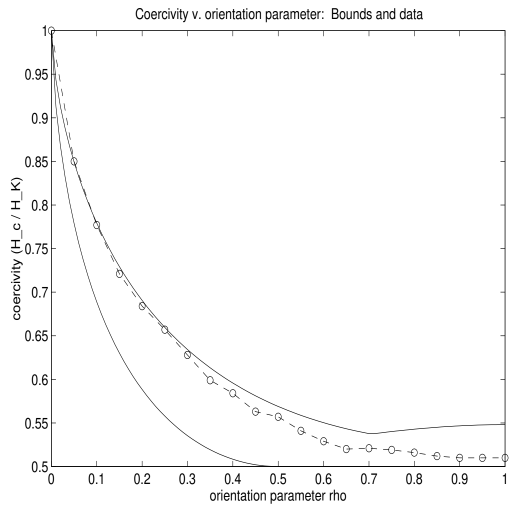

Figure 4.4: Coercivity as a function of orientation parameter

From the solution for θ_c and the relationship between grain orientation and switching field in Fig. 4.2, the upper bound on coercive field may be calculated. The uppermost solid line in Fig. 4.4 is a plot of the upper bound on coercive field. This analysis is similar to one by Hughes [41] who in turn was inspired by Chapter 12 of [21]. In this presentation however, an extension has been made to general uniform distributions of orientation angle (Hughes considered only our case where $\rho = 1$), and a careful note has been made that the expression derived is an upper bound on the coercivity, not the coercivity itself.

For values of $\rho < 0.5$, there is also a simple lower bound. For such a distribution of easy axis orientation angles, each grain has a coercivity equal to its switching field. The coercivity of the assembly of grains is clearly greater than the minimum coercivity of any single grain in the assembly, which is the switching field of the grains with orientation furthest from the applied field direction. Therefore, the switching field for a grain of orientation $\theta = \rho\pi/2$ is a lower bound for the coercivity of an assembly with orientation parameter ρ. Fig. 4.4 also displays this lower bound as a solid line. The open circles of Fig. 4.4 are the coercivity values of loops calculated by the model for an assembly of approximately 1600 non-interacting grains. The dashed line connecting the circles is an aid for the eye, not an interpolation. The circles lie between the bounds, indicating that the model calculations are consistent with our predictions.

In concluding this section we summarize some of the dependence of parameters of hysteresis loops calculated by the medium model on the parameters of the model.

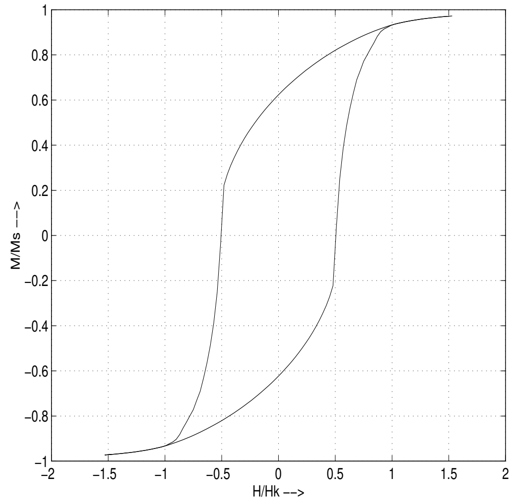

Figure 4.5: Hysteresis loop for non-oriented media, no interactions

Magnetizations are normalized to M_s, so an increase in M_s will increase M_r. Likewise, fields are normalized to the anisotropy field H_K, so an increase in K_A will increase coercivity, and an increase in M_s will decrease coercivity. Finally, we see that as the orientation of a medium is increased (ρ is given a value closer to 0), both the remanent magnetization and the coercivity are increased. These trends are important in trying to choose model parameters to represent medium material with known hysteresis properties.

4.1.3 Effect of Interactions

Up to this point the grains have been non-interacting. Now we consider the introduction of interactions into the model calculations, and determine how the interactions change the hysteresis loop properties. For simplicity, we consider only non-oriented media ($\rho = 1$). For non-oriented media, the hysteresis loop calculated for a non-interacting assembly of grains is displayed in Fig. 4.5. This figure serves as a baseline against which to compare hysteresis loops calculated for interacting assemblies. The loop properties are a remanence squareness S of $2/\pi \approx 0.64$, a normalized coercivity H_c/H_K of 0.51, and a coercivity squareness S^* of 0.85. A notable feature of this loop is the break near $h_a = 0.5$ where switching begins. Only for applied fields larger than this break point will there be minor loops. Between these break points, only reversible changes of magnetization occur.

Exchange

First consider the addition of exchange interactions only. The magnetostatic interactions are still eliminated artificially by setting the calculation truncation radius R_L to a very small value. The exchange interaction is introduced as an effective field component added to the applied field. From the model definition in Chapter 2 and the normalization to the anisotropy field H_K, we may express the normalized exchange field at grain k,

$$\mathbf{h}_{e,k} = \frac{\mu_0 M_s}{2K_A} \cdot \frac{\sqrt{K_A}}{M_s^2} \cdot \frac{f\sqrt{A_e}}{\mu_0} \cdot M_s \sum_{l \in N(k)} \frac{\ell_{kl}}{\mathcal{A}_k} \mathbf{m}_l \tag{4.15}$$

$$= \frac{f\sqrt{A_e}}{2\sqrt{K_A}} \sum_{l \in N(k)} \frac{\ell_{kl}}{\mathcal{A}_k} \mathbf{m}_l. \tag{4.16}$$

It is convenient to introduce a normalization of grain size. If we consider a regular grain structure of square grains of side length D m, then the factor of $\frac{\ell_{kl}}{\mathcal{A}_k}$ becomes D^{-1}. Other grain structures may also be normalized to a quantity of length we identify as the linear dimension of a grain and which we denote by D. For hexagonal grains with edge-to-edge diameter A m, the length of each edge is $A/\sqrt{3}$, and the grain area is $\frac{\sqrt{3}}{2}A^2$. In order to maintain an interpretation of the value D which is consistent over different grain structures, we always define it so that the average area of a grain is D^2. Therefore, for hexagonal grains,

$$D \triangleq \sqrt{\frac{\sqrt{3}}{2}} A \approx 0.931A, \tag{4.17}$$

for irregular grains,

$$D \triangleq \lambda^{-1/2}, \tag{4.18}$$

and for rectangular grains (not square),

$$D \triangleq \sqrt{XZ}. \tag{4.19}$$

Having made the appropriate definition for D, we then write

$$\mathbf{h}_{e,k} = \frac{f\sqrt{A_e}}{2D\sqrt{K_A}} \sum_{l \in N(k)} \frac{\ell_{kl}}{\mathcal{A}_k} \mathbf{m}_l \tag{4.20}$$

with the understanding that all units of length and area have been normalized so that D is the unit. Finally, we define a new constant

$$K_e \triangleq \frac{f\sqrt{A_e}}{2D\sqrt{K_A}} \tag{4.21}$$

which we refer to as the *exchange constant*. It is a dimensionless parameter which characterizes the magnitude of the exchange interaction represented in the model. Using it, the normalized exchange field is expressed

$$\mathbf{h}_{e,k} = K_e \sum_{l \in N(k)} \frac{\ell_{kl}}{\mathcal{A}_k} \mathbf{m}_l. \tag{4.22}$$

In this expression all the effects of the medium material properties, including grain size, have been encapsulated in the exchange constant K_e. The effect of microstructure is represented by the coefficients of the summation.

In order to explore the effect of the magnitude of the exchange constant on the hysteresis properties predicted by the model, hysteresis loops were calculated for several values of K_e. A fixed irregular grain structure was generated with $\lambda = 4 \times 10^{14}$ m^{-2}, so that $D = 50$ nm, and a fixed set of anisotropy axes were drawn at random with $\rho = 1$. Hysteresis loops were then calculated for a set of values of K_e. A convenient single model parameter to vary is $f\sqrt{A_e}$. The anisotropy energy density was set to $K_A = 10^6$, so that

$$K_e = 10^4 f\sqrt{A_e}. \tag{4.23}$$

This value of K_A is not chosen for realism, but for the convenient relationship it creates between $f\sqrt{A_e}$ and K_e. The values of M_s and δ are irrelevant, as they influence only the magnetostatic interaction which is artificially removed in this investigation. The values of $f\sqrt{A_e}$ for which hysteresis loops were calculated are $1, 2, 5, 10, 15, 20, 30, 40,$ and 60×10^{-6} $(\mathrm{J/m})^{-1/2}$, with corresponding values of K_e: $0.01, 0.02, 0.05, 0.10, 0.15, 0.20, 0.30, 0.40,$ and 0.60. Fig. 4.6 is a plot of the calculated hysteresis loops. The trends are that normalized coercivity h_c decreases as the exchange constant K_e increases over the range of values tested, and remanence squareness S and coercivity squareness S^* both increase to a maximum and then decrease. These trends are graphed in Fig. 4.7.

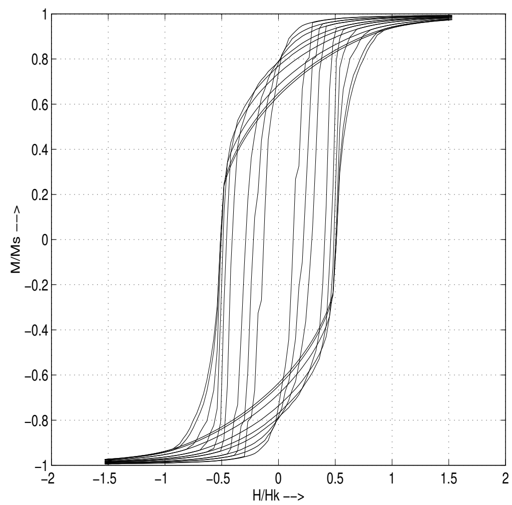

Figure 4.6: Hysteresis loops for varying K_e (greater K_e yields lesser H_c), no magnetostatic interaction

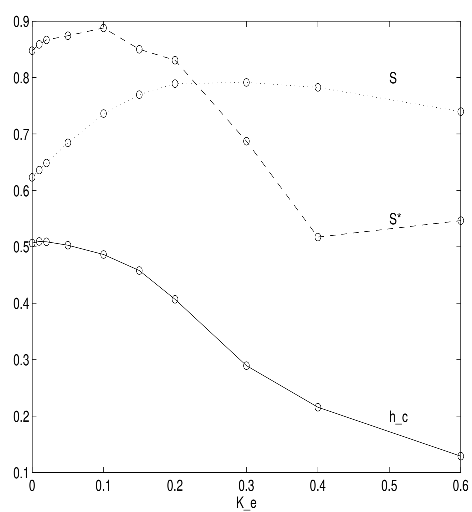

Figure 4.7: Hysteresis parameters (S, S^{*}, h_c) vs. K_e, no magnetostatic interaction

Magnetostatic

Next consider the addition of magnetostatic interactions only. The exchange interactions are suppressed by setting $f\sqrt{A_e}$ to zero value. From the model definition in Chapter 2 and the normalization to the anisotropy field H_K, we may express the normalized magnetostatic field at grain k,

$$\mathbf{h}_{m,k} = \frac{\mu_0 M_s}{2K_A} \cdot \frac{M_s \delta}{4\pi} \cdot \sum_{\substack{l\in\mathcal{I} \\ l\neq k}} \frac{\mathcal{A}_l}{(x_{kl}^2 + z_{kl}^2)^{5/2}} \begin{bmatrix} 2x_{kl}^2 - z_{kl}^2 & 3x_{kl}z_{kl} \\ 3x_{kl}z_{kl} & 2z_{kl}^2 - x_{kl}^2 \end{bmatrix} \mathbf{m}_l \quad (4.24)$$

$$= \frac{\mu_0 M_s^2 \delta}{8\pi K_A} \cdot \sum_{\substack{l\in\mathcal{I} \\ l\neq k}} \frac{\mathcal{A}_l}{(x_{kl}^2 + z_{kl}^2)^{5/2}} \begin{bmatrix} 2x_{kl}^2 - z_{kl}^2 & 3x_{kl}z_{kl} \\ 3x_{kl}z_{kl} & 2z_{kl}^2 - x_{kl}^2 \end{bmatrix} \mathbf{m}_l \quad (4.25)$$

With the same normalization of all lengths and areas (but not medium thickness δ) to grain size D as introduced for the exchange interaction, we may write

$$\mathbf{h}_{m,k} = \frac{\mu_0 M_s^2 \delta}{8\pi K_A D} \cdot \sum_{\substack{l\in\mathcal{I} \\ l\neq k}} \frac{\mathcal{A}_l}{(x_{kl}^2 + z_{kl}^2)^{5/2}} \begin{bmatrix} 2x_{kl}^2 - z_{kl}^2 & 3x_{kl}z_{kl} \\ 3x_{kl}z_{kl} & 2z_{kl}^2 - x_{kl}^2 \end{bmatrix} \mathbf{m}_l. \quad (4.26)$$

Finally, we define a new constant

$$K_m \triangleq \frac{\mu_0 M_s^2 \delta}{8\pi K_A D} \quad (4.27)$$

which we refer to as the *magnetostatic constant*. It is a dimensionless parameter which characterizes the magnitude of the magnetostatic interaction represented in the model. Using it, the normalized magnetostatic field is expressed

$$\mathbf{h}_{m,k} = K_m \sum_{\substack{l\in\mathcal{I} \\ l\neq k}} \frac{\mathcal{A}_l}{(x_{kl}^2 + z_{kl}^2)^{5/2}} \begin{bmatrix} 2x_{kl}^2 - z_{kl}^2 & 3x_{kl}z_{kl} \\ 3x_{kl}z_{kl} & 2z_{kl}^2 - x_{kl}^2 \end{bmatrix} \mathbf{m}_l. \quad (4.28)$$

In this expression all the effects of the medium material properties, including grain size have been encapsulated in the magnetostatic constant K_m. The effect of microstructure is represented by the coefficients of the summation.

In order to explore the effect of the magnitude of the magnetostatic constant on the hysteresis properties predicted by the model, hysteresis loops were calculated for several values of K_m. The same fixed irregular grain structure was used as in the exchange interaction investigation, as well as the same set of anisotropy axes.

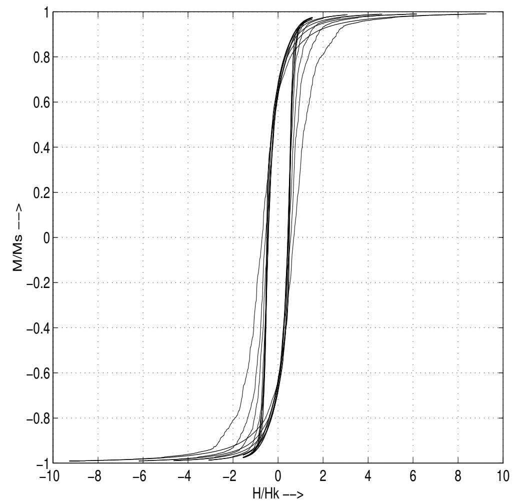

Figure 4.8: Hysteresis loops for varying K_m, no exchange interaction

Hysteresis loops were then calculated for a set of values of K_m. A convenient single model parameter to vary to create this set of values is δ. The value of $f\sqrt{A_e}$ was set to zero to eliminate the exchange interaction. The other medium properties were set to be $K_A = 10^5$ J/m^3 and $M_s = 10^6$ A/m, so that

$$K_m = 10^7 \delta. \tag{4.29}$$

These values of K_A and M_s are not chosen for realism, but for the convenient relationship they create between δ and K_m. The values of δ for which hysteresis loops were calculated are $1, 2, 5, 10, 15, 20, 30, 40,$ and 60 nm, with corresponding values of K_m: $0.01, 0.02, 0.05, 0.10, 0.15, 0.20, 0.30, 0.40,$ and 0.60. Fig. 4.8 is a plot of the calculated hysteresis loops. An expanded range of applied field values was used in the calculation of loops for larger values of K_m so that saturation could be reached. Media with greater normalized magnetostatic interactions require greater normalized applied fields to reach saturation so that the demagnetizing effects of the magnetostatic interaction may be overcome. The trends of hysteresis loop parameters h_c, S, and S^* over the range of K_m in this investigation are graphed in Fig. 4.9.

Combined

Two constants K_e and K_m have been identified which characterize the strength of the exchange and magnetostatic interactions respectively. The medium properties of the

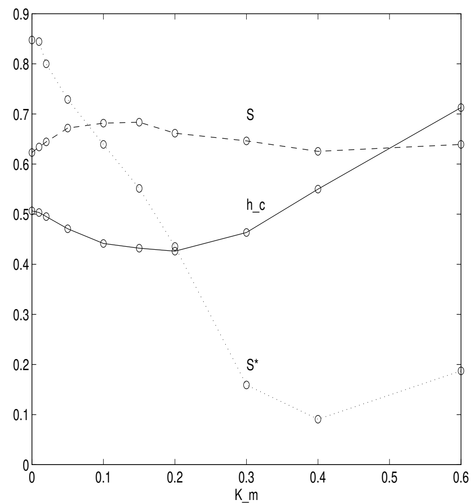

Figure 4.9: Hysteresis parameters (S, S^*, h_c) vs. K_m, no exchange interaction

model influence the calculations of the model only through their presence in the definition of these constants. The only other part of the model which influences the calculations is the particular microstructure (grain structure and anisotropy axes). For a fixed microstructure, an investigation of model predictions over a two-dimensional space of values of the pair (K_e, K_m) yields the same information as an investigation over a five-dimensional space of values of the model parameters representing medium properties, $(\delta, M_s, K_A, f\sqrt{A_e}, D)$. Therefore, any medium described in the model by a particular quintuple of medium property values may be replaced by an *equivalent medium* described by the corresponding pair (K_e, K_m). The equivalence is that all calculations of the medium model will be unchanged in their normalized form. This reduction of the parameter space to be investigated is of great assistance in mapping out the possible behaviors predicted by the model. A similar representation of the material properties of a medium in a model by a pair of values is found in [134], where Zhu first uses the notation h_e and h_m for two model parameters scaling the interactions due to exchange and magnetostatic energies respectively. Zhu has continued to use this notation in subsequent work, so it is convenient to know the relationship between these constants and our K_e and K_m in order to make comparisons. In the notation of our model, the relationships are

$$h_e = \sqrt{\frac{2}{3\sqrt{3}}} K_e \approx 1.075 K_e, \tag{4.30}$$

where the scale factor arises from Zhu's hexagonal grain structure, and

$$h_m = \frac{M_s}{H_K} = \frac{4\pi D}{\delta} K_m. \tag{4.31}$$

It should be noted that Zhu's work considers only one microstructure, hexagonal grain structure, so that the values of h_e and h_m together with the anisotropy axes are sufficient to completely describe an instance of his model. We must also consider the effect of grain structure to completely investigate the predictions of our model. Also, though the substitutions of (K_e, K_m) for (h_e, h_m) serve as a basis for comparison between the two models on a normalized basis, the two models do not predict the same variation of these reduced parameter pairs with the material properties of the medium, as noted in Chapter 3.

Now let us consider the combined effect of exchange and magnetostatic interactions on the hysteresis loop parameters calculated by the model. The same fixed grain structure and anisotropy axes as in the investigations of exchange and magnetostatic interactions separately are retained. The same set of values of K_e and K_m are also used, but now each combination is considered. The input to this investigation is a (K_e, K_m) pair. The output is the triplet of calculated values, h_c, S, and S^*. The results of these calculations are tabulated in Tables 4.1 and 4.2.

This investigation has been for a single fixed microstructure, and for a non-oriented medium ($\rho = 1$). Further investigation into the effect of these remaining elements of the medium model on hysteresis loop parameters is warranted in future work.

4.2 Model Parameter Identification

The five model parameters which represent material properties, $(\delta, M_s, K_A, f\sqrt{A_e}, D)$, or the pair of reduced parameters (K_e, K_m) derived from them are intrinsic parameters of the medium model. They represent properties of the medium at a microscopic scale. These properties are not easily measured in a magnetic recording laboratory without special equipment. More easily available are measurements of extrinsic parameters, such as the parameters of macroscopic hysteresis loops. The preceding section presented the calculation of extrinsic parameter values by the model from the intrinsic parameter values. Using those results, in this section we derive a method for

Table 4.1: Hysteresis loop parameter dependence on (K_e, K_m), part one

K_e	K_m	h_c	S	S^*	K_e	K_m	h_c	S	S^*
0.00	0.00	0.51	0.64	0.85	0.05	0.00	0.50	0.68	0.87
0.00	0.01	0.50	0.63	0.84	0.05	0.01	0.50	0.69	0.87
0.00	0.02	0.50	0.64	0.80	0.05	0.02	0.49	0.70	0.84
0.00	0.05	0.47	0.67	0.73	0.05	0.05	0.47	0.72	0.79
0.00	0.10	0.44	0.68	0.64	0.05	0.10	0.44	0.73	0.73
0.00	0.15	0.43	0.68	0.55	0.05	0.15	0.42	0.73	0.56
0.00	0.20	0.43	0.66	0.44	0.05	0.20	0.43	0.72	0.53
0.00	0.30	0.46	0.65	0.16	0.05	0.30	0.48	0.70	0.28
0.00	0.40	0.55	0.63	0.09	0.05	0.40	0.55	0.68	0.27
0.00	0.60	0.71	0.64	0.19	0.05	0.60	0.73	0.67	0.19
0.01	0.00	0.51	0.64	0.86	0.10	0.00	0.49	0.74	0.89
0.01	0.01	0.50	0.65	0.85	0.10	0.01	0.48	0.74	0.87
0.01	0.02	0.50	0.66	0.84	0.10	0.02	0.47	0.75	0.85
0.01	0.05	0.47	0.68	0.76	0.10	0.05	0.45	0.76	0.84
0.01	0.10	0.44	0.69	0.63	0.10	0.10	0.44	0.77	0.73
0.01	0.15	0.42	0.70	0.56	0.10	0.15	0.43	0.76	0.67
0.01	0.20	0.42	0.67	0.50	0.10	0.20	0.43	0.75	0.59
0.01	0.30	0.45	0.66	0.29	0.10	0.30	0.50	0.73	0.48
0.01	0.40	0.54	0.64	0.24	0.10	0.40	0.56	0.72	0.42
0.01	0.60	0.70	0.65	0.14	0.10	0.60	0.74	0.70	0.17
0.02	0.00	0.51	0.65	0.87					
0.02	0.01	0.50	0.66	0.86					
0.02	0.02	0.50	0.67	0.84					
0.02	0.05	0.47	0.69	0.77					
0.02	0.10	0.44	0.70	0.64					
0.02	0.15	0.42	0.71	0.53					
0.02	0.20	0.43	0.69	0.52					
0.02	0.30	0.46	0.68	0.26					
0.02	0.40	0.53	0.66	0.21					
0.02	0.60	0.72	0.66	0.09					

Table 4.2: Hysteresis loop parameter dependence on (K_e, K_m), part two

K_e	K_m	h_c	S	S^*	K_e	K_m	h_c	S	S^*
0.15	0.00	0.46	0.77	0.85	0.40	0.00	0.22	0.78	0.52
0.15	0.01	0.45	0.77	0.86	0.40	0.01	0.22	0.79	0.56
0.15	0.02	0.44	0.78	0.84	0.40	0.02	0.21	0.79	0.57
0.15	0.05	0.41	0.78	0.86	0.40	0.05	0.21	0.78	0.67
0.15	0.10	0.41	0.78	0.72	0.40	0.10	0.26	0.80	0.67
0.15	0.15	0.40	0.78	0.71	0.40	0.15	0.27	0.80	0.59
0.15	0.20	0.42	0.77	0.61	0.40	0.20	0.36	0.82	0.60
0.15	0.30	0.50	0.75	0.54	0.40	0.30	0.50	0.81	0.72
0.15	0.40	0.57	0.74	0.36	0.40	0.40	0.58	0.80	0.66
0.15	0.60	0.74	0.71	0.25	0.40	0.60	0.81	0.78	0.41
0.20	0.00	0.41	0.79	0.83	0.60	0.00	0.13	0.74	0.55
0.20	0.01	0.40	0.79	0.84	0.60	0.01	0.13	0.74	0.51
0.20	0.02	0.40	0.80	0.86	0.60	0.02	0.13	0.74	0.74
0.20	0.05	0.36	0.79	0.80	0.60	0.05	0.14	0.73	0.56
0.20	0.10	0.38	0.80	0.81	0.60	0.10	0.16	0.76	0.43
0.20	0.15	0.39	0.79	0.73	0.60	0.15	0.21	0.75	0.41
0.20	0.20	0.43	0.78	0.75	0.60	0.20	0.26	0.84	0.26
0.20	0.30	0.50	0.77	0.44	0.60	0.30	0.39	0.84	0.54
0.20	0.40	0.58	0.75	0.42	0.60	0.40	0.57	0.82	0.68
0.20	0.60	0.75	0.73	0.43	0.60	0.60	0.84	0.81	0.62
0.30	0.00	0.29	0.79	0.69					
0.30	0.01	0.28	0.79	0.61					
0.30	0.02	0.28	0.79	0.70					
0.30	0.05	0.27	0.78	0.75					
0.30	0.10	0.29	0.79	0.75					
0.30	0.15	0.35	0.80	0.61					
0.30	0.20	0.40	0.79	0.59					
0.30	0.30	0.48	0.80	0.75					
0.30	0.40	0.58	0.79	0.60					
0.30	0.60	0.81	0.75	0.29					

reversing the procedure, so that given a hysteresis loop measurement of a material, a set of model parameters may be determined to match that hysteresis behavior.

4.2.1 Model Parameter Ranges

First let us consider the range of reasonable values to consider for each of the model parameters, so that the model represents thin film magnetic recording media. Where the boundaries of physical realizability are not clear, the reasonable range of values is taken to be large enough to contain the physically realizable range.

Magnetic Layer Thickness

The thickness, δ, of the magnetic layer of thin-film disk media ranges from 20 to 100 nm (200 to 1000 Å) [43].

Saturation Magnetization

The saturation magnetization, M_s, of Co alloys used in thin-film media has values between 500 and 800 kA/m (500 and 800 emu/cm^3). An absolute upper bound on the saturation magnetization of Co-based media is the saturation magnetization of pure Co, 1722 kA/m. [43, p. 14].

The saturation magnetization M_s is rarely reported for recording media. Instead the remanent-magnetization-thickness product, $M_r \cdot \delta$ is reported. The trend of recent years has been a steady decrease in $M_r \cdot \delta$. A demonstration of 3 Gbit/in^2 recording [114] made use of a quaternary CoPtCr-based medium with $M_r \cdot \delta = 5.3$ mA (0.53 memu/cm^2). Even assuming a very thin 20 nm magnetic layer, a remanent magnetization of only 265 kA/m is implied. In these advanced low disk noise media, both M_s and S are small. A reasonable range of M_s to consider in the model is 200 to 2000 kA/m (200 to 2000 emu/cm^3).

Anisotropy Energy Density

The uniaxial anisotropy energy density, K_A, of pure Co is about 400 kJ/m^3 (4 Merg/cm^3). [43, 49]. Larger values of K_A lead to larger coercivity H_c in a recording material. In order to record a magnetic pattern on a recording medium, a recording head must be capable of generating magnetic fields above the medium coercivity. Limits on the head fields generated by recording heads are expected to keep the anisotropy energy density of practical recording media below 400 kJ/m^3 for the foreseeable future. [55] A reasonable range of K_A to consider in the model as representing physically realizable recording media is 100 to 1000 kJ/m^3. Much smaller values of K_A (e.g. 500 J/m^3) correspond to soft magnetic materials like permalloy rather than hard magnetic materials suitable for recording media.

Exchange Energy Constant

When a thin-film recording medium is composed of well-segregated grains, or when one considers particulate media, there is no exchange interaction. Thus, a lower bound of zero is appropriate. For an upper bound, consider that the exchange energy constant A_e for some materials is tabulated [98, p. 194], a typical value for magnetic elements is 10 pJ/m, and the value for Fe is 14.9 pJ/m (1.48 μerg/cm) [21, p. 190]. A safe upper bound for A_e appears to be 100 pJ/m. The corresponding upper bound on $f\sqrt{A_e}$ is 10^{-5} (J/m)$^{1/2}$.

One check on a reasonable value for the exchange energy constant is its relationship to the thickness of domain walls. The thickness of a domain wall between domains of anti-parallel magnetization is predicted to be

$$\delta_w = \pi\sqrt{\frac{A_e}{K_A}}, \tag{4.32}$$

in the theory of domain walls [21]. So long as the thickness of domain walls is predicted to be less than the grain size D, the value of the exchange energy constant can be accepted as reasonable.

Grain Size

Some caution must be exercised in specifying a range of reasonable values for the grain size. Transmission electron microscopy (TEM) studies reveal that magnetic recording media are made up of building blocks of size 10 to 50 nm. [43] These building blocks are usually called grains. We have also used the term "grains" to refer to the elements of our model. This is perhaps unfortunate, as there is no necessary implication that the grains of our model represent the grains observed in TEM studies. Instead, the grains of the model represent regions of recording media with uniform magnetization and a single axis of uniaxial anisotropy. These are magnetic properties, and do not necessarily coincide with the physical properties observed in TEM studies. Stated

Table 4.3: Physical ranges of model parameter values

Symbol	*Low*	*High*	*Units*
δ	20	100	nm
M_s	200	2000	kA/m
K_A	100	1000	kJ/m^3
$f\sqrt{A_e}$	0	10^{-5}	(J/m)$^{1/2}$
D	10	1000	nm
K_e	0	1.58	-
K_m	4×10^{-5}	20	-

another way, our grains represent magnetic microstructure which need not necessarily coincide with physical microstructure. A safe range of values for our magnetic grain size D is 10 to 1000 nm.

Summary

Table 4.3 summarizes the ranges of model parameter values which include physically realizable media, as well as the corresponding ranges of the reduced parameter pair (K_e, K_m).

4.2.2 Parameter Identification Procedure

Experimental measurements of hysteresis loops are made on a vibrating sample magnetometer (VSM). VSM measurements are observed as hysteresis loops of total magnetic moment responding to applied field. From the measured loops, the parameters H_c, S, and S^* for the material are directly available. To determine M_r, the volume of the magnetic layer of the sample must be known. A sample of recording medium measured in a VSM is of macroscopic size, so measuring its area is straightforward. To determine volume, however, the magnetic layer thickness δ must be known, or a reasonable guess as to its value must be made. In the procedure which follows, we assume a value for δ is already available. The remainder of the identification task is to determine values for the other four medium parameters in Table 4.3 so that the measured hysteresis loop may be reproduced by the calculations of the model.

First, there is the simple observation that

$$M_s = \frac{M_r}{S}. \tag{4.33}$$

Therefore, under our assumption that δ is known, M_r and S are available from the measured hysteresis loop, and M_s is a straightforward calculation.

Next, we wish for our selected parameters to reproduce the measured hysteresis loop. In particular, the calculated loop should have the same values for S and S^*. Toward that end, we search Tables 4.1 and 4.2 for a pair of values for S and S^* which most nearly match those of the measured loop. This table search yields corresponding values for K_e, K_m, and h_c.

Next, consider the definition of K_m (4.27) and the coercivity normalization

$$\frac{H_c}{h_c} = H_K = \frac{2K_A}{\mu_0 M_s}. \tag{4.34}$$

Substitution yields an expression for K_m which includes several loop parameters

$$K_m = \frac{M_r \delta h_c}{S H_c 4\pi D}, \tag{4.35}$$

and which can be solved for D,

$$D = \frac{1}{4\pi} \cdot \frac{M_r \delta}{S H_c} \cdot \frac{h_c}{K_m}. \tag{4.36}$$

The first factor is just a scale factor. The second includes quantities from the measured hysteresis loop. The third includes quantities derived from the table search procedure. In this manner, a value for grain size D can be derived to match hysteresis measurements without reference to microscopy measurements.

To determine a value for K_A, we solve the coercivity normalization for K_A to yield

$$K_A = \frac{\mu_0}{2} \cdot \frac{M_r H_c}{S} \cdot \frac{1}{h_c}, \tag{4.37}$$

with the same grouping of factors into scale factor, measured quantities and quantities derived from the table search.

Finally, a value for $f\sqrt{A_e}$ may be computed from the relation

$$f\sqrt{A_e} = 2DK_e\sqrt{K_A}. \tag{4.38}$$

At the end of this procedure, a set of five model parameters will be determined such that the model will calculate a hysteresis loop which matches the measured loop. As a test of this procedure, consider the hysteresis loop on page 9 of [43], described as

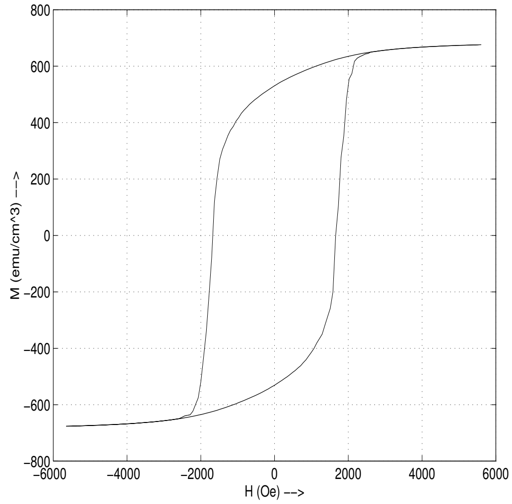

Figure 4.10: Verification of parameter identification procedure

representative of thin-film disk media. The loop parameters are $\delta = 30$ nm (300 Å); $M_r = 537$ kA/m (537 emu/cm^3); $H_c = 132$ kA/m (1658 Oe); $S = 0.78$; $S^* = 0.83$. A good match in the table search is $K_e = 0.10$ and $K_m = 0.05$, with the consequence that $h_c = 0.45$. Completion of the identification procedure as described yields $M_s = 688$ kA/m; $K_A = 126$ kJ/m^3; $f\sqrt{A_e} = 7.81 \times 10^{-6}$ (J/m)$^{-1/2}$; and $\lambda = 81 \times 10^{12}$ m^{-2} (derived from $D = 111$ nm). Using these parameters, a medium patch measuring 4.4μm square was generated comprising 1629 irregular grains. The calculated hysteresis loop for this instance of the medium model is graphed in Fig. 4.10. The units of this hysteresis loop plot are in the Gaussian system for direct comparison with the original loop in [43]. The calculated loop parameters are $M_r = 531$ kA/m (531 emu/cm^3); $H_c = 133$ kA/m (1674 Oe); $S = 0.77$; $S^* = 0.85$, all of which match the prescribed hysteresis loop parameters to within 3% or better. The value of exchange energy constant $f\sqrt{A_e}$ derived from the identification procedure is quite large. However, consideration of the domain wall thickness does not show it to be unreasonable. The domain wall thickness between anti-parallel domains is about 70 nm, which is less than the grain size D of 111 nm. For future simulations, we adopt these parameters as a default set of values for representing recording media.

Of course, the agreement of calculated and measured hysteresis loops is not by any means a verification that we have selected a uniquely correct set of model parameters to represent the medium for which we have a measured hysteresis loop. We used the hysteresis loop as the basis of our parameter identification. It is not surprising that a test of the ability of the derived parameters to reproduce hysteresis

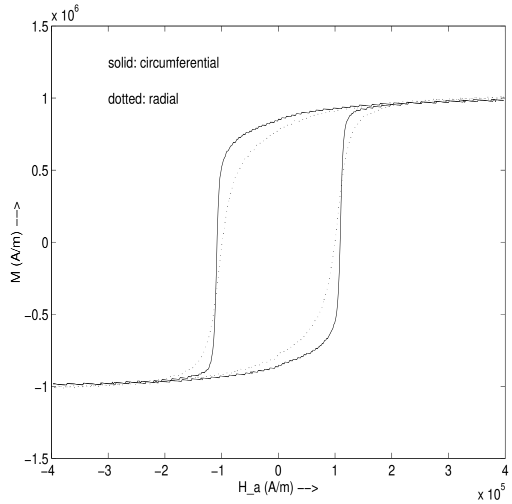

Figure 4.11: Measured hysteresis loops of recording medium sample

loops succeeds. A more remarkable test would be to show agreement between model calculations and experimental measurements for another independent measurement. One possibility is to compare the results of recording experiments to recording simulations, discussed in the next section.

The next test of our identification procedure is to apply it to actual VSM measurements. Fig. 4.11 is a plot of the hysteresis loops measured from a sample of thin-film Co-based recording medium used in the manufacture of commercial magnetic disk storage devices in the early 1990s. The sample is a 1 cm diameter circle cut from the disk, and marked so that its radial and circumferential directions could be distinguished. A magnetic layer thickness of 50 nm was assumed in the generation of Figure 4.11 from the raw measured data. Figure 4.11 shows that the hysteresis properties of the sample vary with orientation. In the circumferential direction, the loop parameters are $H_c = 108$ kA/m; $M_r = 856$ kA/m; $S = 0.84$ and $S^* = 0.95$. In the radial direction, the loop parameters are $H_c = 99$ kA/m; $M_r = 780$ kA/m; $S = 0.77$ and $S^* = 0.73$. Clearly such properties indicate an oriented medium, and we must permit $\rho \neq 1$ in our model to represent such a medium. However, our identification procedure is based on the assumption that $\rho = 1$. Identification of model parameters for this experimental measurement must wait until the identification procedure is extended to account for the possibility of oriented media.

4.2.3 Algorithm Verification

Before proceeding to the next section, let us tie up a few loose ends. In Chapter 3, two possible problems with the model's magnetic state evolution algorithm were identified. First, the possibility was noted that the algorithm could terminate in a magnetic state which was not a local minimum of total magnetic energy, but only a saddle point of the energy. Second, the concern was raised that the sequential alignment of single grains to their local energy minimum orientation might lack physical plausibility since such updating skips all the intermediate magnetization states. In this section, we note the results of simulations which allay these concerns.

An additional local minimum verification routine is included in the simulation software which computes the full Hessian matrix, determines its eigenvalues, and on the discovery of a negative eigenvalue, reports that the Hessian matrix is not non-negative definite. This condition indicates that the stable state calculated by the algorithm is a saddle point rather than a local minimum. This routine is expensive, both in processing time and use of computer memory, so it is not used routinely. For a modest number of grains, however, it may be employed to allay concerns. A full hysteresis loop was calculated for 82 grains with the verification routine active. The medium properties were those determined by the example identification procedure earlier in this section. An entire loop was calculated without detection of a saddle point falsely claimed to be a local minimum. Although this test is not a definitive verification of the algorithm employed, it does indicate that the potential problems with it do not occur regularly when simulating the behavior of our default recording medium. Future work should aim toward an algorithm which efficiently avoids this identified weakness.

The second concern is addressed by the simulation results depicted in Fig. 4.12. Hysteresis loops were calculated for the default recording medium parameters using two distinct algorithms: the Lagrange multiplier algorithm, and the alternative algorithm in which the maximum rotation of a magnetization vector in a single step is limited to no more than 0.1 radians. As can be seen in Fig. 4.12 the differences in the calculated loops are only very small ones in the region of reversal. The computation times required, however, are quite different. The Lagrange multiplier algorithm completes the calculation of a full hysteresis loop in about 73 minutes. The limited rotation algorithm requires 148 minutes. Since there is so little difference in the calculated results, the Lagrange multiplier algorithm is clearly preferred.

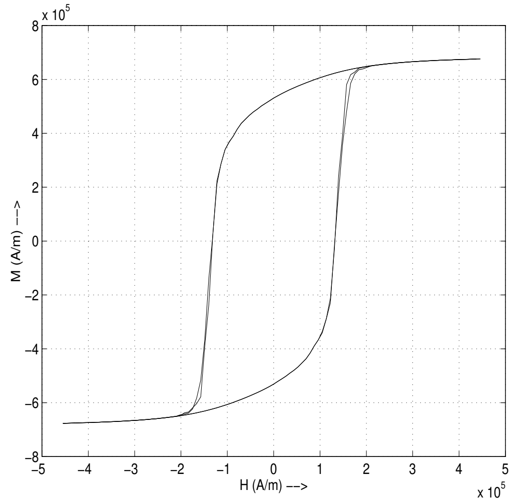

Figure 4.12: Comparison of results from two algorithms

4.2.4 Effect of Grain Structure

Up to this point, all hysteresis loops have been calculated for instances of the model with irregular grain structure. Now, we briefly consider what effect the grain structure may have on the calculated hysteresis loops.

The first hysteresis loop calculations were for a single Stoner-Wohlfarth particle. The equations describing the magnetization response of a Stoner-Wohlfarth particle to an applied field do not include any influence of the particle shape. Likewise, when an assembly of non-interacting grains is simulated, the results are the same as if each single Stoner-Wohlfarth particle in the assembly were investigated separately, and the results were averaged. Thus, when there are no interactions in the model ($K_e = K_m = 0$), the grain structure has no influence on the calculated hysteresis loop.

When interactions are added, the possibility arises that grain structure may have an effect on the calculated hysteresis loops. Fig. 4.13 displays three calculated hysteresis loops for media represented by our default parameters (so that $K_e = 0.10$ and $K_m = 0.05$). The only differences in the model for these three loops are microstructural. The three loops represent a square grain structure, a hexagonal grain structure, and an irregular grain structure, all with the same average grain size. The particular set of anisotropy easy axes are different as well. The calculated loops do not show a great deal of difference. The coercivity squareness values for the regular grain structures are slightly larger than that for the irregular grain structure. This

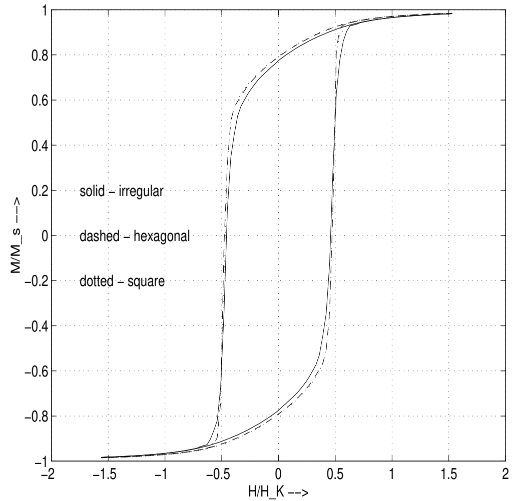

Figure 4.13: Effect of grain structure for small interactions

Table 4.4: Hysteresis parameter variation with grain structure

Microstructure	h_c	S	S^*
Irregular	0.46	0.75	0.71
Hexagonal	0.33	0.83	0.87
Square	0.29	0.81	0.72

result indicates that for our default medium material properties, the effect of grain structure is not a major concern.

For larger interactions, though, grain structure can have a marked effect on the calculated hysteresis loops. Fig. 4.14 displays three calculated hysteresis loops for media with material parameters represented by $K_e = 0.10$ and $K_m = 0.20$. Again, the microstructures represented are square grain structure, hexagonal grain structure, and an irregular grain structure, all with the same average grain size. This time, the different grain structures yield significantly different values for the loop parameters of remanent magnetization and coercivity. Table 4.4 summarizes the different hysteresis properties calculated by model instances with different microstructures. In particular, the coercivity value predicted for an irregular grain structure is more than 30% larger than that for the regular (square or hexagonal) structures. Since the value of coercivity plays a key role in magnetic recording, it is important that this result be explained. It must be determined whether models with regular microstructure underestimate coercivity, or models with irregular microstructure overestimate it. Schrefl, Fidler, and Kronmüller have also observed differences in the calculated coercivity for

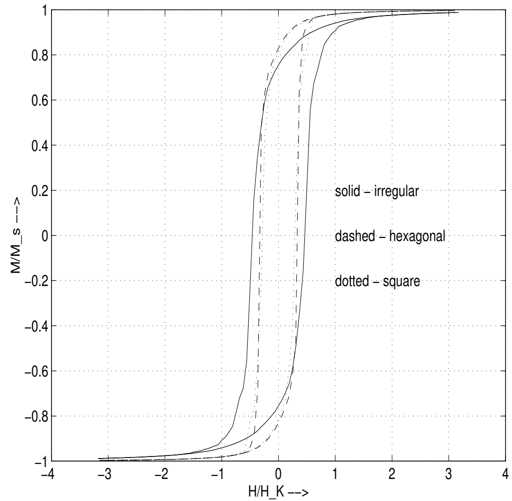

Figure 4.14: Effect of grain structure for larger interactions

irregular grain structures as compared with regular grain structures [104] in micromagnetic models of nanocrystalline permanent magnets [103, 105]. In their model, however, regular grain structures have the effect of *increasing* coercivity. The models are very different, and represent materials with different properties, so it is not alarming that they calculate different results. These results do demand further investigation, however, and resolving this matter is one of the most vital issues to be addressed in future work.

4.3 Recording Simulations

The second major category of simulations involving the medium model are simulations of the recording and playback of information-bearing signals to and from the medium. In particular, we are interested in demonstrating some of the features of playback signals observed in experimental measurements on a recording tester, including the variation of medium noise power with magnetization state, and the high correlation between separately measured particulate noise waveforms read back from the same location on a recording medium, which is also in the same magnetic state [39, 38].

The calculation of playback voltage waveforms representing the response of a Karlqvist model of an inductive head to a recorded magnetic pattern has been discussed in detail in previous chapters. The Karlqvist model includes several parameters in addition to those of the medium model. There are also parameter values to be defined which describe the head-medium interface. Table 4.5 summarizes the

Table 4.5: Head and head-medium interface parameter values

Parameter	*Symbol*	*Value*	*Units*
Gap Length	g	180	nm
Flying Height	d	25	nm
Head-Medium Velocity	V	10	m/s
Deep-gap Field per Amp	H_g	55.6	$(\mu m)^{-1}$
Write Head Width	-	2.5	μm
Read Head Width	W	2.0	μm

parameter values used in the calculation of playback voltage waveforms. The parameter values are representative of a thin-film head with narrower gap length and lower flying height than currently available in commercial drives. These values have been selected to give the simulated playback voltage waveforms finer resolution (smaller pulse width at half-height). This fine resolution is useful in simulating the narrow tracks and closely spaced transitions required for high density recording. In practice, the fine resolution required is attained by use of magnetoresistive (MR) heads in the playback process. Rather than complicate matters further here with a discussion of MR head technology, we continue to use the Karlqvist inductive head model, with parameters chosen to attain the necessary resolution of medium noise features.

Within the framework of the medium model, we may represent ideal recording without medium noise, recording with perfectly repeatable medium noise, and a realistic representation of recording with medium noise which exhibits both repeatable and non-repeatable components. We now consider each of these cases in turn.

4.3.1 Ideal Recording

The idealized view of longitudinal digital magnetic recording was presented in Chapter 1. The ideal view assumes a written track comprises regions magnetized alternately in opposite directions. The regions are assumed to be magnetized perfectly along the track, in one direction or the opposite. Furthermore, the magnetization is assumed to be fully saturated, and the transition from one region to the next is assumed to be perfectly sharp. Under these assumptions, a read-back waveform may be predicted as a deterministic function.

The medium model is able to satisfy all of the assumptions of ideal recording by appropriate selection of the model parameters. In order to align all grain magnetizations with the direction of the recorded track, we assume a perfectly oriented

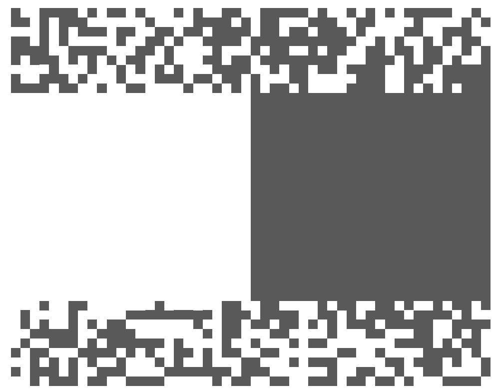

Figure 4.15: Ideal recording of a single transition

medium, one in which all easy axes are aligned with the track. Setting the value of ρ to zero achieves this constraint. A perfectly sharp transition requires two additional constraints on the model. First the grain structure must permit a perfectly sharp and square transition to be defined along the boundaries of grains. This implies a rectangular grain structure. Second, the perfectly sharp transition must be a stable state. When the grains are non-interacting, any magnetic state in which grain magnetizations are aligned with easy axes is stable. Therefore, we add the constraints to the model that it be composed of non-interacting grains ($K_e = K_m = 0$) in a rectangular grain structure.

Fig. 4.15 displays the constrained model's representation of a recorded track with a single transition. The size of the total patch represented in Fig. 4.15 is 5.55μm long by 4.44μm wide. In the coordinate system of the model, the medium patch lies in the range of x between -1.275μm and 4.275μm and in the range of z between -2.22μm and 2.22μm. A 2.5μm wide track was "recorded" with a transition at $x = 1.5\mu$m by directly setting the magnetization of grains within the track width to positive saturation for grains with centroid x coordinates less than 1.5μm, and to negative saturation for grains with centroid x coordinates more than 1.5μm. Because there are no interactions, this recorded pattern is a stable state, and is the pattern which gives rise to the playback voltage waveform. The magnetization profile is an ideal step function from $+M_s$ to $-M_s$ at $x = x_0 = 1.50278\mu$m. The slight displacement from 1.5μm arises because the grain structure demands the transition occur at grain boundaries. We have already derived the Karlqvist playback waveform as a function of the magnetization pattern on a rectangular grain structure (3.21), and for the ideal transition we derive

$$v_I(t) = -\frac{\mu_0 V H_g \delta M_s W}{\pi} \sum_k [s_k - s_{k-1}] f(x_k - Vt), \tag{4.39}$$

where $s_k \in \{\pm 1\}$ specifies the magnetization direction of grain k, $+1$ for grains with centroid x-coordinate less than x_0 and -1 for grains with centroid x-coordinate greater than x_0. x_k is the x-coordinate of the left edge of grain k, and

$$f(u) = \tan^{-1} \frac{g/2 - u}{d + \delta/2} + \tan^{-1} \frac{g/2 + u}{d + \delta/2}. \tag{4.40}$$

The voltage pulse has a peak value at $t = x_0/V$ of

$$v_p = v_I(x_0/V) = \frac{4}{\pi} \mu_0 V H_g \delta M_s W \tan^{-1}(\frac{g}{2d + \delta}) \approx 42.29 \mu\text{V}, \tag{4.41}$$

and a pulse width at half height (in downtrack distance, not time) which satisfies

$$PW_{50}^2 = g^2 + (2d + \delta)^2, \tag{4.42}$$

so that

$$PW_{50} \approx 197\text{nm}. \tag{4.43}$$

The playback voltage pulse calculated by the model is displayed in Fig. 4.16. It differs from the predicted expression only by the small amount of controlled error introduced by the truncation of sums in the calculation as discussed in detail in Chapter 3.

The ideal recording of a sequence of bits may be achieved as a sequence of such ideal transitions. So long as they are well-separated, the playback voltage waveform will be a sequence of ideal pulses with every other one inverted. If the length of the recorded bit cells is too small, however, the playback pulses will overlap and intersymbol interference (ISI) will adversely affect the signal. It is clear then that ISI may be present even in a system where the medium behavior is ideal, as it arises from the blurring action of the head in transforming the magnetization patterns into a voltage waveform. Thus, equalization techniques to overcome ISI are a field of study separable from the study of medium noise. Since we are interested in sources of medium noise, we shall ignore the issue of ISI. Instead, we focus only on the way deviations of the model away from the constraints of ideality affect the playback voltage waveform.

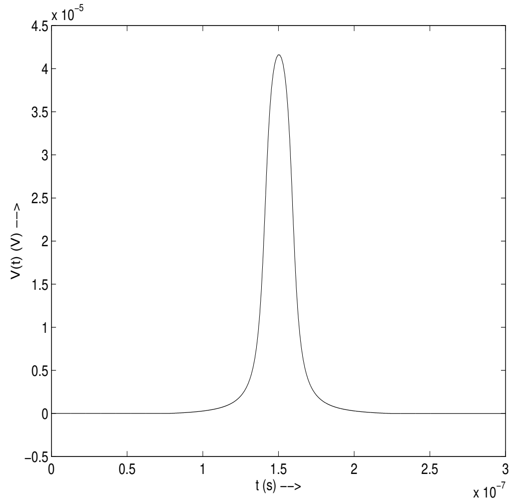

Figure 4.16: Ideal playback of a single transition

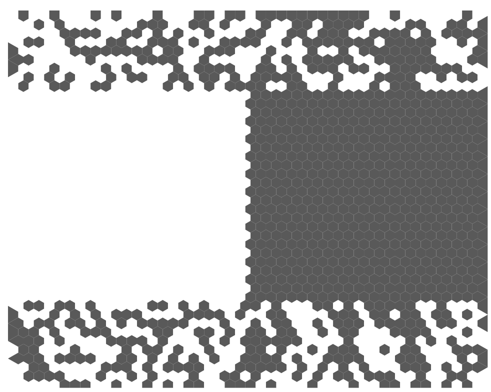

Figure 4.17: Ideal single transition recording on hexagonal grains

Before leaving consideration of ideal recording behind, we consider the alternative choices for grain structure. Although strictly ideal recording is not possible for non-rectangular grain structure, we may simulate recording which is as nearly ideal as the grain structure will allow. For hexagonal grain structure, Fig. 4.17 displays an ideal representation of a recorded track with a single transition, and Fig. 4.18 displays the playback voltage response calculated by the model. For an irregular grain structure, Fig. 4.19 displays an ideal representation of a recorded track with a single transition, and Fig. 4.20 displays the playback voltage response calculated by the model. In both instances, the playback voltage pulse has a reduced peak value and a larger pulse width at half-height than strictly ideal recording, due to the non-square transition structure.

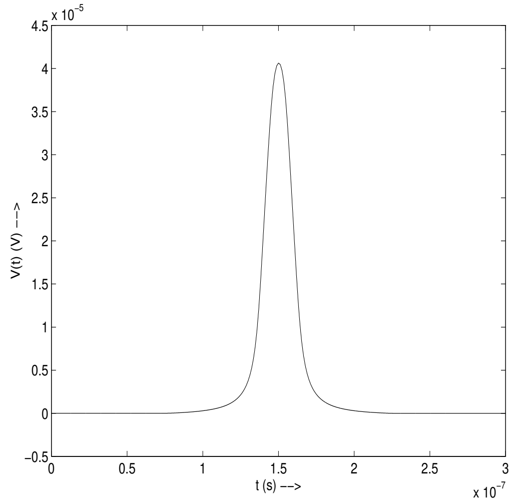

Figure 4.18: Ideal single transition playback from hexagonal grains

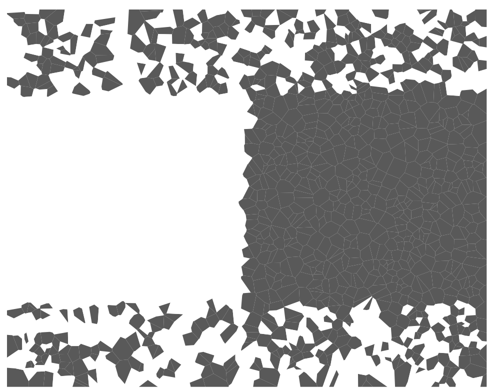

Figure 4.19: Ideal single transition recording on irregular grains

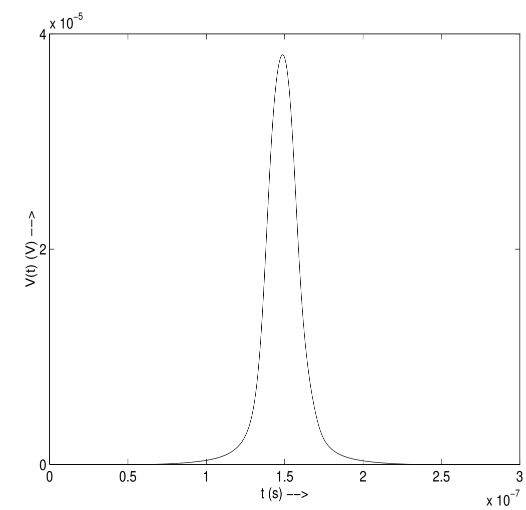

Figure 4.20: Ideal single transition playback from irregular grains

4.3.2 Repeatable Medium Noise

Let us now consider the removal of some of the constraints which led to ideal recording behavior. First, we consider the effect of a medium which is not perfectly oriented. In the terminology of the model, we consider the possibility that $\rho \neq 0$. Let the other constraints of ideality remain in effect: the grains are non-interacting, and the grain structure is rectangular. The playback waveform in this situation is expressed as in (3.21). Since the grains are non-interacting, each grain magnetization is aligned parallel to its easy axis, with direction determined by the recorded pattern.

First consider a recorded track so narrow that it consists of a single row of rectangular grains of with Z. Assume the grain indices k are ordered so that they increase incrementally down the recorded track. Then the playback voltage may be expressed

$$v(t) = -\frac{\mu_0 V H_g \delta M_s Z}{\pi} \sum_k \left[s_k \cos\theta_k - s_{k-1} \cos\theta_{k-1} \right] f(x_k - Vt). \tag{4.44}$$

Then consider assembling a track out of several of these narrow tracks laid side by side. The number of narrow tracks in the whole track is

$$N_t \stackrel{\triangle}{=} W/Z, \tag{4.45}$$

which we will assume to be integer-valued. The total playback voltage from the whole track may then be expressed

$$v(t) = -\frac{\mu_0 V H_g \delta M_s W}{\pi} \sum_k \left[s_k \left(\frac{1}{N_t} \sum_{l=1}^{N_t} \cos\theta_{k,l} \right) - s_{k-1} \left(\frac{1}{N_t} \sum_{l=1}^{N_t} \cos\theta_{k-1,l} \right) \right] f(x_k - Vt). \tag{4.46}$$

The sums over l take the average of identical functions of independent, identically distributed random variables. When the track width W is much larger than the grain width Z, these averages may be approximated by expected values over the random anisotropy axis orientation angles $\theta_{k,l}$. In this limit, the playback waveform is

$$\bar{v}(t) = -\frac{\mu_0 V H_g \delta M_s W}{\pi} E_\theta\{\cos\theta\} \sum_k \left[s_k - s_{k-1} \right] f(x_k - Vt). \tag{4.47}$$

Where there is no transition, $s_k = s_{k-1}$, for all k, and the playback voltage waveform is zero-valued everywhere. When there is a transition, other simplifications may be made. For the non-interacting grains assumption, the expected value is recognized from our hysteresis simulations as the remanence squareness of the medium,

$$S = E_\theta\{\cos\theta\}, \tag{4.48}$$

so that by the relationship $M_r = SM_s$ we may write

$$\bar{v}(t) = -\frac{\mu_0 V H_g \delta M_r W}{\pi} \sum_k \left[s_k - s_{k-1}\right] f(x_k - Vt). \tag{4.49}$$

This expression is different from the ideal playback waveform expression only by substitution of M_r for M_s. Therefore, even when a medium is not perfectly oriented, the ideal playback waveform expression is still useful for wide tracks.

In order to increase areal storage density, however, tracks have grown narrower in comparison to the width of magnetic microstructural features. The replacement of the cross track averages with expected values is no longer a good approximation. The spatial variations of magnetization arising from the spatial variation of easy axis orientation give rise to responses in the playback voltage waveform which do not sum to zero. For tracks of these widths, the expression (4.49) represents only an expected value of the playback waveform. If the same magnetic pattern is recorded at many different locations on a medium, and the average of all the playback voltage waveforms is taken, we expect the average to converge to the expression (4.49) as the number of locations included in the average increases. When a single location is considered, however, there is no such convergence, because the random variables representing the easy axis orientations have their values fixed at the time of manufacture. As a consequence, the same non-ideal features of the playback voltage waveform will be calculated each time the same pattern is recorded at the same location as represented by the medium model. We may write

$$v(t) = \bar{v}(t) + n_m(t) \tag{4.50}$$

The local "medium noise" $n_m(t)$ is repeatable.

Fig. 4.21 displays the model's representation of a recorded track on non-oriented media ($\rho = 1$) with a single transition. The same patch size and coordinate system are used as in the ideal recording simulations. The corresponding playback waveform $v(t)$ is displayed in Fig. 4.22 as a solid line, along with the expected playback voltage waveform $\bar{v}(t)$ for a very wide track as a dashed line. The difference between

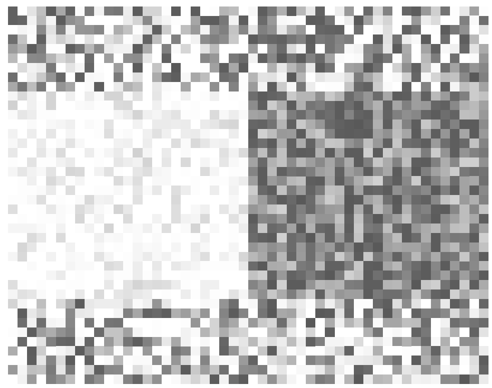

Figure 4.21: Single transition recording on non-interacting square grains

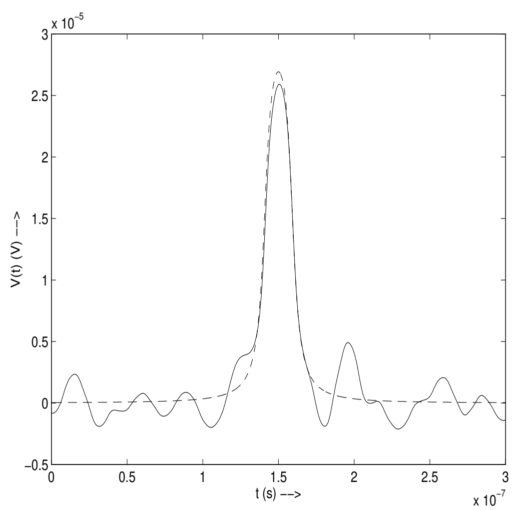

Figure 4.22: Single transition playback from non-interacting square grains

these two waveforms is the quantity $n_m(t)$ known as "medium noise." The reader is cautioned that the term "noise" in no way implies uncertainty or randomness. Given the fixed microstructure represented by the easy axis orientation angles $\theta_{k,l}$ and the magnetization pattern recorded on the track, the solid waveform of Fig. 4.22 is a *deterministic function*. It is only "noisy" in the sense that it deviates from the ideal dashed waveform.

Although medium noise as represented thus far by our model is a deterministic quantity, we may consider the statistical representation of the variation of medium noise waveforms arising from many different recording locations. Averaging playback waveforms from identical recorded patterns at a large number of different recording locations corresponds to taking the expected values over the microstructure random variables. Such a procedure is frequently used experimentally to characterize the noise properties of a recording medium [53, 54, 136].

Consider again a track so narrow that it includes a single row of rectangular grains. The expected value of the playback voltage waveform arising from that narrow track we have already seen to be equal to the wide track waveform. Therefore, the ensemble of medium noise waveforms observed over many locations has an average value of zero. So long as the proper interpretation of randomness is made, $n_m(t)$ is a zero-mean random process. To consider the noise power, we turn to the covariance function of an ensemble of waveforms $v(t)$ measured from many medium locations. The covariance function is defined

$$C_v(t_1, t_2) \triangleq E\{v(t_1)v(t_2)\} - E\{v(t_1)\}E\{v(t_2)\}. \tag{4.51}$$

For simplicity, let us consider medium noise only in a region without transitions. That is, we consider the particulate noise power predicted by this version of the model. Without transitions,

$$E\{v(t_1)\} \equiv E\{v(t_2)\} \equiv 0, \tag{4.52}$$

and the covariance function of $v(t)$ can be shown to be

$$\begin{aligned} C_v(t_1, t_2) \quad = \quad & \mathrm{Var}\{\cos\theta\} \left(\frac{\mu_0 V H_g \delta M_r W}{\pi}\right)^2 \cdot \\ & \sum_k \left[2f(x_k - Vt_1)f(x_k - Vt_2) - f(x_k - Vt_1)f(x_{k-1} - Vt_2)\right. \\ & \left.-f(x_k - Vt_1)f(x_{k+1} - Vt_2)\right], \end{aligned} \tag{4.53}$$

where

$$\mathrm{Var}\{\cos\theta\} \triangleq E\{\cos^2\theta\} - E^2\{\cos\theta\}. \tag{4.54}$$

For a track made up of N_t independent narrow tracks, the covariance expression will be scaled by $1/N_t$, which is equal to Z/W. Therefore, for a track of width W made up of N_t independent narrow tracks of width Z, the covariance function is expressed

$$\begin{aligned} C_v(t_1, t_2) \quad = \quad & \mathrm{Var}\{\cos\theta\} \left(\frac{\mu_0 V H_g \delta M_r}{\pi} \right)^2 \cdot WZ \cdot \\ & \sum_k \left[2f(x_k - Vt_1) f(x_k - Vt_2) - f(x_k - Vt_1) f(x_{k-1} - Vt_2) \right. \\ & \left. - f(x_k - Vt_1) f(x_{k+1} - Vt_2) \right]. \end{aligned} \tag{4.55}$$

The noise power profile is

$$NP(t) \triangleq C_v(t,t), \tag{4.56}$$

which we can see is proportional to track width. Signal power is proportional to the square of track width, and it is because of expressions such as this that it is said that signal-to-medium-noise ratio decreases as tracks become narrower. It must be remembered, though, that this interpretation is only valid as a description of ensembles of playback voltage waveforms measured from many recording locations. At any single location, the model as currently constrained predicts a single deterministic medium noise waveform for any recorded pattern.

The covariance, and therefore the noise power, are also proportional to $\mathrm{Var}\{\cos\theta\}$. This quantity is entirely determined by the value of ρ in our model, by the expression

$$\mathrm{Var}\{\cos\theta\} = \frac{1}{2} + \frac{\sin\rho\pi}{2\rho\pi} - \frac{4\sin^2\frac{\rho\pi}{2}}{\rho^2\pi^2}. \tag{4.57}$$

For $\rho = 0$, we also have $\mathrm{Var}\{\cos\theta\} = 0$, which agrees with the observation that perfectly oriented media generate playback voltage waveforms with no medium noise. For a non-oriented medium ($\rho = 1$), we have

$$\mathrm{Var}\{\cos\theta\} = \frac{1}{2} - \frac{4}{\pi^2} \approx 0.0947. \tag{4.58}$$

Finally, note that the covariance function of $v(t)$ cannot be expressed as a function of the difference between t_1 and t_2. That is, when considered as a random

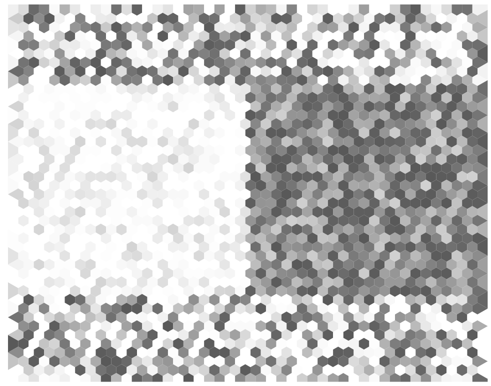

Figure 4.23: Single transition recording on non-interacting hexagonal grains

process, $v(t)$ is not stationary, and therefore, the medium noise $n_m(t)$ is not a stationary random process. Instead it exhibits a dependence on the underlying granularity of the medium microstructure.

Similar studies of the statistics of medium noise predicted by the model may be performed when there is a recorded signal present, though they will be more complicated. Such a study should be pursued in future work.

Before concluding this section, we also use the model to predict the repeatable medium noise waveforms from other grain structures. Although the analysis for these structures is not as straightforward as for rectangular grain structure, the computer simulations work equally well. Fig. 4.23 displays the model's representation of a recorded track with a single transition on non-oriented media with hexagonal grain structure. The corresponding playback waveform $v(t)$ is displayed in Fig. 4.24. Fig. 4.25 displays the model's representation of a recorded track with a single transition on non-oriented media with irregular grain structure. The corresponding playback waveform $v(t)$ is displayed in Fig. 4.26.

4.3.3 Non-repeatable Medium Noise

The medium noise waveforms predicted in the preceding section had several desirable properties. However, the model considered in that section was constrained to have non-interacting grains. With no interactions, every magnetic pattern with local magnetization vectors aligned with easy axes is a stable state. As a consequence the repeatability of medium noise waveforms is not a remarkable simulation result, but a direct consequence of the particular model constraints applied. In this section, we

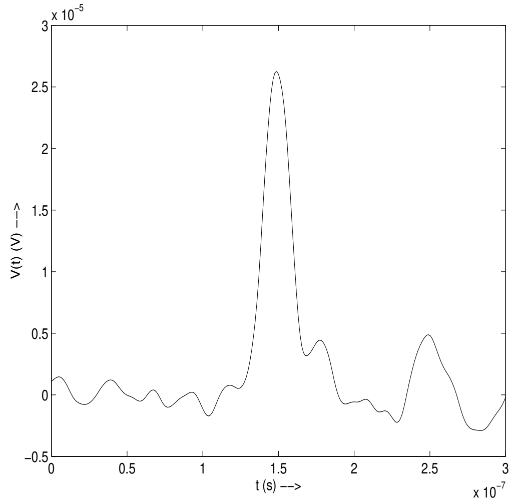

Figure 4.24: Single transition playback from non-interacting hexagonal grains

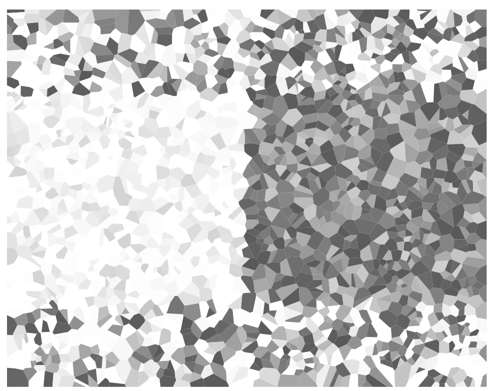

Figure 4.25: Single transition recording on non-interacting irregular grains

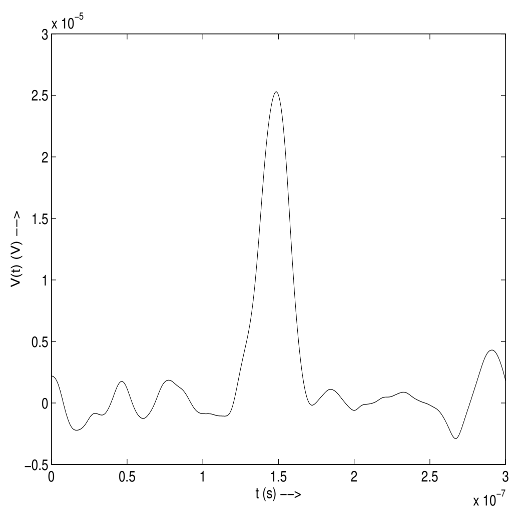

Figure 4.26: Single transition playback from non-interacting irregular grains

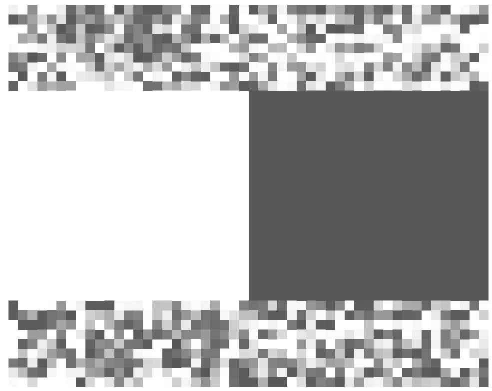

Figure 4.27: Initial state: recording of a single transition

permit grain interactions and see to what degree the desirable medium noise properties are retained. We make use of the default parameters values derived from our parameter identification procedure to match the hysteresis properties of the "typical recording medium" in [43]. Therefore, the interaction constants have values $K_e = 0.10$ and $K_m = 0.05$. As in the parameter identification procedure, we will assume in this section that we are working with non-oriented media ($\rho = 1$).

The simulation proceeds as follows. Fig. 4.27 displays the representation of a recorded track with a single transition. The patch size and coordinate system are the same as for previous simulations. A 2.5μm wide track was "recorded" with a transition at $x = 1.5\mu$m by directly setting the magnetization of grains within the track width to positive saturation for grains with centroid x coordinates less than 1.5μm, and to negative saturation for grains with centroid x coordinates more than 1.5μm. Then a rotation-relaxation algorithm is applied to the medium model. The rotation-relaxation algorithm is applied 50 separate times, each time beginning with the state depicted in Fig. 4.27. One of the stable states arrived at by the rotation-relaxation algorithm is displayed in Fig. 4.28 Because we employ a randomized relaxation algorithm, the particular stable computed by the simulation will vary from one run to the next. As a consequence, the playback voltage waveform will also have some variability. There will not in general be perfect repeatability. Fig. 4.29 is a plot of all 50 playback voltage waveforms calculated by this set of simulations. There is indeed variation from one playback waveform to the next. However, there are also features which all the waveforms share in common. The medium noise may be said to have a repeatable component as well as a non-repeatable component.

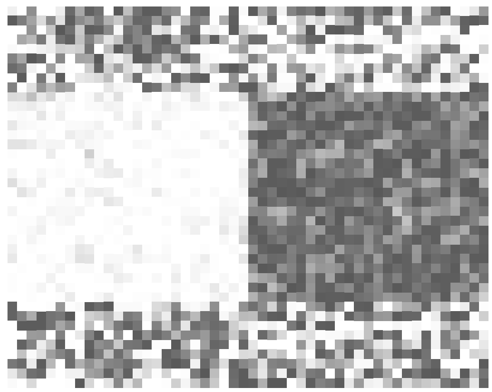

Figure 4.28: Example stable state: recording of a single transition

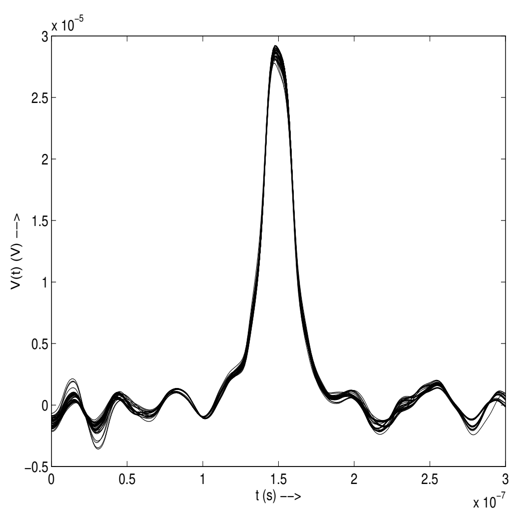

Figure 4.29: Ensemble of playback waveforms from a single transition

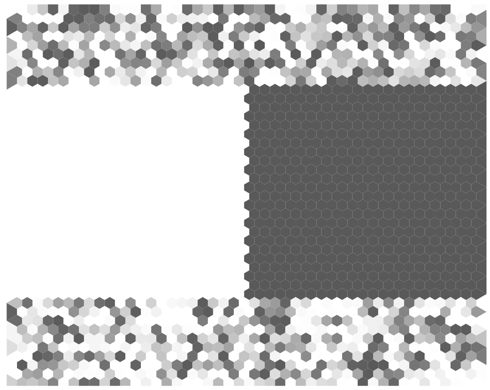

Figure 4.30: Initial state: recording of a single transition

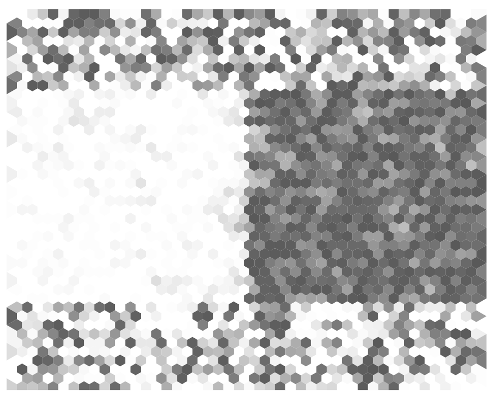

Figure 4.31: Example stable state: recording of a single transition

Similar simulations for other grain structures yield similar results. Fig. 4.30 displays the representation of a recorded track with a single transition, this time recorded on a medium with hexagonal grain structure. A rotation-relaxation algorithm is applied to the medium model 50 separate times, each time beginning with the state depicted in Fig. 4.30. One of the stable states arrived at by the rotation-relaxation algorithm is displayed in Fig. 4.31, and Fig. 4.32 is a plot of all 50 playback voltage waveforms calculated by this set of simulations. Fig. 4.33 displays the representation of a recorded track with a single transition, this time recorded on a medium with irregular grain structure. A rotation-relaxation algorithm is applied to the medium model 50 separate times, each time beginning with the state depicted in Fig. 4.33. One of the stable states arrived at by the rotation-relaxation algorithm is displayed in Fig. 4.34, and Fig. 4.35 is a plot of all 50 playback voltage waveforms calculated by

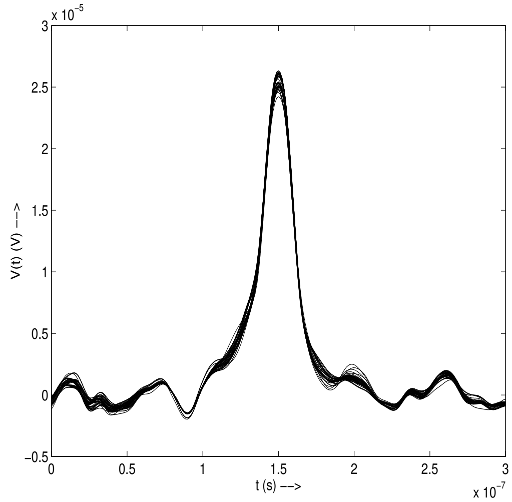

Figure 4.32: Ensemble of playback waveforms from a single transition

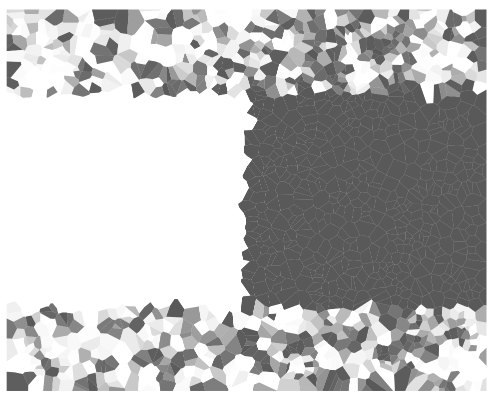

Figure 4.33: Initial state: recording of a single transition

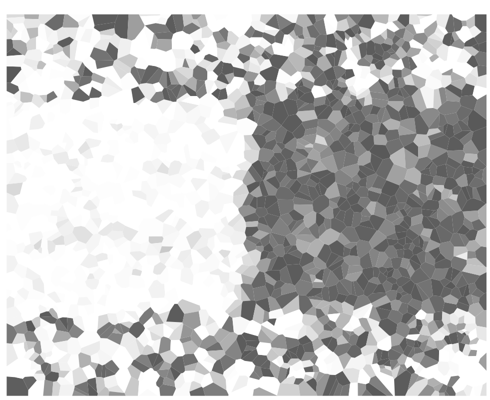

Figure 4.34: Example stable state: recording of a single transition

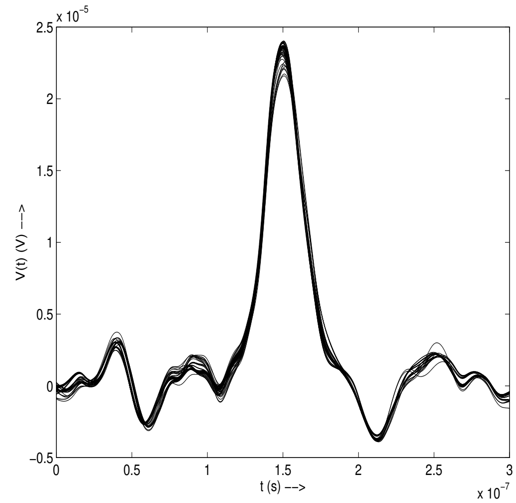

Figure 4.35: Ensemble of playback waveforms from a single transition

this set of simulations. These simulations for media with other types of grain structure also exhibit medium noise with both repeatable and non-repeatable components.

4.3.4 Mirror Imaging

Another type of medium noise repeatability observed in the experiments of Hoinville [38, 39] was the large negative correlation between medium noise waveforms measured at a particular recording location when the recorded magnetization patterns were saturation magnetization in opposite directions. To illustrate the model's ability to generate this type of medium noise repeatability, a patch of medium was generated with dimensions of 15.7μm long by 4.44μm wide In the coordinate system of the model, the medium patch lies in the range of x between -1.1μm and 14.6μm and in the range of z between -2.22μm and 2.22μm. Two separate recording simulations were performed. In the first, a single transition was recorded at $x = 4.5\mu$m. In the second, a single transition was recorded at $x = 9.0\mu$m. The two playback waveforms are displayed in Fig. 4.36. It can be seen that in those regions of the medium where the two recorded patterns have saturation magnetization in the same direction, the medium noise waveforms have large positive correlation. In the middle region where the two recorded patterns have saturation magnetization in opposite directions, the medium noise waveforms have large negative correlation – they appear to be near mirror-images of one another.

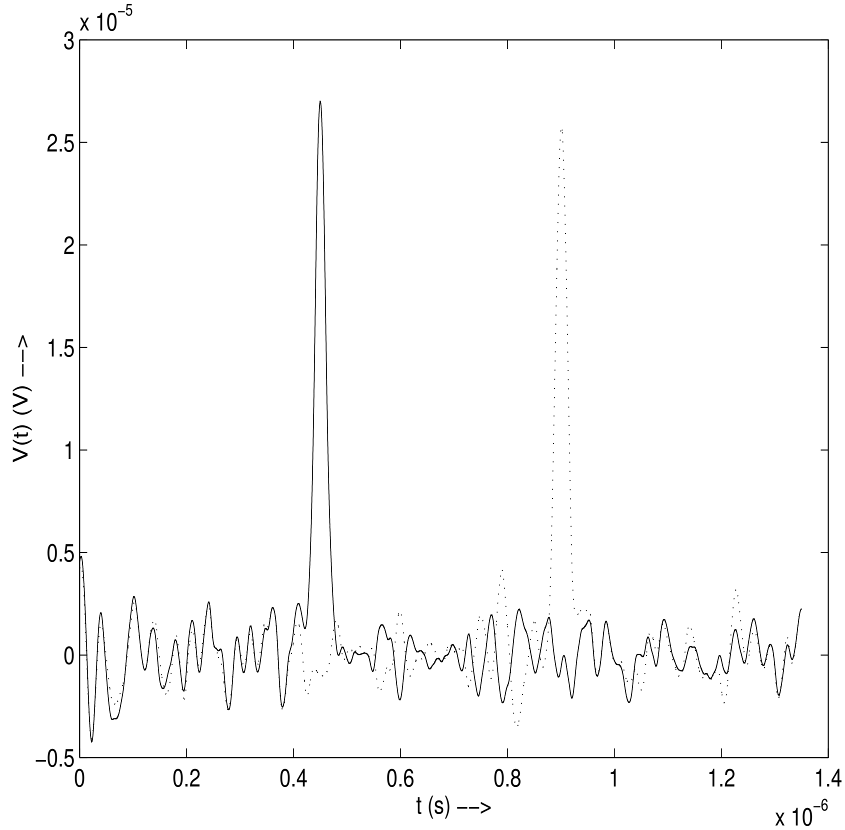

Figure 4.36: Illustration of medium noise mirror image behavior

4.3.5 Write Head Simulation

In all of the recording simulations described so far, the recording process was represented simply by initializing the magnetization vectors of the medium grains to match a desired magnetic pattern. Physical recording is not achieved by such magical means, but by the magnetizing of regions of medium with strong magnetic fields generated by energizing a recording head with a signal current. The Karlqvist model serves as a reasonable representation for the write field generation function of a record head, just as it does for the playback operation. As for the playback operation, its primary weakness is its failure to properly model the head fields at the track edge. Nevertheless, we now consider the simulation of the recording process by simulating the response of the recording medium to the write fields generated by a simulated Karlqvist record head.

The medium model already accounts for an applied field. In simulating the record process, we assume that the applied field component comes from the record head. The Karlqvist model expression for the head fields generated by a current of I amperes driven through the head coil when the record head is at downtrack position x_0 is

$$\mathbf{H}_a(x,z) = \frac{H_g I(x_0)}{\pi}\left(\tan^{-1}\frac{g/2+x-x_0}{d+\delta/2} + \tan^{-1}\frac{g/2-x+x_0}{d+\delta/2}\right)\hat{\mathbf{x}} \qquad (4.59)$$

for z within the width of the write head and zero applied field for z outside the width of the write head. The write current $I(x_0)$ is explicitly shown to be a function of the downtrack position of the head. Fig. 4.37 is a graph of the write current as a function of record head downtrack position. The write current amplitude is 15 mA, a typical value for experimental recording operations. At a downtrack position of $x_0 = 1.5\mu$m, the write current switches from $+15$ mA to -15 mA. This reverses the magnetic fields generated by the record head, so that the magnetization recorded on the medium reverses direction. A transition is thus recorded. In a computer simulation, we must represent the trajectory of the head along the recorded track as a sequence of discrete head positions. The X's in Fig. 4.37 indicate those positions. A denser sampling of the trajectory is used near the transition to improve the accuracy of the simulation in the region of greatest interest. For each discrete record head position, the head fields are calculated and applied to the medium model. A rotation-relaxation algorithm is run until a stable state is reached. Then the head is advanced to the next position in

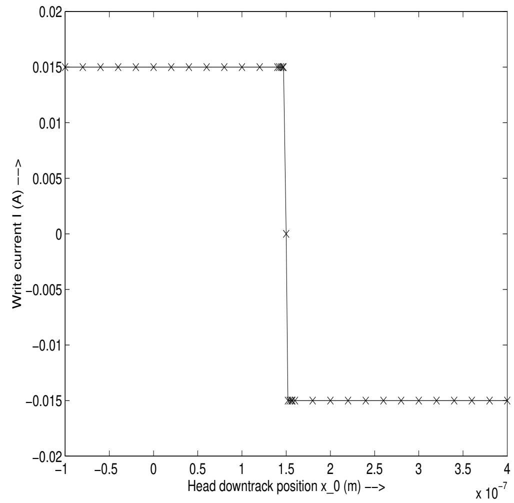

Figure 4.37: Write current for record process simulations

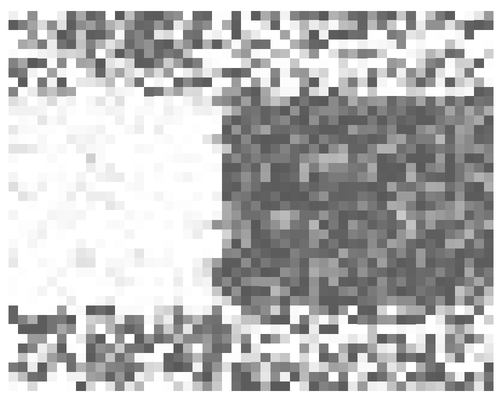

Figure 4.38: Transition recorded by write head simulation

the sequence and the procedure is repeated until the complete record head trajectory has been simulated.

The results of one such simulated recording process are displayed in Fig. 4.38 for a medium with rectangular grain structure. There are two notable features of the recorded transition. First, it exhibits more of a zig-zag structure than the transitions which were generated by an initialization procedure. Second, it is shifted somewhat to the left. The shift is explained by consideration of the write field generated by the head. Write fields above some magnitude will have the effect of magnetizing the medium. The write head generates a write field not only at its location x_0, but over an interval of downtrack positions centered at x_0. For large enough write current I, the medium will be magnetized below the head at x_0, and also at locations to the left of x_0

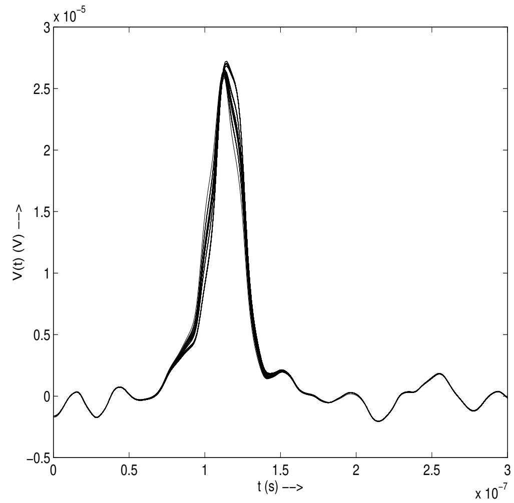

Figure 4.39: Playback waveforms from transitions recorded by write head simulation

as far back as the write field remain sufficiently large. Thus, the recorded transition will always be written some distance to the left of the record head position at the time the write current switches. This feature of magnetic recording is sometimes described by stating that record heads write "with the trailing edge."

The simulation of recording with a Karlqvist record heads was repeated 100 times. For each recorded transition, a playback voltage waveform was calculated. All 100 waveforms are displayed in Fig. 4.39. A comparison with the playback waveforms calculated by previous simulations reveals that the medium noise is far more repeatable away from the transition, and far less repeatable near the transition. This indicates that the properties of medium noise depends not only on the physical and microstructural properties of the medium, but also on the details of the recording process.

As in previous investigations, we may repeat the simulations for other grain structures. For hexagonal grain structure, an example recorded transition is displayed in Fig. 4.40 and a graph of the playback waveforms calculated from 100 separately recorded transitions is displayed in Fig. 4.41. For irregular grain structure, an example recorded transition is displayed in Fig. 4.42 and a graph of the playback waveforms calculated from 100 separately recorded transitions is displayed in Fig. 4.43. The simulations for hexagonal and irregular grain structures yield the same qualitative features as the simulations for rectangular grain structure.

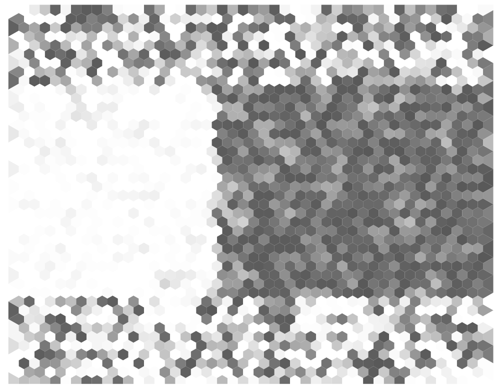

Figure 4.40: Transition recorded by write head simulation

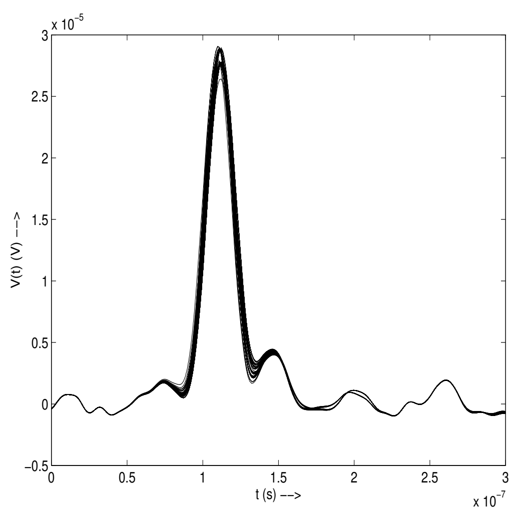

Figure 4.41: Playback waveforms from transitions recorded by write head simulation

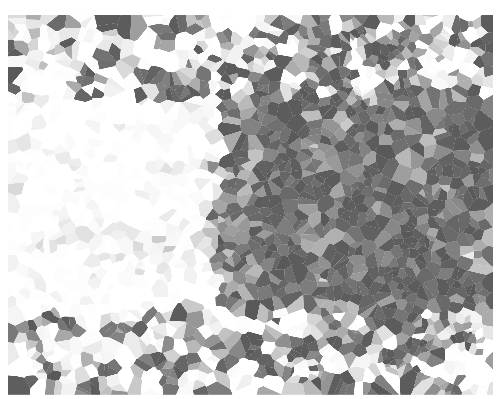

Figure 4.42: Transition recorded by write head simulation

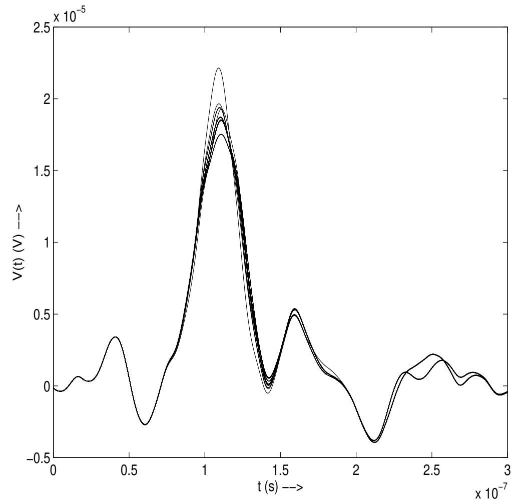

Figure 4.43: Playback waveforms from transitions recorded by write head simulation

4.3.6 Future Recording Simulation Work

Our simulations of recording and playback processes within the framework of the medium model have exhibited qualitative agreement with the experimental medium noise measurements reviewed in Chapter 1. The recording simulations exhibit both a spatially local repeatability, and a mirror imaging property as measured by Hoinville [38, 39]. When an ensemble of medium noise waveforms are calculated from many different recording locations, the statistics of the ensemble are non-stationary, and include the granularity effects of microstructure as the measurements of Mian [70, 71] suggest. Previous recording simulation work [96, 97] also exhibits these properties, but was based on the flip-relaxation algorithm. The results reported here are preferred for their greater physical plausibility.

In order to be more quantitative, we might next apply the Karhunen-Loéve (KL) decomposition [115] to our calculated medium noise waveform ensembles to determine what components, or "noise modes" dominate in our medium noise simulations. The application of KL decomposition to medium noise in magnetic recording has been successfully made before by other researchers [129, 136]. Quantitative characterizations of medium noise could then be applied to both simulated medium noise and experimentally measured medium noise to verify or refute a claim that a particular instance of a medium model is a good representation of a particular physical recording medium. As noted before, however, this investigation must wait for the time being, until our model parameter identification procedure can be extended to consider oriented media, which in practice nearly all recording media are to some degree.

4.4 Summary

The results of many simulations of the medium model were presented in this chapter, divided into two categories, hysteresis loop simulations and recording simulations. Calculation of the hysteresis properties of isolated Stoner-Wohlfarth particles verified the correctness of the magnetic state evolution algorithms which form the heart of the model simulation programs. The remanent magnetization and coercivity of an assembly of non-interacting Stoner-Wohlfarth particles were predicted analytically as functions of model orientation parameter ρ and simulations were found to agree. The effect of exchange and magnetostatic interactions on hysteresis loop properties were investigated both separately and in combination. A table of data was computed, which was subsequently used as the basis for a model parameter identification procedure. This procedure determines the values of the five intrinsic parameters of our micromagnetic medium model which represent material properties given that the following hysteresis properties are known: remanent magnetization, coercivity, remanence squareness, and coercivity squareness. This procedure was then used to select a default set of model parameters to represent a typical magnetic recording medium. Finally, some details of the simulation algorithms were verified and the dependence of hysteresis loop properties on grain structure when the intergranular interactions are large was noted.

Within the category of recording simulations, a special case of the model was identified which could simulate ideal recording. The deviations of the more general model from this special case give rise to responses in the playback voltage waveform which are known as medium noise. For non-interacting assemblies of grains, medium noise is a deterministic function of local microstructure and local magnetic state. Medium noise waveform ensemble calculated for many different recording locations may be described statistically. For non-interacting grains, the statistics of medium noise ensembles was derived as a function of the model orientation parameter ρ and other model parameters. When grains do interact, a non-repeatable component of medium noise arises. So long as the interactions are not too large, however, a repeatable component to medium noise also remains, which arises from the local microstructure. The medium noise calculated by simulation was found qualitatively to have the same features as medium noise measured experimentally. Finally, the simulation of the recording process by calculation of write fields from an energized record head was performed. The calculated medium noise from that set of simulations was markedly different from others, indicating that medium noise depends on the recording process as well as medium material and microstructural properties.

Throughout this chapter several important avenues for future research have been identified. The development of an efficient relaxation algorithm is desired that more rigorously assures a local minimum of magnetic energy, rather than a saddle point. The model parameter identification procedure must be extended to consider the possibility of oriented media. The effect of grain structure on hysteresis properties when intergranular interactions are large requires a fuller explanation. Quantitative analysis of simulated medium noise should be pursued, along with comparison to measured medium noise once a sufficiently strong identification procedure allows the representation of a particular physical recording medium as a particular instance of the recording medium model.

Chapter 5

Storage Density Limits via Simulation

In this chapter, we turn to the stated subject of this thesis, investigation of the fundamental limits of areal storage density on magnetic recording media, as predicted by a micromagnetic model. The principle underlying this investigation is this: only those magnetic states of the medium which persist over long periods of time may be used to store information. According to the model, these states are exactly those which are stable states of the magnetic state evolution algorithm. Thus, determining the number of magnetic states available to store information boils down to counting the number of magnetic states which are stable states of the evolution algorithm. As argued in Chapter 2, the number of fixed points of a flip-relaxation algorithm is conceptually simpler, and is a reasonable proxy for the number of stable states of a rotation-relaxation algorithm. This chapter reports the use of model simulations to compute the number of fixed points, the corresponding limits on storage density, and how these limits vary with the material properties of the recording medium, as represented by the constants K_e and K_m.

5.1 Model Simplifications

We make several additional assumptions and simplifications to the medium model for the sake of this investigation. Although the simplified model is less attractive for predicting the detailed physical behavior of a magnetic recording medium, it serves well as a representation of a medium's limited ability to store information. First let us consider only a regular grain structure of square grains ($X = Z = D$), with bounding box dimensions that are an integer multiple of D, so that all grains are the same shape and have area D^2. Figure 5.1 depicts the simplified microstructure. Second, let us consider only non-oriented media ($\rho = 1$). Third, since our interest is in the storage capability of the medium over long periods of time between recording and playback, assume that the applied field is zero-valued over this interval of time. Finally, let us consider only the flip-relaxation algorithm of magnetic state evolution.

In Chapter 3 the parameters of the model were classified into three types, those representing material properties, those representing microstructure, and those representing magnetic state. Under the simplifications just declared, the microstructure of a medium is completely characterized by the set of easy axis orientation angles, $\{\theta_k\}$. Also, given a particular microstructure, the magnetic state of the medium is completely characterized by the set of magnetization directions, $\{s_k\}$. As shown in Chapter 4, the material properties as represented in the model may be summarized by the pair of parameters (K_e, K_m).

Let us now summarize the equations of the recording medium model, taking into consideration the additional simplifications. The medium is represented by a finite collection of grains, indexed by a set $\mathcal{I}$. Let $|\mathcal{I}| = N$. The normalized magnetization of grain k is expressed

$$\mathbf{m}_k = s_k(\cos\theta_k \hat{\mathbf{x}} + \sin\theta_k \hat{\mathbf{z}}), \tag{5.1}$$

so that the total magnetic state is represented by the vector of sign values $\mathbf{s} \in \{\pm 1\}^N$. The normalized exchange field component for grain k is

$$\mathbf{h}_{e,k} = K_e \sum_{l \in N(k)} \mathbf{m}_l, \tag{5.2}$$

and the normalized magnetostatic field component for grain k is

$$\mathbf{h}_{m,k} = K_m \sum_{\substack{l \in \mathcal{I} \\ l \neq k}} \frac{1}{(p_{kl}^2 + q_{kl}^2)^{5/2}} \begin{bmatrix} 2p_{kl}^2 - q_{kl}^2 & 3p_{kl}q_{kl} \\ 3p_{kl}q_{kl} & 2q_{kl}^2 - p_{kl}^2 \end{bmatrix} \mathbf{m}_l, \tag{5.3}$$

where p_{kl} and q_{kl} are integer-valued displacements indicating the number of columns and rows, respectively, which separate grains k and l. The definitions of the exchange constant K_e and the magnetostatic constant K_m are reprinted here as a convenience

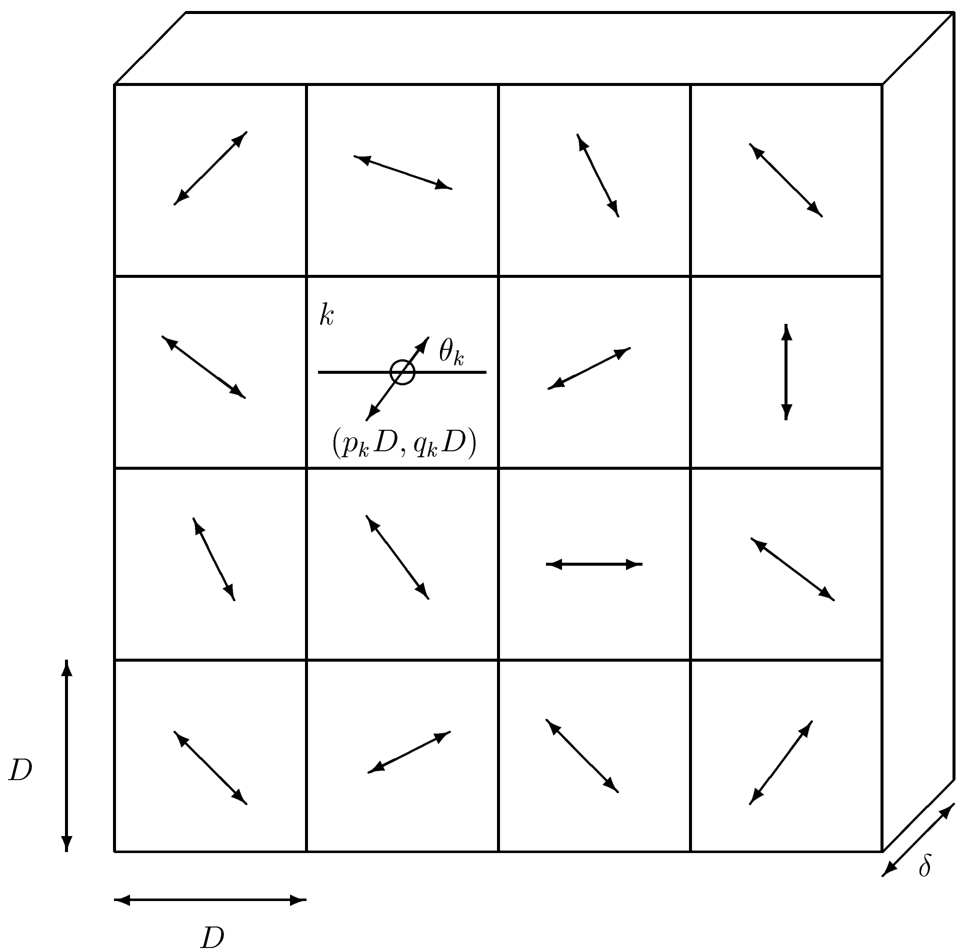

Figure 5.1: Simplified microstructure for density limit analysis

for the reader:

$$K_e \triangleq \frac{f\sqrt{A_e}}{2D\sqrt{K_A}}; \tag{5.4}$$

$$K_m \triangleq \frac{\mu_0 M_s^2 \delta}{8\pi K_A D}. \tag{5.5}$$

The normalized effective field at grain k is the sum of these two components,

$$\mathbf{h}_k = \mathbf{h}_{e,k} + \mathbf{h}_{m,k}, \tag{5.6}$$

which is then resolved into components parallel and perpendicular to the local easy axis,

$$h_{\|,k} = \begin{bmatrix} \cos\theta_k & \sin\theta_k \end{bmatrix} \mathbf{h}_k; \tag{5.7}$$

$$h_{\perp,k} = \begin{bmatrix} -\sin\theta_k & \cos\theta_k \end{bmatrix} \mathbf{h}_k. \tag{5.8}$$

The flip-relaxation update rule (2.77) is

$$s_k^{\text{new}} = U(s_k, \mathbf{h}_k) \triangleq \begin{cases} \operatorname{sgn}(h_{\|,k}), & |h_{\|,k}|^{2/3} + |h_{\perp,k}|^{2/3} \geq 1 \\ s_k, & |h_{\|,k}|^{2/3} + |h_{\perp,k}|^{2/3} < 1 \end{cases}, \tag{5.9}$$

which is applied to grains selected in a pseudo-random sequence. The set of magnetization states which are fixed points of this update rule may then be denoted

$$\Omega = \{\mathbf{s} \in \{\pm 1\}^N : \forall_{k\in\mathcal{I}} : s_k = U(s_k, \mathbf{h}_k(\mathbf{s})).\} \tag{5.10}$$

5.2 Storage Capacity

In this section, we consider the set of fixed points Ω and determine from its cardinality an upper bound on the number of bits which may be stored on the medium as represented by the simplified model. Procedures for computing the upper bound are then presented.

5.2.1 Definition of Storage Capacity

The set of fixed points Ω does not depend on the updating sequence, though it does depend on the particular microstructure, represented by the easy axis orientations, θ_k, and the material properties, represented by K_e and K_m. These parameters are exactly those which specify a particular instance of the simplified medium model.

Specification of a pair of values for K_e and K_m defines the material properties, which are shared by all media manufactured of the same materials by the same process. Specification of the microstructure as values of θ_k defines the particular microstructure of a particular disk, distinguishing it from the lot. The set of stable states, then, will in general be different for each disk represented by the model. When we wish to emphasize the dependence of the set of fixed points on the properties and microstructure of a particular disk, we shall use the notation $\Omega(K_e, K_m, \mathbf{\Theta})$, where $\mathbf{\Theta}$ stands for the entire set of microstructure variables θ_k.

The set $\Omega(K_e, K_m, \mathbf{\Theta})$ contains exactly those magnetic states which persist over long periods of time in the absence of an applied field. Each element $\mathbf{s}$ of Ω may therefore be used as a state with which to store information, and the number of such states may be denoted

$$F(K_e, K_m, \mathbf{\Theta}) \triangleq |\Omega(K_e, K_m, \mathbf{\Theta})|. \tag{5.11}$$

The maximum number of bits which may be stored by the particular medium represented by the instance of the model specified by the values of K_e, K_m, and $\mathbf{\Theta}$ is then

$$B(K_e, K_m, \mathbf{\Theta}) \triangleq \log F(K_e, K_m, \mathbf{\Theta}). \tag{5.12}$$

In this manner, the model can in principle compute the maximum storage limit of any particular medium represented by the simplified model.

The constraints of the simplified model determine an upper bound on the maximum storage limits. The set of all magnetic states is represented by the set of all $\mathbf{s} \in \{\pm 1\}^N$. The set of storage states must be a subset of $\{\pm 1\}^N$, so that

$$F = |\Omega| \leq |\{\pm 1\}^N| = 2^N. \tag{5.13}$$

Thus,

$$B = \log F \leq N, \tag{5.14}$$

that is, a medium represented by N grains can store no more than N bits of information. The definition of a storage capacity

$$\begin{aligned} C(K_e, K_m, \mathbf{\Theta}) &\triangleq \frac{B(K_e, K_m, \mathbf{\Theta})}{N} & (5.15)\\ &= \frac{1}{N} \log F(K_e, K_m, \mathbf{\Theta}), & (5.16) \end{aligned}$$

gives a value computable by the model which characterizes the storage capacity of the represented recording medium in units of bits per grain, with upper limit

$$C(K_e, K_m, \mathbf{\Theta}) \leq 1. \tag{5.17}$$

More commonly, storage density is expressed in units of bits per units area. The capacity C defined above may be converted into a value representing the storage capacity of the medium in units of areal storage density by dividing the capacity C by the area of a single grain D^2. The capacity C is defined above only in terms of the normalized quantities of the medium model. As a consequence, the capacity C is a function of the pair of reduced material property parameters K_e and K_m. However different the material properties of two media may be, if they share the same values of the pair of parameters (K_e, K_m) and the same microstructure $\mathbf{\Theta}$ is assumed in the calculation, then the model will predict the same value of storage capacity C in units of bits per grain. If these two media have different grain sizes D, however, then their storage capacity limits expressed in units of bits per unit area will be different.

In what sense does the quantity C defined above, and termed a "capacity" correspond to the information theoretic notion of a channel capacity? Let us consider the medium model as a communications channel. Its input set is the set of all magnetic states, represented by $\{\pm 1\}^N$. Its output set is the same. The input-output relationship of the channel corresponds to the magnetic state evolution algorithm of the medium model. Therefore, the only output states which will be observed are those belonging to $\Omega(K_e, K_m, \mathbf{\Theta})$. If the input state is taken from the set Ω, the output state will be exactly the input state. That is, so long as the input states are limited to the elements of Ω, the storage operation of the medium, as represented by the simplified model, is a channel with no noise. Its capacity is limited only by the size of its input (or output) set. The Shannon channel capacity of our medium model is then exactly $B(K_e, K_m, \mathbf{\Theta})$ bits of information. Then, division by the number of grains N to get C yields a storage capacity value in terms of which fair comparisons of the storage capacity of media represented by different numbers of grains may be made.

This particular view of the recording medium as a communications channel assumes that all of the magnetic states are available to us as input states, and that all of the magnetic states are distinguishable as output states. This point of view ignores any role played by the limited capabilities of particular recording and playback devices and methods. It reveals only the limits on storage capacity imposed by the internal physics of the medium itself. In this sense the storage capacity defined in this analysis represents a technology-independent upper limit on the storage capacity possible in any recording system using the particular medium under investigation as its recording medium. It may be true that the recording medium ultimately is capable of storing at a density far greater than practical devices are capable of recording and reading. For this reason, the limits calculated by our medium model may be much greater than storage limits which are practically achievable. To the extent that our model is a good representation of physical recording media, however, no recording technology will ever be capable of storing at a density greater than that predicted by the capacity defined above.

One other feature of the storage capacity is noteworthy. In arguing that the capacity represents a density of storage which is achievable given arbitrarily good recording and playback capability, we made an assumption that the input states recorded on the medium would be selected only from the set $\Omega(K_e, K_m, \mathbf{\Theta})$. In order to apply this recording strategy, the set of fixed points Ω must be known. Because Ω depends on the local microstructure represented by $\mathbf{\Theta}$, it follows that the local microstructure must be known. If the local microstructure is not known, we do not expect to be able to record at the density predicted by the medium storage capacity C. Instead, the density of storage will be limited to a smaller value. A simple investigation of the limiting effect on storage density when local microstructure is unknown will be described in Chapter 6.

5.2.2 Calculation of Storage Capacity

Calculation of the number of fixed points by computer simulation may be accomplished by a brute-force counting method. The number of fixed points may be expressed

$$F = \sum_{\mathbf{s} \in \{\pm 1\}} I_\Omega(\mathbf{s}). \tag{5.18}$$

This expression for F suggests an algorithm for its calculation. Generate all magnetic states $\mathbf{s}$ in sequence. Test each one for membership in Ω. Increment a counter for every state which is in Ω. Some improvements to this basic algorithm are possible if we first observe some properties of the set of stable states Ω.

Proposition 5.1 For any medium represented by the flip-relaxation model (fixed N, K_e, K_m, and Θ), the set of stable states Ω is non-empty.

The set of stable states Ω is defined so that a state $\mathbf{s}$ is not in Ω only if there exists another state $\mathbf{s}'$ for which an application of the update rule would change the state of the model from $\mathbf{s}$ to $\mathbf{s}'$. The update rule is defined so that it changes the model state from $\mathbf{s}$ to $\mathbf{s}'$ only if the energy of the model in state $\mathbf{s}$ is greater than the energy of the model in state $\mathbf{s}'$. Using the notation $W(\mathbf{s})$ to denote the energy of the model in state $\mathbf{s}$, we may write

$$\mathbf{s} \notin \Omega \Rightarrow \exists \mathbf{s}' : W(\mathbf{s}) > W(\mathbf{s}'). \tag{5.19}$$

The proposition that Ω is empty may be expressed

$$\forall \mathbf{s} \in \{\pm 1\}^N : \mathbf{s} \notin \Omega. \tag{5.20}$$

If this proposition is accepted as true and combined with the inference above, the conclusion is

$$\forall \mathbf{s} \in \{\pm 1\}^N : \exists \mathbf{s}' : W(\mathbf{s}) > W(\mathbf{s}'), \tag{5.21}$$

which may be more simply stated as a claim that the function W has no minimum over the set $\{\pm 1\}^N$. This is impossible, because $\{\pm 1\}^N$ is a finite set, and any function defined on a finite set attains its minimum value over that set. The only valid conclusion is that the set Ω may not be empty. The model must have at least one stable state.

Corollary 5.1 For any medium represented by the flip-relaxation model, the number of stable states F is positive.

Proposition 5.2 For any medium represented by the flip-relaxation model, the set of stable states Ω has the property:

$$\mathbf{s} \in \Omega \Leftrightarrow -\mathbf{s} \in \Omega. \tag{5.22}$$

The proof of this property is simple. The calculation of normalized field vectors $\mathbf{h}_k$ is a linear function of the magnetic state vector $\mathbf{s}$, so we have for all $k \in \mathcal{I}$,

$$\mathbf{h}_k(-\mathbf{s}) = -\mathbf{h}_k(\mathbf{s}). \tag{5.23}$$

Then, because the Stoner-Wohlfarth astroid is symmetric about the origin, and the sgn function is odd,

$$U(-s_k, -\mathbf{h}_k) = -U(s_k, \mathbf{h}_k). \tag{5.24}$$

Therefore the two tests

$$s_k = U(s_k, \mathbf{h}_k), \tag{5.25}$$

and

$$-s_k = U(-s_k, \mathbf{h}_k(-\mathbf{s})) \tag{5.26}$$

have the same outcome, and the symmetry of membership in Ω is established. Therefore, there is no need to test every state $\mathbf{s}$ for membership in Ω. Only half the states need be tested to compute F. Furthermore, we have a simple corollary,

Corollary 5.2 For any medium represented by the flip-relaxation model, the number of stable states F is even.

In addition to these properties, we have already noted in our description of magnetic state evolution algorithms the efficiencies in the calculation of magnetic field values made possible if the sequence of magnetic states has the property that each new state differs from the previous state in the magnetization of only one grain. In the simplified model of this chapter, this corresponds to a sequence of magnetic state vectors $\mathbf{s}$ each of which has Hamming distance of 1 from its predecessor. A sequence with this property is known as a Gray code [100], and is easily generated. Application of these observations improves the efficiency of the calculation of F somewhat.

The main obstacle to direct calculation of F remains, however, the exponentially large number of states to consider. For a medium of N grains, 2^{N-1} tests of Ω-membership must be made to complete direct calculation of the value of F. For this reason, direct calculation of F is only feasible for relatively small values of N. One alternative solution is to replace direct calculation of F with an estimation of the value of F by a Monte Carlo method. In this alternative strategy, magnetic states $\mathbf{s}$ are generated at random, and the fraction of generated states which are stable is taken as representative of the fraction of all states which are stable. This method is also limited however. We expect to compute a capacity value $C \leq 1$ for which the number of stable states is

$$F = 2^{CN}. \tag{5.27}$$

For $C < 1$, the fraction of states which are stable,

$$\frac{F}{2^N} = 2^{(C-1)N}, \tag{5.28}$$

goes to zero at an exponential rate with increasing N. The event for which we seek a Monte Carlo estimation of the probability has exponentially decreasing probability with increasing N. Monte Carlo methods are unable to cope with the estimation of probabilities of such rare events. As a consequence, the Monte Carlo approach also fails with increasing N, and determination of F is limited to media represented by small numbers of grains. One strategy for adapting Monte Carlo methods to deal with rare events is the technique of importance sampling [101, 52], but to date, no such technique has been developed for this problem.

The calculation of the storage capacity of a magnetic recording medium by the method presented above was first reported in our paper [90] at the 1993 INTERMAG Conference. At that time, we had not made a careful identification of the parameters of the medium model with physical properties of a recording medium. In hindsight, though, we can identify the results reported in [90] as equivalent to those calculated for material properties represented by $K_e = 0.5$ and $K_m = 5 \times 10^{-9}$. For $N = 25$ grains arrayed in a 5×5 configuration, and a fixed microstructure $\mathbf{\Theta}$, a capacity value of $C = 0.52$ was computed by a brute force calculation.

5.2.3 Storage Capacity vs. Material Properties

Let us now consider how the storage capacity of a medium as predicted by the model varies for media with different material properties, represented by different values of K_e and K_m. A 4×4 array of $N = 16$ grains was generated, and a single fixed microstructure was determined by selection of the 16 values of the elements of $\mathbf{\Theta}$. For this single fixed microstructure, we consider the storage capacity C computed by brute force methods for several different values of the model material parameters K_e and K_m. The range of values considered includes the range of values listed as representative of physically realizable recording media in Table 4.3. In addition, these ranges were extended in the high range, so that the storage capacity of magnetic materials could be investigated as they move from the domain of hard magnetic materials to the domain of soft magnetic materials. For this extended investigation, anisotropy energy density values as small as 500 J/m^3 were considered, leading to the

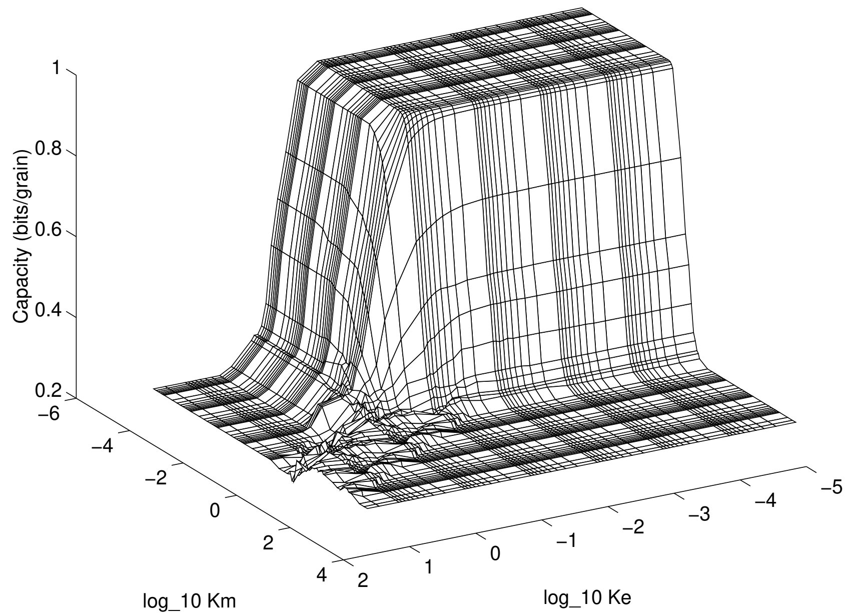

Figure 5.2: Capacity C as a function of parameters (K_e, K_m)

parameter ranges

$$10^{-5} \leq K_e \leq 30; \tag{5.29}$$

$$4 \times 10^{-5} \leq K_m \leq 4000. \tag{5.30}$$

Within these ranges, a grid of (K_e, K_m) pairs was defined for which the values of K_e and K_m are all integer multiples of powers of 10. At each pair within this grid, the storage capacity of the 4×4 medium was directly calculated. Fig. 5.2 displays the computed storage capacity in bits per grain as a function of the base 10 logarithms of the medium material parameters K_e and K_m. The logarithmic scaling of the model material parameters is required because of the large range of values to be considered.

Consider now the features of the graph in Fig. 5.2. The portion of the graph farthest back in the figure shows the capacity for small values of both K_e and K_m. In this region, the grains are practically non-interacting. For media represented by (K_e, K_m) values in this region, every magnetic state is stable under an assumption of zero applied field, because there are no interaction fields to cause a change in the magnetization state. Therefore, the maximum possible capacity consistent with the simplified model, 1 bit per grain, is calculated. An important feature of the graph is that it lets us set boundaries on the K_e and K_m values below which we may claim that grains are practically non-interacting. There is no need to set K_e and K_m to zero, as long as they are small enough. From Fig. 5.2, the boundaries of the region for which grains may be considered non-interacting is given by

$$K_e \leq 0.1, \quad \text{when} \quad K_m \leq 0.04 \tag{5.31}$$

and

$$K_m \leq 0.07 \quad \text{when} \quad K_e \leq 0.02, \tag{5.32}$$

with a small region near $K_e = K_m = 0.07$ where the boundary is not a straight line. It is for media in this range that the replacement of the rotation-relaxation evolution algorithm with the flip-relaxation evolution algorithm is least objectionable. When grains are practically non-interacting, their magnetizations remain nearly aligned with the easy axes. As a consequence, any medium noise observed in playback voltage waveforms is entirely of the repeatable kind, and could in principle, with knowledge of the microstructure, be completely removed so that it did not interfere with the recovery of stored information.

As either K_e or K_m increase, there is a range of about one order of magnitude in either parameter over which the capacity C decreases with increasing interactions. For small values of K_m and large values of K_e a constant capacity of $C = 0.27$ bits per grain is reached, which does not change with further increases of K_e, even into the range of soft magnetic materials. Likewise, for small values of K_e and large values of K_m a constant capacity of $C = 0.29$ bits per grain is reached, which does not change with further increases of K_m, even into the range of soft magnetic materials. There is also a transition between these two values in the region where K_e and K_m are approximately equal. In part of this transition region, the capacity is slightly larger than in either of the two regions separated by the transition.

One should be careful not to make too much of these results. They are for only one microstructure, and for a medium consisting of only 16 grains. Furthermore, as the interactions increase the differences between the flip-relaxation and rotation-relaxation models become more important, and it becomes increasingly more likely that the value of C calculated overestimates the true number of stable states of a physical medium. However, as an illustration of the basic trends of interactions on storage capacity, Fig. 5.2 is useful. Some of its weaknesses will be addressed in later sections and chapters.

A figure much like Fig. 5.2 was included in our paper [91] at the 1993 Magnetism and Magnetic Materials Conference and a related report [95]. In those works, a different pair of parameters, denoted (K_e', δ') was used to represent the scale of exchange and magnetostatic interactions. The relationship of those parameters to K_e and K_m in the current work is

$$K_e = \frac{K_e'}{2}; \tag{5.33}$$

$$K_m = 5 \times 10^{-9} \delta'. \tag{5.34}$$

We see now that the material parameters $K_e = 0.1, K_m = 0.05$ determined by the parameter identification procedure as representative of a typical recording medium in Chapter 4 are only slightly outside the range of practically non-interacting grains. For these values, the calculated capacity is $C = 0.9984$, and with the identified grain size $D = 111.11$ nm, we have an areal capacity of 80.9 Mbits/mm^2 (52.2 Gbits/in^2). Recording at areal densities greater than this capacity value will require recording media with smaller magnetic microstructural features and/or lesser intergranular interactions. These two strategies of increasing areal capacity are at odds, however. Both interaction parameters K_e and K_m are inversely proportional to grain size D. As grain size D decreases, then, increasing effective intergranular interactions act to decrease the capacity C in bits per grain. This effect is in addition to the increasing effect of thermal decay with decreasing grain size, which also acts to reduce storage capacity. The goal of maximizing areal storage density will ultimately involve a compromise among these competing factors.

5.3 Summary and Future Work

A simplified version of the medium model was presented for which the storage capacity C could be defined. Model simulations calculated the value of storage capacity C in bits per grain for media represented by a small number of grains. An investigation of the dependence of medium storage capacity on material parameters K_e and K_m revealed that capacity is maximized for media of practically non-interacting grains. As intergranular interactions increase, storage capacity in bits per grain decreases. Because intergranular interactions increase with decreasing grain size, areal storage density may not be maximized simply by decreasing grain size, but a compromise between grain size and interaction strength must be considered.

In Chapter 4, the dependence of hysteresis properties on material parameters K_e and K_m was investigated. In this chapter the dependence of capacity C on the same parameters was investigated. An investigation of the dependence of medium noise calculated in recording simulations could also be performed. A comparison of these three investigations may reveal the connections between these features of the model. A simple attempt at this was made considering only the flip-relaxation model, with results reported in [96, 97]. A repetition of this investigation making use of the relaxation-rotation model for recording and hysteresis simulations is in order in future work.

Chapter 6

Effect of Microstructure on Capacity

As noted in Chapter 5, the set of fixed points Ω depends on the microstructure, represented by $\mathbf{\Theta}$. Therefore the number of fixed points F, and the capacity C calculated by the method of Chapter 5 depend on the microstructure. The microstructure investigated by simulation in Chapter 5 was generated at random from a planar isotropic distribution of easy axes, represented in our model by the value of $\rho = 1$. Different distributions on easy axes can lead to different model predictions of hysteresis properties, recording properties, and capacity. A limited investigation of the dependence of hysteresis properties on easy axis distribution was reported in Chapter 4, by varying the value of ρ. Other distributions on the easy axes may be considered and their effects on hysteresis and recording properties have been investigated by other researchers [38, 128, 19]. In this chapter, we consider the effect of different microstructures $\mathbf{\Theta}$ on the storage capacity defined in the preceding chapter. First we consider a specialized microstructure representative of bicrystal media, and its influence on capacity. Next, we consider the expected value of the capacity of media, taken over an ensemble of non-oriented media representing many disks in a lot (or many patches on a disk). Finally, we consider a simple illustration of the additional limits on capacity which arise when the microstructure is unknown. These limits demonstrate that knowledge of the microstructure is crucial to achieving areal storage densities approaching the fundamental limits of storage capacity for any particular recording medium.

6.1 Bicrystal Media

Under certain manufacturing conditions, Co-based alloy thin films can be sputtered on Cr underlayers so that the easy axes of the resulting magnetic layer lie along one of two orthogonal directions [81, 124]. Subsequent measurements confirm an anisotropy of magnetic properties with four-fold symmetry. Such magnetic materials are known as bicrystal films. Previous work in micromagnetic modeling has been aimed at representing bicrystal films and investigating their suitability for high density magnetic recording, investigating their hysteresis and recording properties [125, 137, 126] as well as their thermal stability [46, 47]. These investigations show that bicrystal film media exhibit good thermal stability, high coercivity and coercivity squareness, and low medium noise. The difficulty of manufacturing a circular disk recording medium from a material with inherently square microstructure may be overcome by the development of nanocrystalline media, in which small clusters of bicrystal grains are deposited with random orientation, so that the medium is microscopically textured, but macroscopically planar isotropic.

In this section, we consider a representation of bicrystal film media within our model framework, and determine the effect of the bicrystal microstructure on storage capacity. Fig. 6.1 depicts the microstructure of a bicrystal medium, as represented within our model framework. All the easy axes θ_k take on values from $\{\pm\frac{\pi}{2}\}$, and form a "checkerboard" pattern.

With the microstructure of Fig. 6.1 in effect, we repeat the capacity calculations of section 5.2.3, yielding values for storage capacity C as a function of material properties K_e and K_m as graphed in Fig. 6.2. Fig. 6.2 exhibits the same basic properties seen in Fig. 5.2. For small values of K_e and K_m, the grains of the model are practically non-interacting and every magnetic state is a fixed point, leading to a capacity of one bit per grain, the maximum capacity consistent with the simplified model. For increasing values of either K_e or K_m, the storage capacity of the medium is reduced. However, for large values of K_e and moderate values of K_m, Fig. 6.2 indicates that bicrystal media have considerably higher capacity than planar isotropic media with the same material properties. Therefore, if the constraints of manufacturing restrict media to that range of material parameters, but the manufacture of bicrystal anisotropy structure is feasible, Fig. 6.2 indicates that building such structure into media will have the effect of increasing its storage capacity. In other regions of material properties K_e and K_m, bicrystal structure can be expected to have little

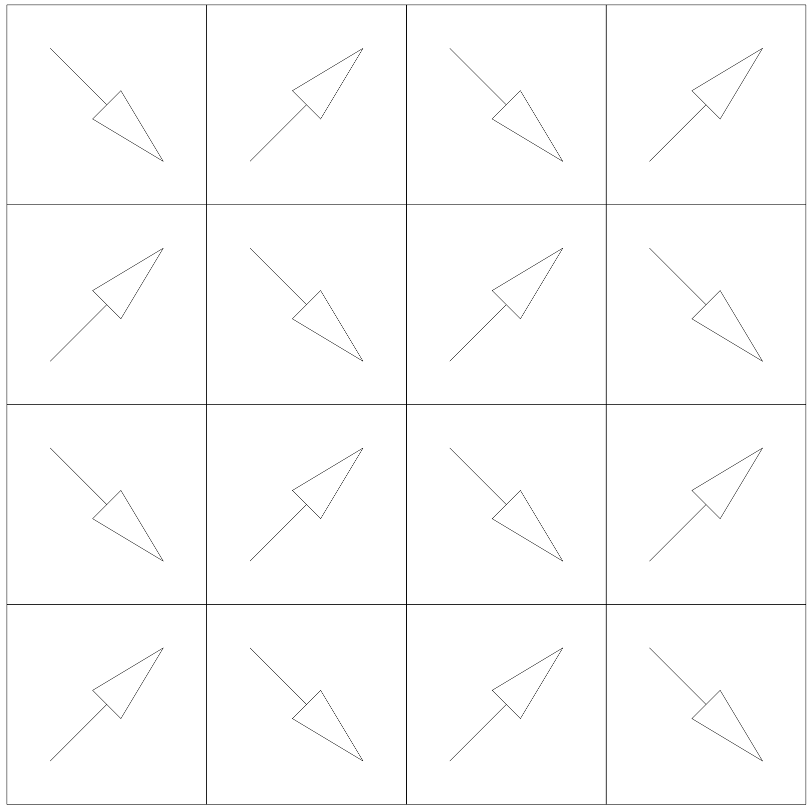

Figure 6.1: Microstructure of bicrystal media

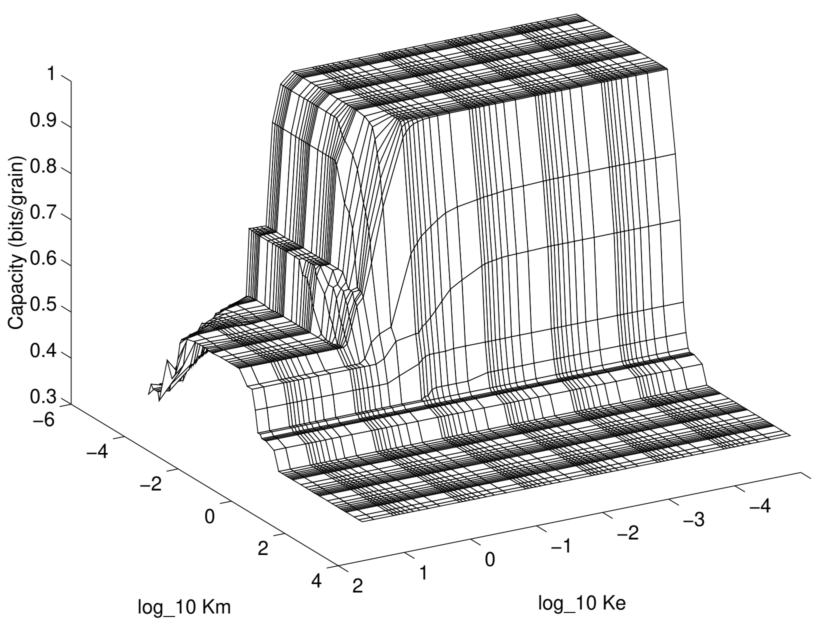

Figure 6.2: Capacity of bicrystal media

effect on storage capacity. However, it cannot be concluded that there is nothing to be gained by adding such structure to media with material properties in such regions. It may be that bicrystal microstructure does not increase the number of fixed points, but it *does* cause the states which are fixed points to be more easily distinguished in recording or playback. Such differences would not affect the capacity value we calculate, but would influence the practical ability to record and playback at storage densities approaching the capacity.

6.2 Ensemble Capacity of Non-oriented Media

The main point to take from the preceding section is that the capacity of a recording medium depends on its microstructural properties. The microstructure investigated in that section is a very specialized one, though. One would not expect such a structure to arise without a manufacturing process designed to create it. In the manufacture of planar isotropic (that is, non-oriented) media, we would not expect to observe such a specialized structure. Even less striking variability in microstructure could significantly impact capacity, though, so we now investigate the effect of microstructural variation of non-oriented media on the calculated capacity by considering the capacity of an ensemble of microstructures of non-oriented media.

6.2.1 Expected Capacity

Consider a sequence of recording media all with the same number of grains N, with the same material properties K_e and K_m, and with non-oriented microstructure generated by a random manufacturing process. Let the ith microstructure in this sequence be represented by the vector of easy axis orientations $\mathbf{\Theta}_i$, and let the manufacturing process independently generate L media. The capacity of the ith medium is expressed in the notation of our earlier work

$$C_i = \frac{1}{N} \log F(K_e, K_m, \mathbf{\Theta}_i). \tag{6.1}$$

Because the microstructure is represented by the outcome of a random manufacturing process, the random variable $\mathbf{\Theta}_i$, the resulting capacity is therefore also a random variable. If we consider the empirical average of the capacities of all the media in the sequence,

$$\langle C\rangle = \frac{1}{L}\sum_{i=1}^{L} C_i, \tag{6.2}$$

we conclude that for large numbers L of media, the empirical average storage capacity of the ensemble of non-oriented media generated by the random manufacturing process converges to an expected value,

$$E_{\mathbf{\Theta}}\{C\} = \frac{1}{N} E_{\mathbf{\Theta}}\{\log F(K_e, K_m, \mathbf{\Theta})\}. \tag{6.3}$$

In this way, we may analyze not only the capacity of a single medium represented by a single microstructure, but the capacity which may be expected on average over all the non-oriented media represented by our model. If the separate media in this random sequence are considered as representative of patches on a single disk, rather than disks in a lot, this analysis makes even more sense as characterizing the storage capacity of non-oriented media.

6.2.2 Bounds on Expected Capacity

In order to continue the analysis of the expected storage capacity of non-oriented recording media, we must take the expectation of the logarithm of a random variable. Given the probability distribution of F, this is not a difficult operation. However, F is a complicated function of $\mathbf{\Theta}$, which is itself an N-dimensional random vector, requiring an N-dimensional probability distribution function to fully characterize its stochastic properties. It seems unlikely that a form for the probability distribution of F can be determined. A lesser goal is the calculation of an upper bound and a lower bound on the expected capacity between which the expected capacity takes its value. Let us now determine bounds on the expected capacity of our medium model for a fixed number of grains N.

In the formulation of bounds it is often helpful to recognize limits on the range of possible values for a given quantity. The number of fixed points F cannot be larger than 2^N, and we have observed in Corollaries 5.1 and 5.2 that F must be a positive, even integer. Therefore,

$$2 \leq F \leq 2^N \tag{6.4}$$

and

$$1 \leq \log F \leq N. \tag{6.5}$$

Another property important to determining the bounds on the expected capacity is that the logarithm is a *concave* function over the positive reals. That is, for any $0 < a < b$,

$$\forall_{0 \leq \lambda \leq 1} : \log(\lambda a + (1-\lambda)b) \geq \lambda \log(a) + (1-\lambda)\log(b). \tag{6.6}$$

Finally, we make note of Jensen's inequality [23, p. 25] which in one form states that for any concave function f with domain containing the range of a random variable X,

$$E\{f(X)\} \leq f(E\{X\}), \tag{6.7}$$

with equality if and only if X is a constant almost everywhere. We are now ready to state upper and lower bounds on the expected capacity.

A very simple upper bound on the capacity follows from the upper limit on the range of F,

$$E_{\mathbf{\Theta}}\{C\} \leq 1. \tag{6.8}$$

Direct application of Jensen's inequality yields a lesser upper bound on our expected storage capacity,

$$E_{\mathbf{\Theta}}\{C\} = \frac{1}{N} E_{\mathbf{\Theta}}\{\log F(K_e, K_m, \mathbf{\Theta})\} \leq \frac{1}{N} \log E_{\mathbf{\Theta}}\{F(K_e, K_m, \mathbf{\Theta})\}, \tag{6.9}$$

where equality holds only when F has a constant value except for a set of $\mathbf{\Theta}$ values with zero probability. In the terminology of probability theory (or measure theory), we would say equality holds only when F is a constant $\mathbf{\Theta}$-almost everywhere.

From our calculations of storage capacity by simulation, it appears that F is a constant with respect to microstructure only for values of material properties K_e and K_m small enough that the capacity for any microstructure is 1 bit per grain. For larger values of either K_e or K_m, (6.9) can only provide an upper limit on the expected storage capacity.

A very simple lower bound on the capacity follows from the lower limit on the range of F,

$$E_{\mathbf{\Theta}}\{C\} \geq \frac{1}{N}. \tag{6.10}$$

For a greater lower bound, let us apply 6.6 with a and b denoting the endpoints of the valid range of values for F, $a = 2$ and $b = 2^N$. Then, when an expected value is taken, we are left with a bound

$$\begin{aligned} E_{\mathbf{\Theta}}\{C\} &= \frac{1}{N} E_{\mathbf{\Theta}}\{\log F(K_e, K_m, \mathbf{\Theta})\} \\ &\geq \frac{1}{N}\left[\frac{N-1}{2^N-2} E_{\mathbf{\Theta}}\{F(K_e, K_m, \mathbf{\Theta})\} + \frac{2^{N-1}-N}{2^{N-1}-1}\right]. \end{aligned} \tag{6.11}$$

6.2.3 Expected Number of Fixed Points

Both the upper bound and the lower bound are functions of the expected number of fixed points F. To proceed further, we turn to the calculation of this quantity.

$$\begin{aligned} E_{\mathbf{\Theta}}\{F(K_e, K_m, \mathbf{\Theta})\} &= E_{\mathbf{\Theta}}\{\sum_{\mathbf{s}\in\{\pm 1\}} I_{\Omega(K_e,K_m,\mathbf{\Theta})}(\mathbf{s})\} \\ &= E_{\mathbf{\Theta}}\{2^N \sum_{\mathbf{s}\in\{\pm 1\}} 2^{-N} I_{\Omega(K_e,K_m,\mathbf{\Theta})}(\mathbf{s})\} \\ &\overset{\text{(a)}}{=} 2^N E_{\mathbf{\Theta}}\{E_{\mathbf{s}}\{I_{\Omega(K_e,K_m,\mathbf{\Theta})}(\mathbf{s})|\mathbf{\Theta}\}\} \\ &= 2^N E_{(\mathbf{s},\mathbf{\Theta})}\{I_{\Omega(K_e,K_m,\mathbf{\Theta})}(\mathbf{s})\}, \end{aligned} \tag{6.12}$$

where step (a) replaces the sum over magnetic states $\mathbf{s}$ with an expected value under the assumption that the magnetic state $\mathbf{s}$ is a uniformly distributed random vector over the set $\{\pm 1\}^N$. At this point, note that there exists a one-to-one mapping from the pair of N-vectors, $\mathbf{s}$ and $\mathbf{\Theta}$ to the set of N 2-vectors, $(\mathbf{m}_1, \ldots, \mathbf{m}_N)$, representing the reduced grain magnetization vectors of the model. That mapping is

$$\mathbf{m}_k = s_k \begin{bmatrix} \cos\theta_k \\ \sin\theta_k \end{bmatrix}. \tag{6.13}$$

Under that mapping, the magnetization vectors $\mathbf{m}_k$ are independent, identically distributed random vectors. The expectation may be taken equivalently over these random variables, leading to

$$E_{\mathbf{\Theta}}\{F(K_e, K_m, \mathbf{\Theta})\} = 2^N E_{(\mathbf{m}_1,\ldots,\mathbf{m}_N)}\{I_{\Omega(K_e,K_m)}(\mathbf{m}_1, \ldots, \mathbf{m}_N)\}, \tag{6.14}$$

where the notation has been abused somewhat so that the set Ω is now taken as a subset of $(\mathbf{R}^2)^N$, including exactly those N-tuples of magnetization vectors with unit magnitude which, when transformed into $\mathbf{s}$ and $\mathbf{\Theta}$ by the inverse of the mapping (6.13) yield a value of 1 from the indicator function $I_{\Omega(K_e,K_m,\mathbf{\Theta})}(\mathbf{s})$. Then, since the expected value of an indicator function is the probability of the indicator function's set, we have

$$\begin{aligned} E_{\mathbf{\Theta}}\{F(K_e, K_m, \mathbf{\Theta})\} &= 2^N \Pr\{(\mathbf{m}_1, \ldots, \mathbf{m}_N) \in \Omega(K_e, K_m)\} \\ &\triangleq 2^N P_N(K_e, K_m), \end{aligned} \tag{6.15}$$

where the notation P_N has been introduced to simplify matters. Stated in words, the expected number of fixed points is 2^N times the probability that a magnetic state of N unit magnetization vectors randomly generated with orientations uniformly distributed in the plane is a fixed point of the flip-relaxation update rule, assuming the randomly generated magnetization vectors lie on easy axes, P_N. Substitution into (6.9) yields

$$E_{\mathbf{\Theta}}\{C\} \leq 1 + \frac{1}{N} \log P_N(K_e, K_m), \tag{6.16}$$

and substitution into (6.11) yields

$$E_{\mathbf{\Theta}}\{C\} \geq \frac{2^N(N-1)}{N(2^N-2)} P_N(K_e, K_m) + \frac{2^{N-1}-N}{N(2^{N-1}-1)}. \tag{6.17}$$

Both expressions are functions of the probability of a fixed point, P_N.

6.2.4 Probability of a Fixed Point

Let us now consider the calculation of the probability of a fixed point. A magnetic state $\mathbf{s}$ is a fixed point if and only if the flip-relaxation update rule, when applied to every grain k, causes no change in the magnetic state. In terms of the magnetization vector $\mathbf{m}_k$, the flip-relaxation update rule applied to grain k is

$$\mathbf{m}_k^{\text{new}} = U(\mathbf{m}_k, \mathbf{h}_k) \triangleq \begin{cases} \mathbf{m}_k, & |\mathbf{h}_k \cdot \mathbf{m}_k|^{2/3} + |\mathbf{h}_k \times \mathbf{m}_k|^{2/3} \geq 1 \wedge \mathbf{h}_k \cdot \mathbf{m}_k \geq 0 \\ \mathbf{m}_k, & |\mathbf{h}_k \cdot \mathbf{m}_k|^{2/3} + |\mathbf{h}_k \times \mathbf{m}_k|^{2/3} < 1 \\ -\mathbf{m}_k, & |\mathbf{h}_k \cdot \mathbf{m}_k|^{2/3} + |\mathbf{h}_k \times \mathbf{m}_k|^{2/3} \geq 1 \wedge \mathbf{h}_k \cdot \mathbf{m}_k < 0 \end{cases}. \tag{6.18}$$

This update rule may be written

$$U(\mathbf{m}_k, \mathbf{h}_k) = \begin{cases} \mathbf{m}_k, & \mathbf{h}_k \in Q(\mathbf{m}_k) \\ -\mathbf{m}_k, & \mathbf{h}_k \notin Q(\mathbf{m}_k) \end{cases}, \tag{6.19}$$

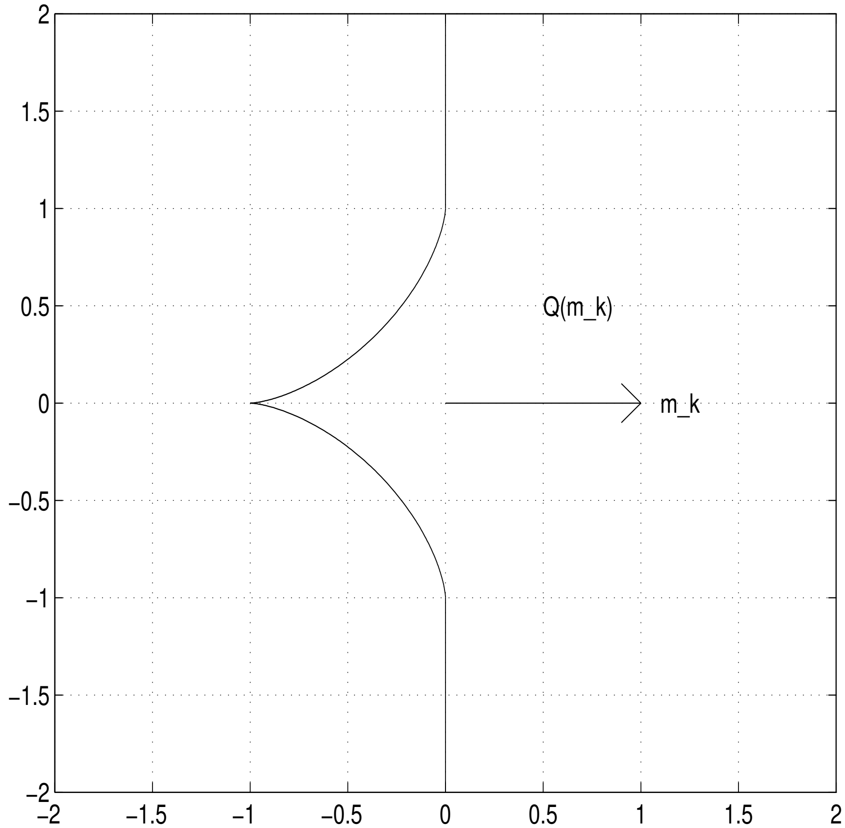

Figure 6.3: Definition of $Q(\mathbf{m}_k)$

where the set $Q(\mathbf{m}_k) \subset \mathbf{R}^2$ is defined with reference to $\mathbf{m}_k$ as illustrated in Fig. 6.3. Then the probability of a fixed point may be expressed

$$\Pr\{(\mathbf{m}_1, \ldots, \mathbf{m}_N) \in \Omega(K_e, K_m)\} = \Pr\left\{\bigcap_{k=1}^{N} \{(\mathbf{m}_1, \ldots, \mathbf{m}_N) : \mathbf{h}_k \in Q(\mathbf{m}_k)\}\right\}. \quad (6.20)$$

In (6.20), we have expressed the probability of a fixed point as the probability of the intersection of N events. If these events were independent, then the probability of the intersection would be the product of the single event probabilities,

$$P_N(K_e, K_m) = \prod_{k=1}^{N} \Pr\{(\mathbf{m}_1, \ldots, \mathbf{m}_N) : \mathbf{h}_k \in Q(\mathbf{m}_k)\}. \quad (6.21)$$

However, we may not just assume independence of these events. When the events are not independent, we may still bound the quantity we seek to compute above and below. An upper bound is

$$P_N(K_e, K_m) \le \min_{1\le k\le N} \Pr\{(\mathbf{m}_1, \ldots, \mathbf{m}_N) : \mathbf{h}_k \in Q(\mathbf{m}_k)\}. \tag{6.22}$$

A lower bound is

$$\begin{aligned} P_N(K_e, K_m) &= \Pr\left\{\bigcap_{k=1}^{N} \{(\mathbf{m}_1, \ldots, \mathbf{m}_N) : \mathbf{h}_k \in Q(\mathbf{m}_k)\}\right\} \\ &\overset{(a)}{=} 1 - \Pr\left\{\bigcup_{k=1}^{N} \{(\mathbf{m}_1, \ldots, \mathbf{m}_N) : \mathbf{h}_k \notin Q(\mathbf{m}_k)\}\right\} \\ &\overset{(b)}{\ge} 1 - \sum_{k=1}^{N} \Pr\{(\mathbf{m}_1, \ldots, \mathbf{m}_N) : \mathbf{h}_k \notin Q(\mathbf{m}_k)\} \\ &\ge 1 - N \max_{1\le k\le N} \Pr\{(\mathbf{m}_1, \ldots, \mathbf{m}_N) : \mathbf{h}_k \notin Q(\mathbf{m}_k)\}, \end{aligned} \tag{6.23}$$

where (a) follows from DeMorgan's Law and (b) follows from the Union Bound. To further simplify the notation, let us define

$$\mathsf{p}_k(K_e, K_m) \triangleq \Pr\{(\mathbf{m}_1, \ldots, \mathbf{m}_N) : \mathbf{h}_k \in Q(\mathbf{m}_k)\}, \tag{6.24}$$

so that the upper bound is expressed

$$P_N(K_e, K_m) \le \min_{1\le k\le N} \mathsf{p}_k(K_e, K_m), \tag{6.25}$$

and the lower bound is expressed

$$\begin{aligned} P_N(K_e, K_m) &\ge 1 - N \max_{1\le k\le N} (1 - \mathsf{p}_k(K_e, K_m)) \\ &= 1 - N + N \min_{1\le k\le N} \mathsf{p}_k(K_e, K_m). \end{aligned} \tag{6.26}$$

Substitution back into (6.16) yields

$$E_{\boldsymbol{\Theta}}\{C\} \le 1 + \frac{1}{N} \min_{1\le k\le N} \log \mathsf{p}_k(K_e, K_m), \tag{6.27}$$

and substitution back into (6.17) yields

$$E_{\boldsymbol{\Theta}}\{C\} \ge \frac{2^N(N-1)}{N(2^N-2)} \left(1 - N + N \min_{1\le k\le N} \mathsf{p}_k(K_e, K_m)\right) + \frac{2^{N-1} - N}{N(2^{N-1}-1)}. \tag{6.28}$$

Both of these expressions ultimately depend on the calculation of the probability that a field vector $\mathbf{h}_k$ is in some subset of $\mathbf{R}^2$. In order to compute such probabilities, we need to compute the probability density function for $\mathbf{h}_k$.

6.2.5 Magnetic Field Probability Density Function

The magnetic field at grain k may be expressed

$$\begin{aligned} \mathbf{h}_k &= \sum_{\substack{l=1 \\ l\neq k}}^{N} \mathbf{A}_{kl}(K_e, K_m)\mathbf{m}_l \qquad (6.29) \\ &= \sum_{\substack{l=1 \\ l\neq k}}^{N} \left\{ K_e I_{N(k)}(l) \begin{bmatrix} 1 & 0 \\ 0 & 1 \end{bmatrix} + \frac{K_m}{(p_{kl}^2 + q_{kl}^2)^{5/2}} \begin{bmatrix} 2p_{kl}^2 - q_{kl}^2 & 3p_{kl}q_{kl} \\ 3p_{kl}q_{kl} & 2q_{kl}^2 - p_{kl}^2 \end{bmatrix} \right\} \mathbf{m}_l. \end{aligned}$$

In the last two subsections we have established a probabilistic framework for computing the expected number of fixed points over randomly generated microstructures. Within this framework, the only random quantities are the magnetization vectors $\mathbf{m}_l$, which are statistically independent and identically distributed. The terms of the sum above are random vectors each of which is a linear transformation of one magnetization vector. Because the magnetization vectors are statistically independent, so are the terms of the summation. Therefore, the magnetic field vector $\mathbf{h}_k$ is the sum of $N-1$ independent random vectors. Its probability density function is therefore the convolution of the probability density functions of the terms of the summation.

Computing the convolution of probability density functions is simplified by the use of characteristic functions. The characteristic function of the sum of $N-1$ independent random vectors is the product of the $N-1$ characteristic functions of those random vectors. Thus,

$$\Phi_{\mathbf{h}_k}(\underline{\omega}) = \prod_{\substack{l=1 \\ l\neq k}}^{N} \Phi_{\mathbf{A}_{kl}(K_e,K_m)\mathbf{m}_l}(\underline{\omega}). \qquad (6.30)$$

The characteristic function of a linear transformation of a random vector is easy to derive,

$$\begin{aligned} \Phi_{\mathbf{Am}}(\underline{\omega}) &= E\left\{ e^{j\underline{\omega}^T \mathbf{Am}} \right\} \qquad (6.31) \\ &= E\left\{ e^{j\left(\mathbf{A}^T\underline{\omega}\right)^T \mathbf{m}} \right\} \end{aligned}$$

$$= \Phi_{\mathbf{m}}(\mathbf{A}^T \underline{\omega}).$$

All the interaction matrices of the model are symmetric, so we may write

$$\Phi_{\mathbf{h}_k}(\underline{\omega}) = \prod_{\substack{l=1 \\ l \neq k}}^{N} \Phi_{\mathbf{m}_l}(\mathbf{A}_{kl}\underline{\omega}). \tag{6.32}$$

Next, all the magnetization vectors are identically distributed, so they share the same characteristic function. Thus,

$$\Phi_{\mathbf{h}_k}(\underline{\omega}) = \prod_{\substack{l=1 \\ l \neq k}}^{N} \Phi_{\mathbf{m}}(\mathbf{A}_{kl}\underline{\omega}), \tag{6.33}$$

and the characteristic function of a magnetic field vector $\mathbf{h}_k$ is expressed in terms of the interaction matrices and the characteristic function of a randomly generated unit magnitude magnetization vector.

Finally, because our simplified model has a regular grain structure, the interaction matrices $\mathbf{A}_{kl}$ are space-invariant. That is, they do not depend on the values of k and l, but only on the spatial displacements between grains k and l which we represent symbolically by $k - l$,

$$\Phi_{\mathbf{h}_k}(\underline{\omega}) = \prod_{\substack{l=1 \\ l \neq k}}^{N} \Phi_{\mathbf{m}}(\mathbf{A}_{k-l}\underline{\omega}). \tag{6.34}$$

The only way the probability density function of the magnetic field vector $\mathbf{h}_k$ may differ from that of magnetic field vector $\mathbf{h}_l$ is if the two grains k and l have a different spatial relationship to the rest of the grains. For any finite collection of grains, such differences will exist because some grains will be near edges, and will not have the same spatial relationship with the same number of other grains as grains near the center of the assembly. This effect is an artifact of the model however. Our interest is in modeling thin-film media which extend far beyond the limits of any bounding box we care to simulate. Within this analysis we have the opportunity to remove the edge effects of the model. Doing so means that the probability density function of a magnetic field vector does not depend on the particular grain k, but may be expressed for all k as

$$\Phi_{\mathbf{h}}(\underline{\omega}) = \prod_{k-l \neq 0} \Phi_{\mathbf{m}}(\mathbf{A}_{k-l}\underline{\omega}). \tag{6.35}$$

As a consequence of the removal of spatial dependence, the minimization operation in earlier expressions may be removed. Let us re-examine those expressions in that light, using p in place of p_k to indicate the lack of dependence on k. Then the upper bound on expected capacity is

$$E_{\Theta}\{C\} \leq 1 + \frac{1}{N} \log \mathsf{p}(K_e, K_m). \tag{6.36}$$

Since $\mathsf{p} \leq 1$, this upper bound is an improvement on the very simple upper bound of

$$E_{\Theta}\{C\} \leq 1. \tag{6.37}$$

The lower bound on expected capacity is

$$E_{\Theta}\{C\} \geq \frac{2^N(N-1)}{N(2^N-2)}\left(1 - N + N\mathsf{p}(K_e, K_m)\right) + \frac{2^{N-1} - N}{N(2^{N-1}-1)}, \tag{6.38}$$

which is an improvement over the very simple lower bound

$$E_{\Theta}\{C\} \geq \frac{1}{N} \tag{6.39}$$

only when

$$\mathsf{p}(K_e, K_m) > \frac{N - 1 + 1/2^{N-1}}{N}. \tag{6.40}$$

These bounds will only yield significant information about the expected capacity when they are near one another and when they are significant improvements on the very simple bounds. It is clear for useful numbers of grains, this is only true when the value of p is near 1. As we continue deriving the dependence of p on K_e and K_m, we must keep in mind that we are most interested only in those values of K_e and K_m for which p is equal or nearly equal to 1. This corresponds to the values of K_e and K_m for which the expected capacity is equal or nearly equal to 1. The bounds we are now applying tell us most reliably only the boundary in the (K_e, K_m) plane across which the expected capacity falls significantly away from 1.

With that limitation in mind, we complete the derivation of the probability density function of a magnetic field vector by deriving the characteristic function of a randomly generated unit-magnitude magnetization vector. The magnetization vector

$\mathbf{m}$ may be expressed

$$\mathbf{m} = \begin{bmatrix} \cos\alpha \\ \sin\alpha \end{bmatrix}, \tag{6.41}$$

where α is a random variable with probability density function

$$p_\alpha(\lambda) = \frac{1}{2\pi}, \quad -\pi < \lambda \leq \pi. \tag{6.42}$$

The characteristic function of $\mathbf{m}$ is

$$\begin{aligned} \Phi_{\mathbf{m}}(\underline{\omega}) &= E_{\mathbf{m}}\left\{e^{j\underline{\omega}^T\mathbf{m}}\right\} \\ &= E_\alpha\left\{e^{j(\omega_x\cos\alpha+\omega_z\sin\alpha)}\right\} \\ &= \int_{-\pi}^{\pi}\frac{1}{2\pi}e^{j(\omega_x\cos\lambda+\omega_z\sin\lambda)}d\lambda \\ &= \frac{1}{2\pi}\int_{-\pi}^{\pi}e^{j|\underline{\omega}|\cos(\lambda-\phi)}d\lambda, \end{aligned} \tag{6.43}$$

where $\phi = \tan^{-1}\frac{\omega_z}{\omega_x}$. The integral is truly over any interval of length 2π, so the shift in the cosine argument by ϕ is irrelevant. We conclude,

$$\Phi_{\mathbf{m}}(\underline{\omega}) = \frac{1}{2\pi}\int_{-\pi}^{\pi}e^{j|\underline{\omega}|\cos\lambda}d\lambda. \tag{6.44}$$

This final expression may be recognized as equivalent to one of the integral representations of the Bessel function of the first kind of order zero [1, p. 360, Eq. 9.1.21], so that

$$\Phi_{\mathbf{m}}(\underline{\omega}) = J_0(|\underline{\omega}|), \tag{6.45}$$

and

$$\Phi_{\mathbf{h}}(\underline{\omega}) = \prod_{k-l\neq 0} J_0\left(|\mathbf{A}_{k-l}(K_e, K_m)\underline{\omega}|\right). \tag{6.46}$$

Given any pair of values for K_e and K_m, the ability to evaluate the Bessel function, and a number of grains N suitable to approximate the field arising from an infinitely-extended plane of thin-film media, (6.46) may be used to calculate the value of the characteristic function of $\mathbf{h}$ for any value of its argument $\underline{\omega}$. The probability density function of $\mathbf{h}$ is determined from the characteristic function by the relationship

$$p_{\mathbf{h}}(\underline{\lambda}) = \frac{1}{4\pi^2}\int\Phi_{\mathbf{h}}(\underline{\omega})e^{-j\underline{\omega}^T\underline{\lambda}}d\underline{\omega} \tag{6.47}$$

Application of numerical methods is necessary for the approximate calculation of this integral. Before considering numerical methods, let us first consider how the results will be used. We wish to integrate the probability density function $p_{\mathbf{h}}(\underline{\lambda})$ over a set of $\underline{\lambda}$ values to compute a probability. We consider the details of this integration in the next section.

6.2.6 Probability Calculations

Both the upper bound and the lower bound on the expected capacity of our model of the recording medium are functions of the probability,

$$\mathsf{p}_k(K_e, K_m) \triangleq \Pr\left\{\mathbf{h}_k \in Q(\mathbf{m}_k)\right\} = \int\int p_{(\mathbf{h}_k,\mathbf{m}_k)}(\underline{\lambda}, \underline{\xi}) I_{Q(\underline{\xi})}(\underline{\lambda})\ d\underline{\lambda}\ d\underline{\xi}. \tag{6.48}$$

All the magnetization vectors $\mathbf{m}_k$ are statistically independent. The magnetic field vector $\mathbf{h}_k$ is a function of all the magnetization vectors, *except* $\mathbf{m}_k$. Therefore, the magnetic field vector $\mathbf{h}_k$ and the magnetization vector $\mathbf{m}_k$ at any particular grain k are statistically independent. Also, the probability density function of $\mathbf{h}_k$ depends on the values of K_e and K_m. Thus,

$$p_{(\mathbf{h}_k,\mathbf{m}_k)}(\underline{\lambda}, \underline{\xi}) = p_{\mathbf{h}}\left(\underline{\lambda} : K_e, K_m\right) p_{\mathbf{m}}(\underline{\xi}), \tag{6.49}$$

which as we have already noted does not depend on the grain index k. Therefore, we may write

$$\mathsf{p}(K_e, K_m) = \int p_{\mathbf{h}}\left(\underline{\lambda} : K_e, K_m\right) \int p_{\mathbf{m}}(\underline{\xi}) I_{Q(\underline{\xi})}(\underline{\lambda})\ d\underline{\xi}\ d\underline{\lambda}. \tag{6.50}$$

The inner integral evaluates to a function of $\underline{\lambda}$, which we may denote $\Upsilon(\underline{\lambda})$, so that

$$\mathsf{p}(K_e, K_m) = \int p_{\mathbf{h}}\left(\underline{\lambda} : K_e, K_m\right) \Upsilon(\underline{\lambda})\ d\underline{\lambda}. \tag{6.51}$$

In Appendix C it is shown that

$$\Upsilon(\underline{\lambda}) = \frac{1}{2} + \frac{1}{2}\Psi(|\underline{\lambda}|), \tag{6.52}$$

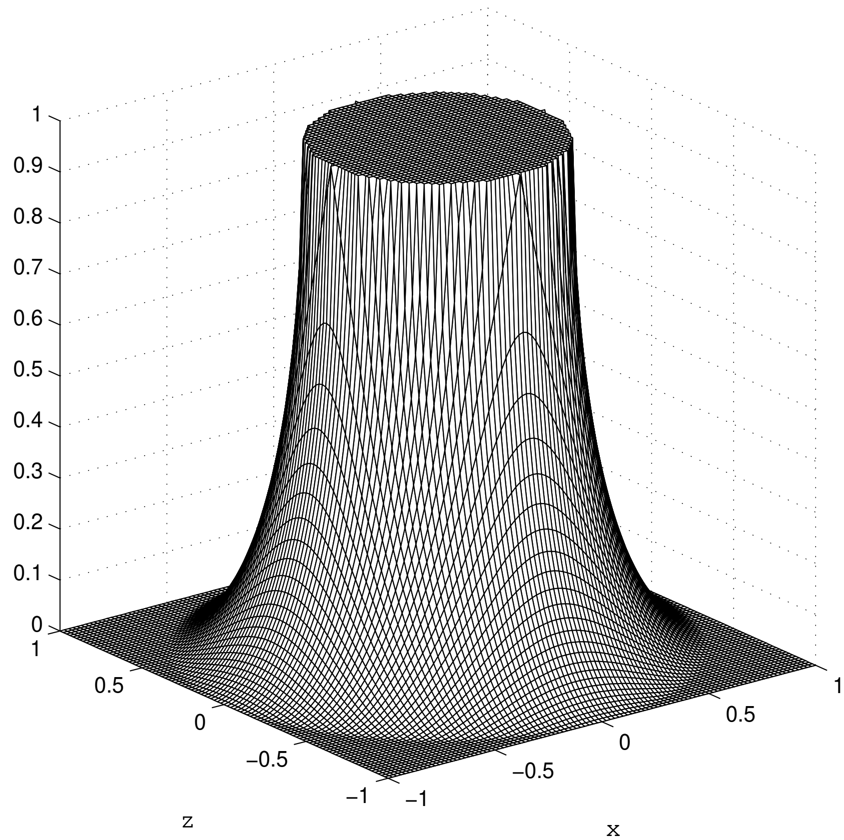

Figure 6.4: Plot of $\Psi(|\mathbf{h}|)$

where

$$\Psi(r) = \begin{cases} 1, & r \leq \frac{1}{2} \\ \frac{4}{\pi}\ \tan^{-1}\left[\left(\frac{1-\sqrt{\frac{4r^2-1}{3}}}{1+\sqrt{\frac{4r^2-1}{3}}}\right)^{\frac{3}{2}}\right], & \frac{1}{2} < r < 1 \\ 0, & r \geq 1 \end{cases} \tag{6.53}$$

Fig. 6.4 displays a plot of the function $\Psi(|\underline{\lambda}|)$. As discussed in Appendix C, the function $\Psi(|\underline{\lambda}|)$ represents a circularly symmetric form of the Stoner-Wohlfarth astroid. Note that the function $\Psi(|\underline{\lambda}|)$ has a finite region of support, and that for any $\underline{\lambda}$ with $|\underline{\lambda}| < \frac{1}{2}$, $\Psi(|\underline{\lambda}|) = 1$.

Continuing the derivation, we write

$$\begin{aligned} \mathsf{p}(K_e, K_m) &= \frac{1}{2}\int p_{\mathbf{h}}\left(\underline{\lambda} : K_e, K_m\right)\ d\underline{\lambda} \\ &+ \frac{1}{2}\int p_{\mathbf{h}}\left(\underline{\lambda} : K_e, K_m\right)\Psi(|\underline{\lambda}|)\ d\underline{\lambda}. \end{aligned} \tag{6.54}$$

The first integral is of a probability density function over its domain, yielding a value of one, so that

$$\mathsf{p}(K_e, K_m) = \frac{1}{2} + \frac{1}{2}\int p_{\mathbf{h}}\left(\underline{\lambda} : K_e, K_m\right) \Psi(|\underline{\lambda}|)\, d\underline{\lambda}. \tag{6.55}$$

Because Ψ takes on values between 0 and 1, it is clear that the range of possible values for $\mathsf{p}(K_e, K_m)$ is

$$\frac{1}{2} \leq \mathsf{p}(K_e, K_m) \leq 1. \tag{6.56}$$

We have already noted that the lower bound on expected capacity is an improvement on a trivial lower bound of $\frac{1}{N}$ only when

$$\mathsf{p}(K_e, K_m) > \frac{N - 1 + 1/2^{N-1}}{N}. \tag{6.57}$$

Therefore we are most interested in computing p as a function of K_e and K_m in that region of the (K_e, K_m) plane for which $\mathsf{p}(K_e, K_m) \approx 1$. From (6.55) it is clear that $\mathsf{p}(K_e, K_m) = 1$ if and only if the support of the probability density function $p_{\mathbf{h}}\left(\underline{\lambda} : K_e, K_m\right)$ has a radius of $\frac{1}{2}$ or less.

Let us define the radius of support of $p_{\mathbf{h}}\left(\underline{\lambda} : K_e, K_m\right)$ as a function of K_e and K_m,

$$\begin{aligned} h_{\max}(K_e, K_m) &\triangleq \max_{\Theta} |\mathbf{h}(K_e, K_m, \Theta)| \\ &= \max_{(\mathbf{m}_1, \ldots, \mathbf{m}_N)} \left| \sum_{l \neq k} \mathbf{A}_{kl}(K_e, K_m)\mathbf{m}_l \right|. \end{aligned} \tag{6.58}$$

The triangle inequality yields an upper bound

$$h_{\max} \leq \sum_{l \neq k} \max_{\mathbf{m}_l} |\mathbf{A}_{kl}(K_e, K_m)\mathbf{m}_l|, \tag{6.59}$$

in which the lth term of the sum is maximized by choosing $\mathbf{m}_l$ to be the unit eigenvector of $\mathbf{A}_{kl}(K_e, K_m)$ corresponding to the maximum eigenvalue. For the four grains which are neighbors of grain k at which $\mathbf{h}$ is being computed, the maximum eigenvalue is $2K_m + K_e$, and for any other grain l, the maximum eigenvalue is $\frac{2K_m}{(p_{kl}^2 + q_{kl}^2)^{\frac{3}{2}}}$. Therefore,

$$h_{\max} \leq 4K_e + 2K_m \sum_{p=-\infty}^{\infty} \sum_{\substack{q=-\infty \\ (p,q)\neq(0,0)}}^{\infty} \frac{1}{(p^2 + q^2)^{\frac{3}{2}}}. \tag{6.60}$$

The doubly-infinite sums may be transformed by the symmetry of the terms into singly-infinite form

$$h_{\max} \leq 4K_e + 8K_m \sum_{p=1}^{\infty} \sum_{q=0}^{\infty} \frac{1}{(p^2+q^2)^{\frac{3}{2}}}. \tag{6.61}$$

Then an upper bound on the remaining double sum may be derived by the approximation of a double-integral by a double sum,

$$\frac{\pi}{2} \int_1^{\infty} \frac{1}{R^3} dR > \sum_{p=1}^{\infty} \sum_{\substack{q=1 \\ (p,q)\neq(1,1)}}^{\infty} \frac{1}{(p^2+q^2)^{\frac{3}{2}}}. \tag{6.62}$$

Therefore, an upper bound on $h_{\max}$ is

$$\begin{aligned} h_{\max} &< 4K_e + 8K_m \left[2^{-\frac{3}{2}} + \frac{\pi}{4} + \sum_{p=1}^{\infty} p^{-3} \right] \\ &\overset{(a)}{<} 4K_e + 8K_m \left[2^{-\frac{3}{2}} + \frac{\pi}{4} + 1.2021 \right] \\ &< 4K_e + 18.7284 K_m, \end{aligned} \tag{6.63}$$

where (a) is established by a table of values for infinite series [12, p. 74]. From this upper bound on $h_{\max}$ we conclude that for any pair of values (K_e, K_m) for which $4K_e + 18.7284K_m < \frac{1}{2}$, the value of $\mathsf{p}(K_e, K_m)$ is exactly 1. Consequently the expected capacity for all media with such values for K_e and K_m is exactly one bit per grain. That is, for any realization of Θ whatsoever, all magnetic states of the flip-relaxation model are fixed points.

The quantity $h_{\max}$ is defined as the maximum value of an expression evaluated over a set of possible arguments. Clearly, the expression evaluated at any one choice of these arguments serves as a lower bound on $h_{\max}$. Let the normalized magnetization of all four neighbor grains of grain k be unit vectors in the positive x direction, $\hat{\mathbf{x}}$. Then the field components arising from all four neighbors also point in the positive x direction. Furthermore, every other grain l may have its normalized magnetization $\mathbf{m}_l$ set to a particular value $\mathbf{m}_l^*$ so that its field component,

$$\mathbf{h}_{kl} = \mathbf{A}_{kl}(K_e, K_m)\mathbf{m}_l^* \tag{6.64}$$

also points in the positive x direction. For such a magnetic state, the vector sum of field components simplifies to a scalar sum of field component magnitudes, and we may write

$$\begin{aligned} h_{\max} &\geq \sum_{l \neq k} |\mathbf{A}_{kl}(K_e, K_m)\mathbf{m}_l^*| \\ &= (K_e + 2K_m) + (K_e - K_m) + (K_e + 2K_m) + (K_e - K_m) \\ &\quad + \sum_{l \notin N(k)} |\mathbf{A}_{kl}(K_e, K_m)\mathbf{m}_l^*| \end{aligned} \tag{6.65}$$

Clearly, the sum of field component magnitudes is lower bounded by the sum over minimum field component magnitudes,

$$\sum_{l \notin N(k)} |\mathbf{A}_{kl}(K_e, K_m)\mathbf{m}_l^*| \geq \sum_{l \notin N(k)} \min_{\mathbf{m}_l} |\mathbf{A}_{kl}(K_e, K_m)\mathbf{m}_l|. \tag{6.66}$$

Furthermore, each minimum field component magnitude is known to be that which arises when $\mathbf{m}_l$ is the unit eigenvector of $\mathbf{A}_{kl}$ corresponding to the eigenvalue of least magnitude. That value is

$$\min_{\mathbf{m}_l} |\mathbf{A}_{kl}(K_e, K_m)\mathbf{m}_l| = \frac{K_m}{(p_{kl}^2 + q_{kl}^2)^{\frac{3}{2}}}. \tag{6.67}$$

Combining these inequalities yields

$$\begin{aligned} h_{\max} &\geq 4K_e - 2K_m + K_m \sum_{p=-\infty}^{\infty} \sum_{\substack{q=-\infty \\ (p,q)\neq(0,0)}}^{\infty} \frac{1}{(p^2+q^2)^{\frac{3}{2}}} \\ &= 4K_e - 2K_m + 4K_m \sum_{p=1}^{\infty} \sum_{q=0}^{\infty} \frac{1}{(p^2+q^2)^{\frac{3}{2}}} \\ &> 4K_e - 2K_m + 4K_m \sum_{p=1}^{500} \sum_{q=0}^{500} \frac{1}{(p^2+q^2)^{\frac{3}{2}}} \\ &> 4K_e + 7.022K_m \end{aligned} \tag{6.68}$$

From this lower bound on $h_{\max}$ we conclude that for any pair of values (K_e, K_m) for which $4K_e + 7.022K_m > \frac{1}{2}$, the value of $\mathsf{p}(K_e, K_m)$ is strictly less than 1. Consequently the expected capacity for all media with such values for K_e and K_m is strictly less than one bit per grain. That is, there must exist some realization of Θ for which some magnetic states are not fixed points of the flip-relaxation model.

Fig. 6.5 displays the upper bound (solid line) and the lower bound (dashed line) as functions of K_e and K_m on a log-log scale. The boundary of the region in

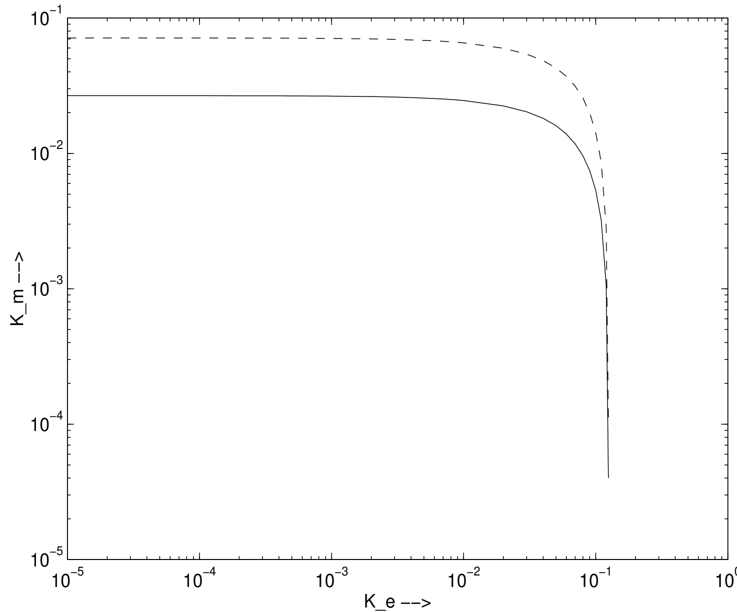

Figure 6.5: Bounds on the boundary of the $E\{C\} = 1$ region of the (K_e, K_m) plane

the (K_e, K_m) plane for which the expected capacity is exactly one must lie between these two bounding curves. For more precise location of the boundary, we must turn to numerical methods.

6.2.7 Numerical Results

We now turn to the numerical calculation of the quantity

$$\mathsf{p}(K_e, K_m) = \frac{1}{2} + \frac{1}{2} \int \frac{1}{4\pi^2} \int \Phi_{\mathbf{h}}(\underline{\omega} : K_e, K_m) e^{-j\underline{\omega}^T \underline{\lambda}} d\underline{\omega} \Psi(|\underline{\lambda}|) d\underline{\lambda} \tag{6.69}$$

over the region of the (K_e, K_m) plane between the two bounds identified in the preceding subsection. A generalized form of this expression which includes a degree of flexibility useful for numerical calculation is

$$\mathsf{p}(K_e, K_m) = \frac{1}{2} + \frac{1}{2} \int \frac{1}{4\pi^2} \int \Phi_{\gamma\mathbf{h}}(\underline{\omega} : K_e, K_m) e^{-j\underline{\omega}^T \underline{\lambda}} d\underline{\omega} \Psi\left(\frac{|\underline{\lambda}|}{\gamma}\right) d\underline{\lambda} \tag{6.70}$$

The outer integral has an integrand with finite support, so it is possible to approximate the integral with a finite sum. The inner integral is a two-dimensional Fourier transform, which we may approximate using discrete Fourier transform techniques.

The details of these approximate calculation techniques are available in [27]. The resulting approximate expression is

$$\mathsf{p}(K_e, K_m) \approx \frac{1}{2} + \frac{1}{2} \sum_{\nu_1=-L}^{L} \sum_{\nu_2=-L}^{L} \Psi\left(\frac{2\lambda_{\max}}{\gamma(2L+1)}\sqrt{\nu_1^2+\nu_2^2}\right)\left(\frac{2\lambda_{\max}}{2L+1}\right)^2 \cdot \frac{1}{4\pi^2} \sum_{\eta_1=-L}^{L} \sum_{\eta_2=-L}^{L} \Phi_{\gamma\mathbf{h}}(\eta_1 \frac{\pi}{\lambda_{\max}}, \eta_2 \frac{\pi}{\lambda_{\max}} : K_e, K_m)\left(\frac{\pi}{\lambda_{\max}}\right)^2 \cdot e^{-j\frac{2\pi}{2L+1}(\nu_1\eta_1+\nu_2\eta_2)} \tag{6.71}$$

$$= \frac{1}{2} + \frac{1}{2} \sum_{\nu_1=-L}^{L} \sum_{\nu_2=-L}^{L} \Psi\left(\frac{2\lambda_{\max}}{\gamma(2L+1)}\sqrt{\nu_1^2+\nu_2^2}\right) \cdot \left[\left(\frac{1}{2L+1}\right)^2 \sum_{\eta_1=-L}^{L} \sum_{\eta_2=-L}^{L} \Phi(\eta_1, \eta_2 : \lambda_{\max}, \gamma, K_e, K_m) e^{-j\frac{2\pi}{2L+1}(\nu_1\eta_1+\nu_2\eta_2)}\right], \tag{6.72}$$

where $\lambda_{\max}$ is a value larger than the radius of support of the integrand of (6.70). In the limit as $L \to \infty$, the approximate expression converges to the true value. The portion of (6.72) contained in square brackets is the inverse discrete Fourier transform (DFT) of $\Phi(\eta_1, \eta_2 : \lambda_{\max}, \gamma, K_e, K_m)$, defined

$$\Phi(\eta_1, \eta_2 : \lambda_{\max}, \gamma, K_e, K_m) \triangleq \Phi_{\gamma\mathbf{h}}(\eta_1 \frac{\pi}{\lambda_{\max}}, \eta_2 \frac{\pi}{\lambda_{\max}} : K_e, K_m). \tag{6.73}$$

Judicious selection of a value for γ can lead to greater efficiency of calculation by obviating the need to recalculate new matrices of values, $\Phi(\eta_1, \eta_2 : \lambda_{\max}, \gamma, K_e, K_m)$, for new values of K_e and K_m.

For the first example, let $K_m = 0$ and let $\gamma = \frac{1}{K_e}$. Then

$$\Phi\left(\eta_1, \eta_2 : \lambda_{\max}, \frac{1}{K_e}, K_e, 0\right) = J_0\left(\frac{\pi}{\lambda_{\max}}\sqrt{\eta_1^2+\eta_2^2}\right)^4, \tag{6.74}$$

which does not depend on K_e. Therefore, the calculation of the elements of the matrix Φ and the inverse discrete Fourier transform need be computed only once, then used repeatedly to compute $\mathsf{p}(K_e, 0)$ for any value of $0 \leq K_e \leq \frac{\lambda_{\max}}{4}$. For any $\lambda_{\max} \geq 4$, the result of the inverse discrete Fourier transform is a matrix of samples which, when scaled by a factor of $\left(\frac{2L+1}{2\lambda_{\max}}\right)^2$, approximate samples of $p_{\mathbf{h}}(\underline{\lambda} : 1, 0)$. Fig. 6.6 is a plot of samples of the probability density function $p_{\mathbf{h}}(\underline{\lambda} : 1, 0)$ computed with $\lambda_{\max} = 4$ and $L = 500$. Since there is no magnetostatic interaction ($K_m = 0$), the plot represents the probability density function of the exchange field alone. Using these samples, approximate values for $\mathsf{p}(K_e, 0)$ for values of K_e between 0.1 and 1 were calculated

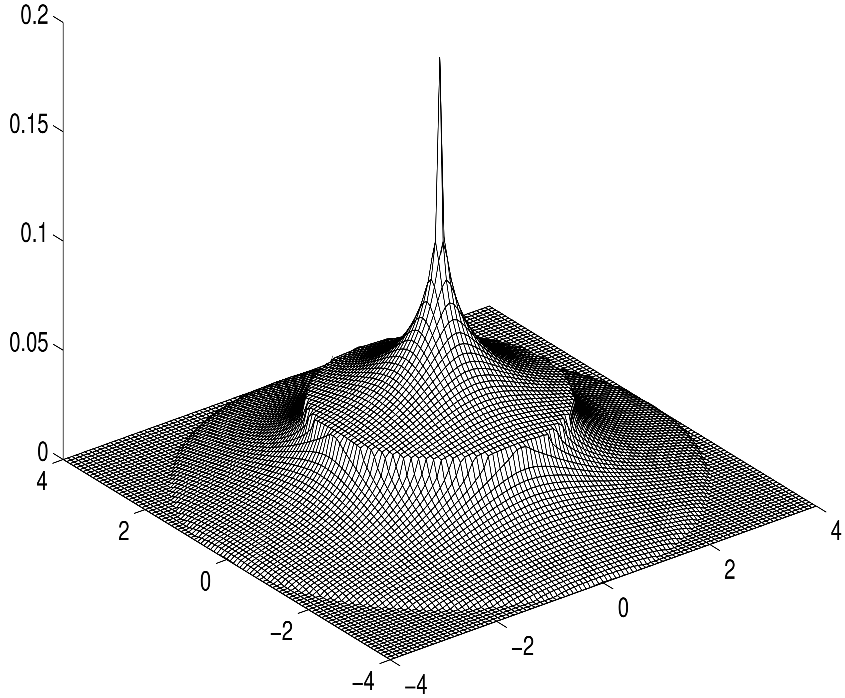

Figure 6.6: Probability density function $p_{\mathbf{h}}(\cdot : K_e = 1, K_m = 0)$

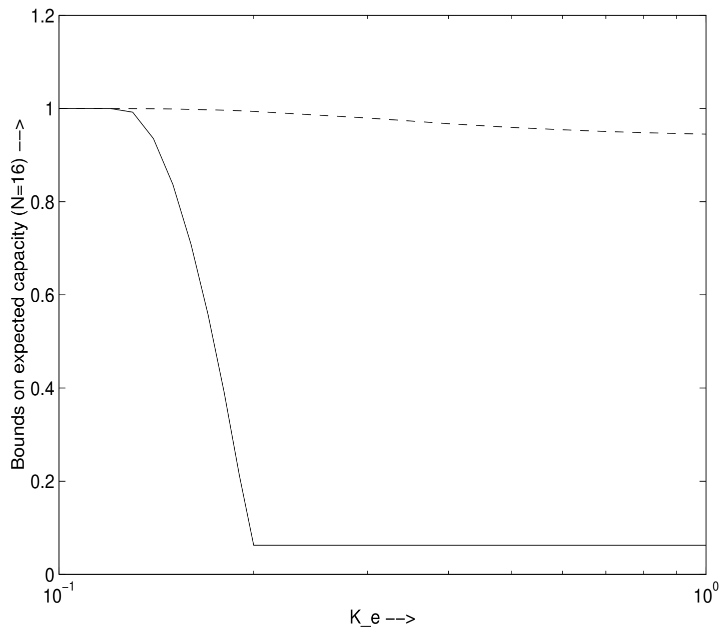

Figure 6.7: Bounds on expected capacity when $0.1 \leq K_e \leq 1, K_m = 0$

and used to compute values of the upper and lower bounds on expected capacity over that range of K_e. Fig. 6.7 is a plot of the upper bound (dashed line) and lower bound (solid line) on the expected capacity as a function of K_e when $K_m = 0$ for $N = 16$. The bounds were computed for a medium of 16 grains for easy comparison with the simulation results in Chapter 5.

For the second example, let $K_e = 0$ and let $\gamma = \frac{1}{K_m}$. Then

$$\Phi\left(\eta_1, \eta_2 : \lambda_{\max}, \frac{1}{K_m}, 0, K_m\right) = \prod_{\iota \triangleq k-1 \neq 0} J_0\left(\frac{\pi}{\lambda_{\max}} \left| \frac{1}{(p_\iota^2 + q_\iota^2)^{5/2}} \begin{bmatrix} 2p_\iota^2 - q_\iota^2 & 3p_\iota q_\iota \\ 3p_\iota q_\iota & 2q_\iota^2 - p_\iota^2 \end{bmatrix} \begin{bmatrix} \eta_1 \\ \eta_2 \end{bmatrix} \right| \right). \tag{6.75}$$

which does not depend on K_m. Therefore, the calculation of the elements of the matrix Φ and the inverse discrete Fourier transform need be computed only once, then used repeatedly to compute $\mathsf{p}(0, K_m)$ for any value of K_m for which the maximum field does not exceed $\lambda_{\max}$. The product is over the $N - 1$ other grains in the assembly, and in order to represent the model without edge effect, should be extended to the number of factors necessary to compute to within an acceptable error the probability density function of the magnetostatic field vector arising from an infinitely extended,

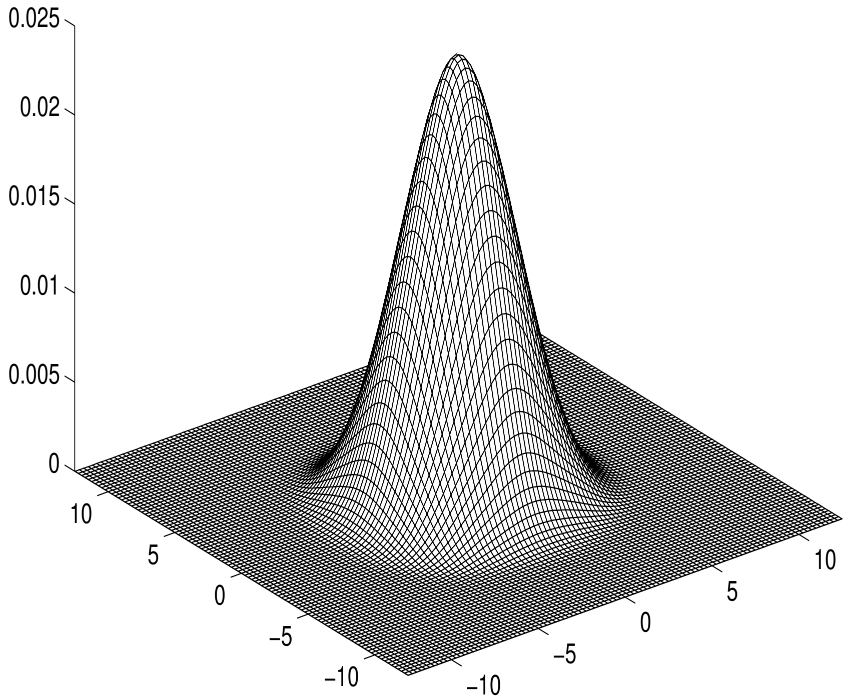

Figure 6.8: Probability density function $p_{\mathbf{h}}(\cdot : K_e = 0, K_m = 1)$

randomly generated medium. Application of the calculation radius guidelines derived in section 3.3.1, with $\epsilon = 1$, predicts that the field computed from a 27×27 array of grains is a good approximation to that computed from an infinite plane of grains. To continue the calculation, let $\lambda_{\max} = 25$ and $L = 500$. Then the result of the inverse discrete Fourier transform is a matrix of samples which, when scaled by a factor of $\left(\frac{2L+1}{2\lambda_{\max}}\right)^2$, approximate samples of $p_{\mathbf{h}}(\underline{\lambda} : 0, 1)$. Fig. 6.8 is a plot of samples of the probability density function $p_{\mathbf{h}}(\underline{\lambda} : 0, 1)$ computed with $\lambda_{\max} = 25$ and $L = 500$. Since there is no exchange interaction ($K_e = 0$), the plot represents the probability density function of the magnetostatic field alone. Using these samples, approximate values for $\mathsf{p}(0, K_m)$ for values of K_m between 0.02 and 0.075 were calculated and used to compute values of the upper and lower bounds on expected capacity over that range of K_m. Fig. 6.9 is a plot of the upper bound (dashed line) and lower bound (solid line) on the expected capacity as a function of K_m when $K_e = 0$ for $N = 16$. The bounds were computed for a medium of 16 grains for easy comparison with the simulation results in Chapter 5.

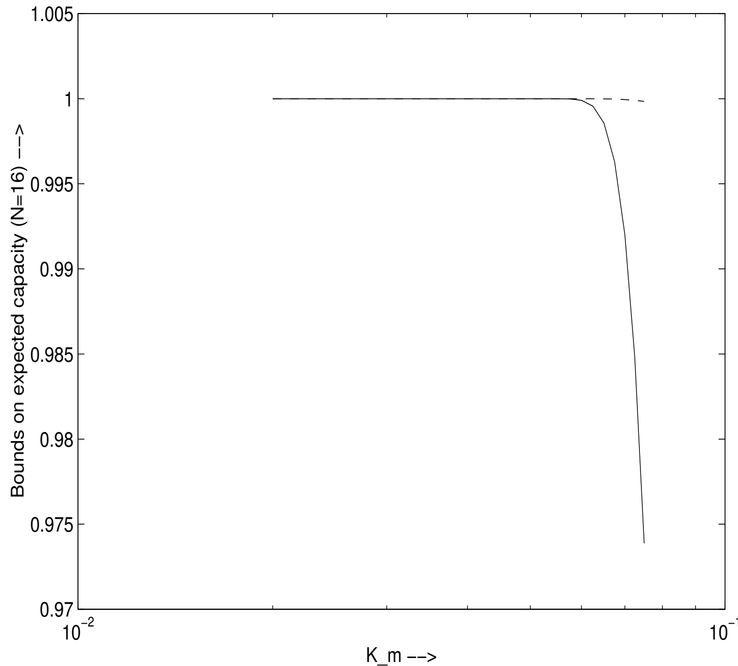

Figure 6.9: Bounds on expected capacity when $0.02 \leq K_m \leq 0.075, K_e = 0$

When both K_m and K_e are non-zero, the magnetic field vector $\mathbf{h}$ includes both an exchange and a magnetostatic component. These components are not statistically independent however. The exchange field arises from the neighboring grains, which also give rise to a substantial portion of the magnetostatic field component. As a consequence, the two field components are statistically correlated. The probability density function of the total magnetic field $\mathbf{h}$ may not be computed as a convolution of the two probability density functions already displayed, but must be computed from its characteristic function, given by (6.46).

Here again, an intelligent choice for γ can relieve some of the computational burden. With $\gamma = \frac{1}{K_m}$, we have

$$\begin{aligned}
\Phi_(\eta_1, \eta_2) &= \left[J_0 \left(\frac{\pi}{\lambda_{\max}} \left\| \begin{bmatrix} \frac{K_e}{K_m} + 2 & 0 \\ 0 & \frac{K_e}{K_m} - 1 \end{bmatrix} \begin{bmatrix} \eta_1 \\ \eta_2 \end{bmatrix} \right\| \right) \right]^2 \\
&\times \left[J_0 \left(\frac{\pi}{\lambda_{\max}} \left\| \begin{bmatrix} \frac{K_e}{K_m} - 1 & 0 \\ 0 & \frac{K_e}{K_m} + 2 \end{bmatrix} \begin{bmatrix} \eta_1 \\ \eta_2 \end{bmatrix} \right\| \right) \right]^2 \\
&\times \left[\prod_{l \notin N(k)} J_0 \left(\frac{\pi}{\lambda_{\max}} \left| \frac{1}{(p_{kl}^2 + q_{kl}^2)^{5/2}} \begin{bmatrix} 2p_{kl}^2 - q_{kl}^2 & 3p_{kl}q_{kl} \\ 3p_{kl}q_{kl} & 2q_{kl}^2 - p_{kl}^2 \end{bmatrix} \begin{bmatrix} \eta_1 \\ \eta_2 \end{bmatrix} \right\| \right) \right]
\end{aligned} \tag{6.76}$$

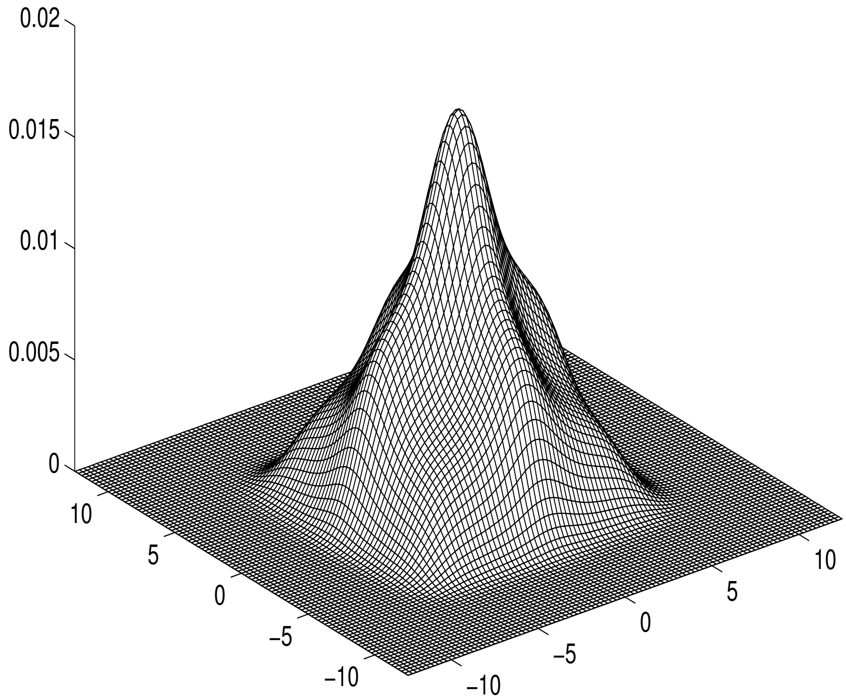

Figure 6.10: Probability density function $p_{\mathbf{h}}(\cdot : K_e = 1, K_m = 1)$

for which the last factor represents the bulk of the calculation. The last factor does not depend on the values of K_e and K_m, so it may be calculated once and used repeatedly in the calculation of several values of $\mathsf{p}(K_e, K_m)$. Furthermore, the first two factors depend on K_e and K_m only through the ratio $\frac{K_e}{K_m}$, so $\mathsf{p}(K_e, K_m)$ may be calculated for several (K_e, K_m) pairs having that ratio constant without recalculation of the matrix Φ.

As an example, let us calculate the probability density function when $K_e = K_m = 1$. Fig. 6.10 is a plot of samples of the probability density function of the total magnetic field $\mathbf{h}$ computed for $K_e = K_m = 1$ computed with $\lambda_{\max} = 25$ and $L = 500$. The statistical correlation of the exchange field and the magnetostatic field is exhibited in Fig. 6.10 by the lack of radial symmetry in the probability density function of $\mathbf{h}$, even though both $\mathbf{h}_e$ and $\mathbf{h}_m$ exhibit probability density functions with radial symmetry or radial near-symmetry. This feature is seen more easily in the contour plot of Fig. 6.11.

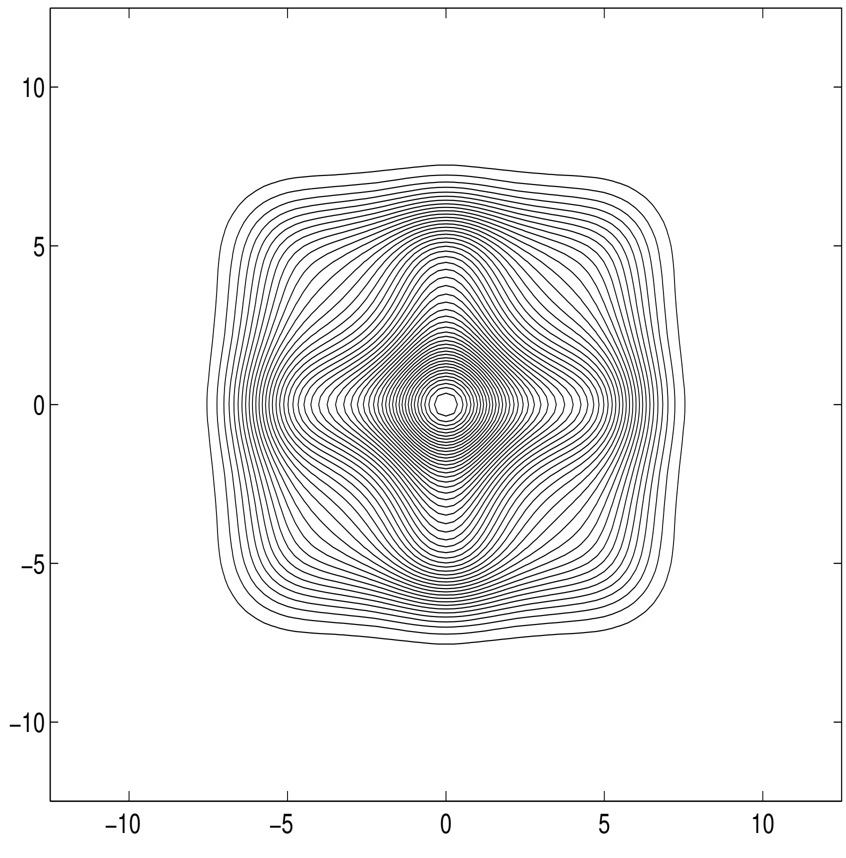

Figure 6.11: Contour plot of $p_{\mathbf{h}}(\cdot : K_e = 1, K_m = 1)$

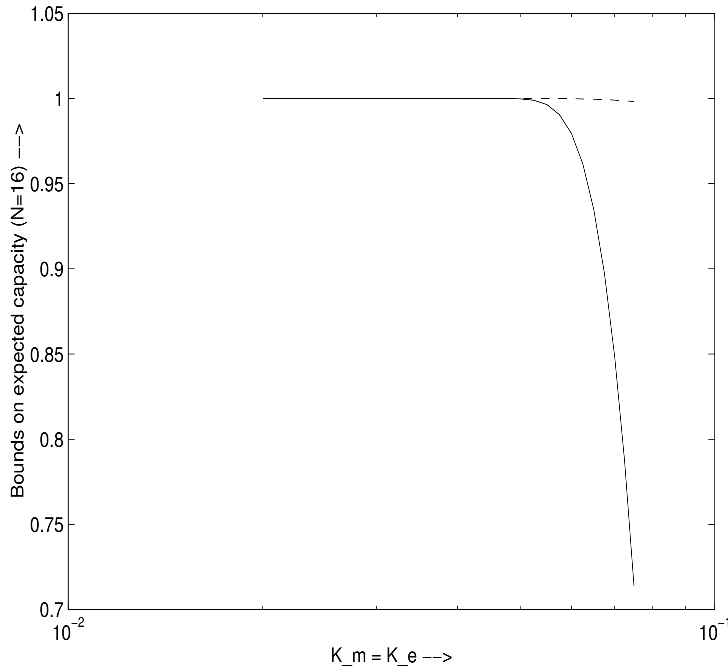

Figure 6.12: Bounds on expected capacity when $0.02 \leq K_m \leq 0.075, K_e = K_m$

Using the calculated samples of $p_{\mathbf{h}}(\cdot : K_e = 1, K_m = 1)$, approximate values for $\mathsf{p}(K_m, K_m)$ for values of K_m between 0.02 and 0.075 were calculated and used to compute values of the upper and lower bounds on expected capacity over that range of K_m, along the contour $K_e = K_m$. Fig. 6.12 is a plot of the upper bound (dashed line) and lower bound (solid line) on the expected capacity as a function of K_m when $K_e = K_m$ for $N = 16$. The bounds were computed for a medium of 16 grains for easy comparison with the simulation results in Chapter 5.

Figures 6.12 and 6.9 each depict upper and lower bounds on capacity as functions of K_m, each for a fixed ratio K_e/K_m. Several calculations of this type have been performed for different values of the ratio K_e/K_m between 0 and 1.5. Fig. 6.13 is a plot of the lower bound on expected capacity derived from these calculations as a function of K_e and K_m. The contour on this plot surrounding the region where the computed lower bound is equal to one is a good approximation of the contour surrounding the region of the (K_e, K_m) plane for which the expected capacity is equal to one bit per grain.

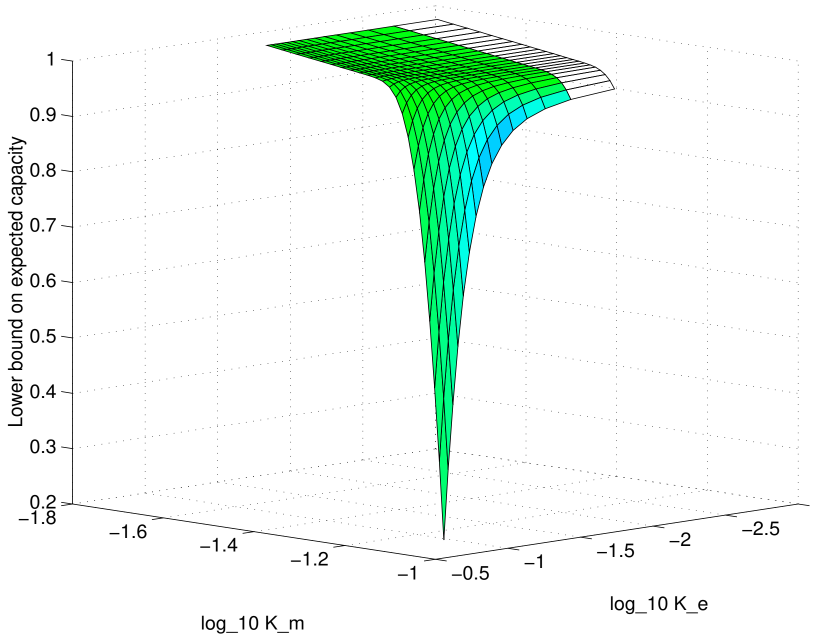

Figure 6.13: Lower bound on expected capacity as function of (K_e, K_m)

6.2.8 Summary

This section has considered the expected capacity of non-oriented media represented by the flip-relaxation model. Although direct calculation of the exact value of expected capacity has not been presented, both upper and lower bounds on this quantity have been calculated. As part of these calculations, expressions for the probability density functions of the normalized magnetic field arising from a randomly generated, non-oriented medium have been derived. For media characterized by values of K_e and K_m within a region of the (K_e, K_m) plane in which both variables have small values, the upper bound and the lower bound are equal and equal to one bit per grain. The calculations presented in this section permit approximate calculation of the boundary of that region. Outside of that region, the bounds are weak improvements, if improvements at all, on very simple upper and lower bounds. For large values of either K_e or K_m, then, other analysis must be pursued. Such analysis is the subject of Chapter 7.

6.3 Microstructure Knowledge and Capacity

The storage capacity C of a patch of recording media represented by the simplified flip-relaxation model has been defined as a function of the number F of states of the model which are fixed points of the model's update rule. As observed in Chapter 5, achieving this capacity depends on a recording technology which can impose on the recording medium only those recorded magnetic patterns which are fixed points. There are two requirements for such a technology. Clearly the ability to manipulate magnetic states at a fine level of spatial detail is required. The other requirement is that somehow the set of magnetic states $\Omega(K_e, K_m, \mathbf{\Theta})$ which are fixed points for a particular patch of media must be known. Since this set of fixed points depends on the microstructure $\mathbf{\Theta}$, at least some knowledge about the microstructure of the medium must be gathered and used to implement a recording technology capable of achieving the storage capacity C computed by analysis of our model. When only statistical properties, but no specific knowledge of the microstructure is available, the possible density of information storage, considered over a large number of medium patches, must be reduced below C. In this section, we consider a very simple two-grain medium patch to illustrate the dependence of achieving the fundamental limits on areal storage density on knowledge of the medium microstructure.

6.3.1 Two-grain Medium Patch

Let us consider the simplest medium patch for which the microstructure $\mathbf{\Theta}$ has an effect on capacity, one comprising two grains. We further specify the simplified medium model of Chapter 5 by declaring $\mathcal{I} = \{1, 2\}$, so that $N = 2$, and $\mathbf{\Theta} = [\theta_1, \theta_2]$. The two square grains of the model are neighbors, arranged as a rectangular patch with long x axis and short z axis. Thus, the normalized spatial relationship of grains 1 and 2 is represented by $p_{21} = -p_{12} = 1$ and $q_{21} = -q_{12} = 0$. There are four magnetic states of the two-grain model, which may be enumerated for convenience,

$$\begin{aligned}
\mathbf{s}_0 &= (-1, -1), \\
\mathbf{s}_1 &= (-1, 1), \\
\mathbf{s}_2 &= (1, -1), \\
\mathbf{s}_3 &= (1, 1).
\end{aligned}$$

A particular instance of the two-grain patch model is completely identified by the values of four parameters, K_e, K_m, θ_1, and θ_2. In particular, the set of fixed points Ω is a function of those four values.

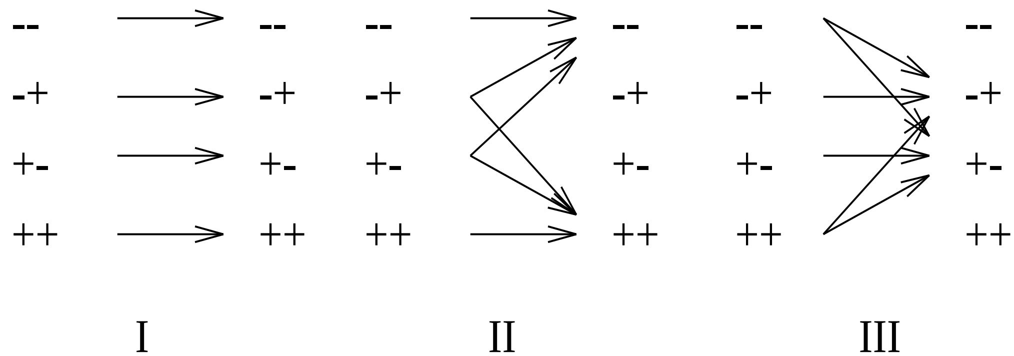

Figure 6.14: Three possible information channels corresponding to a grain pair

The properties of the set of fixed points Ω stated as Propositions 5.1 and 5.2 permit only three possible values for Ω, enumerated,

$$\begin{aligned}\Omega_{\mathrm{I}} &= \{\mathbf{s}_0, \mathbf{s}_1, \mathbf{s}_2, \mathbf{s}_3\}, \\ \Omega_{\mathrm{II}} &= \{\mathbf{s}_0, \mathbf{s}_3\}, \\ \Omega_{\mathrm{III}} &= \{\mathbf{s}_1, \mathbf{s}_2\}.\end{aligned}$$

An interesting property of the two-grain patch is that if any state $\mathbf{s}$ is not a fixed point, then reversal of the magnetization of either grain will result in a stable state. Therefore the process of relaxation for the two-grain medium patch consists of at most one flip of magnetization. Given this property and the value of Ω, a representation of the model as an information channel mapping an input state to an output state is determined. Since there are three possible values for Ω, the representation of the two-grain medium patch as an information channel must be one of only three different information channels depicted in Fig. 6.14. The channels have been enumerated with Roman numerals corresponding to the enumeration of the possible values of Ω. Each information channel may then be represented by a transition probability matrix. The enumerated transition probability matrices are

$$P_{\mathrm{I}} = \begin{bmatrix} 1 & 0 & 0 & 0 \\ 0 & 1 & 0 & 0 \\ 0 & 0 & 1 & 0 \\ 0 & 0 & 0 & 1 \end{bmatrix}, \tag{6.77}$$

$$P_{\mathrm{II}} = \begin{bmatrix} 1 & 0.5 & 0.5 & 0 \\ 0 & 0 & 0 & 0 \\ 0 & 0 & 0 & 0 \\ 0 & 0.5 & 0.5 & 1 \end{bmatrix}, \tag{6.78}$$

$$P_{\mathrm{III}} = \begin{bmatrix} 0 & 0 & 0 & 0 \\ 0.5 & 1 & 0 & 0.5 \\ 0.5 & 0 & 1 & 0.5 \\ 0 & 0 & 0 & 0 \end{bmatrix}. \tag{6.79}$$

Every quadruple of values $(K_e, K_m, \theta_1, \theta_2)$ corresponds to exactly one of these three possible information channels. For fixed values of K_e and K_m, and independent, uniformly distributed orientation of anisotropy axes, we may compute the probability of each of the three information channels as the values q_{I}, q_{II}, and q_{III}, all three quantities functions of the fixed values of K_e and K_m.

Consider the recording of information on a large number of two-grain medium patches, all described by fixed pair of values K_e and K_m representing material properties, and each having a different pair of values for θ_1 and θ_2 drawn independently from a uniform distribution between $-\pi/2$ and $\pi/2$. The average storage capacity achievable depends on whether knowledge of the microstructure may be used in the recording and reading processes. Let us now compare these two cases.

6.3.2 Known Microstructure

When information about the microstructure (θ_1, θ_2) is available to the recording and reading processes, these processes may be adapted to the particular microstructure to increase storage capacity. As an idealized case, let us assume the values of (θ_1, θ_2) are known, and furthermore, the particular set of stable states $\Omega(K_e, K_m, \theta_1, \theta_2)$ determined by the microstructure is known. Under these assumptions, every two-grain medium patch can be identified as one of the three possible corresponding information channels, I, II, or III. Once the information channel is identified, error-free recording is possible using only those magnetic states in Ω, those which are fixed points.

This recording strategy records two bits of information on every two-grain medium patch which corresponds to channel I, and one bit of information on every two-grain medium patch which corresponds to channels II or III. The average number of bits stored on each two-grain medium patch is then

$$E\{B\} = 2q_{\mathrm{I}} + q_{\mathrm{II}} + q_{\mathrm{III}}. \tag{6.80}$$

Because

$$q_{\mathrm{I}} + q_{\mathrm{II}} + q_{\mathrm{III}} = 1, \tag{6.81}$$

we may write

$$E\{B\} = 1 + q_{\mathrm{I}}. \tag{6.82}$$

Finally, each patch comprises two grains, so the average storage capacity in bits per grain is

$$E\{C(K_e, K_m)\} = \frac{1}{2} + \frac{q_{\mathrm{I}}(K_e, K_m)}{2}, \tag{6.83}$$

where the dependence on the material parameters K_e and K_m has been made explicit. Numerical calculation of q_{I} is deferred until after the case for unknown microstructure is considered.

6.3.3 Unknown Microstructure

When there is no information about the particular values of (θ_1, θ_2) available to the recording and reading processes, the only recourse is to adopt one general recording/reading method which performs best on average over the distribution of possible microstructures. In this investigation, the recording process is represented by the selection of an input state $\mathbf{s}$. Because the microstructure variables are unknown, the exact magnetization vectors corresponding to the input state are also unknown, but the elements of $\mathbf{s}$ indicate the sign of the magnetization components in the x direction. Therefore, an interpretation of the record process is an attempt to magnetize the grains along the x axis, and a result that the grains are magnetized along their anisotropy axes so that the x component of magnetization agrees with the recording attempt. Similarly, the output state $\mathbf{s}$ is interpreted as the sign of the projection of the grain magnetizations onto the x axis.

Since no information about the microstructure is available, the different medium patches cannot be separated into the three types of information channels. Instead, all of them must be represented as a single information channel representing a combination of the three possibilities. The combined information channel is the one

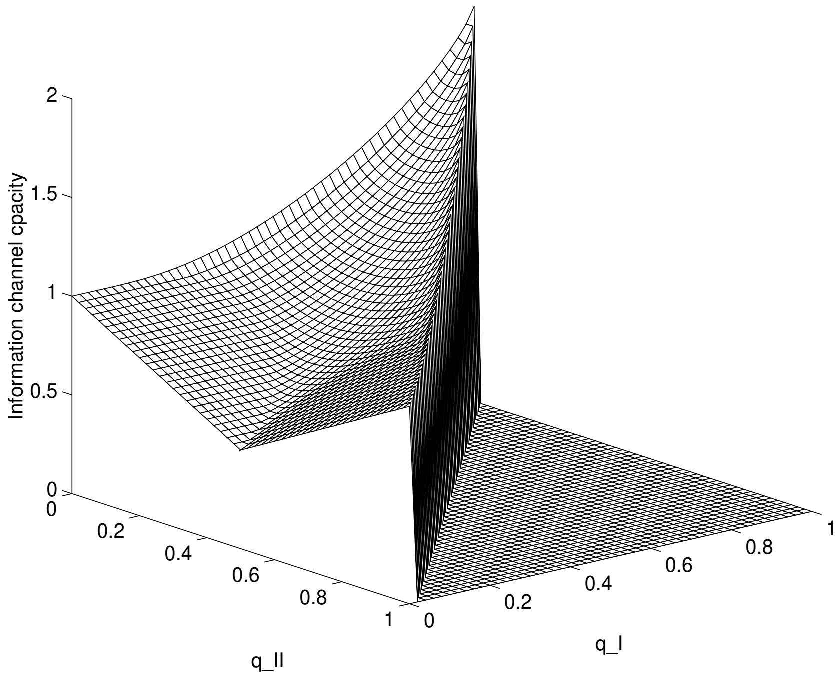

Figure 6.15: Capacity of combined information channel as function of $(q_{\mathrm{I}}, q_{\mathrm{II}})$

represented by the transition probability matrix,

$$P = \begin{bmatrix} q_{\mathrm{I}} + q_{\mathrm{II}} & 0.5q_{\mathrm{II}} & 0.5q_{\mathrm{II}} & 0 \\ 0.5q_{\mathrm{III}} & q_{\mathrm{I}} + q_{\mathrm{III}} & 0 & 0.5q_{\mathrm{III}} \\ 0.5q_{\mathrm{III}} & 0 & q_{\mathrm{I}} + q_{\mathrm{III}} & 0.5q_{\mathrm{III}} \\ 0 & 0.5q_{\mathrm{II}} & 0.5q_{\mathrm{II}} & q_{\mathrm{I}} + q_{\mathrm{II}} \end{bmatrix}. \tag{6.84}$$

The constituent information channels have been combined in proportion to their probability. This transition probability matrix is parameterized by the values of $q_{\mathrm{I}}, q_{\mathrm{II}}$, and q_{III}. Since the sum of these values is 1, any pair is sufficient to parameterize the transition probability matrix.

Given any triple of values $(q_{\mathrm{I}}, q_{\mathrm{II}}, q_{\mathrm{III}})$ between 0 and 1 which sum to 1, a transition probability matrix is determined which in turn completely describes an information channel. To compute the capacity of a discrete information channel for which the transition probability matrix is known, we may apply the Blahut-Arimoto algorithm [23, pp. 364-367]. Using samples of values of the pair $(q_{\mathrm{I}}, q_{\mathrm{II}})$ to sample the possible transition probability matrices, the Blahut-Arimoto algorithm was applied to each sample matrix to compute the capacity of the corresponding information channel. The results of this computation are plotted in Fig. 6.15. The capacity

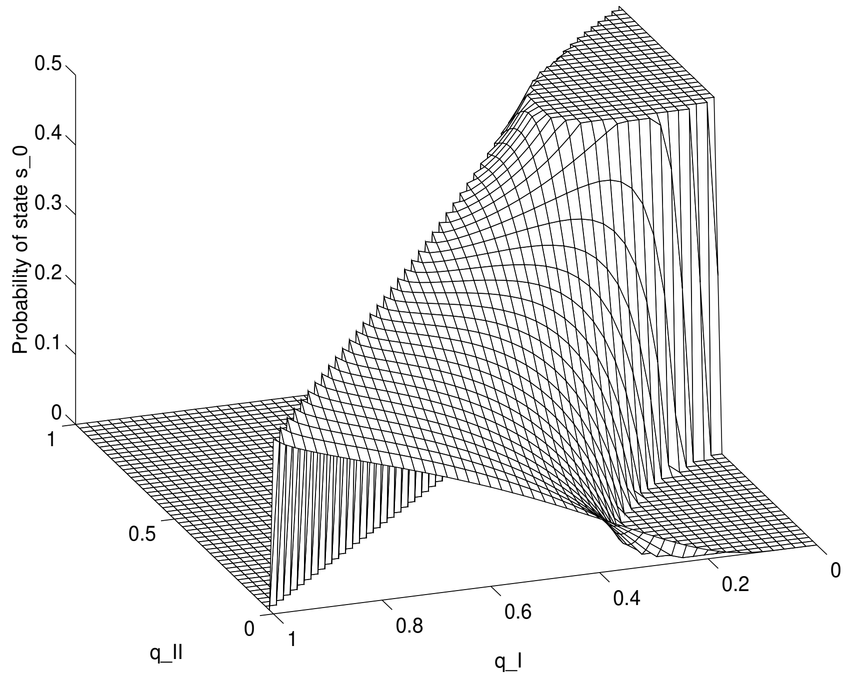

Figure 6.16: Probability of state $\mathbf{s}_0$ which achieves capacity

values at the three corners of Fig. 6.15 are 2 bits, 1 bit, and 1 bit in agreement with the capacities of the three component information channels which are combined in the combined information channel. This plot demonstrates the ability to compute the average number of bits which can be reliably stored per two-grain medium patch given a pair of values for $(q_{\mathrm{I}}, q_{\mathrm{II}})$. The Blahut-Arimoto algorithm also computes the probabilities with which the input states must be chosen in order to achieve the capacity of the combined information channel. In all cases the choice of input state probabilities which achieves capacity has the property that the probabilities of states $\mathbf{s}_0$ and $\mathbf{s}_3$ are equal and the probabilities of states $\mathbf{s}_1$ and $\mathbf{s}_2$ are equal. The sum of all four probabilities must be 1, so all four values may be derived from the value of the probability of state $\mathbf{s}_0$. Fig. 6.16 is a plot of the probability of state $\mathbf{s}_0$ which achieves the capacity plotted in Fig. 6.15 for the corresponding values of $(q_{\mathrm{I}}, q_{\mathrm{II}})$. The probability values at the three corners of Fig. 6.16 are 0.25, 0.5, and 0 in agreement with the probability of state $\mathbf{s}_0$ which achieves capacity in each of the three component information channels which are combined in the combined information channel. Notice the broad ranges of values of $(q_{\mathrm{I}}, q_{\mathrm{II}})$ for which the probability of input state $\mathbf{s}_0$ is either 0 or 0.5. Within these ranges, recording is done using only states $\mathbf{s}_1$ and $\mathbf{s}_2$ or only states $\mathbf{s}_0$ and $\mathbf{s}_3$ respectively. With the ability of computing both capacity and the input probabilities which achieve capacity demonstrated, we may turn to the computation of values for $(q_{\mathrm{I}}, q_{\mathrm{II}})$, given the values of (K_e, K_m).

6.3.4 Capacity Gain from Microstructure Information

The large number of two-grain medium patches under consideration are assumed to share material properties represented by fixed values of material parameters K_e and K_m. The variation of microstructure from one patch to the next is represented by drawing the variables θ_1 and θ_2 for each patch independently from a uniform distribution between $-\pi/2$ and $\pi/2$. Each patch so generated then corresponds to exactly one of the three information channels of Fig. 6.14. For a sufficiently large number of patches, the fraction of patches corresponding to information channel I converges to a quantity $q_{\mathrm{I}}(K_e, K_m)$, defined

$$q_{\mathrm{I}}(K_e, K_m) \stackrel{\triangle}{=} \Pr\{(\theta_1, \theta_2) : \Omega(K_e, K_m, \theta_1, \theta_2) = \Omega_{\mathrm{I}}\}. \tag{6.85}$$

The quantities $q_{\mathrm{II}}(K_e, K_m)$ and $q_{\mathrm{III}}(K_e, K_m)$ are defined analogously.

To calculate these values, the circumstances under which each of the three information channels represents the behavior of the two-grain medium patch must be understood. Information channel I describes the behavior of those medium patches for which both $\mathbf{s}_0$ and $\mathbf{s}_1$ are fixed points. For this to be true, it must be true that the normalized field at grain 1 lies within the Stoner-Wohlfarth astroid of grain 1. That is,

$$|h_{\|,1}(K_e, K_m, \theta_1, \theta_2)|^{2/3} + |h_{\perp,1}(K_e, K_m, \theta_1, \theta_2)|^{2/3} < 1. \tag{6.86}$$

For any quadruple of values $(K_e, K_m, \theta_1, \theta_2)$, the truth of (6.86) can be ascertained. Therefore, the quantity $q_{\mathrm{I}}(K_e, K_m)$ can be approximated by numerical computation by testing a large number of uniformly sampled (θ_1, θ_2) pairs. The results from such numerical calculation of the quantity $q_{\mathrm{I}}(K_e, K_m)$ are plotted in Fig. 6.17 as a function of the base 10 logarithm of K_e and K_m. Substitution into (6.83) yields the average storage capacity which can be achieved on a large number of two-grain medium patches when knowledge of the microstructure is used in recording and reading. Fig. 6.18 is a plot of this capacity as a function of the base 10 logarithm of material parameters K_e and K_m, for ease of comparison with previous plots of capacity as a function of K_e and K_m.

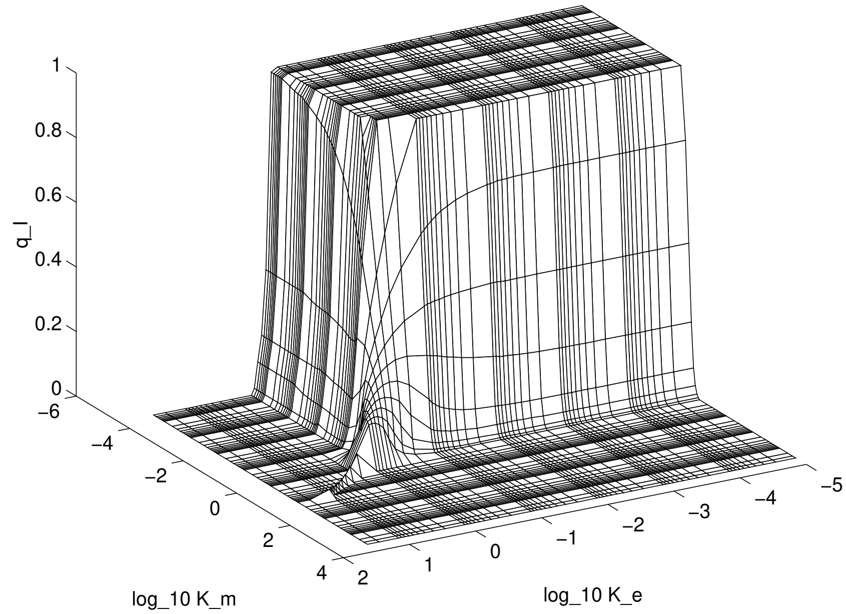

Figure 6.17: Dependence of q_{I} on (K_e, K_m)

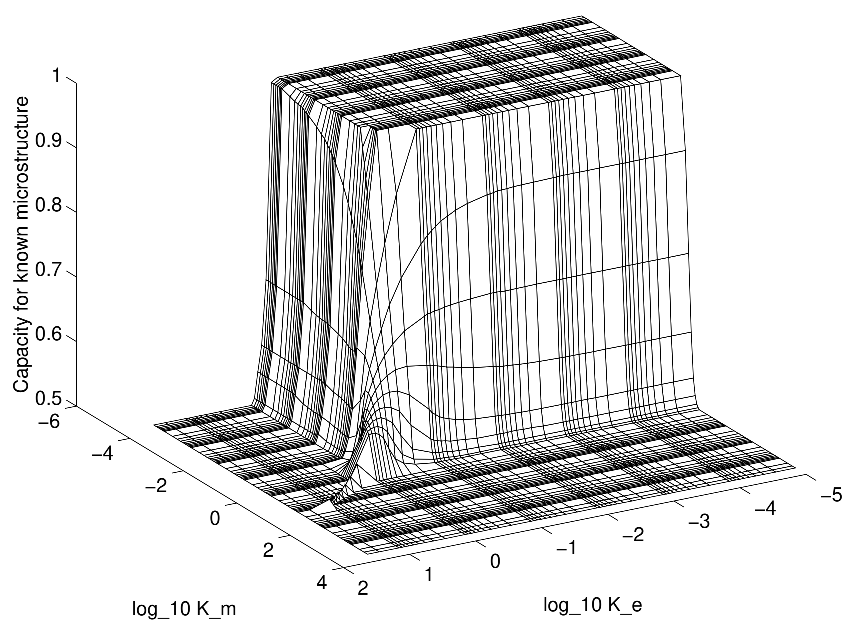

Figure 6.18: Storage capacity of two-grain patches when microstructure is known

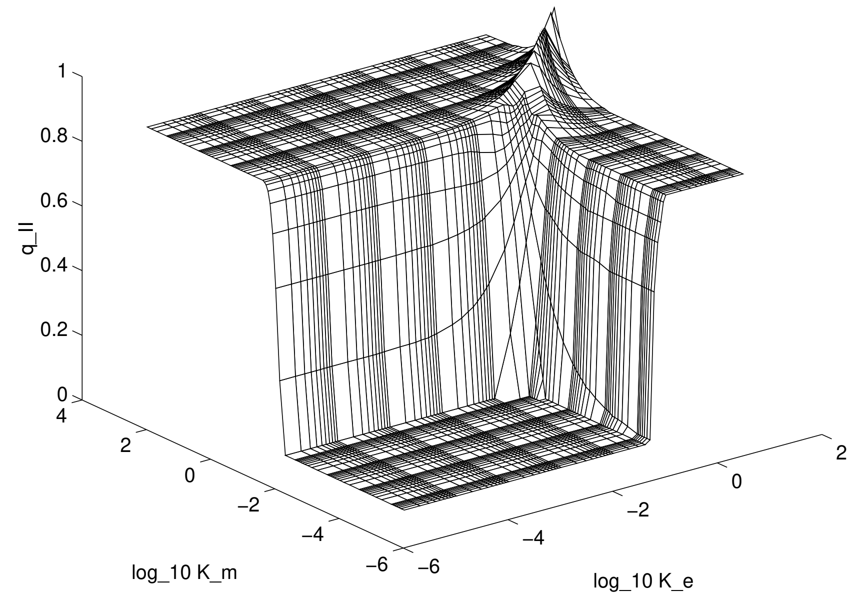

Figure 6.19: Dependence of q_{II} on (K_e, K_m)

Information channel II describes the behavior of those medium patches for which $\mathbf{s}_0$ is a fixed point and $\mathbf{s}_1$ is not. For this to be true, it must be true that the normalized field at grain 1 lies outside the Stoner-Wohlfarth astroid of grain 1. Furthermore, the component of the normalized field at grain 1 along the easy axis of grain 1 must have the same sign as the magnetization of grain 2. That is,

$$|h_{\|,1}(K_e, K_m, \theta_1, \theta_2)|^{2/3} + |h_{\perp,1}(K_e, K_m, \theta_1, \theta_2)|^{2/3} \geq 1, \tag{6.87}$$

and

$$s_2 \cdot h_{\|,1}(K_e, K_m, \theta_1, \theta_2) > 0. \tag{6.88}$$

For any quadruple of values $(K_e, K_m, \theta_1, \theta_2)$, the truth of (6.87) and (6.88) can be ascertained. Therefore, the quantity $q_{\mathrm{II}}(K_e, K_m)$ can be approximated by numerical computation by testing a large number of uniformly sampled (θ_1, θ_2) pairs. The results from such numerical calculation of the quantity $q_{\mathrm{II}}(K_e, K_m)$ are plotted in Fig. 6.19 as a function of the base 10 logarithm of K_e and K_m.

With both q_{I} and q_{II} known as functions of K_e and K_m, the Blahut-Arimoto algorithm may be applied to reveal the capacity of the combined information channel, and the probability of input state $\mathbf{s}_0$ in the input probability vector which achieves the capacity of the combined information channel. The capacity and input probability

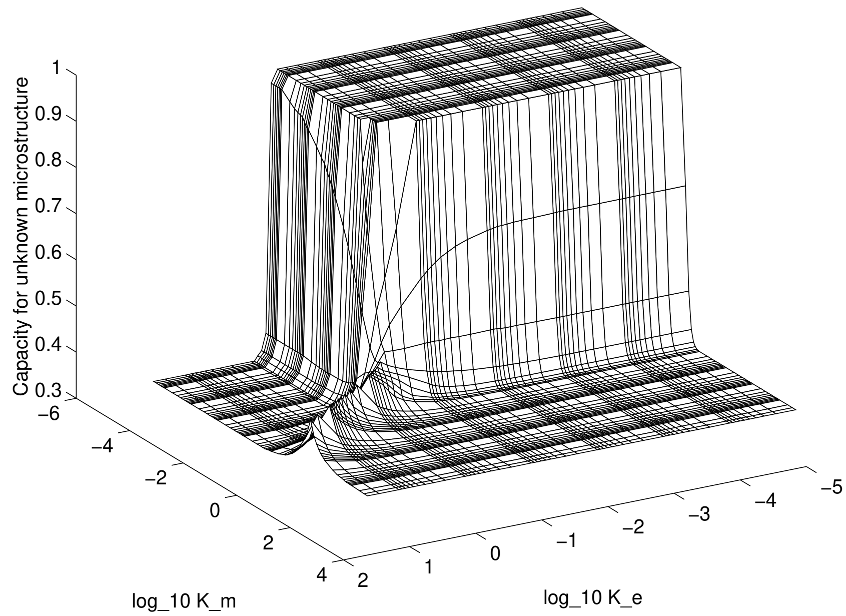

Figure 6.20: Storage capacity of two-grain patches when microstructure is unknown

vector computed by the Blahut-Arimoto algorithm are the greatest storage capacity which can be achieved on average for a large number of two-grain medium patches when no information about the microstructure is available to the recording and reading processes. Fig 6.20 is a plot of the capacity computed by the Blahut-Arimoto algorithm as a function of the material parameters K_e and K_m. The scaling of axes and the view is the same as that of Fig. 6.18 for easy comparison. As expected, for all values of material parameters K_e and K_m, the capacity which can be achieved without knowledge of microstructure is always less than that which can be achieved when knowledge of the microstructure is used to advantage in the recording and reading processes. The probability of input state $\mathbf{s}_0$ necessary to achieve the capacity plotted in Fig. 6.20 is plotted in Fig. 6.21, again as a function of material parameters K_e and K_m. The simplicity of the result may be somewhat surprising. When K_e and K_m are both small enough that information channel I describes all of the two-grain medium patches, then the maximum capacity of 1 bit per grain is possible, only when all input states are equally likely in the recording process. Thus, the value for the probability of state $\mathbf{s}_0$ in this region of the (K_e, K_m) plane is 0.25. For large values of either K_e or K_m, the value for the probability of state $\mathbf{s}_0$ is 0.5. This indicates that recording is done using only states $\mathbf{s}_0$ and $\mathbf{s}_3$, without using states $\mathbf{s}_1$ and $\mathbf{s}_2$ at all. This means that those two-grain patches which have behavior represented by information channels I

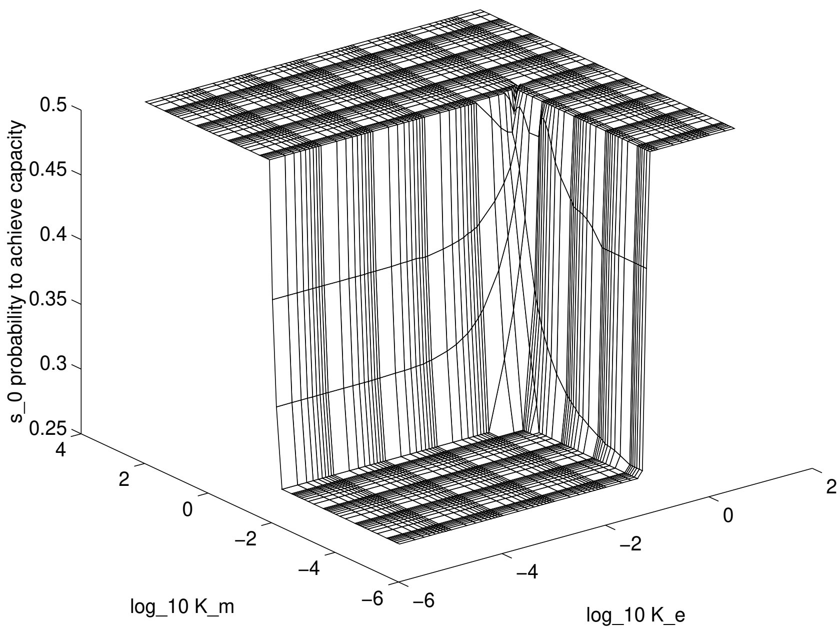

Figure 6.21: Probability of $\mathbf{s}_0$ in input probability vector which achieves capacity for unknown microstructure

or II are able to store one bit of information without error, while those with behavior represented by information channel III can store no information at all because the only fixed points for those patches, $\mathbf{s}_1$ and $\mathbf{s}_2$ are not used by the generic record/read procedure. It is only because patches represented by information channels I and II occur much more often than those represented by information channel III that this is the optimum record and readback strategy for maximum average storage density. More sophisticated coding is only helpful for two-grain patches which have material parameter values K_e and K_m in the rather narrow region of the (K_e, K_m) plane which separates the regions where simple coding achieves capacity.

Finally, with storage capacity computed for both the case when microstructure is completely known and the case where no information about the microstructure is available, we may quantify the gain in storage capacity which results from use of information about microstructure in recording and reading. Fig. 6.22 is a plot of the difference between the plots in Fig. 6.18 and Fig. 6.20.

In the region of the (K_e, K_m) plane where the values of K_e and K_m are both small, storage of one bit per grain is possible whether or not the microstructure is known. In this region, there is no capacity gain from knowledge of the microstructure.

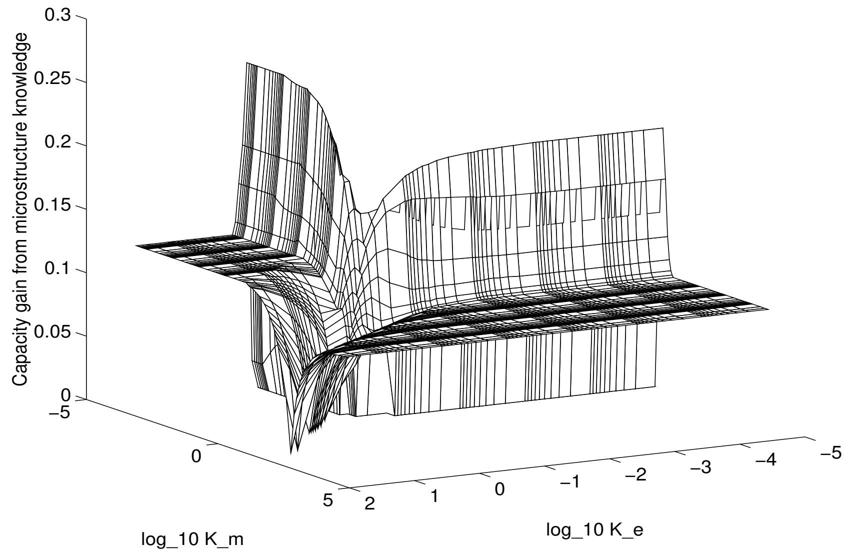

Figure 6.22: Gain in capacity from microstructure knowledge

The conclusion is that the simplified model predicts that if media can be manufactured with material properties for which the grains can be considered essentially non-interacting, then the maximum storage capacity of one bit per grain is achievable even without knowledge of the microstructure. There is nothing to be gained from more complicated recording and reading processes which take microstructure into account.

In the region of the (K_e, K_m) plane where the value of K_e is large and the value of K_m is small, the storage capacity increases from about 0.38 bits per grain to 0.5 bits per grain when information about microstructure is used to modify the recording and reading processes, an increase of more than 30%. In the region of the (K_e, K_m) plane where the value of K_m is large and the value of K_e is small, the storage capacity increases from about 0.41 bits per grain to 0.5 bits per grain when information about microstructure is used to modify the recording and reading processes, an increase of more than 20%. The conclusion is that for both exchange-dominated and magnetostatic-dominated materials information about the microstructure must be used in the recording and reading processes to achieve the maximum possible storage density.

An interesting feature of the capacity gain from microstructure knowledge is that it decreases to zero when the values of K_e and K_m are exactly equal. In the two-grain patches considered in this investigation, a consequence of equal values for K_e and K_m is that all internal magnetic field components along the short axis of the patch cancel. Therefore, both magnetic fields are aligned with the long axis of the patch. Given that constraint on the direction of the magnetic field, no orientation of the easy axes can lead to $\mathbf{s}_1$ or $\mathbf{s}_2$ as fixed points. That is, $q_{\mathrm{III}}(K_m, K_e) = 0$ whenever $K_e = K_m$. When K_e and K_m are large enough that $q_{\mathrm{I}}(K_m, K_e)$ is also zero, it follows that all two-grain patches for this class of materials are represented by information channel II, permitting error-free recording of one bit per two-grain patch whether or not microstructure is known.

6.3.5 Conclusions

The results of this section may be applied to several problems of magnetic recording. Most obviously, they may be taken to prescribe the methods of recording necessary to achieve maximum storage density on a previously chosen recording medium. Given any recording medium, if we can identify its material properties with an appropriate pair of values for K_e and K_m, the plots in Figures 6.18, 6.20, and 6.21 reveal the maximum storage density possible for that medium, whether use of microstructure information in recording and reading is required to achieve that density, what density can be achieved without use of microstructure information, and the recording strategy (input state probabilities) required to achieve the highest storage density possible without microstructure information. All of this information serves to design recording methods for a previously chosen recording medium.

When the recording medium has not been previously chosen, we may also use the results of this section investigation as a guide for making the selection of recording media, as well as the design of the recording and playback processes for maximum areal density of information storage. It has been assumed in this section that the anisotropy axes of the medium are uniformly distributed over all directions in the plane of the medium. Therefore, the results serve only as a guide for selecting among non-oriented recording media. With the distribution of easy axes fixed, and the grain structure fixed as a regular tiling of squares by the simplifications of the model, the only remaining medium properties which we are free to select are the quintuple of material parameters $(\delta, M_s, K_A, f\sqrt{A_e}, D)$.

The manufacture of a magnetic recording medium which exhibits material properties prescribed by a particular quintuple of values is a problem in the realm of materials science. Solutions may well be constrained by interdependencies among the values of the quintuple of material parameters. The solution of this problem is outside the scope of this thesis. In order to illustrate the dependence of maximum areal density of information storage on the material properties of a recording medium, we simply assume as much freedom in the selection of values for material parameters as necessary for the illustration.

Figures 6.18 and 6.20 are plots of how the average capacity $\langle C \rangle$ of a medium made up of a large number of two-grain patches in bits per grain varies with the values of a pair of parameters K_e and K_m which summarize the material properties of the medium. The maximum areal density of storage for a medium characterized by parameters K_e and K_m and with grain size D may then be defined

$$C_A(K_e, K_m, D) \triangleq \langle C \rangle \left(K_e(D), K_m(D)\right) \cdot D^{-2}, \tag{6.89}$$

where the subscript A denotes that this is an areal capacity. Two illustrations of the dependence of the areal storage capacity of a recording medium on its material properties are instructive.

First, consider that the grain size D for a recording medium has been fixed, and the values of the other four material parameters may be freely chosen. With the grain size fixed, the areal storage capacity is proportional to the storage capacity in bits per grain, and both are maximized when the values of the other four material parameters are chosen so that the values of K_e and K_m lie in the region of one bit per grain capacity. This condition prescribes ranges of values for the other four parameters. The selection of particular values may be guided by other considerations such as the difficulty or cost of manufacture of the medium. A side benefit of this solution is that if such media are manufacturable, the maximum storage capacity can be achieved without making use of microstructure information in the recording and reading processes.

Second, consider the opposite constraint on the quintuple of material parameters. Let the value of grain size D be freely chosen with the values of the other four material parameters fixed. The areal capacity C_A depends on D through both parts of the right side of (6.89). A decrease in the grain size D will increase K_e and K_m which are both inversely proportional to D. This will tend to decrease the average capacity per grain $\langle C \rangle$. The decrease in D will also increase the number of grains per unit area. Whether or not areal capacity increases or decreases depends on how these two competing trends compare. It is certainly possible that greater areal densities are achievable using media which do not not support maximum capacity in bits per grain. For materials made up of smaller, significantly interacting grains, the decrease in storage capacity per grain can be more than compensated for by the increase in number of grains per unit area, so long as the grains remain large enough that the model itself does not become invalid. For such media, we must consider selection of recording media and design of recording systems corresponding to the regions of the (K_e, K_m) plane where the average capacity is less than one bit per grain. In these regions, maximum capacity can be achieved in only two ways, either by recording and reading methods which take into account information about the microstructure, or by very carefully controlling the values of material parameters so that K_e equals K_m.

These conclusions are based on an assumption that dividing a recording medium into a large number of independent two-grain patches remains a reasonable representation. Extending these results to larger independent patches is complicated by two facts. First, both the number of magnetic states and the number of information channels necessary to represent all the possible behaviors of a medium patch will increase exponentially with the number of grains N. Listing the possible information channels quickly becomes infeasible as N grows larger. The transition probability matrices also grow exponentially in size, making the Blahut-Arimoto algorithm rapidly more difficult to compute. Second, the two-grain analysis has taken advantage of the fact that the relaxation process consists of at most one application of the update rule. For larger patches, all relaxations of multiple steps must also be considered. If the 2^N magnetic states of the patch are taken as vertices, and all possible outcomes of the update rule are taken as directed edges, then this problem corresponds to counting directed paths on a hypercube. This can only be practical if there are available more powerful analytical methods, perhaps from graph theory. Further research into such methods is necessary to extend the results of this section to larger patches.

One feature of these results which is not expected to persist if larger patches are considered is the lack of capacity gain from microstructure information when K_e and K_m are large and exactly equal. The cancellation of field components which leads to this result depends on each magnetic field arising from only one neighbor grain. As more neighbor grains contribute components to the magnetic field, there will still be cancellations between exchange and magnetostatic fields when K_e and K_m, but they will not all be oriented in the same direction. The influence of these cancellations will not be to force the total effective field to be aligned with a particular axis, but only will be to reduce the mean field magnitude, as might be predicted from the field probability density function in Fig. 6.10. Therefore, for a recording medium for which either K_e or K_m is large, we expect the only way to achieve maximum information storage density on that medium is with recording and reading techniques which take into account information about the local microstructure.

6.4 Summary

In this chapter the effect of medium microstructure on storage capacity has been illustrated through three studies. First, a specially designed microstructure intended to represent bicrystal media was simulated. When exchange interactions are large and magnetostatic interactions are moderate, media with this specially designed microstructure have greater storage capacity than media with the same material parameters but a randomized microstructure. For materials with parameters in this range, bicrystal media have greater storage capacity than randomized, non-oriented media. Second, the average of medium storage capacity over all possible non-oriented microstructure was investigated. Although, exact results were not computed, upper and lower bounds were derived which permitted approximate calculation of the boundary of a region of the (K_e, K_m) plane in which maximum capacity of one bit per grain is achievable. Third, the ability to achieve maximum storage capacity was shown to depend on using information about the medium microstructure in the recording and playback processes when either exchange interactions or magnetostatic interactions are large enough so that they cannot be ignored.

Chapter 7

Connection to Neural Networks

The simplified recording medium model which has been the subject of analysis in the last two chapters shares many properties in common with models of neural networks. Both neural networks and the medium model comprise a number of units, with the state of each unit described by a variable taking values of $+1$ or -1, and in which the total state of the system evolves according to interactions among the units which may be stated as simple update rules. Both models also exhibit memory – some ability to deduce information about an initial state of the system based on a later state after evolution of the system. In this chapter, the correspondence between neural network models and the simplified recording medium model is explored.

7.1 Hopfield Neural Network Model

In a landmark paper [40], Hopfield published a model of a "neural network," a large, richly interconnected set of very simple computing devices. The term "neural network" indicates only some rudimentary qualitative similarity between the operation of the simple computing devices and the functioning of a biological nerve cell. Such an association is not important here. The model is an interesting mathematical object in its own right. Since our interest in the model is mathematical rather than biological, we follow the example of Hertz, Krogh, and Palmer [36] and prefer neutral terms ("unit", "connection", "state") over those borrowed from neurobiology ("neuron", "synapse", "firing").

7.1.1 Definition

The neural network model which has come to be known as the Hopfield model is defined as follows. Let there be N units, identified by indices $1 \leq k \leq N$. Denote the state of unit K with a state variable $s_k \in \{\pm 1\}$. Then the state of the whole network may be represented by an $N \times 1$ vector of state variables, $\mathbf{s}$. Let unit k compute the weighted sum of the state variables of the other units, weighted by real-valued weights w_{kl},

$$h_k \triangleq \sum_{\substack{l=1 \\ l \neq k}}^{N} w_{kl} s_l. \tag{7.1}$$

It is convenient to refer to the quantity h_k as the field at unit k. Let the state s_k of unit k be updated according to the rule,

$$s_k^{\text{new}} = \text{sgn}\,(h_k)\,. \tag{7.2}$$

Two types of updating are considered in investigations of the Hopfield model: synchronous updating, in which the update rule is applied by all units simultaneously, and asynchronous updating, in which the update rule is applied at exactly one unit at a time in such a way that every unit is updated infinitely often. As an aside, it may be interesting to note that this is not the form of the model defined in Hopfield's original paper [40], which used the values $\{0, 1\}$ rather than $\{\pm 1\}$ to represent unit states. The two models are isomorphic through a simple transformation.

The set of system states which are fixed points of the update rule may be defined,

$$\Omega(\mathbf{W}) \triangleq \left\{ \mathbf{s} \in \{\pm 1\}^N : \forall_{1 \leq k \leq N} : s_k^{\text{new}} = s_k \right\}, \tag{7.3}$$

or, equivalently,

$$\Omega(\mathbf{W}) \triangleq \left\{ \mathbf{s} \in \{\pm 1\}^N : \forall_{1 \leq k \leq N} : s_k \cdot h_k > 0 \right\}. \tag{7.4}$$

The notation $\Omega(\mathbf{W})$ calls attention to the fact that the set of fixed points of a neural network is completely determined by the values of the weights which describe the interconnections among the units. Whether synchronous or asynchronous updating is employed, once a Hopfield network is in one of the states belonging to Ω, further applications of the update rule cannot cause any further changes in the network state.

The states in Ω are terminal states of the evolution of network state in the Hopfield model.

Hopfield's important contribution was the demonstration that given certain properties of the weights, repeated asynchronous updates of the Hopfield network must lead the network into one of the states in Ω. We state Hopfield's result as

Proposition 7.1 If the weights of a Hopfield network are symmetric,

$$\forall_{1\leq k,l\leq N} : w_{kl} = w_{lk}, \tag{7.5}$$

then repeated asynchronous updates of the network must lead the network state to converge to a state in $\Omega(\mathbf{W})$.

The key to proving this proposition is the definition of an "energy" function with the set of network states as its domain,

$$E(\mathbf{s}) = \sum_{k=1}^{N} \sum_{\substack{l=1 \\ l\neq k}}^{N} w_{kl} s_k s_l. \tag{7.6}$$

When the weights are symmetric, it is not difficult to show that if a single asynchronous update of the network in state $\mathbf{s}$ leaves the network in state $\mathbf{s}^{\text{new}}$, then exactly one of the following propositions must be true,

$$\mathbf{s}^{\text{new}} = \mathbf{s} \tag{7.7}$$

$$E(\mathbf{s}^{\text{new}}) < E(\mathbf{s}). \tag{7.8}$$

Therefore, the sequence of states in the evolution of the model, must yield a corresponding sequence of energies which is monotonically decreasing. Since there are only a finite number of network states, eventually the network must enter a state which does not change with further applications of the update rule. By definition, such a state is an element of Ω.

Corollary 7.1 For any asynchronous Hopfield network with symmetric weight matrix $\mathbf{W}$, $\Omega(\mathbf{W})$ is not empty.

Proposition 7.1 for associative memory networks corresponds to Proposition 5.1. Likewise, the following proposition corresponds to Proposition 5.2.

Proposition 7.2 For any asynchronous Hopfield network with symmetric weight matrix $\mathbf{W}$, and any state $\mathbf{s} \in \{\pm 1\}^N$,

$$\mathbf{s} \in \Omega(\mathbf{W}) \Leftrightarrow -\mathbf{s} \in \Omega(\mathbf{W}). \tag{7.9}$$

The proof of this proposition is completely analogous to the proof of Proposition 5.2.

If a notation for the number of memories of an associative memory network is defined

$$F(\mathbf{W}) \triangleq |\Omega(\mathbf{W})|, \tag{7.10}$$

then the following corollary follows easily

Corollary 7.2 $F(\mathbf{W})$ **is positive and even.**

7.1.2 Associative Memory

The property of asynchronous Hopfield networks with symmetric weights stated as Proposition 7.1 leads directly to an application: the use of such a network as an associative memory. Asynchronous Hopfield networks with symmetric weights must converge to a state in $\Omega(\mathbf{W})$. Once such a network is in a state in Ω, the network will remain in that state. The network might be said to "remember" that state. Let us call each network state $\mathbf{s} \in \Omega$ a *memory* of the network. The network may then be called on to remember any of its memories. If the network is given an initial state which is not a memory, the evolution of the network will lead it to a state which is a memory. Since the evolution consists of a sequence of asynchronous updates, it is more likely that the network will reach a memory which is nearest to the initial state in Hamming distance among the set of memories than a more distant memory. The Hamming distance between two network states is the number of units on which the two states disagree. In this way, when an associative memory is initialized to a non-memory state, it is likely to evolve to a memory state which is a small Hamming distance away from the initial state. The network is said to recall or remember one of its memories which it associates with the initial state by virtue of their nearness in Hamming distance. The operation of the network may be interpreted as the correction of errors in an initial state by calling forward an error-free memory associated with it. This description is the origin of the name associative memory.

Moving beyond this rough and highly personified description requires specification of a particular algorithm for the asynchronous selection of units for updating.

A simple and convenient algorithm which meets all necessary requirements is the random selection of units from a uniform distribution, with each selection independent from all the others. Given this asynchronous selection algorithm, and a particular symmetric weight matrix $\mathbf{W}$, in principle everything about the network can be determined. Its memories can be enumerated from 1 to F. Given any initial state, the probability of each memory being recalled by the network in response to that state can be determined. If we imagine using such a network as a storage device, we might compute the number of bits of information the network is capable of storing,

$$B(\mathbf{W}) \triangleq \log_2 F(\mathbf{W}), \tag{7.11}$$

or the capacity of the network for information storage in bits per unit

$$C(\mathbf{W}) \triangleq \frac{1}{N} \log_2 |\Omega(\mathbf{W})|\,. \tag{7.12}$$

From this discussion we see that the information storage capacity for any particular network is a deterministic function of the symmetric weight matrix $\mathbf{W}$ which identifies the network. This result is analogous to the statement of (5.15) that the information storage capacity of a patch of our simplified medium model is a deterministic function of the values of K_e, K_m, and the microstructure of the patch $\mathbf{\Theta}$.

As was also the case for the simplified medium model, the ability to write down an expression for the information storage capacity of any one particular associative memory network is of limited interest. Of greater interest is what information storage capacity a whole class of associative memory networks can deliver on average. Since the set of associative memory networks of N units is identified by the set of symmetric $N \times N$ weight matrices, any class of associative memory networks may be identified by a corresponding class of symmetric weight matrices. Furthermore, the taking of averages over the class presumes an appropriate probability distribution over the class which describes the relative frequency with which each network is drawn from the class by whatever natural phenomenon the average is intended to represent. Assuming an appropriate probability distribution for the class of $N \times N$ symmetric weight matrices is chosen, then the information storage capacity $C(\mathbf{W})$ is a random variable, and we may be interested in its expected value,

$$E_{\mathbf{W}}\{C(\mathbf{W})\} = \frac{1}{N} E_{\mathbf{W}}\{\log_2 |\Omega(\mathbf{W})|\}. \tag{7.13}$$

As in Chapter 6, computation of the expected value on the right side is difficult. Instead, an upper bound,

$$E_{\mathbf{W}}\{C(\mathbf{W})\} \leq \frac{1}{N} \log_2 E_{\mathbf{W}}\{F(\mathbf{W})\}, \tag{7.14}$$

and a lower bound

$$E_{\mathbf{W}}\{C(\mathbf{W})\} \geq \max\left(\frac{1}{N}\left[\frac{N-1}{2^N-2}E_{\mathbf{W}}\{F(\mathbf{W})\} + \frac{2^{N-1}-N}{2^{N-1}-1}\right], \frac{1}{N}\right), \tag{7.15}$$

may be considered, both of which are functions of the expected number of fixed points of the associative memory network. We shall return to these expressions later in the chapter after choosing a probability distribution for the weight matrices.

There is a large body of published literature on the use of Hopfield neural networks as associative memories. Much of this literature is devoted to analyzing the "capacity" of the associative memory. Unfortunately, the most common definition of "capacity" in the published literature is not consistent with our definition. Briefly, the perspective taken by most papers on associative memory capacity of Hopfield neural networks is that a particular set of m states, $\{\mathbf{s}_1, \ldots, \mathbf{s}_m\}$ is presented for an associative memory to remember. A weight matrix for the associative memory is generated from the set of desired memories by a learning rule. The most common learning rule is the sum of outer products rule, or Hebb rule,

$$\mathbf{W} \triangleq \sum_{k=1}^{m} \mathbf{s}_k \mathbf{s}_k^T - m\mathbf{I}, \tag{7.16}$$

where $\mathbf{I}$ is the $N \times N$ identity matrix. The sum of outer products rule is so common that it is often taken to be part of the definition of the Hopfield neural network model. When $m = 1$, the sum of outer products rule successfully generates a matrix of weights whose corresponding Hopfield network has as a memory the state $\mathbf{s}_1$. As more desired memories are added, heuristic arguments can be made that the sum of outer products rule remains a sensible strategy. Within this framework, questions about the "capacity" of a network to store desired memories are defined. Roughly stated, the question posed is how large the number of desired memories m can be relative to the number of units N in the network, so that all (or "most") of the desired memories are (or are within a "small" Hamming distance of) actual memories of the network. A large variety of slightly different statements of the problem are considered in a large number of papers. Some papers also consider issues of rates and Hamming radii of convergence. Since this "capacity" problem is not consistent with our notion of capacity, we do not review these papers in detail, but cite several as a starting point for the interested reader [17, 48, 50, 67, 86, 112]. Probably the most accessible for someone new to neural network analysis is [67]. A few of these papers note that in addition to the desired memories, there is also a number of "spurious memories" which is exponential in the number of units in the network. Since our notion of capacity includes all memories of a network, whether desired or not, it is the exponential rate of the number of memories as a function of the number of units in the network which we consider as our information storage capacity. More relevant to our notion of capacity is the smaller number of papers which directly consider the number of fixed points of a neural network (or the number of metastable states of a spin glass) [5, 113]. We will consider the contents of these papers further later in the chapter.

7.2 Hopfield Model for Recording Media

The notation and references to Chapters 5 and 6 in the preceding section already suggest the connection of the Hopfield associative memory neural network model to our simplified recording medium model. Both models are assemblies of N units. Both models identify state as a vector of sign values $\mathbf{s} \in \{\pm 1\}^N$. Both achieve the evolution of state by repeated application of an update rule to a randomly selected unit. In both models, the update rule consists of the computation of a linear function of the global state, followed by a non-linear threshold function. Comparison of the medium model update rule (2.77) to the Hopfield model update rule (7.2) (or a look at Fig. 6.3) leads to the conclusion that they are nearly the same if the Hopfield model value h_k is identified with the medium model value $h_{\|,k}$. With this identification, the two update rules differ only when the magnetic field in the medium model, $\mathbf{h}_k$ lies within the Stoner-Wohlfarth astroid and has negative projection on the magnetization $\mathbf{m}_k$. In all other circumstances, the medium model simplifies to the Hopfield model. The cases in which the models disagree can be made arbitrarily rare by selecting values of either K_e or K_m sufficiently large. In the limit as either K_e or K_e grows large, we conclude that the simplified medium model simplifies further to become the Hopfield model. Therefore, any results from the analysis of the Hopfield model apply to the class of media with large interactions, exactly those media which the analysis of Chapter 6 could say little about.

Having identified the quantity h_k of the Hopfield model with the quantity $h_{\|,k}$ of the simplified medium model, we may then identify the weights w_{kl} of the Hopfield model with the appropriate expression in terms of K_e, K_m, and Θ. The results are

$$w_{kk} = 0, 1 \leq k \leq N, \tag{7.17}$$

and

$$w_{kl} = \begin{bmatrix} \cos\theta_k & \sin\theta_k \end{bmatrix} \mathbf{A}_{kl}(K_e, K_m) \begin{bmatrix} \cos\theta_l \\ \sin\theta_l \end{bmatrix}, k \neq l, \tag{7.18}$$

where

$$\mathbf{A}_{kl}(K_e, K_m) \triangleq \begin{bmatrix} K_e I_{N(k)}(l) + K_m \frac{2p_{kl}^2 - q_{kl}^2}{(p_{kl}^2 + q_{kl}^2)^{5/2}} & K_m \frac{3p_{kl}q_{kl}}{(p_{kl}^2 + q_{kl}^2)^{5/2}} \\ K_m \frac{3p_{kl}q_{kl}}{(p_{kl}^2 + q_{kl}^2)^{5/2}} & K_e I_{N(k)}(l) + K_m \frac{2q_{kl}^2 - p_{kl}^2}{(p_{kl}^2 + q_{kl}^2)^{5/2}} \end{bmatrix}. \tag{7.19}$$

Thus,

$$\begin{aligned} w_{kl} &= (K_e I_{N(k)}(l) + \frac{K_m}{2(p_{kl}^2 + q_{kl}^2)^{3/2}}) \cos(\theta_k - \theta_l) \\ &+ K_m \frac{3(p_{kl}^2 - q_{kl}^2)}{2(p_{kl}^2 + q_{kl}^2)^{5/2}} \cos(\theta_k + \theta_l) \\ &+ K_m \frac{3p_{kl}q_{kl}}{(p_{kl}^2 + q_{kl}^2)^{5/2}} \sin(\theta_k + \theta_l) \end{aligned} \tag{7.20}$$

For any values of K_e, K_m, and Θ, it is true that $w_{kl} = w_{lk}$ so this transformation between the two models yields a symmetric weight matrix as desired.

In the simplified medium model, a class of recording media with common material properties is represented by a fixed pair of values K_e and K_m, and each instance of the class is associated with a particular vector Θ which defines a microstructure. The transformation (7.20) yields a corresponding class of associative memory networks. The probability distribution of the microstructure variables Θ may also be transformed through (7.20) to yield a corresponding probability distribution on zero-diagonal symmetric weight matrices.

7.3 Capacity of Hopfield Associative Memory Network with Independent Gaussian Weights

Having identified the conditions under which our model is well-approximated by the Hopfield model, and the transformation which identifies the class of weight matrices $\mathbf{W}$ and the corresponding probability distribution over the class which identify a class of recording media, we now review previous results in computing the expected number of fixed points of a Hopfield associative memory network, given a probability distribution on the class of weight matrices.

Consider first the probability distribution on zero-diagonal, symmetric $N \times N$ matrices in which each element in the upper triangle of the matrix is an independent Gaussian random variable with mean zero and variance σ^2. For this distribution on the weight matrices, the asymptotics of the expected number of fixed points as N grows large have been computed by Tanaka and Edwards [113], and later by a slightly different method by Baldi and Venkatesh [5]. In this section we present a solution which combines their methods, with adjustments to conform to the notation of this thesis.

The number of fixed points may be expressed

$$F_N(\mathbf{W}) = \sum_{\mathbf{s} \in \{\pm 1\}^N} I_{\Omega(\mathbf{W})}(\mathbf{s}), \tag{7.21}$$

where the subscript N indicates that the number of fixed points depends on the number of units in the network. Taking the expected value,

$$\overline{F}_N \triangleq E\{F_N\} = \sum_{\mathbf{s} \in \{\pm 1\}^N} \Pr\{\mathbf{s} \in \Omega(\mathbf{W})\}. \tag{7.22}$$

In the special case when

$$P_N(\mathbf{s}) \triangleq \Pr\{\mathbf{s} \in \Omega(\mathbf{W})\} = \Pr\{\mathbf{s} = \mathrm{sgn}(\mathbf{W}\mathbf{s})\} = P_N(\mathbf{s}_0), \tag{7.23}$$

is not a function of $\mathbf{s}$, we may write

$$\overline{F}_N = 2^N P_N(\mathbf{s}_0), \tag{7.24}$$

where $\mathbf{s}_0$ is the system state represented by the vector of all $+1$'s. It is important to understand when this simplification can be made.

When two real variables have the same sign, their ratio is a positive scale factor. Thus the condition of $\mathbf{s}$ being a fixed point of the update rule may also be expressed,

$$\forall_{1\leq k\leq N} : \exists_{\lambda_k>0} : h_k(\mathbf{s}) = \lambda_k s_k \tag{7.25}$$

This form for the fixed point condition leads to an expression for the indicator function for fixed points of the system's update rule,

$$I_\Omega(\mathbf{s}) = \prod_{k=1}^{N} \int_0^\infty \delta(h_k(\mathbf{s}) - \lambda_k s_k) d\lambda_k. \tag{7.26}$$

Then,

$$\overline{F}_N = E\left\{ \sum_{\mathbf{s}\in\{\pm 1\}^N} \prod_{k=1}^{N} \int_0^\infty \delta(h_k(\mathbf{s}) - \lambda_k s_k) d\lambda_k \right\}. \tag{7.27}$$

Evaluation of $\overline{F}_N$ begins with the substitution of the Fourier integral form of the Dirac delta function,

$$\delta(t) = \frac{1}{2\pi} \int_{-\infty}^{\infty} e^{j\omega t} d\omega. \tag{7.28}$$

Rearrangement yields

$$\overline{F}_N = \left(\frac{1}{2\pi}\right)^N \sum_{\mathbf{s}\in\{\pm 1\}^N} \int_0^\infty \int_{-\infty}^{\infty} \exp[-j\sum_{k=1}^{N} \omega_k \lambda_k s_k] E\left\{ \exp[j\sum_{k=1}^{N} \omega_k h_k(\mathbf{s})] \right\} d\underline{\omega} d\underline{\lambda}. \tag{7.29}$$

Note that the notation has been simplified so that a single integral symbol stands for the N-fold integral over an entire vector of variables. The expectation may now be recognized as the characteristic function of the vector of field values $\mathbf{h}$,

$$\Phi_{\mathbf{h}(\mathbf{s})}(\underline{\omega}) = E\left\{ e^{j\underline{\omega}\cdot\mathbf{h}(\mathbf{s})} \right\}. \tag{7.30}$$

The vector of field values is computed from the network state and the weight matrix,

$$\mathbf{h}(\mathbf{s}) = \mathbf{W}\mathbf{s}, \tag{7.31}$$

so we may write,

$$\overline{F}_N = \left(\frac{1}{2\pi}\right)^N \sum_{\mathbf{s}\in\{\pm 1\}^N} \int_0^\infty \int_{-\infty}^\infty \exp[-j \sum_{k=1}^N \omega_k \lambda_k s_k] \Phi_{\mathbf{Ws}}(\underline{\omega}) d\underline{\omega} d\underline{\lambda}. \tag{7.32}$$

Consider one term of the summation over all 2^N system states. For that one term, the value of $\mathbf{s}$ is fixed. The sign convention for each unit of the system is arbitrary, so for this fixed $\mathbf{s}$ we may redefine the sign conventions so that the state becomes the vector of all $+1$'s, $\mathbf{s}_0$. Such an operation is known as a *gauge transformation* in the physics literature on spin glass systems. Here the gauge transformation corresponds to a change of variable, $f_k = s_k \omega_k$, resulting in

$$\overline{F}_N = \left(\frac{1}{2\pi}\right)^N \sum_{\mathbf{s}\in\{\pm 1\}^N} \int_0^\infty \int_{-\infty}^\infty \exp[-j\underline{\lambda} \cdot \mathbf{f}] \Phi_{\mathbf{Ws}}(s_1 f_1, \cdots, s_N f_N) d\mathbf{f} d\underline{\lambda}. \tag{7.33}$$

Now, let us assume that the characteristic function has the property

$$\forall_{\mathbf{s}\in\{\pm 1\}^N} : \Phi_{\mathbf{Ws}}(s_1 f_1, \cdots, s_N f_N) = \Phi_{\mathbf{Ws}_0}(f_1, \cdots, f_N). \tag{7.34}$$

Then substitution of this property yields

$$\overline{F}_N = \left(\frac{1}{2\pi}\right)^N \sum_{\mathbf{s}\in\{\pm 1\}^N} \int_0^\infty \int_{-\infty}^\infty \exp[-j\underline{\lambda} \cdot \mathbf{f}] \Phi_{\mathbf{Ws}_0}(f_1, \cdots, f_N) d\mathbf{f} d\underline{\lambda}. \tag{7.35}$$

When property (7.34) is true, the summation over system states is a summation of terms which do not vary with the variables of summation. Also, the innermost integral is recognized as the inverse Fourier Transform of a characteristic function. Hence,

$$\overline{F}_N = 2^N \int_0^\infty p_{\mathbf{h}(\mathbf{s}_0)}(\underline{\lambda}) d\underline{\lambda} = 2^N P_N(\mathbf{s}_0). \tag{7.36}$$

So, (7.34) is a sufficient condition for the validity of expressing the mean number of fixed points as the product of the total number of system states and the probability that state $\mathbf{s}_0$ is a fixed point (or, by the symmetry of the gauge transformation, the probability that any particular system state is a fixed point). Note that (7.34) is not a necessary condition for this result, merely a sufficient one.

Let us now introduce the particular probability distribution into the solution of the problem. Since the elements of the upper triangle of the weight matrix $\mathbf{W}$ are independent random variables, and the matrix is symmetric, the characteristic function of the vector $\mathbf{Ws}$ may be expressed as a product of characteristic functions of the elements of the weight matrix,

$$\Phi_{\mathbf{Ws}}(\underline{\omega}) = \prod_{l>k}^{N} \Phi_{w_{kl}}(s_l\omega_k + s_k\omega_l). \tag{7.37}$$

Next consider multiplication of the argument of each characteristic function $\Phi_{w_{kl}}$ by the $s_k s_l$. This corresponds to multiplication by either $+1$ or -1. Each weight w_{kl} is assumed to have an even, Gaussian distribution, so in either case the value of the characteristic function is not changed. Thus,

$$\Phi_{\mathbf{Ws}}(\underline{\omega}) = \prod_{l>k}^{N} \Phi_{W_{kl}}(s_k\omega_k + s_l\omega_l) = \Phi_{\mathbf{Ws_0}}(s_1\omega_1, \cdots, s_N\omega_N). \tag{7.38}$$

This demonstrates property (7.34) for the chosen probability distribution on the weight matrices, which in turn justifies the gauge transformation.

With the gauge transformation justified, we may restate the problem in terms of the probability of an arbitrary state being a fixed point. The state $\mathbf{s}_0$ is a convenient state to consider. It is a fixed point exactly when the vector of field values $\mathbf{h}$ has all positive elements. We seek the probability that a random N-vector $\mathbf{h}$ is in the *positive orthant* of $\mathbf{R}^N$. Since it is a linear combination of zero-mean Gaussian random variables, $\mathbf{h}$ is a zero-mean Gaussian random vector, and its covariance matrix is

$$\mathbf{K} = \begin{bmatrix} (N-1)\sigma^2 & \sigma^2 & \cdots & \sigma^2 \\ \sigma^2 & (N-1)\sigma^2 & \cdots & \sigma^2 \\ \cdot & \cdot & \cdot & \cdot \\ \sigma^2 & \sigma^2 & \cdots & (N-1)\sigma^2 \end{bmatrix}. \tag{7.39}$$

We assume $N > 2$ so that the covariance matrix is non-singular. Because we are interested only in the positive orthant probability, the value of σ^2 is of no consequence and can be taken to be 1. We must compute

$$P_N = \int_0^{\infty} (2\pi)^{-\frac{N}{2}} \exp[-\frac{1}{2}\underline{\lambda} \cdot \mathbf{K}^{-1}\underline{\lambda}]d\underline{\lambda}. \tag{7.40}$$

The solution is achieved by replacing this problem by another with an equivalent solution. This technique is known as the method of equivalent Gaussians.

The Gaussian random vector $\mathbf{h}$ has been shown to have zero mean, and covariance matrix K. These moments completely characterize the joint Gaussian probability distribution. Therefore any Gaussian random vector with the same mean and covariance matrix will have the same probability of having a value in the positive orthant as does $\mathbf{h}$. We now construct another zero-mean Gaussian random vector in such a way as to have covariance matrix $\mathbf{K}$. Let $(y_0, y_1, \ldots, y_N)$ be $N+1$ independent Gaussian random variables with zero mean and variance σ^2. From these random variables, define a random N-vector $\mathbf{v}$ with elements defined,

$$v_k = \sqrt{N-2}y_k + y_0, 1 \leq k \leq N. \tag{7.41}$$

The random vector $\mathbf{v}$ is then a zero-mean Gaussian random vector with covariance matrix $\mathbf{K}$, equivalent to the random vector $\mathbf{h}$. From the definition of $\mathbf{v}$, however, we have another way of stating the quantity we seek. The random variable v_k is positive exactly when

$$y_k > -\frac{1}{\sqrt{N-2}}y_0. \tag{7.42}$$

Conditioned on a particular value of y_0, the probability of this event is

$$\Pr\left(y_k > -\frac{1}{\sqrt{N-2}}y_0|y_0\right) = \operatorname{erf}_*\left(\frac{y_0}{\sqrt{N-2}}\right). \tag{7.43}$$

These events are conditionally independent, so

$$\Pr\left(\forall_{1\leq k\leq N} y_k > -\frac{1}{\sqrt{N-2}}y_0|y_0\right) = \operatorname{erf}_*^N\left(\frac{y_0}{\sqrt{N-2}}\right), \tag{7.44}$$

and taking the expected value over y_0 removes the conditioning. Thus, after normalization of the variable of integration,

$$\begin{aligned} P_N &= \int_{-\infty}^{\infty} \frac{\sqrt{N-2}}{\sqrt{2\pi}} \exp\left(-\frac{(N-2)\beta^2}{2}\right) \operatorname{erf}_*^N(\beta)d\beta & (7.45)\\ &= \int_{-\infty}^{\infty} \frac{\sqrt{N-2}}{\sqrt{2\pi}} \exp\left[-N\left(\frac{(N-2)\beta^2}{2N} - \ln \operatorname{erf}_*(\beta)\right)\right] d\beta & (7.46) \end{aligned}$$

The integrand is a positive quantity, and for large N, its value away from its maximum must be exponentially smaller than the maximum value. Thus for large N, the value of the integral is determined by the value of the maximum of the integrand. For such problems, solutions by the Laplace method (sometimes called a saddle point method) are appropriate [25]. In this problem, we find the value β^* which minimizes the quantity

$$f(\beta) = \frac{\beta^2}{2} - \ln \operatorname{erf}_*(\beta). \tag{7.47}$$

Numerical solution yields

$$\beta^* = 0.5061, \tag{7.48}$$

and

$$f(\beta^*) = 0.4939. \tag{7.49}$$

Conversion of the expressions so that 2 is the base of any exponent, and careful attention to the leading factor from Laplace method analysis leads to

$$P_N \approx 1.0505 \cdot 2^{-0.7126N} \tag{7.50}$$

for large N. Therefore, the expected number of fixed points over this class of associative memory networks is

$$\overline{F}_N \approx 1.0505 \cdot 2^{0.2874N}, \tag{7.51}$$

for large N. The capacity of any class of recording media which could sensibly be said to be represented by this class of associative memory networks would then have an upper bound of 0.2874 bits per grain.

The chosen probability distribution on the weight matrices is sadly not a sensible representation for any class of recording media. The most obvious objection is that all weights in this analysis are identically distributed. In terms of the physical model, this would mean that the interaction between any pair of grains would be statistically the same as the interaction between any other pair of grains. This is not suitable for our physical model of recording media, as we know that the exchange interactions are limited to neighbors, and the magnetostatic interaction falls off rapidly as the distance separating a pair of grains increases.

A modest refinement to this analysis might then be to retain independent zero-mean Gaussian weights, but permit the variance of weight w_{kl} to vary in some physically sensible way. A review of the preceding analysis indicates that all the steps through the gauge transformation remain valid. Therefore, our task remains one of computing the probability that a zero-mean Gaussian random vector with known covariance takes a value in the positive orthant. The particular covariance matrix $\mathbf{K}$ is a function of the weight variances, but should not in principle be difficult to derive.

This presumably modest extension of the analysis, then, reduces to the problem of finding the probability that a zero-mean Gaussian random N-vector takes a value in the positive orthant, given the value of its covariance matrix $\mathbf{K}$. Unfortunately, this appears to be an unsolved problem of long standing dating back at least to papers by Ludwig Schläfli in 1858 and 1860 [102].

For $N = 2$, the solution is straightforward. The covariance matrix is specified to within an inconsequential scale factor by the correlation coefficient r of the two elements of the Gaussian random vector. Any of several methods [93] yields the answer that

$$P_2 = \frac{1}{2} + \frac{1}{\pi} \tan^{-1} \frac{r}{\sqrt{1 - r^2}} \tag{7.52}$$

For $N = 3$, from knowledge of the covariance matrix $\mathbf{K}$ a linear transformation of the Gaussian 3-vector can be found which yields a Gaussian 3-vector with independent elements. The probability density function of the transformed vector is spherically symmetric, yielding a value dependent only on the magnitude of its vector argument. Applying the same transformation to the boundaries of the positive orthant yields a cone. The cone intersects the unit sphere in a spherical triangle. Then the ratio of the surface area of the spherical triangle to the surface area of the entire unit sphere is the probability we seek. Since formulae for the surface areas of a spherical triangle and a sphere are available [22, 66, 99], P_3 can be found for any valid covariance matrix $\mathbf{K}$.

For larger N, analogous techniques to that used when $N = 3$ may be tried. Such investigations consider the geometry of N dimensions [110]. The technique of transforming the random vector to one with independent elements, and applying the same transformation to the boundaries of the positive orthant generalizes to N dimensions. The resulting cone intersects the sphere in $\mathbf{R}^N$ in an $N - 1$ dimensional surface called a spherical simplex which is bounded by N edges of dimension $N - 2$. An analogous solution would then require that we be able to compute the measure of that spherical simplex and take the ratio of that quantity to the measure of the entire spherical surface in $\mathbf{R}^N$, to obtain the desired probability. For odd N the solution can be stated in terms of solutions of similar sub-problems in dimensions of $N - 1$ and below. However, such reduction formulae are not available for even N, so they cannot take us to practical solutions beyond $N = 3$. Because the simplex is embedded in a spherical surface, non-Euclidean geometry is relevant and related to the problem [13, 116], but to date research in this area has revealed only more equivalent statements of the problem, and some of its properties rather than a solution. A few other references relevant to this problem are [3, 24, 45].

7.4 Summary

The Hopfield model for associative memory neural networks was defined. It was found that under the conditions of a large value for either K_e or K_m, the Hopfield model is a good approximation of our simplified recording medium model. The transformation between the two models was derived so that classes of recording media may be identified by classes of Hopfield network weight matrices. An upper bound on the information storage capacity of Hopfield associative memories was found to be 0.2874 bits per unit for networks with a sufficiently large number of units, and with independent, identically distributed Gaussian weights. Attempts to extend this analysis to classes of weight matrices better suited to a physical interpretation were frustrated by the inability to solve a long-standing unsolved problem.

Chapter 8

Conclusions and Future Work

Many areas of research are relevant to the storage of information as magnetic patterns on magnetic recording media. The research work set forth in this thesis makes contributions to three major research areas: micromagnetic modeling of magnetic recording media, design and analysis of magnetic recording systems by computer simulation, and theoretical analysis of the information storage capacity of magnetic recording systems. In each of these areas, the contents of this thesis raise new questions which motivate future research efforts.

8.1 Micromagnetic Modeling

Micromagnetic modeling underlies all the research presented in this thesis. Micromagnetic modeling is the study of the properties of magnetic materials at a sub-micron level of detail based on the representation of these materials as a set of mathematical equations and the implementation of these equations as numerical algorithms. The promise of micromagnetic modeling is to harness the increasing availability of computing power to investigate properties of magnetic materials in a more precisely controlled manner and over a wider range of possible properties than is economical experimentally, and at a finer level of spatial detail than is possible with simpler models. Though micromagnetic modeling research has made useful contributions, its promise remains largely unfulfilled. The research presented in this thesis makes progress toward fulfillment of the promise of micromagnetic modeling both by identifying some important basic issues in micromagnetic modeling which remain unresolved, and by taking an important first step toward the quantitative identification of model computations with experimental measurements.

Although the fundamental equations of micromagnetics have been known for a long time [16] and are widely accepted, it has been necessary in computational micromagnetics to make additional simplifying assumptions and approximations to define sets of equations and their software implementations to represent magnetic materials. The wide variability in the exact nature of these assumptions and approximations leads to variation in the predictions of micromagnetic models. The dependence of the predictions of micromagnetic calculations on the precise assumptions of each model is not well understood. Gaining an understanding of this issue will require integration of disparate modeling efforts within a common framework, in which differing assumptions are explicitly stated. Toward this end, the micromagnetic model and its variations studied in this thesis have been presented with explicit attention to the set of assumptions and approximations on which they are based.

One important area in which the model studied in this thesis permits investigation of the effect of different modeling assumptions on the predictions of model computations is its support for representation of both regular and irregular grain structure. Since rectangular, hexagonal, and irregular grains are all particular instances of the general model representation of grain structure – the Voronoi diagram – all three types of microstructure may be considered in a common framework. Simulation results such as those in Table 4.4 indicate that the different grain structures yield significantly different predictions of bulk material properties of the material represented by the model. These differences have been observed in earlier research [74], but the model presented in this thesis for the first time makes the comparison within the common framework of Voronoi diagram grain structure. Future work is necessary to establish a common framework analogous to the Voronoi diagram grain structure for other particular modeling assumptions, so that the effect of differing assumptions may be quantified. The many particular features of micromagnetic models which must be reconciled in future work have been discussed at length in Section 3.5.

The intent of micromagnetic models is the representation of physical magnetic materials. Their ultimate success, then, will only be rigorously demonstrated when model predictions and physical measurements yield quantitative agreement. A key step in such model verification is the ability to associate with any physical magnetic material sample a particular instance of a model, identified by a particular set of values of the parameters of the model. The parameter identification procedure presented in Section 4.2 for instances of our model representing non-oriented media represents a first attempt at addressing this important problem. The ability to match the hysteresis properties measured for a physical recording medium with those predicted by an instance of a non-oriented medium model by directed selection of the values of material parameters of the model has been demonstrated in this thesis. Extension of such model parameter identification to models of oriented materials is a goal of future research efforts, as well as the development of additional tests and methods for matching other measured properties of physical medium samples to the corresponding calculations of instances of medium models.

Addressing both the problem of relating model assumptions to model calculations and the problem of identifying and verifying a model instance which represents physical magnetic material sample is the task of the newly-formed Micromagnetic Modeling Activity Group (μMAG). The leadership of μMAG is at the National Institute of Standards and Technology (NIST), where the author of this thesis will continue his research efforts, directed primarily at the first of these two important problems.

8.2 Recording System Simulation

The contents of this thesis also contribute to the understanding of magnetic recording systems by permitting the simulation of their operation, and by establishing a clear connection between the properties of a playback signal called medium noise, and the magnetic features of the recorded pattern which cause them. Special instances of the medium model permit simulation of signals with no medium noise, with only repeatable medium noise, and with both repeatable and non-repeatable medium noise. These demonstrations help establish what is meant by the term "medium noise," and show that it may be considered misleading to refer to these features of the playback signal as "noise" at all. They certainly are not "noise" in the communication theory sense of an additive random process. Attempts to treat medium noise as though it were an additive random process, such as representation of magnetic recording channels by variations on the Gaussian channel, must fail to represent the true physical nature of magnetic recording systems. The important conclusion to be drawn from the recording simulations presented in Section 4.3, then, is that they have features in agreement with experimental observations which are not present in simpler statistical models of magnetic recording channels. Therefore, the capacity limits derived from analysis of the micromagnetic model may more credibly be claimed to represent the limits of actual recording media than those derived from analysis of statistical channel models.

The ability to simulate magnetic recording systems also complements laboratory measurements on recording testers. Simulations permit a precision of control not possible in experimental measurement, and the "measurement" of internal quantities not accessible to experimental measurement. Simulations also permit the testing of hypothetical materials, not physically available. The greatest benefits of recording system simulation will not be achieved until some of the promise of micromagnetic modelling is fulfilled, and good identification of model instances with physical materials is achieved. However, the simulations made possible by the research reported in this thesis are one tool among many now at the disposal of the researchers in the Magnetics and Information Science Center.

Additional simulation studies are clearly desirable, for purposes both of testing the model and of using the model to gain additional understanding of the recording and playback processes. Several specific ideas for future simulation work are identified in Sections 4.3.6 and 5.3, and are not repeated here.

8.3 Storage Capacity of Recording Media

Simple thermal arguments establish the superparamagnetic limit on the areal density of information storage on magnetic recording media. These arguments assume that one bit of information can be stored in each bit cell, and that the size of bit cells is limited only to be larger than the minimum volume needed to sustain a magnetization against thermal fluctuations. These analyses ignore the internal magnetic interactions among the bit cells. Other arguments predicting limits on information storage density have been analyses of statistical representations of recording and playback operations as communication channels, parameterized by bulk properties of the recording medium, and other recording system properties. The most recent such analyses have considered variations of the Gaussian channel. Such channels, however, do not exhibit important properties of medium noise experimentally observed in recording systems. These properties are attributed to microstructural variations in the recording medium. Representation of such medium noise properties requires a model capable of representing microstructure, such as a micromagnetic model. The results of Chapters 5 and 6 represent the first analysis of the fundamental limits on the storage capacity of magnetic recording media based on a micromagnetic model. Consequently, this research is the first to demonstrate the effect of local microstructural properties on the information storage capacity of magnetic recording media.

Identifying a bit cell with one grain of our model, the thermal limit corresponds to the upper bound on capacity for our model of one bit per grain. Simulations and analysis of our micromagnetic model agree that when intergranular interactions are sufficiently small, one bit per grain of storage is possible. For larger interactions of either the magnetostatic or exchange variety, however, a limit on information storage density strictly less than one bit per grain is imposed by the reduced number of stable magnetization patterns available for storage. The boundary in the model material parameter space between these two categories of media has been calculated in Section 6.2 for the class of non-oriented media. Furthermore, the analysis of the micromagnetic model has shown that as the size of grains in the model decreases, the magnitudes of both magnetostatic and exchange interactions increase, indicating further evidence that the limits on information storage density are in fact below the superparamagnetic limit.

A greatly simplified illustration in Section 6.3 established that when the internal magnetic interactions are large enough that one bit per grain capacity cannot be achieved, then in order to record and read back information at densities approaching the fundamental limit, information about the local microstructure must be incorporated into the record and playback processes. This theoretical result constrains the class of recording systems which can hope to continue the increase in information storage density as the fundamental limits are approached.

In Chapter 7, the connection between certain instances of the micromagnetic medium model and the Hopfield model of neural networks has also been established. The reviewed literature on the Hopfield model does not contain results useful for predicting the capacity of our recording medium model, but the established connection warrants further review of the neural network and spin glass literature. Since all three of these fields of study deal with objects capable of memory, an understanding of their common features may be illuminating.

8.4 Impact on Recording Systems

In Chapter 1 the superparamagnetic limit was estimated to be about 10 Gbit/mm^2 (6.45 Tbit/in^2), or about three orders of magnitude greater than the greatest density of information storage so far demonstrated in research prototypes. Given the historical trend of a doubling of information storage density of magnetic recording systems every three years, the fundamental limits of information storage density are increasingly a matter of practical concern. The influence of microstructural features of recording media on recording and playback in contemporary recording systems manifests itself as medium noise. Two major strategies exist for dealing with medium noise. The first is development of new recording materials which exhibit less medium noise. The second is the development of advanced recording and playback techniques which can deal reliably store and retrieve information even with the presence of medium noise. The theoretical results of this thesis have implications for both of these strategies. The problem of developing media which exhibit little medium noise may be restated as the problem of developing media with sufficiently small intergranular exchange and magnetostatic interactions. The boundary calculated in Section 6.2 and its relationship to the model's quintuple of material parameters is a relevant guide to this effort. The problem of developing advanced recording and playback techniques to deal with medium noise is now guided by the theoretical result that the fundamental limits of information storage can be approached only by recording and playback processes which make use of information about local medium microstructure. Practical implementation of this idea may take the form of novel write-read-write or read-write-read recording schemes [89, 88].

8.5 Summary of Research Conclusions

The central tenet of this thesis is that the density of information storage achievable by any magnetic recording system is limited by the density of information storage which can be physically supported on the magnetic recording medium employed by that system. Previous investigations of limits on information storage density of magnetic recording systems are of two kinds. First, thermal stability arguments have been employed to predict limits on how small bit cells may be before they no longer reliably store information at ambient temperature for durations of practical utility. Second, variations of the Gaussian channel intended to represent the recording and playback operations of a magnetic recording system have been defined and analyzed. Both of these kinds of information storage capacity investigations ignore important observed features of magnetic recording system. This thesis improves on such earlier investigations by determining for the first time the limits on information storage density predicted by a micromagnetic model of magnetic recording media. Micromagnetic models are better representations of recording media than simple thermal arguments because they take into account the internal magnetic interactions present in the medium. Micromagnetic models are better representations of recording media than variations on the Gaussian channel because they more accurately predict the non-stationary and microstructure-dependent nature of the medium noise observed in magnetic recording systems. The study of a micromagnetic model of magnetic recording media has yielded a limit on the density of information storage below the thermal limit, the dependence of this limit on the physical properties of a recording medium, and a theoretical prediction of the type of recording and playback processes which are necessary to achieve information storage densities approaching the fundamental limit.

Appendix A

Derivation of Magnetostatic Interaction Coefficients

In this appendix we derive the coefficients of the linear function by which the effective magnetostatic field component arising from a source magnetic dipole. This appendix is an edited version of Appendix A of [94].

From Cheng [20] , if we place a magnetic dipole with moment

$$\mathbf{m} = m\hat{\mathbf{z}} \tag{A.1}$$

at the origin of a standard spherical coordinate system, the magnetic field intensity is expressed as a function of space in the spherical coordinates (R, θ, φ),

$$\mathbf{H}(R, \theta) = \frac{m}{4\pi R^3}((2\cos\theta)\hat{\mathbf{R}} + (\sin\theta)\hat{\theta}), \tag{A.2}$$

where $\hat{\mathbf{R}}$ and $\hat{\theta}$ are the unit vectors in spherical coordinates at the point in question and m is the magnitude of the magnetic dipole moment vector.

As a first step, we convert this equation to an equivalent one in an x'-y'-z' Cartesian coordinate system defined so that the z'-axis is aligned with the dipole, and the x'-z' plane is the plane of the medium in our model. The primes are used to distinguish this coordinate system from the global x-y-z coordinate system used in the definition of the model. Applying the appropriate conversions yields:

$$\mathbf{H}(R, \theta) = \frac{m}{4\pi R^3}[(\pm 3\cos\theta\sin\theta)\hat{\mathbf{x}}' + (2\cos^2\theta - \sin^2\theta)\hat{\mathbf{z}}'], \tag{A.3}$$

where the $\pm$ choice is made based on the location of the point in question with respect to the coordinate system. Let $\mathbf{R}$ be the position vector of the point in question. If $\mathbf{R} \cdot \hat{\mathbf{x}}' > 0$, then choose $+$; otherwise, choose $-$.

At this point, we observe that:

$$\mathbf{m} \cdot \mathbf{R} = mR\cos\theta; \tag{A.4}$$

$$|\mathbf{m} \times \mathbf{R}| = mR\sin\theta. \tag{A.5}$$

Using these equations, we may rewrite the magnetic field intensity expression in a form which does not explicitly include θ:

$$\mathbf{H}(\mathbf{R}) = \frac{1}{4\pi m R^5}[(\pm 3|\mathbf{m} \times \mathbf{R}|(\mathbf{m} \cdot \mathbf{R}))\hat{\mathbf{x}}' + (2(\mathbf{m} \cdot \mathbf{R})^2 - |\mathbf{m} \times \mathbf{R}|^2)\hat{\mathbf{z}}']. \tag{A.6}$$

Next, we rotate the coordinate system to express all vectors in terms of their coordinates in the model's x-z coordinate system, applying the relationships,

$$\hat{\mathbf{x}}' = \frac{m_z}{m}\hat{\mathbf{x}} - \frac{m_x}{m}\hat{\mathbf{z}}; \tag{A.7}$$

$$\hat{\mathbf{z}}' = \frac{m_x}{m}\hat{\mathbf{x}} + \frac{m_z}{m}\hat{\mathbf{z}}, \tag{A.8}$$

where $\mathbf{m} = \begin{bmatrix} m_x & m_z \end{bmatrix}^T$ in x-z coordinates. The expression for magnetic field intensity in x-z coordinates is then

$$\begin{aligned} \mathbf{H}(\mathbf{R}) \quad &= \quad \frac{1}{4\pi m^2 R^5} \cdot \qquad\qquad (\text{A.9}) \\ &\{ \quad [\pm 3|\mathbf{m} \times \mathbf{R}|(\mathbf{m} \cdot \mathbf{R})]m_z\hat{\mathbf{x}} - [\pm 3|\mathbf{m} \times \mathbf{R}|(\mathbf{m} \cdot \mathbf{R})]m_x\hat{\mathbf{z}} \\ &+ \quad [2(\mathbf{m} \cdot \mathbf{R})^2 - |\mathbf{m} \times \mathbf{R}|^2]m_x\hat{\mathbf{x}} + [2(\mathbf{m} \cdot \mathbf{R})^2 - |\mathbf{m} \times \mathbf{R}|^2]m_z\hat{\mathbf{z}}\}. \end{aligned}$$

Let the position vector $\mathbf{R}$ represent the point at coordinates (x, z), so that

$$\mathbf{m} \cdot \mathbf{R} = m_x x + m_z z; \tag{A.10}$$

$$\pm|\mathbf{m} \times \mathbf{R}| = m_z x - m_x z. \tag{A.11}$$

Substituting these expressions yields

$$\mathbf{H}(x, z) \quad = \quad \frac{1}{4\pi m^2 R^5} \cdot \tag{A.12}$$

$$
\begin{aligned}
\{ \quad & [3(m_z x - m_x z)(m_x x + m_z z)m_z + (2(m_x x + m_z z)^2 - (m_z x - m_x z)^2)m_x]\hat{\mathbf{x}} \\
+ \quad & [-3(m_z x - m_x z)(m_x x + m_z z)m_x + (2(m_x x + m_z z)^2 - (m_z x - m_x z)^2)m_z]\hat{\mathbf{z}}\}
\end{aligned}
$$

Simplifying this expression, and making use of $m^2 = m_x^2 + m_z^2$ and $R = (x^2 + z^2)^{-1/2}$ yields

$$
\begin{aligned}
\mathbf{H}(x,z) \quad = \quad & \frac{1}{4\pi(x^2+z^2)^{5/2}} \cdot \\
\{ \quad & [(2x^2 - z^2)m_x + 3xzm_z]\hat{\mathbf{x}} \\
+ \quad & [3xzm_x + (2z^2 - R_x^2)m_z]\hat{\mathbf{z}}\},
\end{aligned}
\tag{A.13}
$$

which may be written in matrix form,

$$
\mathbf{H}(x,z) = \frac{1}{4\pi(x^2+z^2)^{5/2}} \begin{bmatrix} 2x^2 - z^2 & 3xz \\ 3xz & 2z^2 - x^2 \end{bmatrix} \mathbf{m}. \tag{A.14}
$$

Appendix B

An Alternative Representation of Exchange

The exchange interaction in our model is represented by an effective magnetic field component $\mathbf{H}_e$. At grain k, the exchange field is the sum of scalar multiples of the magnetization of those grains which share a boundary with grain k (2.38). The scalar coefficients $K_{x,kl}$ were derived from a study of domain walls, following [84]. The properties of this formulation make it computationally attractive. It is a linear function of the magnetization state, and the exchange field at grain k is not a function of the magnetization of grain k. In this appendix, we present an alternative derivation of the exchange interaction as an effective magnetic field component, also based on the study of domain walls. The resulting formulation has greater physical plausibility, but is not adopted at this time due to its unattractive computational properties.

Consider two grains k and l which share a boundary, and let us examine the domain wall structure between them. For purposes of this analysis, we abandon the simplification that grains are to be uniformly magnetized, so that we may consider the spatial variation of magnetization through the domain wall. Ignore any magnetostatic interaction and any applied field. Then at a distance from the boundary, only the anisotropy energy of a grain will act to direct the magnetization, aligning it with the local easy axis. The magnetization of grains k and l, except near the grain boundaries are then

$$\mathbf{M}_k = M_s \cos\theta_k \hat{\mathbf{x}} + M_s \sin\theta_k \hat{\mathbf{z}} \tag{B.1}$$

$$\mathbf{M}_l = M_s \cos\theta_l \hat{\mathbf{x}} + M_s \sin\theta_l \hat{\mathbf{z}} \tag{B.2}$$

The spatial variation of magnetization as the domain wall is crossed from grain k to grain l is a rotation in the plane through the angle

$$\Delta\alpha \triangleq \theta_l - \theta_k, \tag{B.3}$$

where the difference is taken so that $\Delta\alpha$ is less than π.

There is no physical reason for the domain wall to be asymmetric. Therefore, at the grain boundary, exactly half of the magnetization rotation will be complete. It is convenient to use the grain boundary and the magnetization at the grain boundary as a reference point. Let the orientation reference for magnetization angle be defined so that $\alpha = 0$ at the grain boundary. Then the spatial variation of magnetization across the domain wall is a rotation of α from $-\Delta\alpha/2$ to $\Delta\alpha/2$. This framework for domain wall analysis is in agreement with the treatment in textbooks [21]. Within this framework the competition between exchange effects and anisotropy effects may be investigated. Exchange effects tend to shape the domain wall into a gradual rotation of magnetization from one grain to its neighbor. Anisotropy effect tend to shape the domain wall into an abrupt rotation concentrated near the grain boundary. The sum of these two energies is minimized in a compromise configuration. An important property of the compromise configuration is that the exchange energy density and the anisotropy energy density are equal at all points throughout the domain wall. Thus, the total domain wall energy may be expressed in terms of the anisotropy energy density, after solution of the total energy minimization problem by standard calculus of variations techniques. For details of this procedure, see [21]. If the anisotropy energy density as a function of magnetization orientation α is denoted $g(\alpha)$, then the total domain wall energy may be expressed

$$\gamma_w = 2\sqrt{A_e}\int_{-\Delta\alpha/2}^{\Delta\alpha/2}\sqrt{g(\alpha)}d\alpha. \tag{B.4}$$

From our formulation for anisotropy energy (2.26), we may write

$$g(\alpha) = \begin{cases} K_A \sin^2(\alpha + \frac{\Delta\alpha}{2}), & \alpha < 0 \\ K_A \sin^2(\alpha - \frac{\Delta\alpha}{2}), & \alpha > 0 \end{cases}. \tag{B.5}$$

Solving for γ_w yields

$$\gamma_w = 4\sqrt{A_e K_A}(1 - \cos\frac{\Delta\alpha}{2}). \tag{B.6}$$

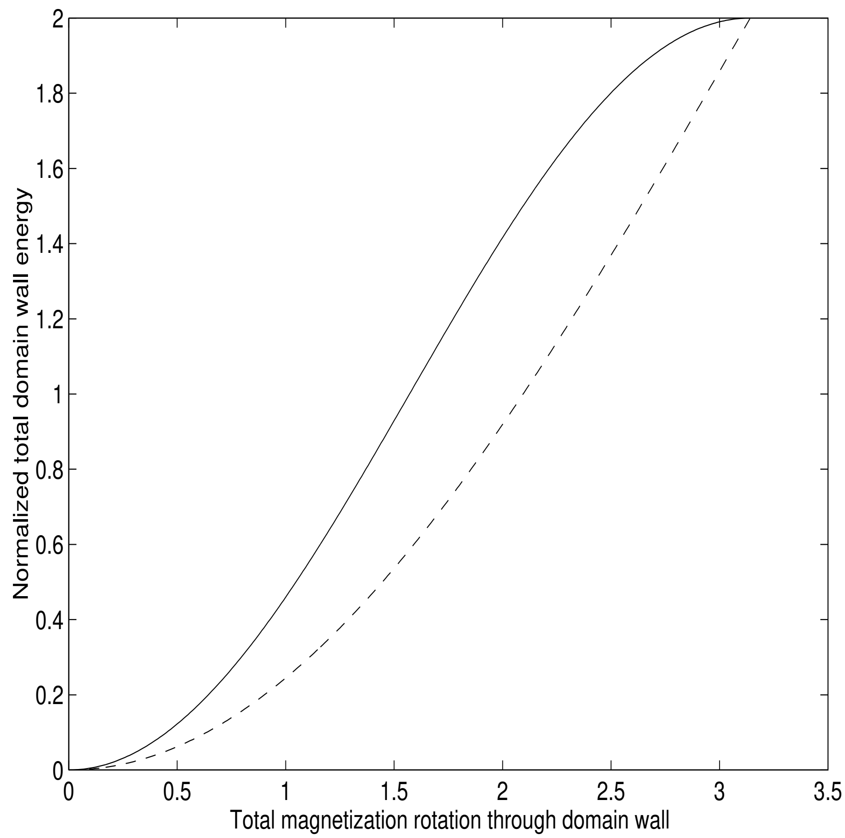

Figure B.1: Domain wall energy comparison of two exchange formulations

Compare this expression with (2.30), which may be rewritten

$$\gamma_w = 2\sqrt{A_e K_A}(1 - \cos\Delta\alpha). \tag{B.7}$$

Fig. B.1 is a plot of normalized domain wall energy, $\gamma_w/2\sqrt{A_e K_A}$, as a function of the total magnetization rotation through the domain wall, $\Delta\alpha$. The formulation used in the model is represented by the solid line. The alternative formulation derived in this appendix is represented by the dashed line. The two models predict the same exchange energy only for very small angles and for a wall between grains of antiparallel magnetization. An even more important difference between the two formulations is the torque due to exchange interaction they predict. The torque is the derivative of magnetic energy with respect to rotation of one of the grain magnetizations. From Fig B.1, it is clear that both formulations predict torques which tend to align the magnetization of neighboring grains parallel to one another. However, the magnitude of the torque predicted by the two formulations is quite different. The formulation of the model predicts maximum torque for grains with magnetization vectors orthogonal to one another. The alternative formulation predicts maximum torque for grains with antiparallel magnetization. The model formulation predicts zero torque for grains aligned perfectly antiparallel. These properties imply that the alternative formulation derived here has more attractive physical properties than the formulation used in the model.

The formulation derived here may also be represented by means of an effective magnetic field component. Setting the exchange energy of a domain wall equal to the energy arising from a magnetic field component and solving for the magnetic field component yields either

$$\mathbf{H}_{e,kl} = \frac{\ell_{kl}}{\mathcal{A}_k} \cdot \frac{2\sqrt{K_A}}{\mu_0 M_s} \cdot f\sqrt{A_e} \cdot \mathbf{u}_{kl} \tag{B.8}$$

where $\mathbf{u}_{kl}$ is a unit vector with orientation halfway between that of $\mathbf{M}_k$ and $\mathbf{M}_l$, or

$$\mathbf{H}_{e,kl} = \frac{\ell_{kl}}{\mathcal{A}_k} \cdot \frac{2\sqrt{K_A}}{\mu_0 M_s^2} \cdot f\sqrt{A_e} \cdot \frac{1 - \cos\frac{\Delta\theta}{2}}{1 - \cos\Delta\theta}\mathbf{M}_l. \tag{B.9}$$

These expressions make evident the computational shortcomings of this formulation. The magnetic field component $\mathbf{H}_{e,kl}$ is not a linear function of $\mathbf{M}_l$, and it is a function of $\mathbf{M}_k$. In (B.8), the non-linearity is grouped into the vector $\mathbf{u}_{kl}$. In (B.9), the non-linearity is grouped into the scalar coefficient. The latter equation has the advantage of avoiding a cusp in the torque for neighboring grains with anti-parallel magnetization. The properties of non-linearity and functional dependence on $\mathbf{M}_k$ invalidate some of the assumptions made in deriving efficient algorithms for energy minimization in the model. For these reasons, we do not adopt this formulation as part of the model, but present it here as an alternative to be considered in future modeling work.

Appendix C

Circularly Symmetric Stoner-Wohlfarth Astroid

In Section 6.2.6, the function $\Upsilon(\underline{\lambda})$ was defined,

$$\Upsilon(\underline{\lambda}) \triangleq \int p_{\mathbf{m}}(\underline{\xi}) I_{Q(\underline{\xi})}(\underline{\lambda})\, d\underline{\xi}, \tag{C.1}$$

where $Q(\mathbf{m})$ is a set derived from a vector $\mathbf{m} \in \mathbf{R}^2$ as in Fig. 6.3. In this appendix we derive a closed form expression for this function.

The integral (C.1) may be interpreted as the expected value of an indicator function, which is known to be the probability of the indicator function's set. Thus,

$$\Upsilon(\underline{\lambda}) = \Pr\{\underline{\lambda} \in Q(\mathbf{m})\}. \tag{C.2}$$

The only feature of this probability which is somewhat unusual is that it is the set Q which is random rather than the vector $\underline{\lambda}$.

The random vector $\mathbf{m}$ has unit magnitude and its orientation is uniformly distributed over a full circle. Each possible value of the random vector $\mathbf{m}$ may be represented as the rotation of a template vector

$$\mathbf{m}_0 \triangleq \begin{bmatrix} 1 & 0 \end{bmatrix}^T, \tag{C.3}$$

through a random angle of α radians. Let the notation $\mathbf{T}_\alpha$ represent the matrix transformation which rotates a vector through an angle of α radians, and we have

$$\mathbf{m} = \mathbf{T}_\alpha \mathbf{m}_0. \tag{C.4}$$

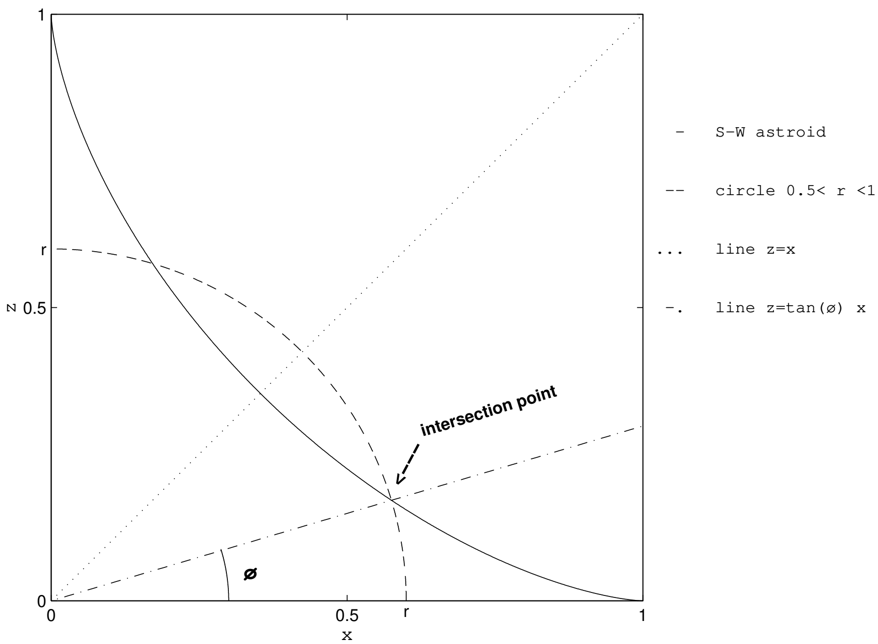

Figure C.1: Intersection of circle with $Q(\mathbf{m}_0)$

Likewise, each set in the family of sets, $\{Q(\mathbf{m}) : |\mathbf{m}| = 1\}$ may be generated by a rotation of the template set $Q(\mathbf{m}_0)$, so that

$$\begin{aligned} \Upsilon(\underline{\lambda}) &= \Pr\{\underline{\lambda} \in \mathbf{T}_\alpha Q(\mathbf{m}_0)\} \\ &= \Pr\{\mathbf{T}_{-\alpha}\underline{\lambda} \in Q(\mathbf{m}_0)\}. \end{aligned} \tag{C.5}$$

In the final expression, we have a more usual probability expression of the probability that a random vector is an element of a fixed set. The random vector $\mathbf{T}_{-\alpha}\underline{\lambda}$ has magnitude $|\underline{\lambda}|$ and has orientation uniformly distributed over a full circle. We now determine the probability that such a random vector is an element of the set $Q(\mathbf{m}_0)$.

Examination of Fig. 6.3 reveals that any circle with radius less than or equal to $\frac{1}{2}$ is contained within $Q(\mathbf{m}_0)$. Therefore, for $|\underline{\lambda}| \leq \frac{1}{2}$, $\Upsilon(\underline{\lambda}) = 1$. Also, any circle with radius greater than or equal to 1 intersects $Q(\mathbf{m}_0)$ over precisely half its circumference. Therefore, for $|\underline{\lambda}| \geq 1$, $\Upsilon(\underline{\lambda}) = \frac{1}{2}$. For values of $|\underline{\lambda}|$ between $\frac{1}{2}$ and 1, further analysis is required. Consider Fig. C.1, which depicts the boundary of the set $Q(\mathbf{m}_0)$ within the region $[0, 1]^2$ and its intersection with a circle or radius r between $\frac{1}{2}$ and 1. The figure is symmetric about the line $x = z$, so that the ratio of the circle arc length within $Q(\mathbf{m}_0)$ to the total circle arc length in this region is equal to the same ratio within the region such that $z \leq x$. Let us now determine the latter ratio.

In Fig. C.1 the point of intersection between the Stoner-Wohlfarth astroid (the boundary of $Q(\mathbf{m}_0)$ and the circle of radius r is marked. This point (x_s, z_s) is the solution of the pair of equations

$$x_s^2 + z_s^2 = r^2 \tag{C.6}$$
$$x_s^{\frac{2}{3}} + z_s^{\frac{2}{3}} = 1, \tag{C.7}$$

for which $z_s \leq x_s$. The angle ϕ indicated in the Fig. C.1 is then expressed

$$\phi = \tan^{-1}\left(\frac{z_s}{x_s}\right), \tag{C.8}$$

and the fraction of the whole circle contained within $Q(\mathbf{m}_0)$ is

$$\frac{1}{2} + \frac{1}{2} \cdot \frac{\phi}{\pi/4}. \tag{C.9}$$

To determine the intersection point (x_s, z_s), solve (C.7) for x_s to get

$$x_s = \left(1 - z_s^{\frac{2}{3}}\right)^{\frac{3}{2}}. \tag{C.10}$$

Substitute into (C.6) and simplify:

$$\left(1 - z_s^{\frac{2}{3}}\right)^3 + z_s^2 = r^2 \tag{C.11}$$
$$\left(1 - 3z_s^{\frac{2}{3}} + 3z_s^{\frac{4}{3}} - z_s^2\right) + z_s^2 = r^2 \tag{C.12}$$
$$1 - 3z_s^{\frac{2}{3}} + 3z_s^{\frac{4}{3}} = r^2. \tag{C.13}$$

Let $y = z_s^{\frac{2}{3}}$ in (C.13). Then the corresponding quadratic equation in y is

$$3y^2 - 3y + (1 - r^2) = 0, \tag{C.14}$$

which has solutions

$$y_{1,2} = \frac{1 \pm \sqrt{\frac{4r^2-1}{3}}}{2}. \tag{C.15}$$

Because the two equations which determine the intersection point are symmetric in x and z, the solutions y_1 and y_2 are equal to $x_s^{\frac{2}{3}}$ and $x_s^{\frac{2}{3}}$. The constraint that $z_s \leq x_s$ leads to the solution pair

$$z_s = y_2^{\frac{3}{2}} = \left(\frac{1-\sqrt{\frac{4r^2-1}{3}}}{2}\right)^{\frac{3}{2}}, \tag{C.16}$$

$$x_s = y_1^{\frac{3}{2}} = \left(\frac{1+\sqrt{\frac{4r^2-1}{3}}}{2}\right)^{\frac{3}{2}}. \tag{C.17}$$

The fraction of the circle of radius r within the set $Q(\mathbf{m}_0)$ is then

$$\frac{1}{2} + \frac{2}{\pi}\tan^{-1}\left[\left(\frac{1-\sqrt{\frac{4r^2-1}{3}}}{1+\sqrt{\frac{4r^2-1}{3}}}\right)^{\frac{3}{2}}\right]. \tag{C.18}$$

We note in passing that this expression is the inverse of the Stoner-Wohlfarth switching field function displayed in Fig. 4.2.

Finally, recall that the radius r of the circle represents the magnitude of the vector $\underline{\lambda}$. Collecting all the partial solutions together, we conclude

$$\Upsilon(\underline{\lambda}) = \begin{cases} 1, & |\underline{\lambda}| \leq \frac{1}{2} \\ \frac{1}{2} + \frac{2}{\pi}\tan^{-1}\left[\left(\frac{1-\sqrt{\frac{4|\underline{\lambda}|^2-1}{3}}}{1+\sqrt{\frac{4|\underline{\lambda}|^2-1}{3}}}\right)^{\frac{3}{2}}\right], & \frac{1}{2} < |\underline{\lambda}| < 1 \\ \frac{1}{2}, & |\underline{\lambda}| \geq 1 \end{cases}. \tag{C.19}$$

This expression may be written in the form

$$\Upsilon(\underline{\lambda}) = \frac{1}{2} + \frac{1}{2}\Psi(|\underline{\lambda}|), \tag{C.20}$$

with $\Psi(r)$ defined as in (6.53).

References

[1] Milton Abramowitz and Irene A. Stegun, editors. *Handbook of Mathematical Functions*. Dover Publications, Inc., New York, 1965.

[2] Dakshi Agrawal. Magnetic recording system design to reduce medium noise through signal precompensation. Master's thesis, Washington University, St. Louis, MO, USA, August 1995. Department of Electrical Engineering.

[3] Kazuhiko Aomoto. Analytic structure of Schläfli function. *Nagoya Math. J.*, 68:1–16, 1977.

[4] F. Aurenhammer. Voronoi diagrams – a survey of a fundamental geometric data structure. *ACM Computing Surveys*, 23(3):345–405, September 1991.

[5] Pierre Baldi and Santosh S. Venkatesh. Number of stable points for spin-glasses and neural networks of higher orders. *Phys. Rev. Lett.*, 58(9):913–917, March 1987.

[6] Israel Bar-David and Shlomo Shamai (Shitz). Information rates for magnetic recording channels with peak- and slope-limited magnetization. *IEEE Trans. Inform. Theory*, 35(5):956–962, September 1989.

[7] C. Bradford Barber, David P. Dobkin, and Hannu Huhdanpaa. The quickhull algorithm for convex hulls. submitted to the ACM Trans. on Mathematical Software, May 25 1995.

[8] H. Neal Bertram. *Theory of Magnetic Recording*. Cambridge University Press, Cambridge, United Kingdom, 1994.

[9] H. Neal Bertram and Xiaodong Che. General analysis of noise in recorded transitions in thin film recording media. *IEEE Trans. Magn.*, 29(1):201–208, January 1993.

[10] H. Neal Bertram and Jian-Gang Zhu. Simulations of torque measurements and noise in thin film magnetic recording media. *IEEE Trans. Magn.*, 27(6):5043–5045, November 1991.

[11] H. Neal Bertram and Jian-Gang Zhu. Fundamental magnetization processes in thin-film recording media. In Henry Ehrenreich and David Turnbull, editors, *Solid State Physics: Advances in Research and Applications*, volume 46, pages 271–371. Academic Press, Inc., 1250 Sixth Avenue, San Diego, CA 92101-4311, 1992.

[12] William H. Beyer, editor. *CRC Standard Mathematical Tables.* CRC Press, Inc., Boca Raton, FL, 25th edition, 1978.

[13] Johannes Böhm and Eike Hertel. *Polyedergeometrie in n-dimensionalen Räumen konstanter Krümmung*, volume 70 of *Lehrbücher und Monographien aus dem Gebiete der exakten Wissenschaften.* Birkhäuser Verlag, Basel, 1981.

[14] Kevin Q. Brown. Voronoi diagrams from convex hulls. *Information Processing Letters*, 9(5):223–228, December 1979.

[15] William Fuller Brown, Jr. Failure of the local-field concept for hysteresis calculations. *J. Appl. Phys.*, 33(3):1308–1309, March 1962.

[16] William Fuller Brown, Jr. *Micromagnetics*, volume 18 of *Interscience Tracts on Physics and Astronomy.* Interscience Publishers, New York, 1963.

[17] David Burshtein. Nondirect convergence radius and number of iterations of the Hopfield associative memory. *IEEE Trans. Inform. Theory*, 40(3):838–847, May 1994.

[18] D. W. Chapman. Theoretical limit on digital magnetic recording density. *Proceedings of the IEEE*, 51:395–395, 1963.

[19] Xiaodong Che and H. Neal Bertram. Dynamics of nonlinearities in high density recording. *IEEE Trans. Magn.*, 29(1):317–323, January 1993.

[20] David K. Cheng. *Field and Wave Electromagnetics.* Addison-Wesley, Reading, Massachusetts, 2d edition, 1989.

[21] Sushin Chikazumi. *Physics of Magnetism.* Robert E. Krieger Publishing Company, 1964.

[22] Levi L. Conant. *Plane and Spherical Trigonometry.* American Book Company, New York, 1909.

[23] Thomas M. Cover and Joy A. Thomas. *Elements of Information Theory.* John Wiley & Sons, Inc., New York, 1991.

[24] H. S. M. Coxeter. The functions of Schläfli and Lobatschefsky. *Quart. J. Math.*, 6:13–29, 1935.

[25] N. G. De Bruijn. *Asymptotic Methods in Analysis.* North-Holland Publishing Co., Amsterdam, 1958.

[26] J. A. Ewing and H. G. Klaussen. Magnetic qualities of iron. *Philosophical Transactions of the Royal Society of London A*, 184:985–1040, 1893.

[27] Monica Lorraine Fisher. Storage capacity of a magnetic recording medium. Technical Report MISC-95-09, Magnetics and Information Science Center, Washington University, St. Louis, MO, May 1995.

[28] Catherine A. French and Jack Keil Wolf. Bounds on the capacity of a peak power constrained Gaussian channel. *IEEE Trans. Magn.*, 24(5):2247–2262, September 1988.

[29] M. Futamoto, F. Kugiya, M. Suzuki, H. Takano, Y. Matsuda, N. Inaba, Y. Miyamura, K. Akagi, T. Nakao, and H. Sawaguchi. Investigation of 2 Gb/in^2 magnetic recording at a track density of 17 ktpi. *IEEE Trans. Magn.*, 27(6):5280–5285, November 1991.

[30] Robert G. Gallager. *Information Theory and Reliable Communication.* John Wiley & Sons, Inc., 1968.

[31] E. N. Gilbert. Random subdivisions of space into crystals. *Ann. Math. Stat.*, 33:958–972, 1962.

[32] T. L. Gilbert. A Lagrangian formulation of the gyromagnetic equation of the magnetization field. *Physical Review*, 100(4):1243, November 1955.

[33] Edward Grochowski and David A. Thompson. Outlook for maintaining areal density growth in magnetic recording. *IEEE Trans. Magn.*, 30(6):3797–3800, November 1994.

[34] Chris D. Heegard, Alexandra Duel-Hallen, and Rajeev Krishnamoorthy. On the capacity of the noisy runlength channel. *IEEE Trans. Inform. Theory*, 37(3):712–720, May 1991.

[35] Chris D. Heegard and Lawrence H. Ozarow. Bounding the capacity of saturation recording: The Lorentz model and applications. *IEEE Journal on Selected Areas in Communications*, 10(1):145–156, January 1992.

[36] John Hertz, Anders Krogh, and Richard G. Palmer. *Introduction to the Theory of Neural Computation*. Addison-Wesley, Redwood City, California, 1991.

[37] Walter Hirt and James L. Massey. Capacity of the discrete-time Gaussian channel with intersymbol interference. *IEEE Trans. Inform. Theory*, 34(3):380–388, May 1988.

[38] Jay Recer Hoinville. *Spatial Media Noise Studies of Longitudinal Magnetic Recording Media*. PhD thesis, Washington University, St. Louis, MO, December 1991. Department of Electrical Engineering.

[39] Jay Recer Hoinville, R. S. Indeck, and M. W. Muller. Spatial noise phenomena of longitudinal magnetic recording media. *IEEE Trans. Magn.*, 28:3398–3406, November 1992.

[40] John J. Hopfield. Neural networks and physical systems with emergent collective computational abilities. *Proc. Natl. Acad. Sci. USA*, 79:2554–2558, April 1982.

[41] Gordon F. Hughes. Magnetization reversal in cobalt-phosphorus films. *J. Appl. Phys.*, 54(9):5306–5313, September 1983.

[42] Ronald S. Indeck and Elias Glavinas. Fingerprinting magnetic media. *IEEE Trans. Magn.*, 29(6):4095–4097, November 1993.

[43] Kenneth E. Johnson. Fabrication of low noise thin-film media. In Thomas C. Arnoldussen and L. L. Nunnelley, editors, *Noise in Digital Magnetic Recording*, pages 7–63. World Scientific, P.O. Box 128, Farrer Road, Singapore, 1992.

[44] O. Karlqvist. Calculation of the magnetic field in the ferromagnetic layer of a magnetic drum. *Transactions of the Royal Institute of Technology (Stockholm)*, 86:3, 1954.

[45] Ruth Kellerhals. On Schläfli's reduction formula. *Mathematische Zeitschrift*, 206:193–210, 1991.

[46] Ivo Klik, Jyh-Shinn Yang, and Ching-Ray Chang. Hysteresis of binary clusters. *J. Appl. Phys.*, 76(10):6493–6495, November 1994.

[47] Ivo Klik, Y. D. Yao, and Ching-Ray Chang. Multilevel master equation for bicrystal clusters. *J. Appl. Phys.*, 79(8):4919–4921, April 1996.

[48] János Komlós and Ramamohan Paturi. Convergence results in an associative memory model. *Neural Networks*, 1:239–250, 1988.

[49] Eberhard Köster and Thomas C. Arnoldussen. Recording media. In C. Denis Mee and Eric D. Daniel, editors, *Magnetics Recording Handbook: Technology and Applications*, pages 101–257. McGraw-Hill Publishing Company, New York, 1990.

[50] Anthony Kuh and Bradley W. Dickinson. Information capacity of associative memories. *IEEE Trans. Inform. Theory*, 35(1):59–68, January 1989.

[51] L. Landau and E. Lifshitz. On the theory of the dispersion of magnetic permeability in ferromagnetic bodies. *Physikalische Zeitschrift Der Sowjetunion*, 8:153–169, 1935.

[52] Khaled Ben Letaief and John S. Sadowsky. New importance sampling methods for simulating sequential decoders. *IEEE Trans. Inform. Theory*, 39(5):1716–1722, September 1993.

[53] Gang Herbert Lin and H. Neal Bertram. Experimental studies of noise autocorrelation in thin film media. *IEEE Trans. Magn.*, 29(6):3697–3699, November 1993.

[54] Gang Herbert Lin and H. Neal Bertram. Noise correlations in dibit recording. *J. Appl. Phys.*, 75(10):5765–5767, May 15 1994.

[55] Pu-Ling Lu and Stanley H. Charap. Thermal instability at 10 Gbit/in^2 magnetic recording. *IEEE Trans. Magn.*, 30(6):4230–4232, November 1994.

[56] John C. Mallinson. On extremely high density digital recording. *IEEE Trans. Magn.*, 10(2):368–373, June 1974.

[57] John C. Mallinson. *The Foundations of Magnetic Recording*. Academic Press, Inc., San Diego, CA, 1987.

[58] John C. Mallinson. On damped gyromagnetic precession. *IEEE Trans. Magn.*, 23(4):2003–2004, July 1987.

[59] John C. Mallinson. A new theory of recording media noise. *IEEE Trans. Magn.*, 27(4):3519–3531, July 1991.

[60] John C. Mallinson. *The Foundations of Magnetic Recording*. Academic Press, Inc., San Diego, CA, second edition, 1993.

[61] Masud Mansuripur. Magnetization reversal dynamics in the media of magneto-optical recording. *J. Appl. Phys.*, 63(12):5809–5823, June 1988.

[62] Masud Mansuripur. Demagnetizing field computation for thin films: Extension to the hexagonal lattice. *J. Appl. Phys.*, 66(8):3731–3733, October 1989.

[63] Masud Mansuripur and Roscoe Giles. Demagnetizing field computation for dynamic simulation of the magnetization reversal process. *IEEE Trans. Magn.*, 24(6):2326–2328, November 1988.

[64] Masud Mansuripur and Roscoe Giles. Simulation of the magnetization-reversal dynamics on the Connection Machine. *Comput. Phys.*, 4:291–302, 1990.

[65] D. H. Martin. *Magnetism in Solids*. Iliffe Books Ltd., London, 1967.

[66] Joseph P. McCormack. *Solid Geometry*. D. Appleton and Company, New York, 1931.

[67] Robert J. McEliece, Edward C. Posner, Eugene R. Rodemich, and Santosh S. Venkatesh. The capacity of the Hopfield associative memory. *IEEE Trans. Inform. Theory*, 33(4):461–482, July 1987.

[68] Steven W. McLaughlin and David L. Neuhoff. Upper bounds on the capacity of the digital magnetic recording channel. *IEEE Trans. Magn.*, 29(1):59–66, January 1993.

[69] J. L. Meijering. Interface area, edge length, and number of vertices in crystal aggregates with random nucleation. *Philips Res. Rept.*, 8:270–290, 1953.

[70] Guo Mian, R. S. Indeck, and M. W. Muller. Transverse correlation length in thin film media. *IEEE Trans. Magn.*, 28(5):2733–2735, September 1992.

[71] Guo Mian, Ronald S. Indeck, and Marcel W. Muller. Micromagnetic transverse correlation length in thin film magnetic recording media, medium noise, and tracking. *Journal of Magnetism and Magnetic Materials*, 152:253–264, 1996.

[72] Barry K. Middleton. Recording and reproducing processes. In C. Denis Mee and Eric D. Daniel, editors, *Magnetics Recording Handbook: Technology and Applications*, pages 24–100. McGraw-Hill Publishing Company, New York, 1990.

[73] James John Miles. *Information Storage on Thin Film Media*. PhD thesis, University of Manchester, 1990.

[74] James John Miles and Barry K. Middleton. The role of microstructure in micromagnetic models of longitudinal thin film magnetic media. *IEEE Trans. Magn.*, 26(5):2137–2139, September 1990.

[75] James John Miles and Barry K. Middleton. A hierarchical micromagnetic model of longitudinal thin film recording media. *Journal of Magnetism and Magnetic Materials*, 95(1):99–108, 1991.

[76] James John Miles and Barry K. Middleton. Micromagnetic simulations of transverse recording. *IEEE Trans. Magn.*, 27(6):4969–4971, November 1991.

[77] James John Miles and Barry K. Middleton. The effect of track width on transition noise in longitudinal thin-film media. *Journal of Magnetism and Magnetic Materials*, 120:375–378, March 1993.

[78] James John Miles and Barry K. Middleton. Micromagnetic simulation of texture induced orientation in thin film media. *IEEE Trans. Magn.*, 31(6):2770–2772, November 1995.

[79] James John Miles, Michal Wdowin, John Oakley, and Barry K. Middleton. The effect of cluster size on thin film media noise. *IEEE Trans. Magn.*, 31(2):1013–1024, March 1995.

[80] Tai Min and Jian-Gang Zhu. Grain height fluctuation and medium noise in longitudinal thin film recording media. *IEEE Trans. Magn.*, 29(6):3706–3708, November 1993.

[81] M. Mirzamaani, C. V. Jahnes, and M. A. Russak. Magnetic properties of CoPtCr thin films with $\langle 11\bar{2}0 \rangle$ crystal orientation. *J. Appl. Phys.*, 69(8):5169–5171, April 1991.

[82] J. J. Miyata and R. R. Hartel. The recording and reproduction of signals on magnetic medium using saturation-type recording. *IRE Transactions on Electronic Computers*, 8:159–169, 1959.

[83] Allan H. Morrish. *The Physical Principles of Magnetism.* Wiley Series on the Science and Technology of Materials. John Wiley & Sons, Inc., New York, 1965.

[84] Marcel W. Muller and Ronald S. Indeck. Intergranular exchange coupling. *J. Appl. Phys.*, 75(4):2289–2290, February 1994.

[85] Edward S. Murdock, Ralph F. Simmons, and Robert Davidson. Roadmap for 10 Gbit/in^2 media: Challenges. *IEEE Trans. Magn.*, 28(5):3078–3083, September 1992.

[86] Charles M. Newman. Memory capacity in neural network models: Rigorous lower bounds. *Neural Networks*, 1:233–238, 1988.

[87] Joseph O'Rourke. *Computational Geometry in C.* Cambridge University Press, 1994.

[88] Joseph A. O'Sullivan, Dakshi Agrawal, Ronald S. Indeck, and Marcel W. Muller. Signal precompensation for multiplicative noise in magnetic recording. In *Proc. 29th CISS*, Baltimore, MD, March 1995.

[89] Joseph A. O'Sullivan, Dakshi Agrawal, Donald Gene Porter, Ronald S. Indeck, and Marcel W. Muller. Magnetic recording system design to reduce medium noise through signal precompensation. In *Proc. 28th CISS*, pages 1152–1155, Princeton, NJ, March 1994. Department of Electrical Engineering, Princeton University.

[90] Joseph A. O'Sullivan, Donald Gene Porter, Ronald S. Indeck, and Marcel W. Muller. Physically based information science of magnetic recording I. Information capacity of a medium model. *IEEE Trans. Magn.*, 29(5):4036–4038, November 1993.

[91] Joseph A. O'Sullivan, Donald Gene Porter, Ronald S. Indeck, and Marcel W. Muller. Recording medium properties and capacity bounds. *J. Appl. Phys.*, 75(10):5753–5755, May 1994.

[92] Lawrence H. Ozarow, Aaron D. Wyner, and Jacob Ziv. Achievable rates for a constrained Gaussian channel. *IEEE Trans. Inform. Theory*, 34(3):365–370, May 1988.

[93] Athanasios Papoulis. *Probability, Random Variables, and Stochastic Processes.* McGraw-Hill Publishing Company, New York, second edition, 1984.

[94] Donald Gene Porter. Physically based models for magnetic recording channels. Master's thesis, Washington University, St. Louis, MO, May 1993.

[95] Donald Gene Porter, Joseph A. O'Sullivan, Ronald S. Indeck, and Marcel W. Muller. Effective field equivalences in thin film recording media for capacity computations. Technical Report WUEE-93-147, Washington University, 1993.

[96] Donald Gene Porter, Joseph A. O'Sullivan, Ronald S. Indeck, and Marcel W. Muller. Physically based information science of magnetic recording II. Physical sources of medium noise. *IEEE Trans. Magn.*, 30(6):4266–4268, November 1994.

[97] Donald Gene Porter, Joseph A. O'Sullivan, Ronald S. Indeck, and Marcel W. Muller. Physically based model and simulations of medium noise. Technical Report WUEE-94-164, Washington University, 1994.

[98] M. Prutton. *Thin Ferromagnetic Films.* Butterworth & Co., Ltd., London, 1964.

[99] M. Richardson. *Plane and Spherical Trigonometry.* The MacMillan Company, New York, 1950.

[100] Kenneth A. Ross and Charles R. B. Wright. *Discrete Mathematics.* Prentice-Hall, Inc., Englewood Cliffs, NJ, 1985.

[101] John S. Sadowsky. On the optimality and stability of exponential twisting in Monte Carlo estimation. *IEEE Trans. Inform. Theory*, 39(1):119–128, January 1993.

[102] Ludwig Schläfli. On the multiple integral $\int^n dxdy \ldots dz$ whose limits are $p_1 = a_1x + b_1y + \ldots + h_1z > 0, p_2 > 0, \ldots, p_n > 0$, and $x^2 + y^2 + \ldots + z^2 < 1$. In *Gesammelte Mathematische Abhandlugen von Luwig Schläfli*, pages 219–269. Verlag Birkhäuser Basel, 1953.

[103] Thomas Schrefl and Josef Fidler. Numerical simulation of magnetization reversal in hard magnetic materials using a finite element method. *Journal of Magnetism and Magnetic Materials*, 111:105–114, 1992.

[104] Thomas Schrefl, Josef Fidler, and H. Kronmüller. Remanence and coercivity in isotropic nanocrystalline permanent magnets. *Physical Review B*, 49(9):6100–6110, March 1994.

[105] Thomas Schrefl, H. F. Schmidts, Josef Fidler, and H. Kronmüller. Nucleation fields and grain boundaries in hard magnetic materials. *IEEE Trans. Magn.*, 29(6):2878–2880, November 1993.

[106] Schlomo Shamai (Shitz) and Israel Bar-David. Upper bounds on capacity for a constrained Gaussian channel. *IEEE Trans. Inform. Theory*, 35(5):1079–1084, September 1989.

[107] Shlomo Shamai (Shitz), Lawrence H. Ozarow, and Aaron D. Wyner. Information rates for a discrete-time Gaussian channel with intersymbol interference and stationary inputs. *IEEE Trans. Inform. Theory*, 37(6):1527–1539, November 1991.

[108] Claude E. Shannon. A mathematical theory of communication. *Bell Sys. Tech. Journal*, 27:379–423,623–656, 1948.

[109] Donald L. Snyder and Michael I. Miller. *Random Point Processes in Time and Space*. Springer-Verlag, New York, 1991.

[110] D. M. Y. Sommerville. *An Introduction to the Geometry of N Dimensions*. Methuen & Co. Ltd., London, 1929.

[111] E. C. Stoner and E. P. Wohlfarth. A mechanism of magnetic hysteresis in heterogeneous alloys. *Phil. Trans. Royal Soc. London*, A240:599–642, 1948.

[112] H. J. Sussmann. On the number of memories that can be perfectly stored in a neural network with Hebb weights. *IEEE Trans. Inform. Theory*, 35(1):174–178, January 1989.

[113] F. Tanaka and S. F. Edwards. Analytic theory of the ground state properties of a spin glass: I. Ising spin glass. *J. Phys. F: Metal Phys.*, 10:2769–2778, 1980.

[114] Ching Tsang, Hugo Santini, Don McCown, Jerry Lo, and Rod Lee. 3 Gb/in^2 recording demonstration with dual element heads & thin film disks. *IEEE Trans. Magn.*, 32(1):7–12, January 1996.

[115] Harry L. Van Trees. *Detection, Estimation, and Modulation Theory*, volume 1. John Wiley & Sons, 1968.

[116] E.B. Vinberg. Volumes of non-Euclidean polyhedra. *Russian Math. Surveys*, 48(2):15–45, 1993.

[117] W. Vogel. *Lectures on Results on Bezout's Theorem.* Springer-Verlag, Berlin, 1984.

[118] Paul A. Voois and John M. Cioffi. Capacity of the single-head magnetic recording process versus capacity of the magnetic medium: A two-dimensional approach. submitted to IEEE Transactions on Information Theory, November 1993.

[119] R. L. Wallace, Jr. The reproduction of magnetically recorded signals. *Bell Sys. Tech. Journal*, 30:1145–1173, 1951.

[120] Ronald K. Wangsness. *Electromagnetic Fields.* John Wiley & Sons, 2nd edition, 1986.

[121] Washington University School of Engineering & Applied Science. *1994-1995 Graduate Programs in Engineering & Applied Science.*

[122] R. M. White. *Quantum Theory of Magnetism*, volume 32 of *Springer Series in Solid-State Sciences.* Springer-Verlag, Berlin, 1983.

[123] M. L. Williams and R. L. Comstock. An analytical model of the write process in digital magnetic recording. *A.I.P. Conf. Proc.*, 5:738, 1972.

[124] B. Y. Wong, D. E. Laughlin, and D. N. Lambeth. Investigation of CoNiCr thin films deposited on [100] and [110] Cr single crystals. *IEEE Trans. Magn.*, 27(6):4733–4735, November 1991.

[125] Xiao-Guang Ye and Jian-Gang Zhu. Micromagnetic study of magnetization process in bicrystal thin film. *IEEE Trans. Magn.*, 28(5):3087–3089, September 1992.

[126] Xiao-Guang Ye and Jian-Gang Zhu. Modeling of thin-film media with advanced microstructure for ultrahigh density recording. *J. Appl. Phys.*, 75(10):6135–6137, May 15 1994.

[127] Tadashi Yogi, Ching Tsang, Thao A. Nguyen, Kochan Ju, Grace L. Gorman, and Gil Castillo. Longitudinal media for 1 Gbit/in^2 areal density. *IEEE Trans. Magn.*, 26(5):2271–2276, September 1990.

[128] Kazuetsu Yoshida, Yasutaro Uesaka, Miki Hara, Yoshinobu Nakatani, and Nobuo Hayashi. Computer simulation of thin-film media noise. Technical Report MR93-5, The Institute of Electronics, Information, and Communication Engineers, 1993. p. 29.

[129] Samuel W. Yuan and H. Neal Bertram. Statistical data analysis of magnetic recording noise mechanisms. *IEEE Trans. Magn.*, 28(1):84–92, January 1992.

[130] A. H. Zemanian. *Distribution Theory and Transform Analysis.* International Series in Pure and Applied Mathematics. McGraw-Hill, Inc., 1965.

[131] Jian-Gang Zhu and H. Neal Bertram. Micromagnetic studies of thin metallic films. *J. Appl. Phys.*, 63(8):3248–3253, April 1988.

[132] Jian-Gang Zhu and H. Neal Bertram. Recording and transition noise simulations in thin film media. *IEEE Trans. Magn.*, 24(6):2706–2708, November 1988.

[133] Jian-Gang Zhu and H. Neal Bertram. Study of noise sources in thin film media. *IEEE Trans. Magn.*, 26(5):2140–2142, September 1990.

[134] Jian-Gang Zhu and H. Neal Bertram. Magnetization structures in thin-film recording media. *IEEE Trans. Magn.*, 27(4):3553–3562, July 1991.

[135] Jian-Gang Zhu and Haiyun Wang. Noise characteristics of interacting transitions in longitudinal thin film media. *IEEE Trans. Magn.*, 31(2):1065–1070, March 1995.

[136] Jian-Gang Zhu, Haiyun Wang, and Thomas C. Arnoldussen. Micromagnetic modeling and experimental study of transition noise correlation in thin-film media. *J. Appl. Phys.*, 75(10):5762–5764, May 15 1994.

[137] Jian-Gang Zhu, Xiao-Guang Ye, and Thomas C. Arnoldussen. Effect of in-plane easy axis orientation in narrow track recording. *IEEE Trans. Magn.*, 29(1):324–329, January 1993.

Vita

DONALD GENE PORTER

Born

4 November 1967, Miami, FL, USA

Education

1996:

Doctor of Science in Electrical Engineering
Washington University, St. Louis, Missouri
Dissertation: *Fundamental Limits on the Storage Capacity of Magnetic Recording Media*

1993:

Master of Science in Electrical Engineering
Washington University, St. Louis, Missouri
Thesis: *Physically Based Models for Magnetic Recording Channels*

Thesis Advisors: Drs. Joseph A. O'Sullivan and Ronald S. Indeck
Research Advisors: Drs. Joseph A. O'Sullivan, Ronald S. Indeck, and Marcel W. Muller

1990:

Bachelor of Science in Electrical Engineering
Bachelor of Science in Computer Science
Washington University, St. Louis, Missouri, *Cum Laude*

Areas of Interest

Information and communications theory, magnetic recording systems, scientific modeling and simulation, use of computer networks in education

Journal Publications

D. G. Porter, E. Glavinas, P. Dhagat, J. A. O'Sullivan, R. S. Indeck, and M. W. Muller, "Irregular Grain Structure in Micromagnetic Simulation," *Journal of Applied Physics*, vol. 79, no. 8, pp. 4695-4697, April 1996.

P. Dhagat, E. Galvinas, A. Jander, D. G. Porter, R. S. Indeck, and M. W. Muller, "Trackwidth Dependence of Transition Jitter," *Journal of Applied Physics*, vol. 79, no. 8, pp. 5652-5654, April 1996.

D. G. Porter, J. A. O'Sullivan, R. S. Indeck and M. W. Muller, "Physically Based Information Science of Magnetic Recording II. Physical Sources of Medium Noise," *IEEE Transactions on Magnetics*, vol. 30, no. 6, pp. 4266-4268, November 1994.

J. A. O'Sullivan, D. G. Porter, R. S. Indeck and M. W. Muller, "Recording Medium Properties and Capacity Bounds," *Journal of Applied Physics*, vol. 75, no. 10, pp. 5753-5755, May 1994.

J. A. O'Sullivan, D. G. Porter, R. S. Indeck and M. W. Muller, "Physically Based Information Science of Magnetic Recording I. Information Capacity of a Medium Model," *IEEE Transactions on Magnetics*, vol. 29, no. 6, pp. 4036-4038, November 1993.

J. A. O'Sullivan, D. L. Snyder, D. G. Porter and P. Moulin, "An Application of Splines to Maximum Likelihood Radar Imaging," *International Journal of Imaging Systems and Technology*, vol. 4, pp. 256-264, 1992.

Conference Publications

D. G. Porter, P. Dhagat, J. A. O'Sullivan, R. S. Indeck and M. W. Muller, "Irregular Grain Structure in Micromagnetic Simulation," *40th Annual Conference on Magnetism and Magnetic Materials: Abstracts*, AR-15, November 1995.

D. G. Porter and J. A. O'Sullivan, "Physical Limits on the Storage Capacity of Magnetic Recording Media," in *Proceedings 1995 IEEE International Symposium on Information Theory*, p. 248, IEEE Information Theory Society, September 1995.

D. G. Porter, J. A. O'Sullivan, R. S. Indeck and M. W. Muller, "Physically Based Information Science of Magnetic Recording II. Physical Sources of Medium Noise," *The 6th Joint MMM-Intermag Conference: Abstracts*, FP-04, pp.397-398, June, 1994.

J. A. O'Sullivan, D. Agrawal, D. G. Porter, R. S. Indeck and M. W. Muller, "Magnetic Recording System Design to Reduce Medium Noise Through Signal Precompensation," in *Proceedings of the 28th Conference on Information Science and Systems*, pp. 1152-1155, (Princeton, NJ), Department of Electrical Engineering, Princeton University, 1994.

J. A. O'Sullivan, D. G. Porter, R. S. Indeck and M. W. Muller, "Recording Medium Properties and Capacity Bounds," *38th Annual Conference on Magnetism and Magnetic Materials: Abstracts*, BC-04, pp. 87-88, November 1993.

J. A. O'Sullivan, D. G. Porter, R. S. Indeck and M. W. Muller, "Physically Based Information Science of Magnetic Recording I. Information Capacity of a Medium Model," *DIGESTS of INTERnational MAGnetics Conference*, GQ-02, April 1993.

J. A. O'Sullivan, D. G. Porter, R. S. Indeck and M. W. Muller, "A Physically Based Approach to Information Theory for Thin Film Magnetic Recording," in *Proceedings of the 30th Allerton Conference on Communication, Control, and Computing*, pp. 792-798, 1992.

Other Papers

D. G. Porter, J. A. O'Sullivan, R. S. Indeck and M. W. Muller, "Physically Based Model and Simulations of Medium Noise," Tech. Rep. WUEE-94-164, Washington University Department of Electrical Engineering, 1994.

D. G. Porter, J. A. O'Sullivan, R. S. Indeck and M. W. Muller, "Effective Field Equivalences in Thin Film Recording Media for Capacity Computations," Tech. Rep. WUEE-93-147, Washington University Department of Electrical Engineering, 1993.

D. G. Porter, "A Computer Simulation of ISAR Data Collection and Image Production," ESSRL Monograph ESSRL-91-36, Electronic Systems and Signals Research Laboratory, 1991.

Presentations

Workshop on Hysteresis Modeling and Micromagnetism
The Institute for Magnetics Research, George Washington University Virginia Campus, Ashburn, VA, 20 May 1996, Invited speaker.

40th Annual Conference on Magnetism & Magnetic Materials
Philadelphia, PA, 6 November 1995, Poster session.

1995 IEEE International Symposium on Information Theory
Whistler, B. C., Canada, 18 September 1995, Short presentation.

The 6th Joint MMM-Intermag Conference
Albuquerque, NM, 22 June 1994, Poster session.

38th Annual Conference on Magnetism & Magnetic Materials
Minneapolis, MN, 15 November 1993, Oral presentation.

INTERMAG '93 Stockholm, Sweden, 16 April 1993, Poster session.

Thirtieth Annual Allerton Conference on Communication, Control, and Computing Robert Allerton Park, IL, 30 September 1992, Oral presentation.

Six Departmental, ESSRL, and Applied Physics Seminars Washington University

Teaching/Grading

1995: Guest Lecturer, **EE512**: Magnetic Recording Technology

1994: Guest Lecturer, **EE379**: Signal Analysis for Electronic Systems and Circuits

Co-presenter, seminar series on signal space coding

1992-1993: Grader, **EE552**: Detection and Estimation Theory

1991: Consultant, **EE280**: Introduction to Electrical Networks; led weekly help sessions.

1989-1990: Head grader, **CS135**: Introduction to Computer Science; duties included laboratory instruction, grader supervision, consulting and textbook editing.

1988: Grader, **EE/CS 360**: Digital Computers I: Organization and Logic Design

Awards

1990: The Computer Science Departmental Award for Professional Excellence, Washington University

Affiliations

Institute of Electrical and Electronics Engineers

Information Theory Society; *Magnetics Society*; *Signal Processing Society*; *Education Society*

Eta Kappa Nu

Chapter President, 1989-1990; Chapter Corresponding Secretary, 1988-1989

Tau Beta Pi

Scholarships and Fellowships

1993-1996: Research Assistantship funded by National Storage Industries Consortium and National Science Foundation

1990-1993: US Department of Education Graduate Assistance in Areas of National Need Fellowship

1988-1990: The Paric Corporation Scholarship

1986-1990: Calvin M. Woodward Fellowship

1986-1987: National Merit Scholarship

December 1996